INFLUENCE OF TIRE-PAVEMENT THERMOMECHANICAL INTERACTION ON CONTACT STRESSES AND ROLLING RESISTANCE

BY

ANGELI MARIZ GAMEZ JAYME

DISSERTATION

Submitted in partial fulfillment of the requirements
for the degree of Doctor of Philosophy in Civil Engineering
in the Graduate College of the
University of Illinois at Urbana-Champaign, 2020

Urbana, Illinois

Doctoral Committee:

Professor Imad L. Al-Qadi, Chair and Director of Research
Professor Carlos Armando Duarte
Professor Yanfeng Ouyang
Associate Professor Hasan Ozer, Arizona State University
Professor Athanasios Scarpas, Khalifa University

ABSTRACT

Roadway networks rely heavily on appropriate design and rehabilitation techniques to promote longevity and maximize infrastructure investments. Considering a loaded-pavement scenario, the behavior of flexible or asphalt-concrete-surfaced pavements is significantly influenced by both loading and environmental conditions. Heavy truck loads govern pavement responses and, thus, the eventual pavement damage. The anticipated increase in freight load and volume along with the prospect of autonomous truck platooning make it imperative that transportation agencies update their corresponding protocols and identify relevant solutions. One of the most critical perspectives in solving this problem begins at the tire-pavement contact.

Traditionally, conventional design and analysis of tire and pavement are done separately, with limited consideration of their inherent coupling. This scenario is ubiquitous for both roadway and airfield pavements. Although numerical models of tire and pavement exist, there is limited understanding of their coupling, especially with respect to heavy truck tire-pavement interaction. In this study, a thermomechanical interaction model is introduced to fill this gap with the overall goal of quantifying the influence of the interaction—specifically, the tire-pavement contact stresses and rolling resistance or loss.

A baseline hyperelastic tire model was generated to understand the effect of the applied load, tire-inflation pressure, and traveling speed on contact stresses. Utilizing tire-pavement contact stresses as the main excitation for pavement responses, Domain Analysis is introduced to evaluate multi-axial pavement responses induced by three-dimensional and non-uniform contact stress distributions. Domain Analysis evaluates bulk pavement behavior and identifies regions of potential damage in lieu of point strains. Furthermore, the turning maneuver of an aircraft landing gear tire on airfield pavements, which exhibits high tire-pavement contact stress levels, exacerbates the near-surface responses that may lead to shear and slippage distresses.

In this dissertation, the perspectives of tire and pavement engineers were merged to guide the design of the interaction model. The developed model represents a fully coupled thermal-stress analysis of a hyper-viscoelastic tire rolling over a deformable pavement

layer under various load conditions and temperature profiles. As the tire model becomes dissipative, both uniform and non-uniform temperature profiles, coupled with mechanical loading, further influenced the resulting contact stresses and rolling loss. Analogous to the seasonal behavior of viscoelastic materials, the resulting contact stresses under temperature conditions corresponding to winter differed than those of summer — higher contact stress magnitudes in "winter" were observed due to a reduced contact area, whereas lower magnitudes became evident during the "summer" as the stresses were distributed over a wider contact imprint. Finally, a prediction scheme using nonlinear regression is presented to provide a practical means of generating tire-pavement contact stress distribution without the need of computationally intensive simulations. Identifying critical thermomechanical tire-pavement interactions provide pavement engineers insights into improving pavement design and maintenance techniques, whereas tire manufacturers gain a deeper understanding of the influence of the tire's operating conditions on pavement performance.

To my parents Pearly, Rolly, and Jeff, for their love and support.

To one of the most incredible human beings who walked this earth, Grandma Inez.

ACKNOWLEDGMENTS

As my doctoral journey comes to an end, I first would like to thank God for making everything possible and for providing a heaping number of opportunities, not only to build my professional career, but also to enrich my personal growth. Throughout my years here in Illinois, I have been undoubtedly blessed to have had Professor Imad Al-Qadi guide, train, support, challenge, mentor, and help me in numerous ways, definitely for and beyond this dissertation; I simply cannot fathom to tally. He has been integral in my discovery of my love of pavements — asphalt concrete, just to clarify. I also am incredibly grateful for my committee members, Professors Duarte, Ouyang, Ozer, and Scarpas. Thank you for being my advocates and for providing invaluable feedback on my dissertation work. Moreover, thank you for the guidance through a prior class, discussions, and interactions.

My experiences would have not been as joyful and successful without the amazing team at the Illinois Center for Transportation (ICT). All the staff and students have imparted many lessons and challenging ideas that have made me a better person and a better researcher. Most especially, to our research group, to every incredible person who has graduated or recently joined, thank you for impacting my graduate school experience. For all the laughter and interesting discussions, Aravind Ramakrishnan, Daniel Castillo, Erman Gungor, Egemen Okte, Heena Dhasmana, Issam Qamhia, Izak Said, Javier Mainieri, Jose Rivera, Mouna Senhaji, Punit Singhvi, Priyanka Sarker, Qingqing Cao, Qingwen Zhou, Rebekah Yang, Saleh Yousefi, Seunggu Kang, Siqi Wang, Watheq Sayeh, Xiuyu Liu, and Zehui Zhu – thank you very much. Additionally, to Zhen Leng, who has been an incredible mentor since my Master's degree; it was a motivating prelude to continue my graduate school experience onto PhD. I also want to commend the camaraderie and vigilance of the ICT staff to help students in so many ways; thank you Emily Jankauski, Greg Renshaw, Kristi Anderson, Marc Killion, McCall Macomber, Noelle Arbulu, and Uthman Mohamed Ali. Moreover, I am grateful to the support by the Civil and Environmental Engineering department, particularly from Joan Christian Etta – many students, including myself, would be at a loss without your help. Additionally, Daniel Wong, thank you for finely combing through and editing my dissertation; our interaction, though brief, has taught me a lot.

I also have been incredibly lucky to have gained many life-long friends, who have become my confidant, cheerleader, and Chambana family. We maybe far away from our Nevada roots, but Amnah and Aqeel Al-Hajer, Amel Alqadah, Khaled Hasiba, Behzad Behnia, Catalina Arboleda, Nathan Kebede, Cristina Tozzo, Eva and Marcelino Anguiano, Hector Lopez, Alex Kreig, Josh Schiller, Paula Arango, Daniel Ribero, Sandra Corredor, Jorge Estrada, Tatiana and Patrick McKay family, Yesica Rojo, and Jaime Hernandez, have defined a new meaning of 'home.' Particularly, to my "Best Friend Forever No Matter What Happens" (BFFNMWH) Jaime, you have been an outstanding mentor and dear friend. My avid liking to automated and efficient post-processing, and creating beautiful plots were made possible as you shared your love for Python. Thank you for being one of the most incredible research partners. You have been a catalyst and advocate in helping me discover my affinity for computational research.

Moreover, to the benevolent and fabulous ladies from the Graduate Society of Women Engineers (GradSWE) – Anna Oldani, Elizabeth Horstman, Samantha Knoll, and Sofie Leon – you all have thought me the incredible value of a loving and empathetic community. GradSWE also led me to meet more remarkable women through the Rogue Book Club – Kate Dahlke, Lexi Sheehan, Megan Witzke, and Pranjali Priyadarshini. We initially met to read books, but left Caffe Bene with life-long friendships.

This year, 2020, has been surreal but even through trials, our family and friends in Nevada have been resolute in providing us unyielding love and support. To our concrete canoe family, Katie and Andrew Durham, Rachel and Mark Cukrov, Katie and Jeff Weagel, Tiffany and Andew Carr, Kelly and Erik Keselica, and Dani Sanford; thank you for prompting my curiosity and defying the norm by making Portland cement concrete float. To Professors David Sanders, Dean Adams, and Luis Loria-Salazar, thank you for being such incredible mentors during my undergraduate degree at the University of Nevada, Reno and for encouraging me to *be bold* to pursue my graduate degree. To Mr. Baer, one of my first American teachers from Wooster High School, thank you for advocating for a young, newly immigrated Filipina. Moreover, to our over-decade-long friendships, Jenn Schumacher, Lesly Betancourt, Stephanie Moore, Roberto Bejarano, and Mary Jane Ubando – thank you for being my pillars, my ground-truth. Thank you for sharing all of my exciting milestones, yet never fearing to challenge me when I need it most.

Most importantly, I am indebted to the unceasing love of my family. My mom Pearly and my sister Kristine have served as my absolute inspirations – they emulate the truest nature of kind hearts, confident minds, sharp wit, creative and hard-working spirit, and boundless compassion. My dad Rolly and stepdad Tito Jeff have given me more than double the love any daughter could ask for. My parents-in-law, Helen and Joel, have shown me their

limitless love and support as if I have always been their own daughter. In addition, Carlos, Joel, Jessica, Justin, Jayden, Jenna, Katie, Jon, Cayman, and Caspian have brought me and my family so much happiness. And to my Bubba, Ethan, thank you for being a bright light in my life; Auntie is and will always be incredibly proud of you. I also want to thank my furry best friend, Shiloh, who has been by my side for 15 years and counting. I am very blessed to have a strong core team that keeps me grounded, but always feeling loved.

Last, and never the least, to my husband, David Fabian Jayme — I would marry you again, even after two ceremonies. You have been my rock in faith and love. You have instilled confidence in me during moments of doubt. You have been my partner-in-crime for the first pasta salad we made with a full head of garlic to simple-home projects that we love to over-engineer because why not? I am thankful to our Lord for showing me the way of real love, devotion, and friendship by having you in my life for over 11 years. Given all my trials and achievements, I offer them to you, in return for being *my person*.

I also would like to acknowledge the collaborators and sponsors of my work throughout my entire graduate experience, including, the Airport Research Cooperative Program, Extreme Science and Engineering Discovery Environment (especially Mahidhar Tatineni), Federal Highway Administration, Illinois Department of Transportation, Illinois Center for Transportation, and Michelin.

TABLE OF CONTENTS

CHAPTER 1

INTRODUCTION

1.1 Introduction

The trucking industry is responsible for transporting more than 70% of all goods in the United States, making it vital for the national economy. More than $10 trillion of goods are moved annually and the corresponding freight shipments consume more than 21 billion gallons of fuel [1]. The demand for truck transport is currently projected to increase, impacting the structural capacity and functionality of pavement systems. The anticipated emergence of autonomous and connected trucks via platooning is expected to exacerbate the impact on the highway network. Hence, transportation agencies are obligated to appropriately consider the potential reduction in pavement service life due to the increasing level of freight traffic. This starts at the tire-pavement interaction.

Rolling resistance at the tire-pavement interface is one of the main factors responsible for fuel consumption. Also called "rolling loss," it is governed by characteristics like the tire, suspension system, hinges, and truck mass. The focus of this dissertation will be on the tire impact. Mammetti et al. [2] indicate that the relative contribution by percentage of truck tire rolling resistance to fuel consumption could vary from 23.2%, 33.3%, and 32.4% for city, rural, and highway driving conditions, respectively. Hence, a small fuel reduction of 1.5% could have a direct and significant influence on the economy and ecology [2].

The cyclic and dynamic deformation of tire materials–i.e. hysteretic losses–account for 90-95% of tire rolling losses, while the remainder can be attributed to interface frictional losses between the tire and road, aerodynamic drag losses, and inertial distortions of the tire [3]. It is also worth noting that due to the viscoelastic nature of the tire, its energy dissipation is strongly dependent on temperature, and vice versa.

In addition to the tire's loading and rolling conditions, the pavement, second body in the interaction, influences the tire's energy dissipation and inherent contact stresses that excite pavement responses. In the case of flexible pavements, this behavior may be exacerbated due to the coupled nature of a rolling tire over an asphalt concrete (AC) layer: both bodies

are viscoelastic materials. The United States' pavement system is mostly comprised of AC, which accounts for over 90% of the roadways. It is also predominantly used by many other countries. Considering the imminent increase in freight load and volume combined with the prospect of applying autonomous truck platooning, it is necessary for transportation agencies to appropriately update their design protocols to adequately serve the expected heavy traffic while maximizing their investments.

Currently, agencies use various pavement design methodologies to determine pavement mechanistic responses; however, empirical transfer functions have been implemented to predict pavement design life. In addition, conventional pavement design approaches assume tire loading to be uniformly distributed and assume the tire-pavement contact stress to be equal to the tire-inflation pressure. However, in reality, the relationship between the tire and pavement is complex and nonlinear. Inadequate characterization of traffic loads is expected to adversely impact pavement damage prediction, which in turn directly influences funding appropriation for new pavement construction, rehabilitation, and maintenance.

The mechanical behavior of the tire-pavement interaction is conventionally characterized by the applied tire load, inflation pressure, tire rolling condition, friction between the tire and pavement surfaces, and pavement roughness. The dependence of tire durability on operating temperatures has been heavily researched by tire designers; however, pavement engineers' perspective is often not considered. Hence, it is important to examine the effect of coupling the thermal exchange with mechanical loading between a rubber truck tire and AC pavements.

1.2 Problem Statement

Most tire-pavement studies have focused on either the tire or the pavement alone. To appropriately characterize the interaction between both load- and temperature-dependent bodies, it is vital to consider the thermomechanical coupling of the tire and pavement. Available models account for the tire temperature distribution using simplified pavement surfaces and are limited to passenger tires. Moreover, work on truck tire interaction with flexible pavement simulation is likewise limited.

Environmental effects on pavement layer characteristics have been considered by pavement engineers, while tire designers typically confine their considerations to the temperature influence on tire operating conditions. A thermomechanical interaction model between the tire and pavement is needed to bridge this gap. This will be accomplished through quantifying tire-pavement contact stresses and rolling resistance, in addition to identifying

the impact of various loading and temperature conditions. Available database of contact stresses based on contact load measurements and pavement structural models were used in this dissertation to illustrate and quantify the importance of the thermomechanical interaction. As the pavement is the other critical part of the interaction, a means to evaluate the impact and extent of the three-dimensional contact stresses on pavement bulk response has been established and discussed in detail in this dissertation.

1.3 Objectives and Methodology

The ultimate goal of this research was to quantify the effects of the thermomechanical interaction between the tire and pavement and impacts on contact stresses, rolling resistance, and pavement bulk response. The following steps were completed to address the research objective:

- Simulated a tire model with accurate geometry and material characterization on a rigid pavement surface.
- Developed a new method to directly link three-dimensional contact stresses to pavement bulk behavior.
- Coupled the tire model with a pavement layer while using appropriate boundary conditions. In this step, the simulation was limited to a representative pavement layer (instead of the full pavement structure) due to computational feasibility.
- Imposed a steady-state thermal exchange on the combined tire-pavement model. First, a static loading condition was applied as a preliminary evaluation of the thermal exchange between the two deformable bodies. Then, the tire was subjected to a free-rolling condition for a realistic simulation of its movement over the pavement layer.

To accomplish these tasks, an incremental progression was followed to simulate the thermomechanical interaction between a truck tire and the pavement layer. First, a finite element model of a truck tire was generated, which considered accurate material characterization and geometry of various tire components. This step simulated an inflated and loaded hyperelastic tire over an infinitely rigid surface and was calibrated using experimental measurements. Secondly, the validated tire model was combined with a pavement layer, which was rolled under the Lagrangian configuration. Given that the focus of this

dissertation was at the immediate contact area between the tire and pavement, and to reduce the required computational effort, the pavement structure was simplified by utilizing a pavement layer.

Next, under static loading, a steady state thermal exchange was imposed on the model to reflect the varying thermal conditions between the tire and pavement. This static analysis provided a preliminary indication of the level of heat exchange between the two deformable bodies. The final simulation step was to impose a free-rolling condition under varying speeds and quantify their impact on the contact stresses and rolling loss. A parametric study was conducted to assess the influence of various loading, speed, and temperature conditions on the tire-pavement interaction. Additionally, pavement structure simulations for roadway and airfield pavements were completed to assess pavement bulk response, induced by tire-pavement contact stresses.

1.4 Research Contributions

In recent decades, environmental requirements have become increasingly stringent. Moreover, truck freight is expected to change due to increased weight and the introduction of an autonomous fleet. This work introduces the impact of the thermomechanical behavior at the tire-pavement interface and effect on contact stresses and rolling resistance. This resulted in overcoming the limitation of using two uncoupled systems. In general, the contributions of this research include the following:

- Development of tire-pavement interaction models that quantified the difference between non-dissipative and dissipative truck tires on a rigid surface and deformable pavement layer, respectively;
- Introduction of the new Domain Analysis to evaluate bulk pavement behavior to capture the full extent and complexity of tire-pavement contact stresses of truck and aircraft tires; and
- Creation of a database and predictive equations of the thermomechanical contact stresses that consider a myriad of loading and rolling conditions coupled with uniform and non-uniform temperature profiles.

Critical loading and thermal conditions will provide pavement engineers insights on strategies for pavement design and maintenance techniques, whereas tire manufacturers can gain a deeper understanding of the influence of a pavement layer on tires' rolling loss.

This would potentially improve pavement and tire designs to reduce rolling resistance, which translates to fuel consumption reduction by means of economic savings and reduced greenhouse gas emissions. In addition, the Domain Analysis is a step forward in quantifying the effect of three-dimensional contact stresses on bulk pavement behavior.

1.5 Dissertation Organization

This dissertation is organized as follows. Chapter 2 presents the validated hyperelastic tire model rolled on a rigid surface to generate contact stresses, considering the tire's mechanical behavior. Chapter 3 introduces the Domain Analysis; the pavement simulations included experimentally and numerically generated free-rolling contact stresses. Chapter 4 details simulations of an aircraft landing gear tire considering a turning maneuver and implementation of the Domain Analysis. Chapter 5 discusses the development of the thermomechanical interaction model between a hyper-viscoelastic tire and a deformable pavement layer, including the implication of the resulting uniform and non-uniform temperature profiles on contact stresses. In Chapter 6, distribution characteristics of heat flux and rolling energy loss are evaluated, including their effect on the tire-pavement contact stresses, were evaluated. Finally, Chapter 7 presents the dissertation findings, conclusions, and recommendations for future research directions.

CHAPTER 2

HYPERELASTIC TIRE MODEL ROLLING ON A RIGID SURFACE

2.1 Introduction

Tire-pavement contact stresses are not only three-dimensional (3D) in nature but are also highly non-uniform. A combination of the tire structure and material; loading, environmental, and rolling conditions; and pavement surface properties governs the stress distribution, and inherently the resulting pavement behavior. Two approaches enable quantifying contact stresses: experimental measurements and numerical modeling.

In the 1990s, Pottinger [4, 5] developed and patented a complex equipment to measure 3D stresses and relative slip. This included a transverse array of 16 sensing elements: each pin or sensing element was designed to measure tri-axial forces. De Beer [6, 7] created the Vehicle-Road Surface Pressure Transducer Array (VRSPTA) that consisted of 1,041 pins with coplanar top ends. The VRSPTA device converts strain gauge voltages of each measuring pin to contact loads, as the tire traverses over the measuring pad. The process to convert the loads into contact stresses requires the assumption of the geometrical area factor, which may not be representative of the actual influence area of each pin in contact with the tire tread. Koehne et al. [8, 9] built a rig that could measure the contact stresses in all directions simultaneously.

The accuracy of the contact stress distribution relies on the robust nature and resolution of the sensing elements, which cannot emulate the surface properties of the pavement in contact with the tire. On the other hand, sensitive sheets may be used in lieu of sensing elements, but can only provide contact stress measurements along the vertical direction and under static loading conditions. Additionally, existing measurement devices tend to have restrictions with respect to the test or traveling speed, rolling condition, and tire type. Hence, creating a numerical air-inflated tire model is an alternative approach to quantify 3D contact stresses, while accounting for the complex geometry and materials within tires along with appropriate characterization of the pavement surface.

In this dissertation, a dual tire assembly (DTA) is modeled to simulate a realistic fi-

nite element (FE) representation of the tire and pavement in contact, while accounting for a myriad of loading and rolling conditions. A detailed description of the model is presented, along with the validation and calibration phases and analysis of the resulting contact stresses.

2.2 Research Objective

There is a need to develop a robust FE model of a rolling truck tire to predict and generate a database of tire-pavement contact stresses. In this dissertation, several model parameters including the truck tire geometry and material characterization, tire-inflation pressure, applied tire load, traveling speed, rolling scenario, and sliding-velocity-dependent friction property were considered—with an overarching goal to capture the complex nature of the tire-pavement interaction. To ensure the fidelity of the tire model, validation and calibration phases were completed using experimental measurements [10, 11].

2.3 Tire Modeling

2.3.1 Geometry

The dual tire assembly, DTA 275/80R22.5, was considered in this dissertation. Based on the tire's nomenclature, the radius was calculated to be 505.7 mm, while the outside perimeter of the tire was estimated to be 686.3 mm (heel to heel, excluding the distance within the grooves). The inside perimeter, from toe to toe (also excluding the distance within the grooves) was 632.2 mm. The tire consisted of three belts, each with a specific reinforcement orientation and width, as presented in Table 2.1. The belt closest to the tire's interior was labeled Belt 1, while the one closest to the tread was named Belt 3. In addition, the number of reinforcement cords within 10 mm was used to infer the reinforcement spacing. Moreover, all belts were contained within the belt package with a thickness of 6.4 mm. Figure 2.1 details the half of the tire cross-section that served as the basis for the AutoCAD drawing of the DTA.

The thickness of the inner liner, which is the inner-most component of the tire, was 2.1 mm. Additionally, the thickness between the inner liner and the belt package (or body ply thickness) was 3.0 mm, while the thickness of the tread in the middle of the tire was 26.1 mm. Summing up the thicknesses of the inner liner, body ply, belt package, and tread

Table 2.1. Reinforcement Orientation and Spacing

Reinforcement	Width (mm)	Orientation (^{o})	Spacing (cords/10 mm)	Area (mm^2)
Belt 1	201.9	113.0	37	1.370
Belt 2	180.1	73.0	41	1.370
Belt 3	137.2	73.0	33	1.704
Ply		1.0	31	1.167

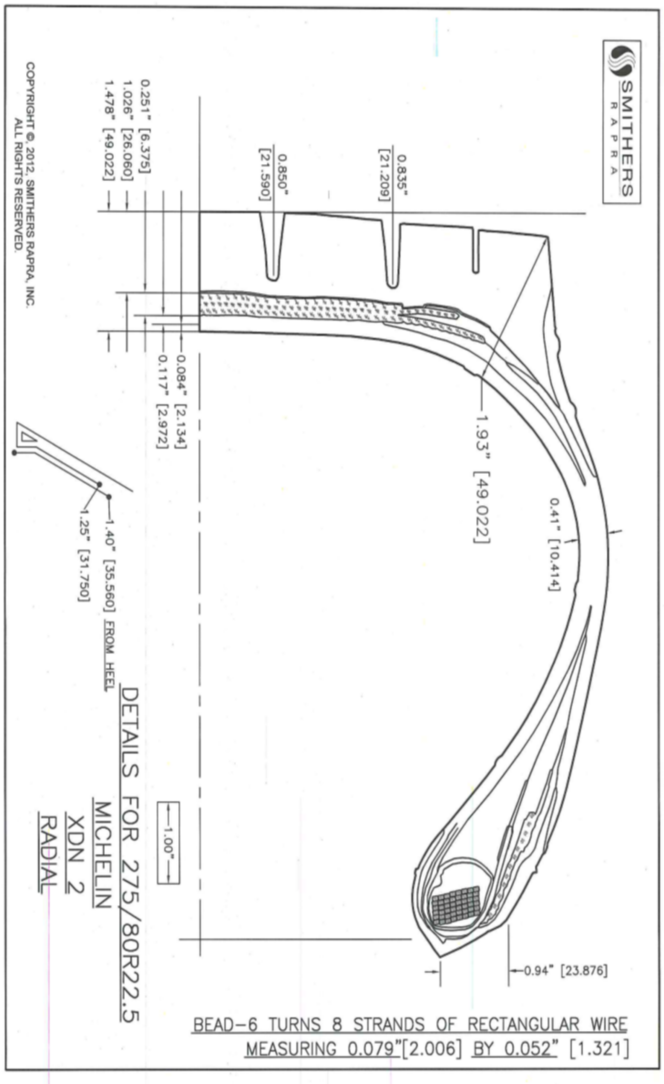

Fig. 2.1. DTA cross-section detailing the geometric measurements.

resulted to a total crown thickness of 37.5 mm. The total shoulder thickness, defined by the distance from the corner of the outer tread to the inner surface of the tire, measured

perpendicularly, was 37.9 mm. In addition, the sidewall was 10.31-mm-thick. The tire bead consisted of a rectangular array of wires (8 by 6), each 2.0 mm wide and 1.3 mm long.

2.3.2 Material Characterization

Two material constitutive models were assumed: linear elasticity for steel reinforcement (ply and belts) and hyperelasticity for rubber. Figure 2.2 illustrates the laboratory measurements that characterized the steel reinforcement embedded within the rubber sections. A summary of the elastic modulus and Poisson's ratio, used for the steel reinforcement, is detailed in Table 2.2. On the other hand, as rubber generally experiences large deformations, characterizing with hyperelasticity is more appropriate than linear elasticity. The tire cross-section was partitioned into different regions to capture the distribution of rubber material characterization, as illustrated in Figure 2.3.

Table 2.2. Reinforcement Details

Reinforcement	Elastic Modulus (MPa)	Poisson's ratio (ν)
Belt 1	82.5	0.30
Belt 2	100.3	0.30
Belt 3	40.4	0.30
Ply	123.8	0.30

Adopting the Mooney-Rivlin behavior for rubber, the variation of strain energy with the principal invariants of the Cauchy-Green deformation tensor is given by Equation 2.1.

$$W = C_{10}(I_1 - 3) + C_{01}(I_2 - 3) \tag{2.1}$$

where W is the strain energy density, I_1 and I_2 are the first and second principal invariants of the right Cauchy-Green deformation tensor, respectively, and C_{01} and C_{10} are the empirically-determined constants. The material constants C_{01} and C_{10} were provided by the tire manufacturer, as presented in Table 2.3.

2.3.3 Mesh Sensitivity Analysis

Mesh optimization defines the appropriate mesh refinement while maintaining a high level of accuracy. Total strain energy, which is minimized by the FE method, was used as

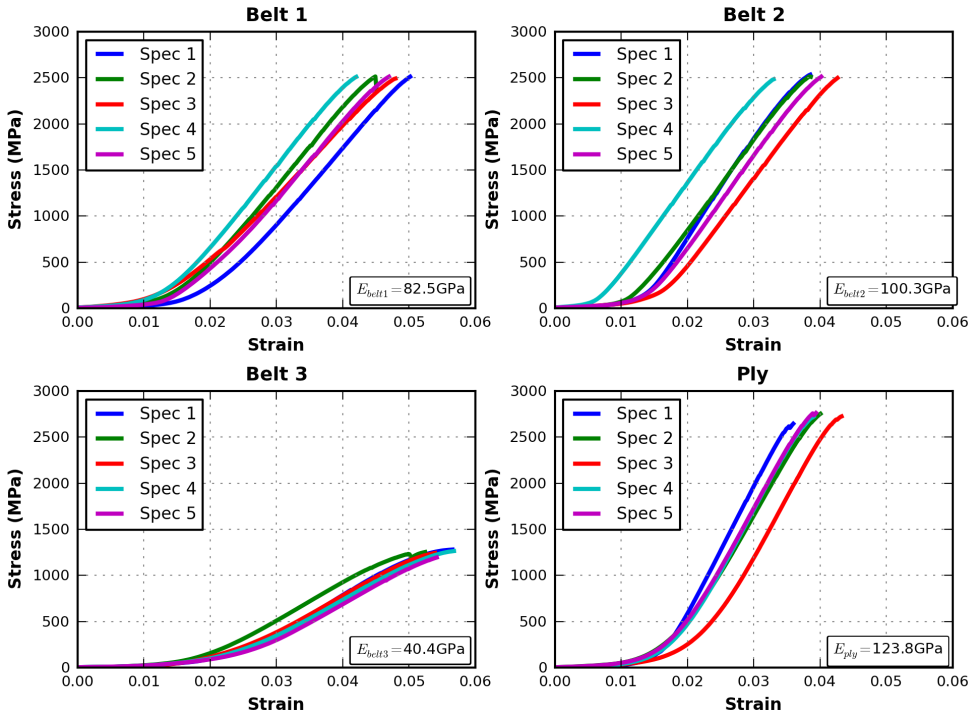

Fig. 2.2. Laboratory measurements of the reinforcement materials [12].

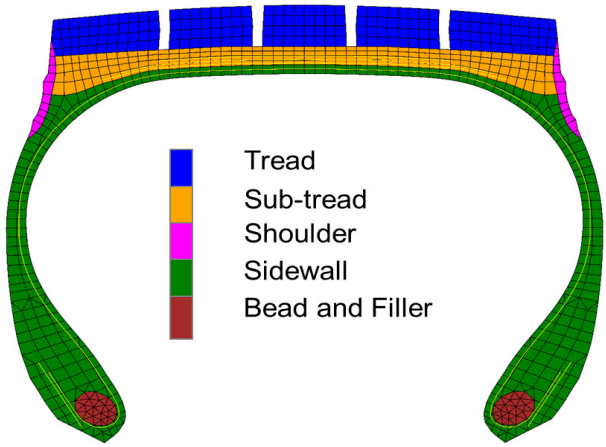

Fig. 2.3. Cross-sectional partition of materials within the tire model.

a criterion to determine the optimum mesh configuration. The reference value of the total strain energy was obtained from the finely-meshed tire model (bottom right of Figure 2.4).

Four sample trials of the mesh sensitivity analysis of the axisymmetric model are presented in Figure 2.5, comparing the total strain energy and number of elements. It should be noted that additional configurations were studied, and factors, such as excessive distortion, geometric constraints, and element types were analyzed. Moreover, the symmetry of

Table 2.3. Mooney-Rivlin Constants for Rubber Components

Component	C_{10} (MPa)	C_{01} (MPa)
Tread	0.9753	0.0
Shoulder	0.9753	0.0
Sidewall	0.5479	0.0
Bead Filler	0.6034	0.0

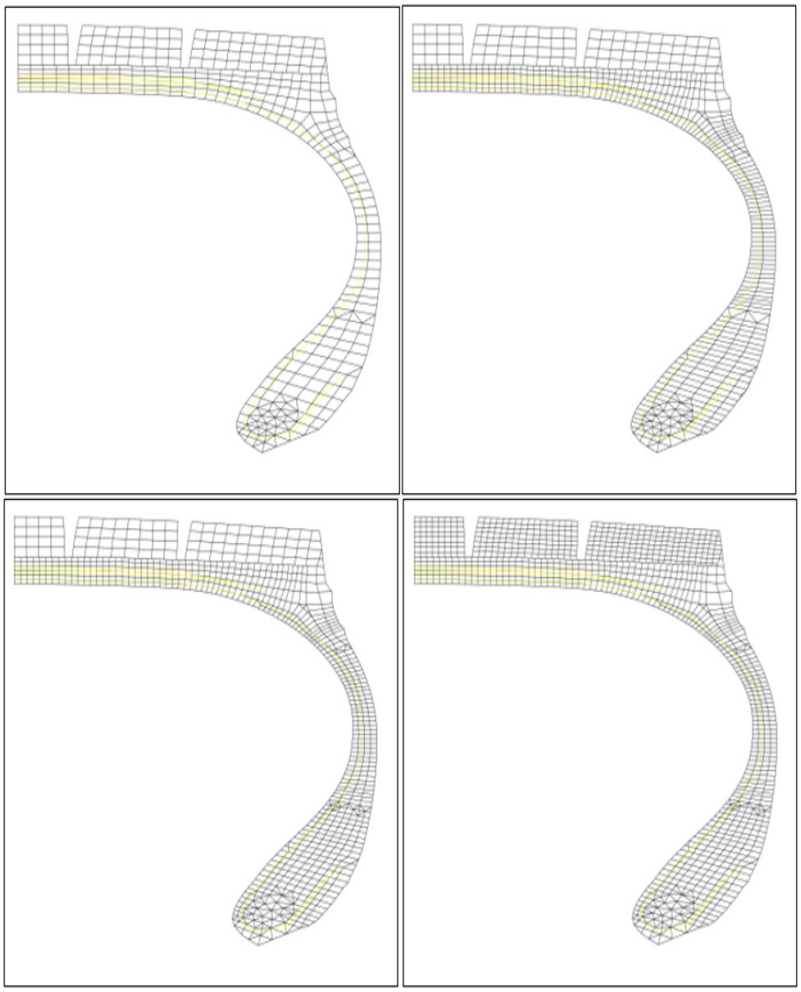

Fig. 2.4. Mesh configuration considered in the half-axisymmetric model.

the axisymmetric model to narrow the mesh sensitivity analysis on only half of the tire cross-section.

From Figure 2.5, it can be concluded that Mesh 1 provided the least accurate results, as the corresponding strain energy was farthest from the finest mesh (Mesh 4). On one hand, the number of elements in Mesh 3 was closest to the finest mesh, wherein the main

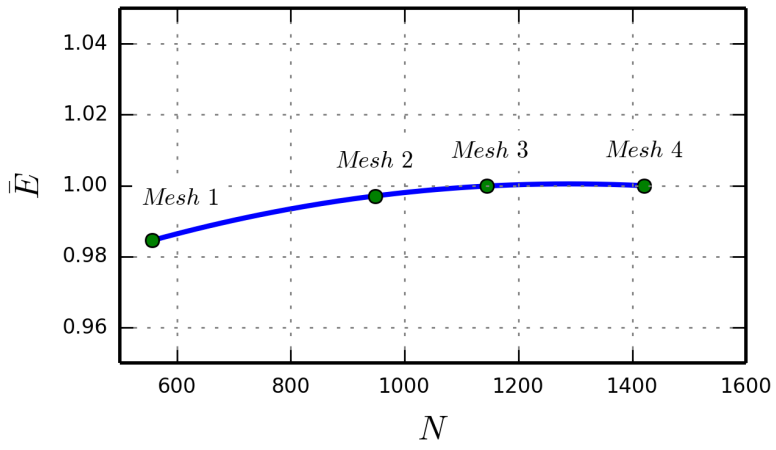

Fig. 2.5. Variation of total strain energy, E, with number of elements, N.

geometric difference lies on the tread mesh configuration. On the other hand, Mesh 2 provided the ratio between its total strain energy and that of the finest mesh to be greater than 0.98 with the number of elements (relative to the finest mesh) significantly reduced. Hence, Mesh 2 was selected to be the optimum configuration of the half-axisymmetric model.

The same approach was carried out to determine the element size and distribution along the circumferential direction of the 3D tire model. Two regions were defined: i) the "Foot" governs the zone of potential contact area with the rigid surface spanning 60 elements, and ii) the remaining tire model region with cylindrical elements. The iterative process initiated by assuming the number of elements in the Foot to a constant value of 60, while the size of the cylindrical elements was changed from 10, 20, 40, 60, 70, to 80 elements along with varying bias factors. After defining the appropriate distribution of cylindrical elements, one could observe that the number of elements within the Foot region varied from 20, 30, 60, 120, to 240 elements. Note that a finer discretization was implemented within the potential region of contact to capture the complexities of the 3D contact stress distribution.

Figure 2.6 presents the variation of the normalized total strain energy as the number of elements was altered. One could observe that the number of elements within the two regions minimally influenced the strain energy values. The final mesh configuration included 60 elements within the Foot region, and 20 cylindrical elements along the rest of the tire circumference (i.e., 10 elements at each side of the Foot).

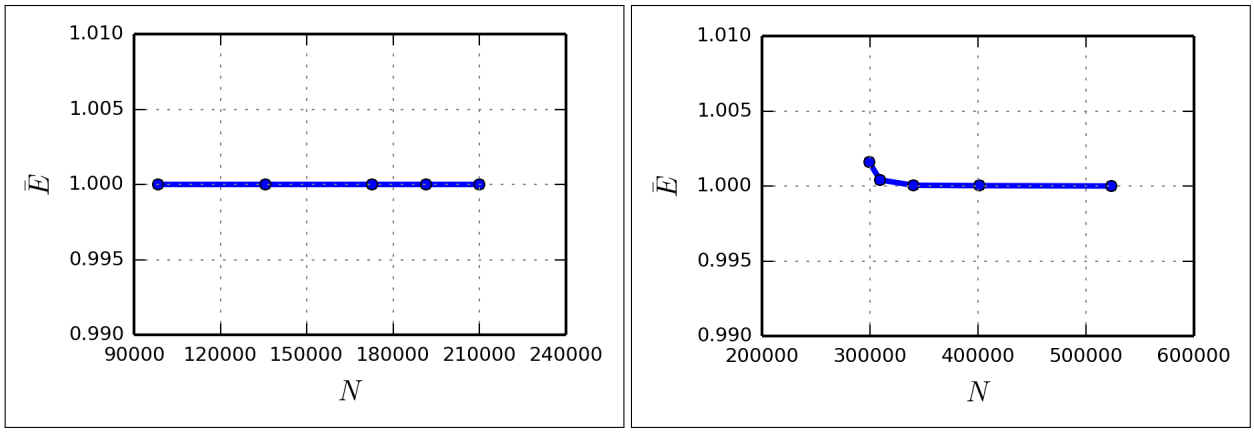

(a) Foot region.

(b) Remaining region with cylindrical elements.

Fig. 2.6. Variation of normalized total strain energy with varying number of elements along the Foot and region with cylindrical elements, respectively.

2.3.4 Element Type

The complex nature of the tire structure required special finite elements, including cylindrical, hybrid, and rebar elements. Cylindrical elements are utilized in the majority of the tire model as they provide an exact representation of the curved geometry in lieu of meshing finely with quadrilateral elements. However, cylindrical elements are numerically more costly than quadrilateral elements. A bias on the element sizing was applied to reduce the number of cylindrical elements and to offset the computational cost, while ideally representing the tire geometry. For simplicity, the tread and groove were assumed to be uniform along the tire circumference.

On one hand, accounting for the incompressible nature of rubber required the use of hybrid elements; the hybrid formulation incorporated pressure as an independent unknown variable in the constitutive equation. On the other hand, rebar elements were used to represent the steel reinforcement. This enabled the analysis to consider rubber and reinforcement independently without the need to discretize the two materials and assume a contact property. The rebar elements provide a means to embed reinforcement within solid elements within the hybrid elements.

2.3.5 Surface Friction

Pavement surface friction is a relevant factor for the tire-pavement interaction, which depends on many factors, such as viscoelastic properties of rubber, pavement texture,

temperature, vehicle speed, slip ratio, and normal stress. A velocity-dependent friction model was adopted [13]. Figure 2.7 represents the variation of friction coefficient with respect to speed for three macro-texture conditions: good, poor, and intermediate. As a baseline, an intermediate surface texture was assumed between the hyperelastic tire model and rolling surface (assumed as a rigid body). The decay friction model is defined in Equation 2.2, wherein the friction coefficient reduces with increasing speed.

$$\mu = \mu_k + (\mu_s - \mu_k)e^{-d_c v} \tag{2.2}$$

where μ is the friction coefficient, μ_k is the kinetic friction coefficient, μ_s is the static friction coefficient, d_c is a user-defined decay coefficient, and v is the slip speed [14]. It is noteworthy that future work on the friction property is warranted by considering pressure dependency and implementing friction as an inherent part of the interaction rather than as input parameter.

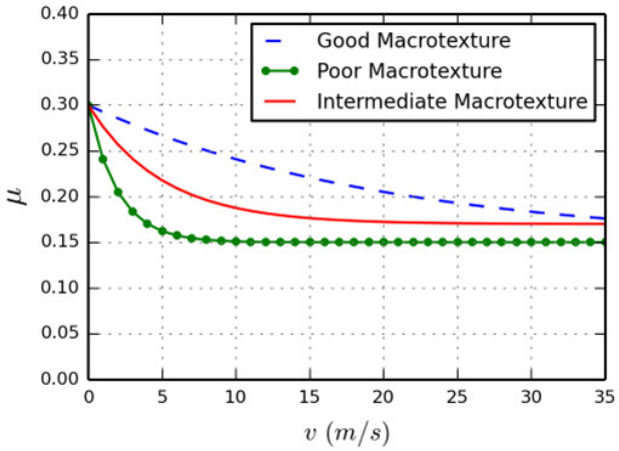

Fig. 2.7. Sliding-velocity-dependent friction model to characterize the tire-pavement contact.

2.3.6 Modeling Approach

Steady-state-transport analysis procedure of ABAQUS was used simulate a rolling tire. This approach is based on the Arbitrary Lagrangian-Eulerian (ALE) formulation, where all derivatives are obtained with respect to space variables, allowing mesh refinement in selected regions of the model. ALE establishes three domains: i) the material domain, which moves with the material; ii) the spatial domain, which represents the current configuration; and iii) the reference domain, which describes the mesh motion. The ALE formulation

significantly reduces the computational cost relative to a rolling tire under Lagrangian formulation and focuses the computational effort at the potential region of tire-pavement contact.

The rolling tire model was prepared in three stages. First, an axisymmetric model was generated based on the tire's cross-section (Figure 2.8a). It is worth noting that the cross-sectional geometry referenced an accurate schematic of the DTA, measured by an external laboratory (Figure 2.1). Tire inflation pressure was applied on the inner surface of the axisymmetric tire model, along with the boundary conditions at the tire-rim contact. Second, the axisymmetric model was revolved using the Symmetric Model Generation module in Abaqus along the circumferential direction to create the full 3D model, as illustrated in Figure 2.8b. Note that the revolution of the axisymmetric model to form the 3D model not only transferred the geometry along the tire circumference but also maintained the material input.

Results of the axisymmetric model was brought into equilibrium within the first step of the 3D model, after transferring the results from the previous simulation. In this step, an inflation pressure was activated inside the 3D tire model. Next, an initial contact between the tire and the rolling surface was established and the tire load was applied. The final stage utilized the Steady State Transport function of Abaqus, wherein the ALE formulation was implemented, as the 3D tire model assumed free-rolling, braking, accelerating, and cornering conditions. It is worth noting that only one tire was modeled due to symmetry of the dual assembly (conventionally used in pairs for the truck trailers). A summary of the modeling assumptions and limitations is tabulated in Appendix A.

2.4 Validation and Calibration of Free-Rolling Condition

Based on experimental measurements [10, 11], the DTA was subjected to various inflation pressures and applied loads–all under free-rolling conditions. Prior to generating the database of contact stresses, it was necessary to validate and calibrate the numerical tire model. The calibration of the FE model was accomplished by comparing the contact area (A_c), tire deflection (δ), and maximum vertical contact stress (σ_{max}). Specifically, the case with an applied load of 44.4 kN and tire inflation pressure of 690 kPa was used to guide the model calibration. After reaching the desired level of accuracy between the predicted and calibrated results, the material properties were fixed, and the full numerical matrix was deployed to simulate various combinations of applied load and tire inflation pressure to validate the model. There were a total of nine free-rolling cases as the applied load was

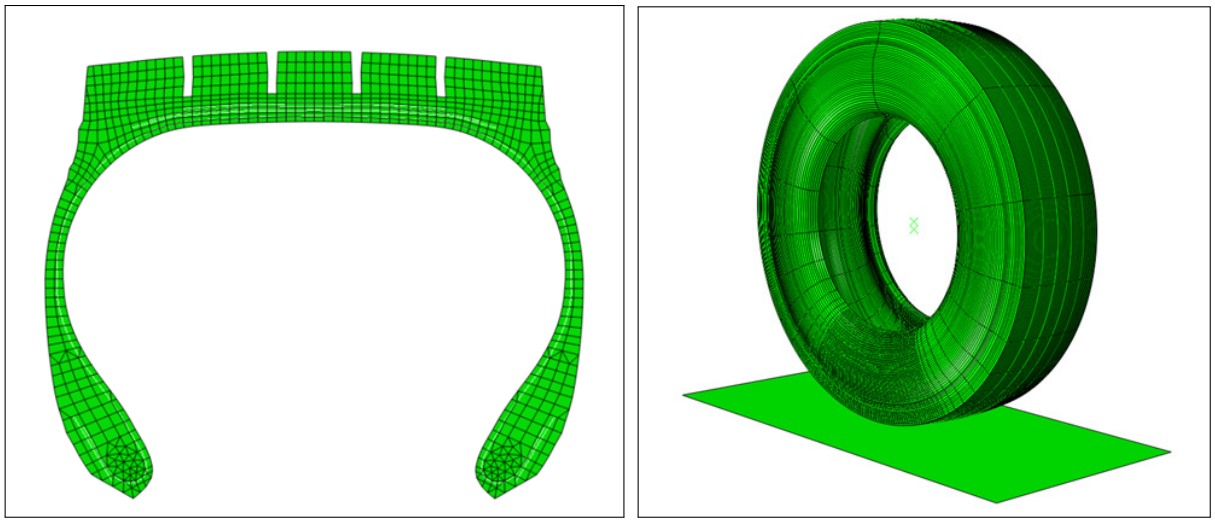

(a) Axisymmetric model. **(b)** 3D model.

Fig. 2.8. Analysis stages of the tire model.

varied to 26.7, 35.6, and 44.4 kN while the tire inflation pressure changed to 552, 690, and 758 kPa.

To quantify the difference between the FE model results and experimental measurements using a single scalar, the mean absolute percentage error ($MAPE$) was adopted. $MAPE$ is calculated by:

$$MAPE = \frac{100}{n} \sum_{i=1}^{n} \left| \frac{Meas_i - Calc_i}{Meas_i} \right| \tag{2.3}$$

where n is the number of measurements, $Meas_i$ is the measurement i, corresponding to a combination of applied load and inflation pressure, and $Calc_i$ is the calculated value i, corresponding to the same combination of applied load and inflation pressure as in $Meas_i$.

As shown in Figures 2.9a and 2.9b, a very good agreement between the measured and calculated contact area and deflection was obtained ($MAPE = 5.3$ and 3.9%, respectively). In contrast, Figure 2.9c illustrates that a higher $MAPE$ of 24.4% was obtained for the maximum vertical contact stresses along the width of the tire and held at the middle of the contact length. This error could be attributed to the assumed full contact between the measuring pin and tread rubber (i.e., the geometrical area factor that transforms contact loads to stresses). During the experimental measurements, the pin was not always in contact with the rubber due to the presence of circumferential and lateral grooves. It is worth noting that there might be inherent effects from the measuring pins. As part of the validation process, contact stress outputs were modified to align with pin locations to

improve the comparison.

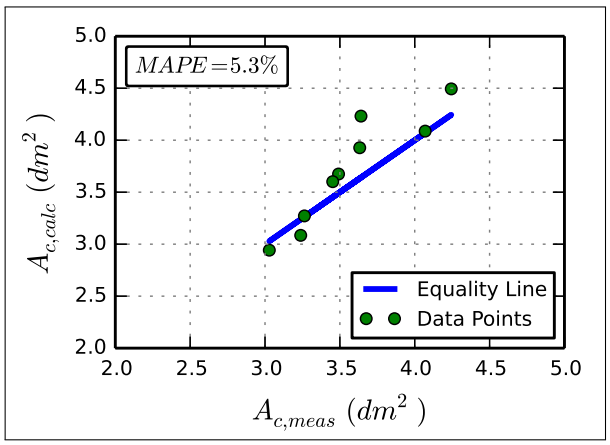

(a) Contact area.

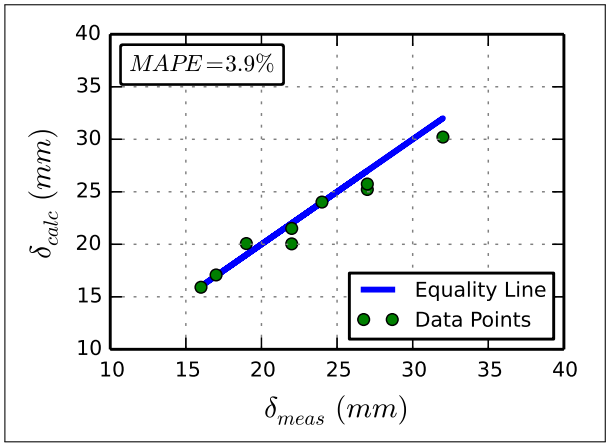

(b) Deflection.

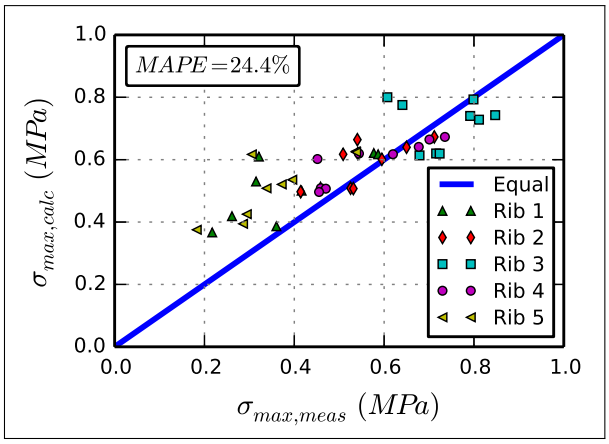

(c) Maximum vertical contact stress.

Fig. 2.9. Measured versus calculated contact area, deflection, and maximum vertical contact stress.

2.5 Three-Dimensional Contact Stresses

A full factorial of the DTA simulations on an infinitely rigid surface was completed, by which the main factors of the parametric study included the applied load P, tire inflation pressure S, rolling speed V, slip ratio $s_{b/t}$, and slip angle θ. The slip ratio and angle accounted for the three steady-state-rolling scenarios, which implemented accelerating, braking, and cornering; resulting in a total of 324 cases by combining the following parameters.

- Half-axle load (kN): $P1 = 26.7$, $P2 = 35.6$, $P3 = 44.4$;

- Tire-inflation pressure (kPa): $S1 = 552$, $S2 = 690$, $S3 = 758$;
- Velocity (km/h): $V1 = 8.0$, $V2 = 65.0$, $V3 = 115.0$;
- Traction slip ratio (%): $T1 = 1.5$, $T2 = 3.0$, $T3 = 4.5$, $T4 = 7.0$;
- Braking slip ratio (%): $B1 = 1.5$, $B2 = 3.0$, $B3 = 4.5$, $B4 = 7.0$; and
- Cornering slip angle (°): $FR = 0$, $FR2 = 2$, $FR4 = 4$, $FR6 = 6$.

The presented nomenclature for each variable is referenced for the succeeding plots. For example, the case $S1P2V3\_FR2$ indicates the combination of 552 kPa ($S1$), 35.6 kN ($P2$), 31.9 m/s ($V3$), and 2° slip angle ($FR2$). It is worth noting that FR denotes the free-rolling condition (i.e. zero resultant torque). A brief overview of the rolling conditions are provided in the following section.

For acceleration, a driving torque is applied about the axis of rotation of the tire, producing a tractive force; whereas a braking torque generates a force to decelerate the tire. In addition, another indicator that differentiates acceleration from deceleration are the directions of the torque and the angular velocity. Given that the torque and angular velocity are moving clockwise (toward the direction of the translational speed), this scenario is characterized as accelerating. On the other hand, when the applied torque is moving counterclockwise and the angular speed tends to the opposite direction, the tire is experiencing a braking condition.

As tractive force at the tire-pavement contact area develops during acceleration, not only does the tire tread at the front of the tire experience compression but it also develops a corresponding shear deformation of the sidewall [15]. The compression of the tread elements before entering the contact area reduces the distance that the tire traverses in comparison to a free-rolling condition. This is a phenomenon often referred to as "longitudinal slip." According to the Society of Automotive Engineers (SAE), longitudinal slip is the ratio between the longitudinal slip velocity and the spin velocity of the straight free-rolling tire, expressed as a percentage. Therefore, the slip ratio at traction, s_t, is defined as follows:

$$s_t = \frac{r\omega}{V - 1} \times 100 = \frac{r}{r_e - 1} \times 100 \tag{2.4}$$

where r is the rolling radius of the free-rolling tire, ω is the angular speed, V is the linear speed, and r_e is the effective rolling tire radius, which is the ratio between the linear and angular speeds of the tire.

In contrast to acceleration, when a braking torque is applied, tread elements are stretched prior to entering the contact area, which indicates that the distance that the tire will

traverse is greater than that of the free-rolling scenario. The slip ratio for the braking condition, s_b, is defined as:

$$s_b = \frac{1 - r\omega}{V} \times 100 = \frac{1 - r}{r_e} \times 100 \tag{2.5}$$

The third rolling condition is cornering. This scenario occurs when a tire is subjected to a force perpendicular to the travel direction. A lateral or "cornering" force is then developed as the tire travels along a path at a given angle with the wheel plane, also called as the "slip angle." Generally, the slip angle impacts the tire's directional control and stability [15]. In order to impose a slip angle, θ, the linear speed is used to generate velocities in the longitudinal and transverse directions, using the following equations.

$$v_x = V cos\theta \tag{2.6}$$

$$v_y = V sin\theta \tag{2.7}$$

where v_x and v_y are the longitudinal and transverse velocities, respectively.

2.5.1 Free-Rolling Condition

After the initial start of rotating the tire, there is a corresponding angular speed wherein the driving torque is zero, generating a "free-rolling" tire. In its physical nature, as the tread enters and traverses along the contact area, the distance from the center of the wheel varies from the unloaded radius to the loaded radius. This phenomenon generates a negative shear stress at the front part of the tire as its speed reduces upon entering (recall the local compression of the tread), and results in a positive shear stress at the trailing edge due to the tread stretch upon its exit [16].

Figure 2.10 shows the typical contact stresses generated by the hyperelastic tire model in the three orthogonal directions, wherein the loading conditions were held constant with the applied load–P =44.4 kN and tire inflation pressure, S=690 kPa–and the translational speeds were varied. The plots represent the contact stress distribution along the contact length (i.e., along the x direction) and at a specific meridian—the longitudinal line that runs along the circumference of the tire. Generally, altering the linear velocities from 8 to 115 km/h has minimal influence on the contact stresses under free-rolling condition.

On the other hand, varying the tire inflation pressure changed the maximum vertical contact stress value, $\sigma_{z,max}$, along the fifth meridian at the middle rib (Rib 3). Given a constant P=26.7 kN, $\sigma_{z,max}$ was estimated to 0.75 MPa when S=552 kPa; this indicated an

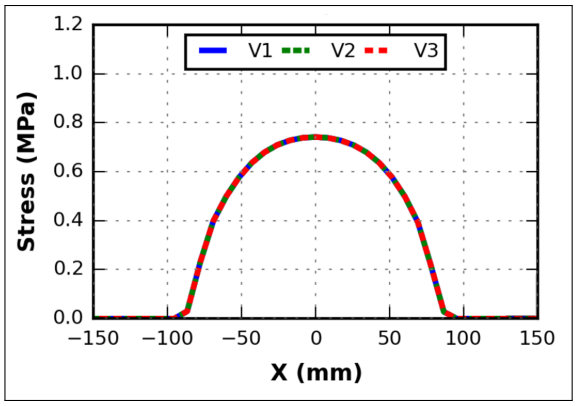

(a) Vertical stresses, σ_{yy}.

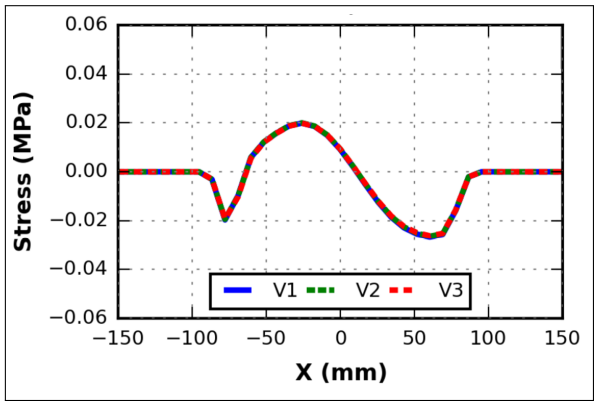

(b) Longitudinal stresses, σ_{xx}.

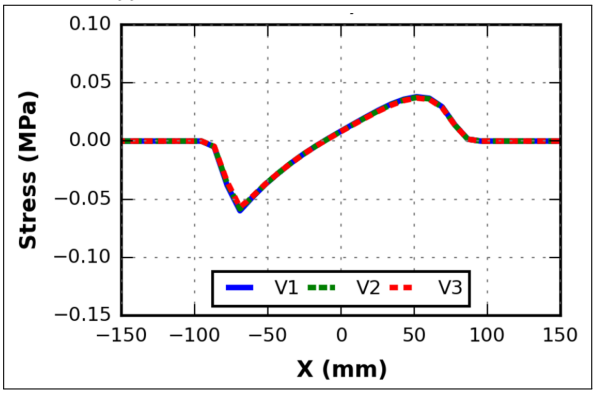

(c) Transverse stresses, σ_{zz}.

Fig. 2.10. Contact stresses under free-rolling conditions. Note that the y, x, and z directions are assumed to correspond to the vertical, longitudinal, and transverse directions

18% increase. As P was varied from 26.7 kN to 44.4 kN, holding S constant did not impact the peak value of the vertical stress, instead increasing the contact length (a complete set of figures is presented in Appendix B). Additionally, with the inherent increase of the applied load, the edges of the outer ribs began to carry a significant amount of load in contrast to other locations.

The longitudinal contact stresses along the fifth meridian of Rib 3, for all combinations of P and S, revealed three distinct peaks (recall Figure 2.10b). This behavior was characterized by the variation of the speed directions along the contact length, from the entrance to the exit of the tire treads. Moreover, as the applied load was increased, the magnitude of all the peaks increased, which was apparent when each tire inflation pressure was held constant.

Conversely, varying S from 552 to 758 kPa led to an evident decrease of the peak longitudinal contact stress values. Due to the dependence of longitudinal contact stresses on

relative tread deformations along the contact length, an increase in the tire inflation constricted the treads to displace, thereby reducing the peak values. For the same reason, an increase in the contact length provided greater freedom for treads to move, resulting in an increase of peak magnitudes.

Last, transverse contact stresses are typically generated due to the lateral displacement of the loaded tire treads. One can observe from the figures within Appendix B that the local maxima and minima slightly increased when the tire inflation pressure was increased. In addition, although the change in applied loads did not vary the peaks of the transverse contact stresses along the second meridian of Rib 3, a small extension of the transverse contact stress distribution was observed along the contact length.

2.5.2 Accelerating Condition

In order to assess the impact of an accelerating tire on contact stresses, the tractive slip ratio, s_t, was varied. The selected values provided a transition from the free-rolling condition with zero torque, to increasing driving torque and angular speeds, until full traction was reached. Figure 2.11 illustrates typical contact stress variations with respect to varying accelerating conditions, given that V=8.0 km/h, P=44.4 kN, and S=690 kPa.

As the tractive slip ratio was increased, the vertical contact stresses remained marginally affected by s_t as the curves were nearly coincidental along the contact length with a slight shift to the right (Figure 2.11a). The same behavior was observed when the velocity was altered from 8 to 115 km/h, wherein the vertical contact stress distributions did not vary (Appendix C).

On the other hand, shear stresses in both longitudinal and lateral directions were influenced, and more significantly along the traveling direction. As the traction level increased, the change in sign for the two peaks in the free-rolling condition (Figure 2.10b) diminished, resulting in higher negative longitudinal contact stresses along the fifth meridian of Rib 3 (Figure 2.11c). One can observe that as a 1.5% tractive slip ratio ($T1$) was imposed, the positive peak at the trailing end under free-rolling condition of the tire changed sign from positive to negative.

As the slip ratio was further increased, higher negative longitudinal contact stress was generated towards the rear end of the tire at a higher rate than the front. Once full traction was reached at 7%, the distribution assumes a convex shape and the initially-observed multiple peaks along the contact length diminishes. Similar trends were seen for the other cases with increasing velocity (Appendix B). However, we observed a slight increase in the

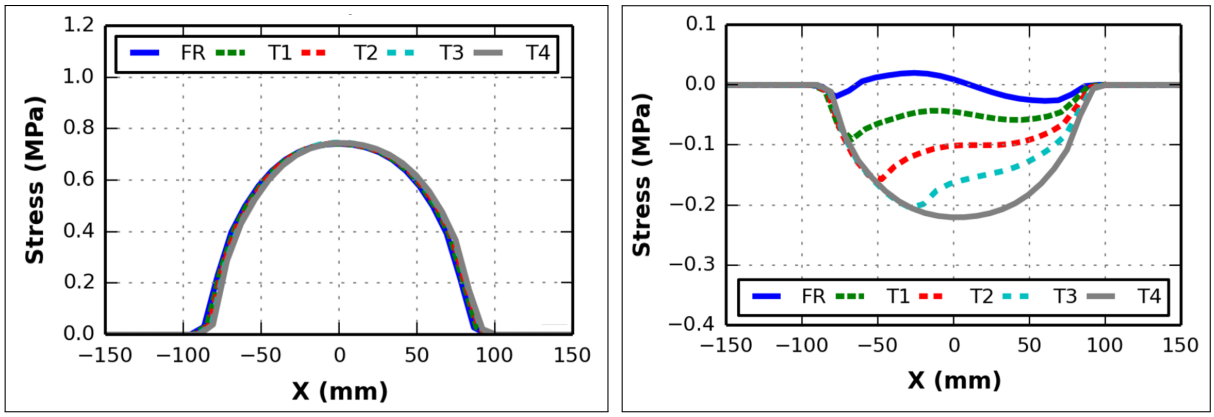

(a) Vertical stresses, σ_{yy}.

(b) Longitudinal stresses, σ_{xx}.

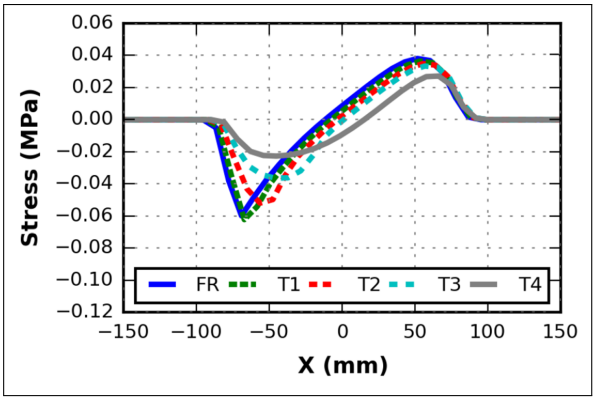

(c) Transverse stresses, σ_{zz}.

Fig. 2.11. Contact stresses under various accelerating conditions.

longitudinal contact stress at trailing end, past the values under full traction, as velocity increased up to 115 km/h.

Conversely, the transverse contact stresses along the second meridian of Rib 3 indicated a more subdued change when the traction level was increased. From a free-rolling condition, both peaks from the front and trailing parts showed reductions, wherein the rear end values tend to zero more evidently than the values towards the front part of the tire (Figure 2.11c). This phenomenon could be explained by the reduction of the restricted movement of tread elements against the infinitely rigid surface as the tractive slip ratio was increased. Furthermore, as velocity was increased, a slight reduction of the peaks was also generated (Appendix B).

Moreover, the summation of forces per meridian in each rib is presented in Figure 2.12 to ensure force equilibrium and to identify the tendency of the contact force distribution. The following plot consists of three rows and three columns that pertain to the three orthogonal forces and three applied loads (26.7, 35.6, and 44.4 kN), respectively. Note that S=552

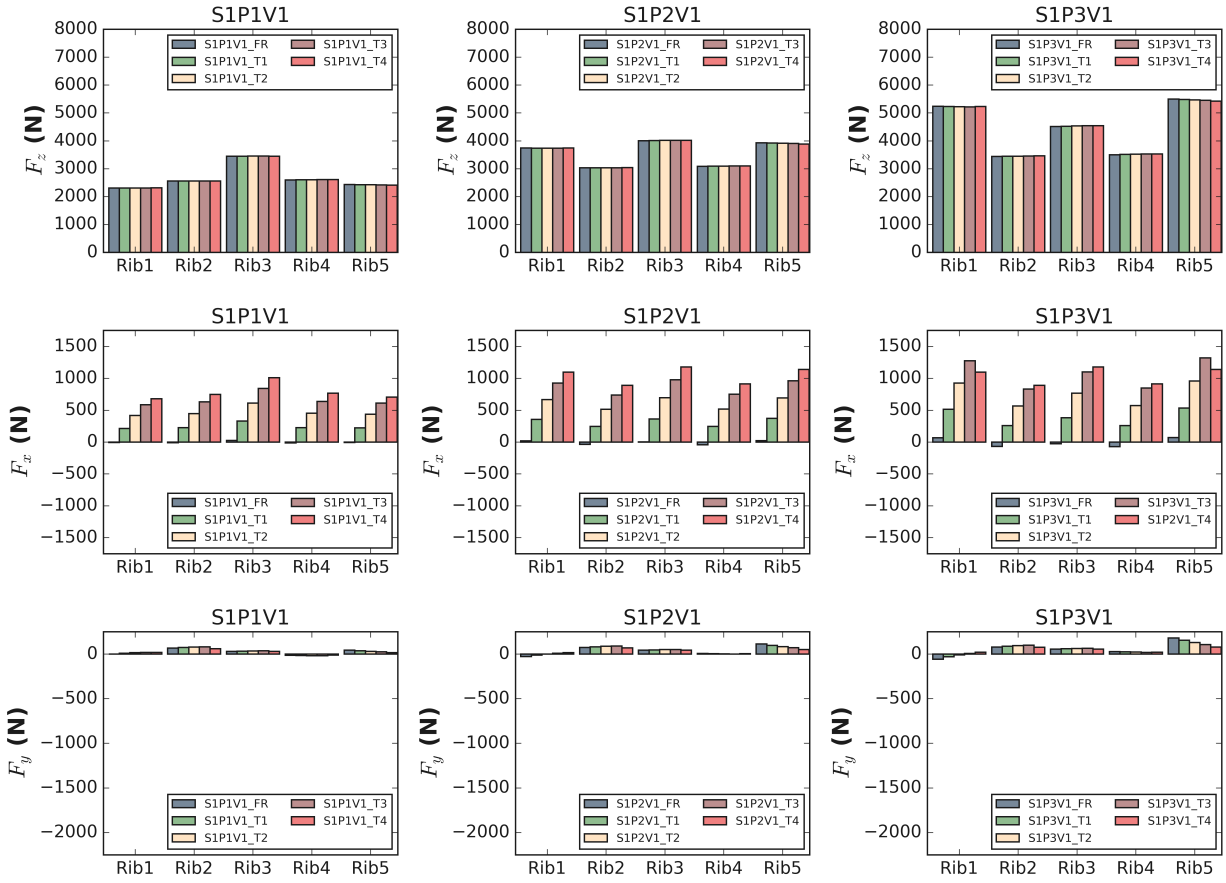

Fig. 2.12. Sum of forces for various accelerating conditions.

kPa and V=8 km/h were implemented for the presented cases.

Given the combination of the lowest S, P, and V values from the numerical matrix, Rib 3 carried most of the applied load. However, as the load increased to 44.4 kN ($P3$), the edge ribs were enforced to carry the majority of the load. Similar to the findings presented in Figure 2.11, the vertical contact force, F_z changed negligibly despite the increased traction or acceleration level.

Contrasting the two shear contact forces, the total longitudinal contact force F_x assumed a compressive state as the forces summed to positive values. Isolating to one of the ribs, a consistent trend of increasing the total longitudinal contact force as the tractive slip ratio increased could be observed. Additionally, the distribution of F_x along the ribs coincided with the F_z distribution. The total transverse contact force F_y, on the other hand, tended to zero—indicative of nearly symmetrical distribution of transverse contact forces along the rib width. The near-symmetry of the transverse contact load/stress is attributed to the lateral deformation of the tire treads. It is worth noting that the orientation of the belts prevents the transverse contact stresses to be symmetric (i.e. the sum of forces to be zero).

2.5.3 Braking Condition

A typical variation of the contact stresses along the representative meridian of Rib 3, under braking condition, is presented in Figure 2.13. These cases considered V=8 km/h, P=44.4 kN, and S=690 kPa. Comparing the contact stresses, as the gravity of braking increased from free-rolling (s_b=0%) to high slip ratio of 7%, it was evident that only the contact stresses along the longitudinal direction were significantly influenced. Figures 2.13a and 2.13c illustrate the vertical and transverse contact stress distributions, respectively, which minimally changed relative to the longitudinal contact stresses (Figure 2.13b).

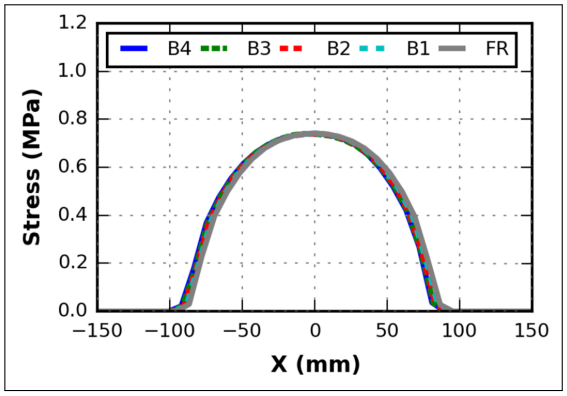

(a) Vertical stresses, σ_{yy}.

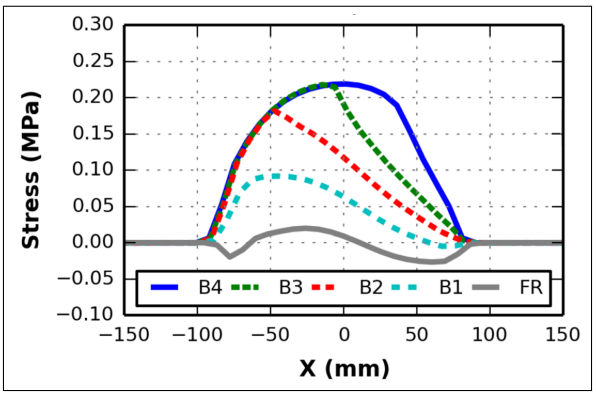

(b) Longitudinal stresses, σ_{xx}.

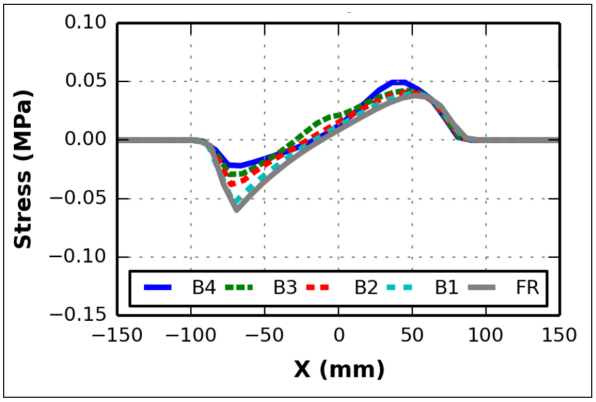

(c) Transverse stresses, σ_{zz}.

Fig. 2.13. Contact stresses under various braking conditions.

The negative peaks of the longitudinal contact stresses at the free-rolling condition diminished and shifted toward positive values. This change in behavior was more predominant at the trailing part of the tire, wherein one could observe that the positive peak of the free-rolling scenario was pulled closer to the distribution of the full traction case. This indicated that the rear end of the tire was first to reach the limit governed by the friction coefficient. As the braking level was further increased, the longitudinal stress variation

from the middle of the contact length on the rear end of tire became coincidental with the full traction values, imposing a further application of the friction limit on the corresponding tire-pavement contact area.

Similar to the accelerating scenarios, the speed variation from 8 to 115 km/h did not significantly alter the vertical and transverse contact stresses. However, for the longitudinal contact stresses, as the translational velocity increased, the magnitudes across the contact length decreased (Appendix D). This might be attributed to the friction coefficient model assumed, wherein the friction coefficient decreased as the sliding speed increased. This relationship significantly influenced longitudinal contact stresses, and thereby explained the corresponding reduction. Lastly, transverse contact stresses indicated a slight reduction with an increase in speed.

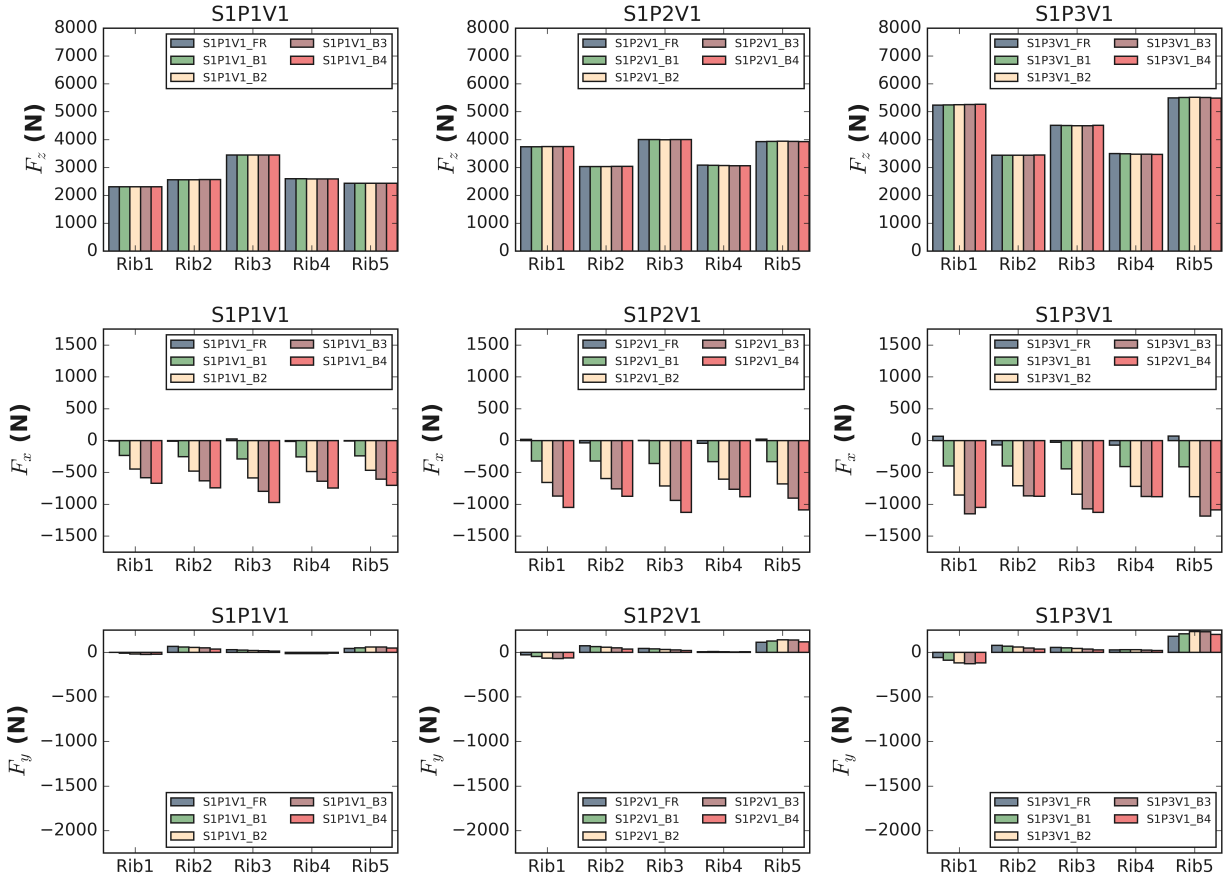

Fig. 2.14. Sum of forces for various braking conditions.

Figure 2.14 illustrates the summation of forces along the z, x, and y directions (following the rows from top to bottom, respectively). The trend of the vertical and transverse contact forces aligned with the accelerating scenario; however, the total contact force in the longitudinal direction resulted in negative values. The observed behavior, nearly equal

and opposite to the traction scenario, is attributed to the same intervals of slip ratios that were applied in the opposing direction.

2.5.4 Cornering Condition

For a cornering condition, the friction at the tire-pavement interface prevented lateral tread movement, thereby producing lateral deformation. By imposing a slip angle, a lateral force induced a movement away from the rolling direction. The lateral force also invoked a shift and concentration of contact stresses towards one side of the contact area, which generally coincided with the inner side of the maneuver. One could then imagine that the symmetry of vertical contact stresses (observed in free-rolling, accelerating, and braking conditions) along the contact width would become asymmetric. In addition, the cornering motion was anticipated to generate in-plane shear stresses that were predominantly in the transverse direction.

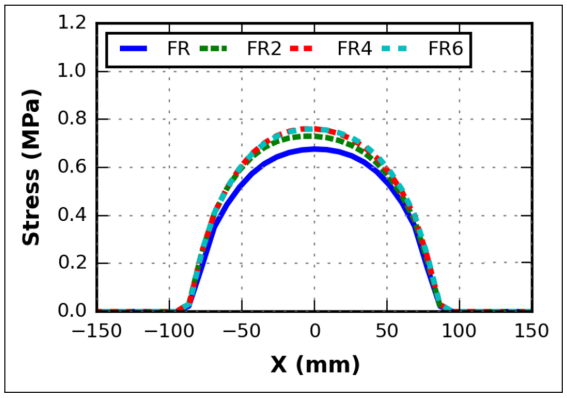

(a) Vertical stresses, σ_{yy}.

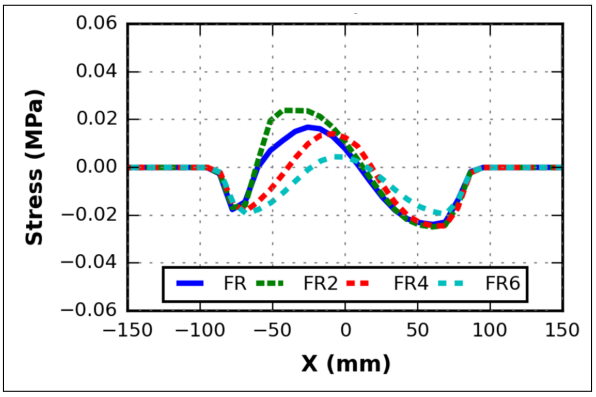

(b) Longitudinal stresses, σ_{xx}.

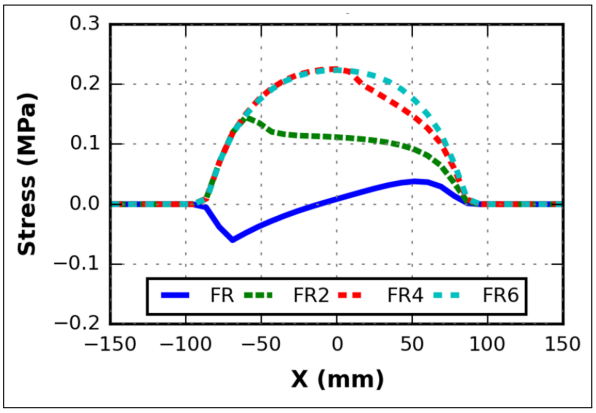

(c) Transverse stresses, σ_{zz}.

Fig. 2.15. Contact stresses under various cornering conditions.

Figure 2.15 illustrates the typical variations of the contact stresses in the three orthogonal directions along the second meridian of Rib 3 considering V=8 km/h, P=44.4 kN, and S=690 kPa. This inner meridian was deemed to be representative as high stress concentrations were anticipated closer to the point of the turning maneuver.

For the vertical contact stresses, their corresponding magnitudes along the contact length increased as the slip angle increased from 2° to 6°, although the difference between 4° and 6° seemed to be minimal. The resulting longitudinal contact stresses indicated some slight variations relative to the free-rolling condition, but the values were arguably small—wherein the scale of the stress values was lower than the vertical contact stresses by one magnitude (Appendix E). This indicated that the impact of longitudinal contact stresses on pavement responses was significantly lower than the stresses in the other two orthogonal directions. In addition, one could observe the load transfer towards Rib 1 (inner rib) based Figure 2.16. This behavior was exacerbated as the applied load was increased from 26.7 to 44.4 kN, as there was a steep increase closer to the inner tire edge (i.e. along the inner part of the cornering maneuver).

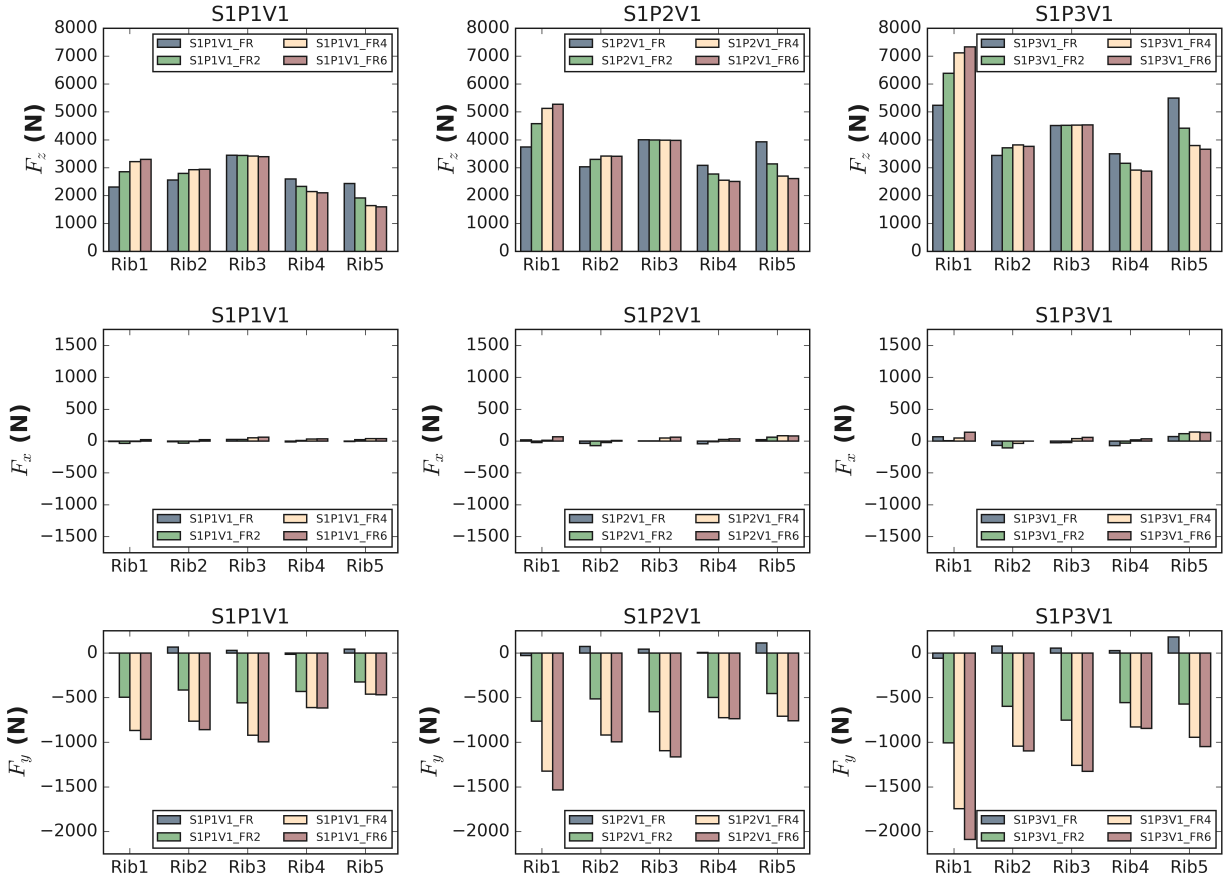

Fig. 2.16. Sum of forces for various cornering conditions.

As anticipated, the transverse contact stresses were greatly impacted by the cornering condition. The negative peak at the rear end of the tire quickly switched signs to positive when the slip angle was changed from the zero slip angle condition to 2°. In addition, closer to the trailing end, this part of the contact patch reached the limit imposed by the friction coefficient as the points of the curves were coincidental on this region. An increment increase of 2° further pushed the transverse contact stress distribution to reach the interfacial friction limit. It was also observed that the resulting contact stress values from the cases considering 4° and are 6° are nearly coincidental.

2.6 Summary

As pavement design and analysis rely on critical pavement response to indicate the potential of damage, establishing a robust control of the load input helps to accurately determine the induced stresses and strains of a loaded-pavement model. Tire-pavement contact stresses are governed by the loading condition, pavement surface property, rolling scenario, tire characteristics, and traveling speed. A validated hyperelastic FE tire model simulated a rolling DTA was developed. The two most prominent parameters that define the contact stress distribution are the tire-inflation pressure and applied load, which affected the stress magnitude and distribution, respectively (i.e. increase in S resulted to increase in maximum contact stress value, while increase in P increase the contact length and maintained the maximum contact stress value). Furthermore, the applied load induced a greater change in contact stress characteristics than the inflation pressure—enforcing the tire edge ribs to carry the load as the highest load of 44.4 kN was imposed.

Under the free-rolling condition, the contact stresses in all three orthogonal directions were minimally influenced by the traveling speed. However, the speed invoked a change in the longitudinal contact stresses for the other rolling conditions. For the tractive cases (accelerating and braking), the vertical and transverse contact stresses did not change significantly, relative to the longitudinal contact stresses. Particularly, the accelerating scenario reached the traction limit within the front part of the tire, while nearly the opposite behavior was observed for the braking condition (i.e. the rear end reached the frictional limit).

Cornering, on the other hand, impacted the vertical and transverse contact stresses more drastically than those in the longitudinal direction. An evident shift of the contact stresses towards the inner part of the turn was captured. In establishing and validating a numerical air-inflated tire model, one can now predict an extensive database of contact

stresses. Not only does the presented modeling approach provide a means to understand critical parameters influencing tire-pavement interaction, but it also enables building the loading input data that would excite pavement responses.

CHAPTER 3

DEVELOPMENT OF DOMAIN ANALYSIS TO EVALUATE PAVEMENT BULK BEHAVIOR

3.1 Introduction

Damage prediction in conventional pavement analysis is handled through empirically derived transfer functions. The AASHTOWare Pavement Mechanistic-Empirical Pavement Design Guide (MEPDG) program is a useful tool for pavement engineers, utilizing critical mechanistic responses (i.e., strains) at predefined points as inputs for transfer functions strains) at predefined points as inputs for transfer functions [17]. Based on an extensive effort of field testing, transfer functions evolve pavement damage by quantifying the number of repetitions to failure. For example, by using the maximum tensile strain at the bottom of the asphalt concrete (AC) layer, the number of repetitions for bottom-up fatigue cracking is predicted.

Two key drawbacks of this approach are the reliance of predicting pavement damage on a single strain value and the lack of transfer functions that appropriately represent near-surface damage. In particular, minor differences in strain inputs (e.g., for fatigue cracking or rutting) would inherently lead to the same damage prediction; thereby, unable to contrast distinct loading scenarios. Furthermore, the multi-layered elastic analysis (MLEA) scheme embedded within the AASHTOWare framework inaccurately accounts for the moving tire load and viscoelastic nature of AC layers. Instead, the load excitation is assumed as a pressure in the vertical direction only and distributed over a circular contact area [18, 19].

Realistic implications of actual tire-pavement contact stresses lie within the near-surface region, where the contact stress influence is highest. For instance, interstate highways experience top-down cracking due to the high level of near-surface shear strains [20, 21, 22, 23]. In the current state of pavement design methodologies, transfer functions relating shear strains to near-surface cracking do not exist. Similar to fatigue cracking and rutting predictions, significant field-testing efforts would be required to generate corresponding transfer functions. To address these shortcomings, several numerical methods exist that evaluate the impact of tire loading on pavement damage at the near-surface region. Currently es-

tablished methods include finite element (FE) modeling of critical structural responses, a combination of FE analysis with limit failure criteria, and fully-coupled damage models within the material domain.

FE analysis is an effective technique to simulate tire-pavement interaction. A robust modeling platform to generate a three-dimensional (3D) flexible pavement model has been implemented by Al-Qadi et al. [24, 25, 26, 27, 28]. Several advancements over two decades of work include: linear viscoelastic material characterization for AC layers, dynamic implicit analysis, layer interaction, continuous moving load, 3D and non- uniform contact stresses, infinite boundary element, and temperature profile along the AC layer depth. Moreover, nonlinear material characterization was appended to account for stress-dependency of granular base layers [29, 30]. Although limitations of MLEA from the mechanistic-empirical approach can be addressed using FE analysis, quantifying pavement damage still relies on strains at point locations without appropriately quantifying near-surface damage. As mentioned previously, regardless of the difference in contact stress distribution at the tire-pavement interface, similar resulting strains would generate the same level of damage. This clearly indicates the limited capability of point strains to represent the full influence of 3D and non-uniform contact stresses.

As an alternative for analysis, past studies presented the use of shear stress ratio to estimate potential damage, without evolving to a fully-damaged state. Using a failure criteria–e.g., Mohr-Coulomb failure surface–the octahedral shear stress ratio at a specific point location can be calculated to compare the critical octahedral shear stress to the material shear strength [31, 32, 33, 34, 35]. The rationale is that as the shear stress ratio tends to unity, the potential for rapid deformation increases accordingly. However, appending a failure surface does not resolve reducing the comparison of pavement structural responses to a single analysis point, thereby still ignoring the influence of multi-axial contact stresses at the near-surface region.

In a different perspective, advanced constitutive models and failure theories have been implemented to analyze damage evolution within pavement layers. Continuum damage theories have been commonly used in predicting fatigue cracking damage in pavements [36, 37, 38, 39, 40, 41, 42]. In contrast, viscoplasticity theories have been used for modeling plastic deformations at relatively high temperatures [43, 44, 45, 46, 47, 48, 49, 50, 51, 52, 53]. Due to the complexity of constitutive models and required computational effort, these analyses are either maintained within the material domain or significant simplifications of the pavement structural model are required. Hence, there exists a need to quantify pavement damage potential at the near-surface region, while accounting for multi-axial structural responses.

3.2 Research Objective

Rather than analyzing pavement responses via critical strains at point locations, there is a need to determine the bulk behavior of a loaded pavement structure. A new post-processing method, called "Domain Analysis," is introduced herein. The proposed method not only provides a means to comprehensively evaluate the realistic impact of 3D tire-pavement contact stresses, but it also assesses the damage potential of the weakened area within a pavement structure. The development and testing of the method are presented, analyzing two distinct pavement structures along with various tire loading conditions and configurations.

3.3 Domain Analysis

The proposed approach allows for the prediction of the damage potential by considering volumetric domains in lieu of a single-point response. This dissertation details the development and implementation of the Domain Analysis using several case studies. The procedure is composed of four main steps:

1. Calculate multi-axial stress and strain states using a pavement model;
2. Discretize the pavement domain to identify critical zones;
3. Compare stress and strain states with respect to a failure criterion; and
4. Combine the failure potential of critical regions to obtain a scalar that indicates the level of demand on the pavement structure (which includes the calculation of weight factors and cumulative ratio).

3.3.1 Pavement Model and Multi-Axial Stress and Strain States

Stresses and strains are calculated using a baseline finite element model (FEM) of a loaded pavement structure. From the pavement FEM, a subdomain that covers an area of 1 m^2 in the xz-plane centered on the middle of the wheel path and extended 0.75 m into the subgrade layer is extracted (Figure 3.1). As the stresses and strains tend to zero at the boundaries of the full pavement FEM, the domain for the multi-axial stress state analysis could be limited to the selected subdomain. Furthermore, the critical loading step is selected when the tire is at the middle of the wheel path.

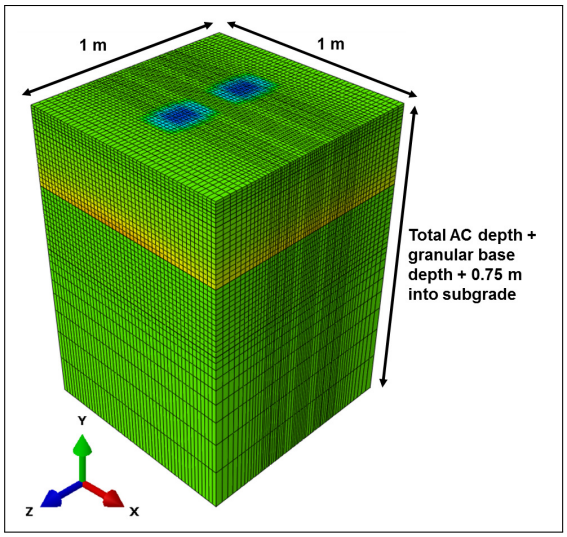

Fig. 3.1. Pavement subdomain.

In general, an element stress state can be represented by normal and tangential stresses. If a material element is rotated in a manner that leads to zero shear stresses, the element stress state can then be characterized using principal stresses, or the normal stresses acting on the element. Using the principal stresses, the hydrostatic stress, p_σ, and shear stress indicator, q_σ, can be defined using the following equations:

$$p_\sigma = \frac{1}{3}(\sigma_1 + \sigma_2 + \sigma_3) \tag{3.1}$$

$$q_\sigma = \sqrt{\frac{1}{2}\left[(\sigma_1 - \sigma_2)^2 + (\sigma_2 - \sigma_3)^2 + (\sigma_1 - \sigma_3)^2\right]} \tag{3.2}$$

where σ_1, σ_2, and σ_3 are the maximum, intermediate, and minimum principal stresses, respectively. Below, the same form of equations represent the hydrostatic strain, p_ε, and shear strain indicator, q_ε:

$$p_\varepsilon = \frac{1}{3}(\varepsilon_1 + \varepsilon_2 + \varepsilon_3) \tag{3.3}$$

$$q_\varepsilon = \sqrt{\frac{2}{9}\left[(\varepsilon_1 - \varepsilon_2)^2 + (\varepsilon_2 - \varepsilon_3)^2 + (\varepsilon_1 - \varepsilon_3)^2\right]} \tag{3.4}$$

where ε_1, ε_2, and ε_3 are the maximum, intermediate, and minimum principal strains, respectively.

Initially, a two-dimensional (2D) plane was held at the mid-length of the pavement model; however, the variation of the given plane along the traffic direction indicated that the maximum stress and strain states occur just behind the middle of the tire footprint. This behavior is due to the viscoelastic nature of AC layers, wherein strain response follows

the loading with a delay. Therefore, maximum stresses and maximum strains may not occur at the same location for varying load simulations. As each loading case generated a different plane of the maximum values, volume averaging was implemented to include all values within the 3D subdomain.

3.3.2 Domain Discretization

Quantifying the bulk behavior was focused on critical zones that coincide with locations where distresses often occur and that are considered in pavement design. In particular, the analysis was focused on the near-surface region and bottom of the layer. At each 2D plane along yz (recall coordinate system from Figure 3.1), a zoning process is introduced to differentiate response magnitudes throughout the layer depth (Figure 3.2).

The horizontal boundary, defined by a given depth v, is a function of the pavement layer thickness and the vertical boundary is defined by the tire width of a specific load case with an addition of $h = 50$ mm to the left and right of the tire edges. This addition corresponds to previous observations wherein high shear values localized near the tire edges [54, 35]. Moreover, the horizontal boundary was confined within 100 mm of the surface, where near-surface cracking is generally observed [23].

Partitioning each 2D slice with the vertical and horizontal limits that enveloped the two regions of interest (near-surface and bottom of the layer), generated nine zones ($Z1 - Z9$) as illustrated in Figure 3.2. The zoning process exhibits domain dependency; i.e., the user-defined limits influence the range of values considered per zone. In addition, as the zoning limits were fixed per pavement structure, they do not significantly influence the ratios of the loading cases considered relative to a reference case. Furthermore, along the longitudinal direction, the cloud of points varied within the nine zones, which is another strong motivation for the Domain Analysis to be implemented three-dimensionally.

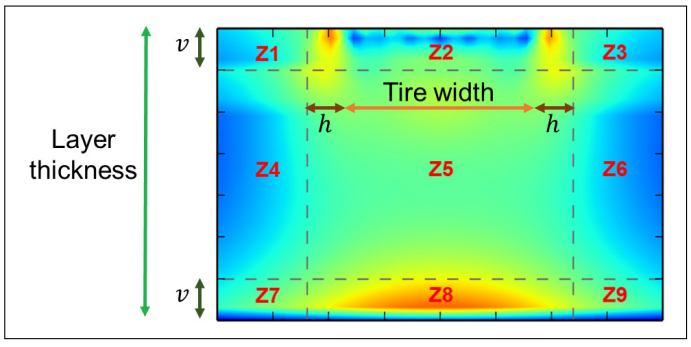

Fig. 3.2. Zoning process.

Using the centroid of each finite element within the subdomain, principal values were obtained and the hydrostatic stress and strain and shear stress and strain indicators were calculated and plotted in the Cartesian plane using Equations 3.1-3.4. Figure 3.3 illustrates a typical p-q diagram in the stress domain. One could observe that the zone directly underneath the tire ($Z2$) experienced the highest levels of compression and shear. In particular, the triangle-up markers scattered over the negative hydrostatic stress had the greatest shear stress values within the p-q diagram.

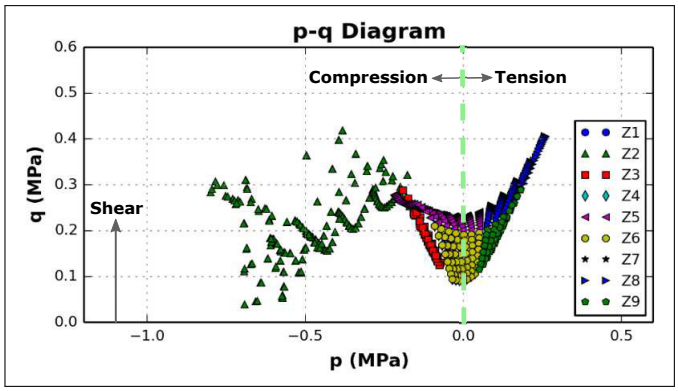

Fig. 3.3. Sample p-q diagram within the AC layer.

Other near-surface regions ($Z1$ and $Z3$) exhibited shear and compression, but at smaller magnitudes. As the zones transition to a greater depth, $Z5$ (middle zone) still exhibited high levels of shear, but normal stresses were slowly transitioning from compression into tension. As the bottom of the layer was bounded by $Z7$, $Z8$, and $Z9$, high shear was still observed, but the normal stresses fully transitioned into tension. This observation was predominant within $Z8$, represented by the triangle-right markers on the positive p regime (Figure 3.3).

From the zoning process of each major pavement layer, four critical zones were identified: (i) $Z2$ within the AC relating to near-surface cracking and rutting; (ii) $Z8$ within the AC relating to bottom-up fatigue cracking; (iii) $Z2$ within the base; and (iv) $Z2$ within the subgrade both related to rutting; the last two are related to secondary rutting.

3.3.3 Failure Criteria

The Modified Drucker-Prager/Cap model was adopted as the failure criteria to relate a given stress/strain state to its damage potential, although other failure theories could be easily implemented. To accomplish this, a p-q coordinate is characterized using its proximity relative to a failure surface. From plasticity theories, the Modified Drucker-

Prager/Cap model is used to account for tension cut-off, compression, and shear. Within the failure surface, the material remains elastic but reaches failure as soon as the material point state coincides with the failure plane.

The yield surface consists of: (i) the Drucker-Prager shear failure surface; (ii) an elliptical cap to limit the hydrostatic pressure; and (iii) a smooth transition zone between the failure surface and the cap. The Drucker-Prager shear failure surface is defined by the following:

$$F_s = q - p\tan\beta - d = 0 \tag{3.5}$$

where β and d are the angle of friction and cohesion, respectively.

Moreover, the cap and transition yield surfaces are calculated as follows:

$$F_c = \sqrt{(p-p_a)^2 + \left[\frac{Rt}{1+\alpha+\alpha/\cos\beta}\right]^2} - R\left(d + p_a\tan\beta\right) = 0 \tag{3.6}$$

$$F_t = \sqrt{(p-p_a)^2 + \left[t - \left(1 - \frac{\alpha}{\cos\beta}\right)\left(d + p_a\tan\beta\right)\right]^2} - R(d + p_a\tan\beta) = 0 \tag{3.7}$$

$$p_a = \frac{p_b - Rd}{1 + R\tan\beta} \tag{3.8}$$

where R is the material parameter that controls the shape of the cap, α defines the smooth transition surface between the Drucker-Prager shear failure surface cap, and p_b is the mean effective yield stress and defines the position of the cap [55].

The baseline values characterizing the Drucker-Prager failure plane, in the stress domain, were obtained from Gokhale et al. [56]; however these model inputs were modified to encase the worst loading case (i.e., one that generates the highest values of p and q). It is noteworthy that the parameters assumed for each major pavement layer were kept constant for all loading conditions (per case study) to eliminate the influence of material damage capacity as a variable. Moreover, given that the FE analysis solely simulates one load pass, it was deemed appropriate to modify the failure surface parameters to envelope the entire p-q point cloud.

A limitation of the Domain Analysis method is that the assumed failure surface may not accurately represent material failure with respect to temperature and loading rate effects. To better represent asphalt concrete material behavior, viscoplasticity should be utilized as a potential solution in the future, instead of the assumed Modified Drucker-Prager failure criteria.

3.3.4 Polar Coordinate Transformation and Weight Factor Calculation

To effectively relate the *p*-*q* diagram values and failure envelope, the values in the Cartesian coordinate were transformed into polar coordinates. Two important parameters can be extracted from the *p*-*q* diagram in the Cartesian plane: (i) the magnitude of the vector connecting the origin to a specific *p*-*q* coordinate, and (ii) the angle θ between the vector and the positive horizontal axis. Additionally, the failure plane was also transformed (Figure 3.4).

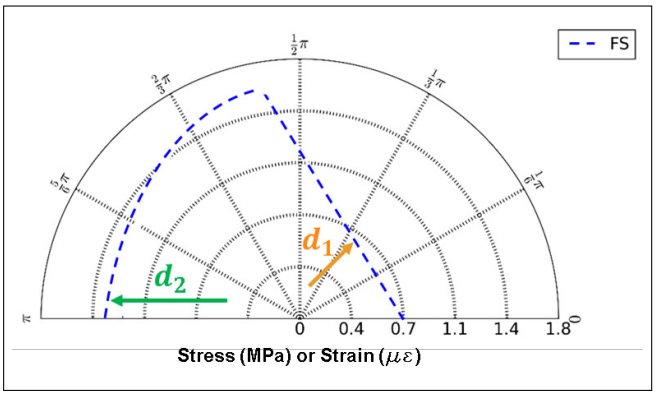

Fig. 3.4. Polar sectors defining the weight factors.

This coordinate transformation allowed the relative comparison of the cloud of stress and strain states to the failure plane. Depending on the proximity of the point to the failure plane, the material may fail in compression and/or shear. Therefore, a weight factor was created to adequately penalize the stress/strain state point based on its location relative to the failure envelope. However, as the coverage of the p-q coordinates varied depending on the load case and pavement structure combination, a constant weighting scheme was implemented on an empty polar coordinate system to prevent an inconsistent definition of weight factors.

Weight factors (independent of the load case) were defined by regionalizing the polar coordinate system into 30 sectors, which stemmed from defining six radii boundaries and seven angle boundaries (0, $\pi/6$, $\pi/3$, $\pi/2$, $2\pi/3$, $5\pi/6$, and π). Using the midpoint of each sector, its shortest distance to the failure surface was calculated. The weights are defined by the stress/strain ratio, i.e., current stress/strain state of the sector midpoint divided by the allowable stress/strain state. A weight of 1.0 indicates that the midpoint sector coincides with the yield surface and failure is reached. From Figure 3.4, the weight assigned to location 1 is greater than that of location 2; therefore, the highest weight factor defines the sector closest to the failure envelope. It must be noted that this process is only implemented in the sectors within the failure envelope, as absolute failure is assumed for

the sectors beyond. As the p-q cloud are also transformed into the same polar coordinate system, each coordinate is weighted depending on its enveloping sector.

3.3.5 Cumulative Ratio

The next step in the Domain Analysis method is to quantify the cumulative impact of the 3D and non-uniform contact stresses. Using the vector magnitude and weight factors, the p-q point cloud can be combined into one cumulative scalar value, coined as the cumulative stress, $C\sigma$, or cumulative strain, $C\varepsilon$. However, a direct comparison between various loading cases is deemed relatively unfair given that their corresponding mesh geometries differ. For instance, the dual tire assembly (DTA) would generate a higher number of points in the p-q diagram than the new generation wide-base tire (NG-WBT) case. Therefore, a homogenizing factor is defined to account for the geometric difference between load cases along the cross-sectional area (yz-plane). The homogenizing factor, a_{jl}/A_l, is calculated by considering the elemental area relative to the total area covered by a specific zone. Note that a_{jl} is the area of element j within zone l, and A_l is the total area of the zone l.

Furthermore, a volumetric factor, l_{elem}/L_{sub}, is also introduced to consider the variation of the stress/strain state along the longitudinal direction, x. This is implemented similarly to the homogenizing factor, except that the extent of the volumetric factor is along the traveling direction of the subdomain. At this point, the presented method captures all stress and strain responses within the 3D subdomain. The resulting scalar is the cumulative ratio, CR, which is calculated by normalizing the cumulative value with respect to the reference load case:

$$C\sigma, C\varepsilon = \frac{\sum_{l=1}^{z}\sum_{j=1}^{e}\sum_{i=1}^{s}|(pq)_{\sigma,\varepsilon}|_{jl} \times a_{jl} \times l_{elem} \times w_i}{A_l \times L_{sub}} \tag{3.9}$$

$$CRS = \frac{C\sigma}{C\sigma_{ref}} \tag{3.10}$$

$$CRE = \frac{C\varepsilon}{C\varepsilon_{ref}} \tag{3.11}$$

where $C\sigma$ is the cumulative stress of the specific load case, $C\varepsilon$ is the cumulative strain of the specific load case, $|(pq)_{\sigma,\varepsilon}|_{jl}$ is the vector magnitude of the element j for a total of e elements within the zone l for a total of z zones, l_{elem} is the element length along the travel direction, w_i is the weight of the specific sector i for a total of s sectors, L_{sub} is the total length of the subdomain, CRS is the unitless cumulative ratio in the stress domain, CRE is the unitless cumulative ratio in the strain domain, $C\sigma_{ref}$ is the cumulative stress of the reference load case, and $C\varepsilon_{ref}$ is the cumulative strain of a reference load case.

Each of the four critical zones can be analyzed to determine the governing zone that may lead to the highest damage potential, e.g., a pavement may fail in subgrade rutting if $Z2$ within the subgrade has significantly high cumulative ratios.

A secondary partition at the middle of the tire width (Z=0 mm) was introduced to capture the near-surface influence of an asymmetric load distribution. For example, asymmetric pavement responses are encased by the two boxes in Figure 3.5. The combined $Z2$ and $Z5$ on the right is termed $ACD1$; whereas, the one on the left is termed $ACD2$. It is noteworthy that this new zoning process was implemented only within the near-surface region of the AC layer.

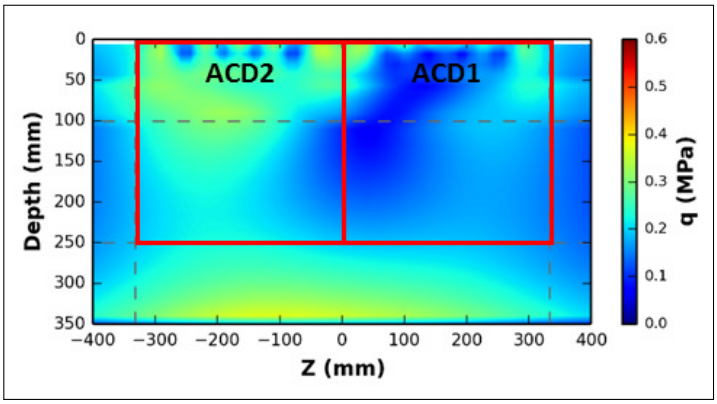

Fig. 3.5. Secondary partitioning along the middle of $Z2$ and $Z5$.

Another approach for comparing the cumulative stress/strain state is to analyze the bulk behavior of the entire pavement structure by combining the four critical zones using a weighted sum. Note that the Domain Analysis equations are interchangeable, depending on whether the analysis considers the stress or strain domain. One advantage of this method is that the same computational engine is used, but the input parameters are altered.

3.4 Numerical Simulation Inputs

Using Abaqus, the pavement FEM considered dynamic implicit analysis, 3D and non-uniform contact stresses, continuous moving load, infinite boundary elements to simulate far-field region behavior, and appropriate layer interaction properties between pavement layers. Additional details of the model generation scheme can be found elsewhere [57, 23, 22, 29, 54]. Limitations of the modeling approach include AC material homogeneity and isotropy; single moving load pass; pavement analysis without crack initiation, healing, or propagation; and assumption of a fixed elasto-plastic limit to define the Domain Analysis

weight factors.

Combinations of applied load and tire-inflation pressure on the DTA and NG-WBT are considered (Table 3.1) to simulate typical tire configurations of the current freight traffic. Additionally, the steer tire (inherently one of the DTA tires) was considered to quantify the impact from the cab of freight trucks; although the load is lower than the half-axle trailer configuration, the tire load could be significantly localized. Given these three tire configurations, various scenarios from the cab and trailer axles were considered. Three distinct case studies were investigated to test the capabilities of the Domain Analysis:

- Case I: comparison of typical loading condition of DTA, NG-WBT, and steer tire;
- Case II: effect of tire-inflation pressures; and,
- Case III: influence of differential tire-inflation pressure on DTA.

Table 3.1. Loading Cases used in Finite Element Analysis

Case Study	Tire	Load (kN)	Inflation Pressure (kPa)
Case I	NG-WBT	44.0	758
	DTA	44.0	758
	Steer Tire	29.7	690
Case II	NG-WBT	37.8	480
	NG-WBT	37.8	690
	NG-WBT	37.8	830
	DTA	37.8	480
	DTA	37.8	690
	DTA	37.8	830
Case III	DTA (Uniform)	44.0	758/758
	DTA (Differential)	44.0	552/758

Figure 3.6 presents a simplified diagram comparing vertical contact stress distributions for each of the three cases. The contact stresses were obtained from measurements by a third party contracted to work for the Illinois Center for Transportation. In addition, the x-axis presents the normalized contact width, wherein the actual width is normalized to the nominal width for comparison purposes. The analysis of the contact stress database was completed by [10].

The analysis matrix of the loading conditions was applied to two pavement structures. Low-volume and interstate roadways were simulated to cover the extremes of pavement

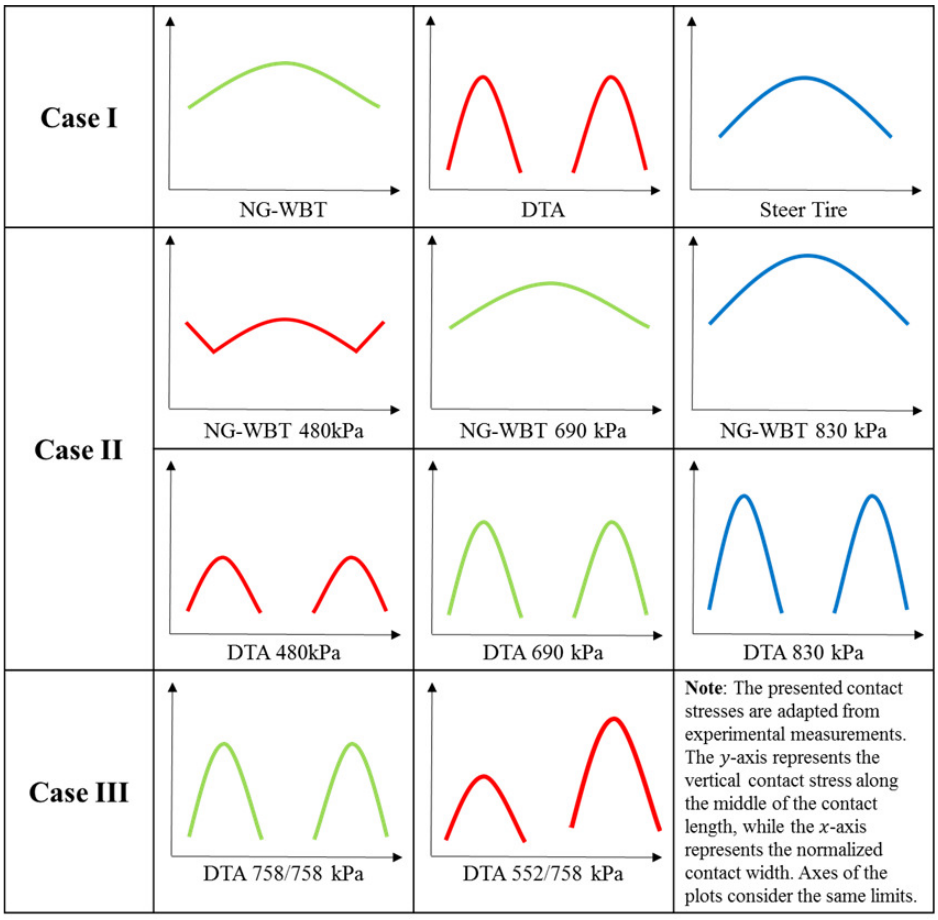

Fig. 3.6. Simplified comparison of vertical contact stress distributions.

structure configurations, which are referred to as thin and thick pavements in the following sections, respectively. It is worth noting that the thick pavement included three AC layers over a granular base layer, whereas the thin pavement considered one AC layer (see Table 3.2). Cases I and III considered the same pavement structure with three AC layers, whereas Case II considered thin and thick pavement structures.

The AC layers were assumed to be linear viscoelastic, wherein the Prony series were computed using the dynamic modulus data from the Long Term Pavement Performance (LTPP) database. From 1000 data sets, material characterizations were narrowed to six data sets based on confidence levels and nominal maximum aggregate sizes (Figure 3.7). The thin and thick pavement structures considered a combination of *strong* and *weak* AC material properties.

The interstate pavement cases assumed the granular layer as linear elastic. However, granular layers were characterized as nonlinear, stress-dependent, and anisotropic for the thin pavement structure as it is assumed that the stress magnitudes were significantly

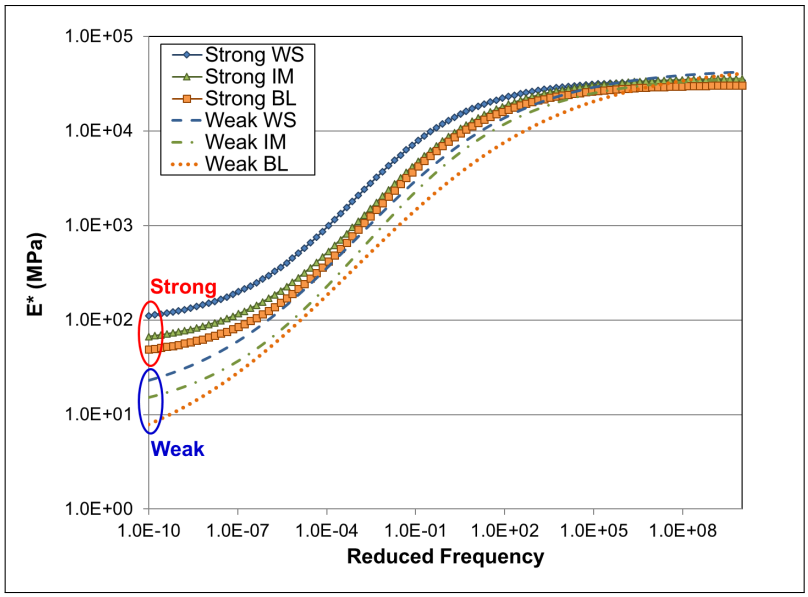

Fig. 3.7. Linear viscoelastic characterization of AC layers extracted from LTPP. WS, IL, and BL corresponds to wearing surface, intermediate layer, and binder layer, respectively.

reduced for thick pavements. Material constants for the nonlinear anisotropic granular materials were obtained from a database. Further details of the material characterization can be found elsewhere [54]. A summary of the modeling assumptions and limitations is tabulated in Appendix A.

Table 3.2. Pavement Structure Configurations

	Layer Thickness (mm)		
	Case I/III	Case II	
Wearing Surface	62.5	100*	50
Intermediate	100	-	50
Binder	250	-	250
Granular Base	150	200	300

**Note: Considers only one AC Layer.*

3.5 Implementation

Three scenarios were considered to test the capabilities of the Domain Analysis method by evaluating the impact of tire type, configuration, and inflation pressures. Implementing

the pavement modeling scheme and material characterization by [54], the output database of the FE simulations were utilized as inputs of the Domain Analysis method. It is worth noting that DTA with uniform tire-inflation pressure was selected as reference for all three cases. The following analysis includes the two main outputs of the Domain Analysis: CRS and CRE, which are the cumulative ratio in the stress and strain domains, respectively.

3.5.1 Case I: Tire Type and Configuration

Three tire configurations are loaded onto a perpetual pavement structure, consisting of AC and granular base layers with thicknesses of 412.5 mm and 150 mm, respectively (Table 3.2). Details of the loading conditions may be found in Table 3.1. Moreover, NG-WBT and DTA load inputs for the FE model were extracted from a database of experimentally measured contact loads [10, 11]; whereas, the load input for the steer tire (placed onto the front-cab axle) were obtained from a FE tire model by a third-party collaboration with the Illinois Center for Transportation.

Critical Strain Input for MEPDG

Prior to presenting the resulting stress/strain ratios, maximum strains at six-point locations are shown. Extracted strain values are important to the conventional mechanistic-empirical pavement design method, wherein critical strains are utilized as input in the transfer function to predict damage. It is noteworthy that the x, y, and z directions correspond to 1, 2, and 3 directions. The variables are $\varepsilon_{33,AC}$, $\varepsilon_{33,surf}$, $\varepsilon_{22,AC}$, $\varepsilon_{22,base}$, $\varepsilon_{22,sg}$, and $\varepsilon_{23,AC}$, which correspond to the critical transverse tensile strains at the bottom of the AC and surface; vertical compressive strain within the AC, base, and subgrade; and vertical shear strain within the AC, respectively. These strain outputs are selected as they are conventional inputs into transfer functions to estimate damage, except for $\varepsilon_{23,AC}$, which was previously introduced by Yoo and Al-Qadi [23] to be a major factor for near-surface cracking.

Figure 3.8 illustrates the variation of the critical strains, normalized to the DTA case. One could observe that the strains within the AC layer were significantly higher than those of the base and subgrade layers. Additionally, at the depth of 23.3 mm, the NG-WBT and steer tire cases generated AC shear strain increments of 70% and 33%, respectively, due to higher contact stress magnitudes relative to DTA. As this response is excluded from the conventional MEPDG approach to estimate damage, near-surface behavior is overlooked.

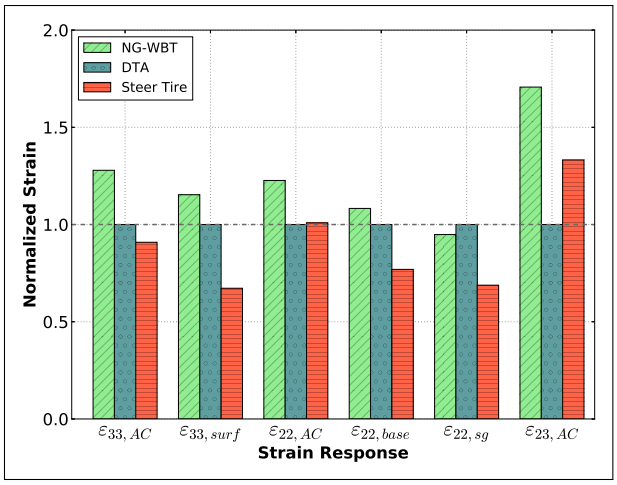

Fig. 3.8. Point responses of Case I for the thick pavement.

On the other hand, Figure 3.9 illustrates the 3D pavement response via p-q diagrams at the critical 2D plane (yz -plane). Clearly, a comparison of the p-q diagrams depicts the significant complexity of pavement responses relative to single-point critical strains. High levels of compression and shear were induced at the near-surface region ($Z2$) directly underneath the tire. One could clearly observe that the NG-WBT generated significantly greater compression and shear as the spread of triangle-up markers tend toward the negative horizontal and positive vertical scales (Figure 3.9a). Moreover, Figure 3.9c shows that the steer tire with a 9% decrement in the tire-inflation pressure but 32.5% increment in the applied load generated more concentrated values than those of the DTA (Figure 3.9b).

Plotting NG-WBT p- and q-values along the layer width and depth, Figure 3.10a highlights high shear concentrations at tire edges. As expected, high compression stresses were found directly underneath the tire (Figure 3.10b). Throughout the remainder of the 2D slices along the contact length, the same trend is observed at varying magnitudes. Another key point of the provided contour plots is the undeniable influence of tire-pavement contact stresses at the near-surface region.

Using the Domain Analysis method, five distinct zones were compared in Figure 3.11, namely: $ACD1$; $ACD2$; $Z2$ and $Z8$ within the AC; $Z2$ within the base; and $Z2$ within the subgrade. All ratios for the DTA case remained equal to unity as DTA was the reference case. On one hand, the NG-WBT case resulted in CRS values within the AC layer to be over 1.0, which suggested higher damage potential relative to the DTA. In addition, the secondary partitioning resulted in a higher $ACD1$ value than that of $ACD2$. This difference was attributed to the asymmetric contact stress distribution based on experimental measurements (recall Figure 3.10). Note that only the CRS values for the critical zones

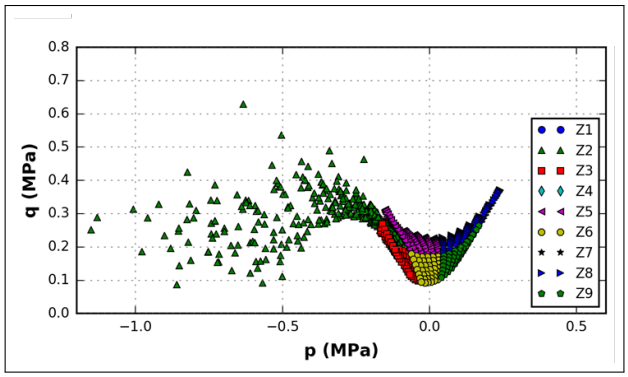

(a) p-q diagram within the AC layer for NG-WBT.

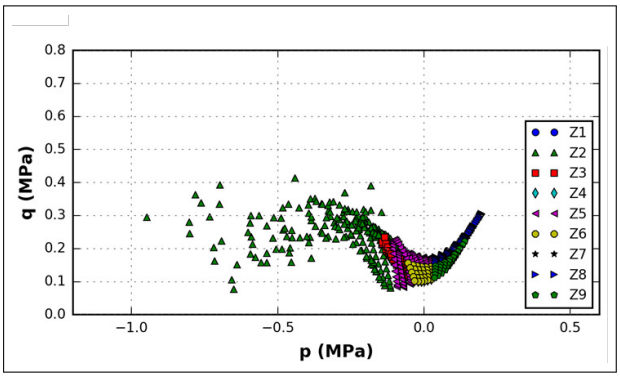

(b) p-q diagram within the AC layer for DTA.

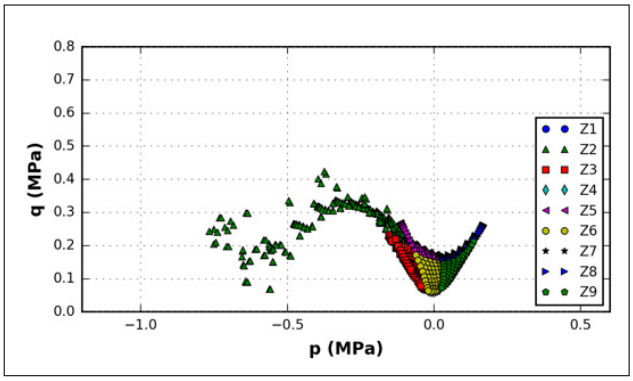

(c) p-q diagram within the AC layer for the steer tire.

Fig. 3.9. Point cloud distributions of the mean stress and shear stress indicator.

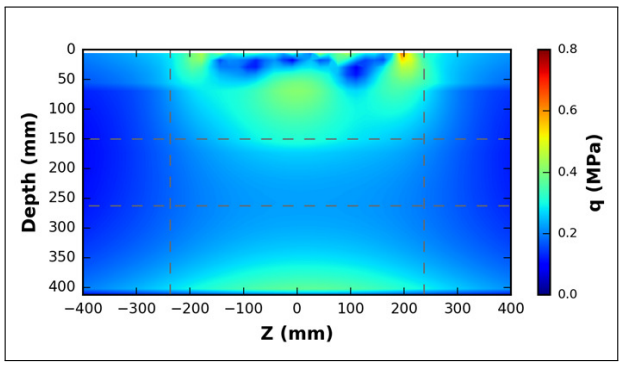

(a) Contour of q along the depth and width.

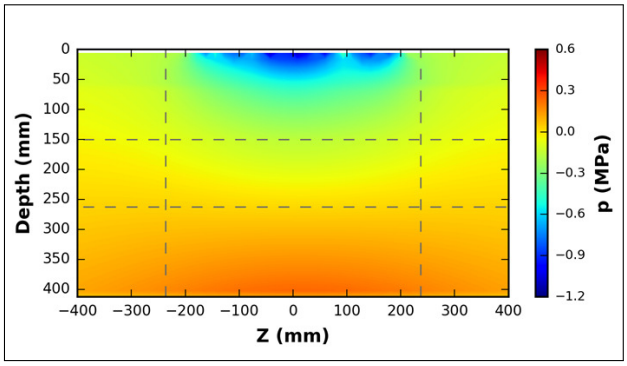

(b) Contour of p along the depth and width.

Fig. 3.10. NG-WBT contours of p and q along the critical 2D plane.

are presented as they have the similar trends in the strain domain.

On the other hand, the steer tire generated CRS increments up to 12% within the AC layer. Conventionally, MEPDG accounts for the front-cab axle based on load distribution; however, under the given tire-inflation pressure and applied load combination, the steer tire

induced a higher damage potential relative to the DTA. Near-surface damage due to shear strain cannot be analyzed using MEPDG; although it clearly governs damage potential as illustrated in Figure 3.8. Additionally, the proposed method captured the reduced influence of contact stresses within the granular layers, as the CRS values for the NG-WBT remained close to 1.0, whereas the ones for the steer tire were significantly less than 1.0 due to the decreased applied load.

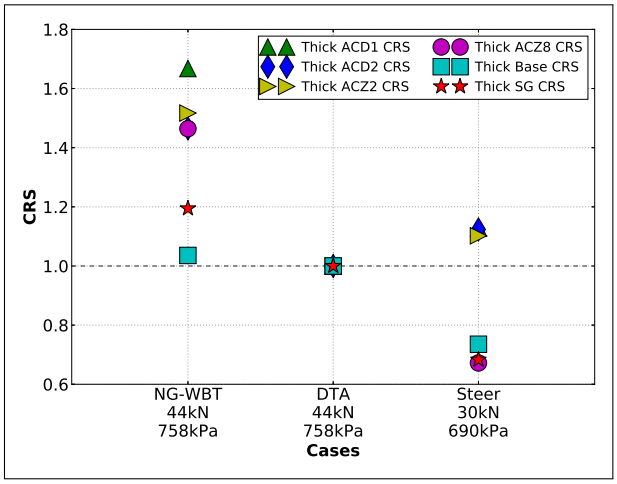

Fig. 3.11. Domain analysis ratios for Case I considering NG-WBT and DTA for thick pavement.

3.5.2 Case II: Uniform Tire-Inflation Pressure

In the second case study, the influence of tire-inflation pressure was analyzed while maintaining an applied load of 37.8 kN. The DTA with tire-inflation pressure of 690 kPa was selected as the reference case. The structures containing AC layers of 100 and 350 mm are referred to as thick and thin pavements, respectively (Table 3.2), which represent low-volume and interstate highway pavements.

Similar to Case I, critical point responses due to NG-WBT loading are illustrated in Figure 3.12 as a link to MEPDG damage evaluation (via transfer functions). Using the conventional method of determining single-point critical strains, one could observe that most of the responses from NG-WBT cases were minimally influenced by varying tire-inflation pressures, except for the shear strain within the thick pavement. Under NG-WBT loading, high level of AC near-surface behavior was captured by the shear strain; however, the differences may not be realistic as it cannot fully capture the 3D influence of the contact stress distribution. Although a difference was observed for $\varepsilon_{33,surf}$ and $\varepsilon_{22,AC}$ for the thick

pavement, the absolute strain difference was within 6 $\mu\varepsilon$. Given the minute difference in strain, the anticipated number of repetitions to failure for these cases would result in similar values despite significant differences in the contact stresses at the tire-pavement interface.

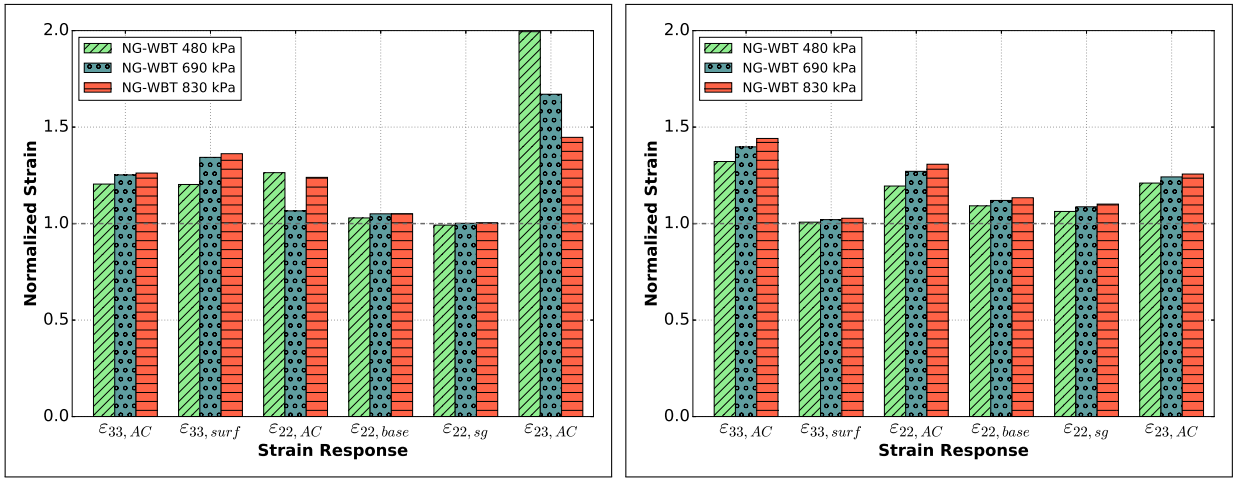

(a) Thick pavement responses.

(b) Thin pavement responses.

Fig. 3.12. Critical strain responses from thick and thin pavements loaded with NG-WBT.

Using Domain Analysis, Figures 3.13 and 3.14 present the effect of tire-inflation pressure on CRE and CRS for both NG-WBT and DTA. The filled and hollow markers correspond to the thick and thin pavements, respectively. As illustrated, the increase in tire-inflation pressure leads to an increase in pavement response, more evidently for NG-WBT than DTA cases. Due to the symmetry of the applied contact stresses, $ACD1$ and $ACD2$ are not included in the following analysis.

The thick pavement, loaded by NG-WBT, was clearly governed by the near-surface zone ($Z2$ within the AC), whereas the highest CRS value of the thin pavement structure was found within the bottom of the AC, followed by the stress-dependent granular base (Figure 3.13a). The highest difference with respect to DTA at 690 kPa was observed for NG-WBT at 830 kPa on the thin pavement model, where CRE was 1.36. On the other hand, the DTA cases were marginally influenced by the tire-inflation pressures as the ratios within the critical zones and weighted sum remained close to unity (Figure 3.14).

Although the lowest tire-inflation pressure generated the lowest bulk stress and strain ratios, the contour plots of the corresponding cases revealed higher stress and strain values within the tire edges at near-surface. As shown in Figure 3.6, NG-WBT with tire-inflation pressure of 480 kPa generated significantly high tire-edge contact stresses. Localizing the Domain Analysis results for tire edges revealed that the NG-WBT with lowest tire-inflation

pressure could lead to the highest near-surface damage potential. As shown, the Domain Analysis effectively captured the 3D stress/strain state of pavement responses, while point strain inputs for MEPDG transfer functions could not adequately quantify the influence of varying tire-inflation pressures.

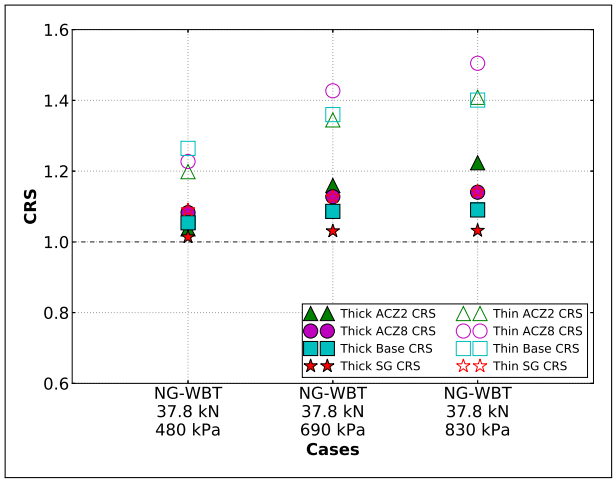

(a) Cumulative stress ratios of individual critical zones within the thick and thin pavements.

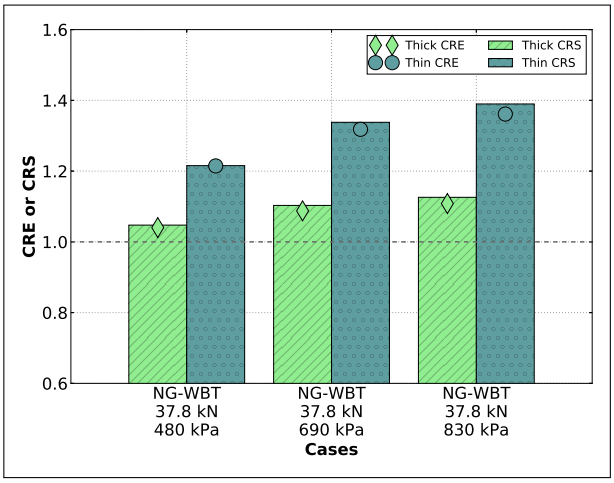

(b) Weighted sum of critical zones within the thick and thin pavements.

Fig. 3.13. Domain analysis ratios for Case II considering NG-WBT with varying tire-inflation pressures.

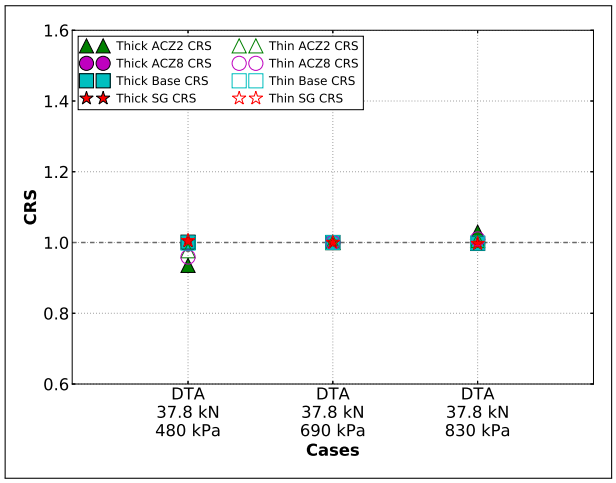

(a) Cumulative stress ratios of individual critical zones within the thick and thin pavements.

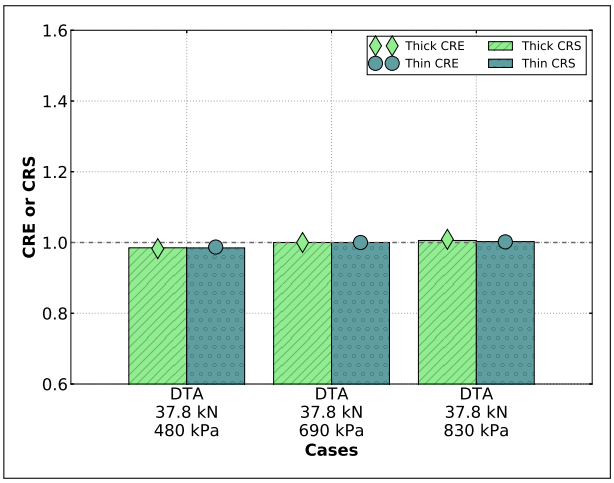

(b) Weighted sum of critical zones within the thick and thin pavements.

Fig. 3.14. Domain analysis ratios for Case II considering DTA with varying tire-inflation pressures.

3.5.3 Case III: Differential Tire-Inflation Pressure

DTA with differential tire-inflation pressures represent the typical operating conditions of heavy truck tires due to the difficulty of maintaining the inner tire pressure. The pavement structure considered AC and base layer thicknesses of 412.5 and 150 mm, respectively (Table 3.2).

The loading condition included a differential tire-inflation pressure of 552 and 758 kPa, while maintaining the applied load at 44 kN (Table 3.1). In contrast to the p-q diagram of the DTA with uniform inflation pressure of 758 kPa in Figure 3.9b, the differentially inflated DTA resulted in higher magnitudes and wider distribution (Figure 3.15a). Particularly as illustrated in Figure 3.15b, the tire inflated to 758 kPa generated higher states of shear and compression at near-surface ($ACD2$, which is the left-hand combination of $Z2$ and $Z5$).

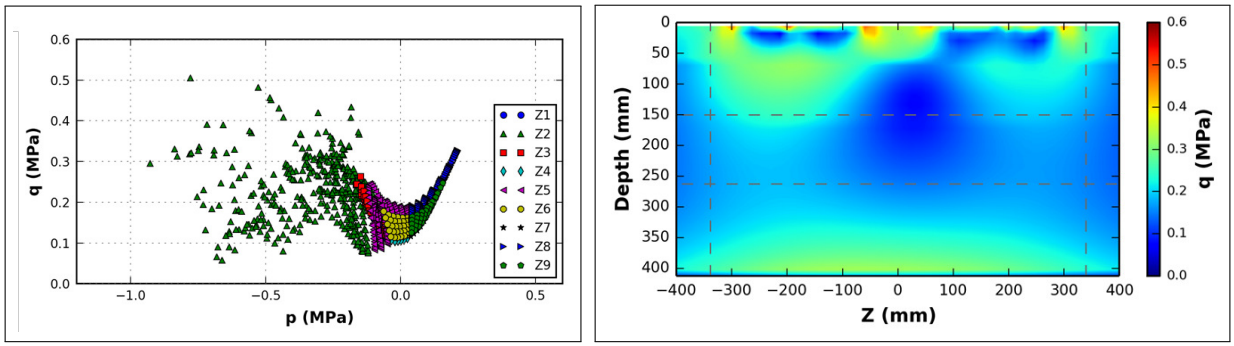

(a) p-q diagram within the AC layer.

(b) Contour of q along the depth and width of the subdomain.

Fig. 3.15. Critical 2D plane for the DTA with differential tire-inflation pressure.

Contrasting the point strain and domain analysis outputs, Figure 3.16a showcases that the differential tire-inflation pressure has minimal influence on the maximum strains. For fatigue cracking and rutting evaluation using MEPDG, the resulting number of repetitions to failure would be nearly similar; whereas the potential damage could lead up to a 20% increase for the tire with higher tire-inflation pressure based on the domain analysis.

On one hand, the CRS increment for $ACD2$ of the DTA with differential tire-inflation pressure was 14% greater than the reference DTA (Figure 3.16b). On the other hand, $ACD1$ CRS for the differentially inflated DTA was less than 1.0 due to the 27% decrease of tire-inflation. Additionally, combining the critical zones into the weighted sum dilutes the localization of stresses and strains (Figure 3.16c). Therefore, secondary partitioning of the domain analysis ($ACD1$ and $ACD2$) allows to distinguish the influence of each tire on multi-axial pavement responses.

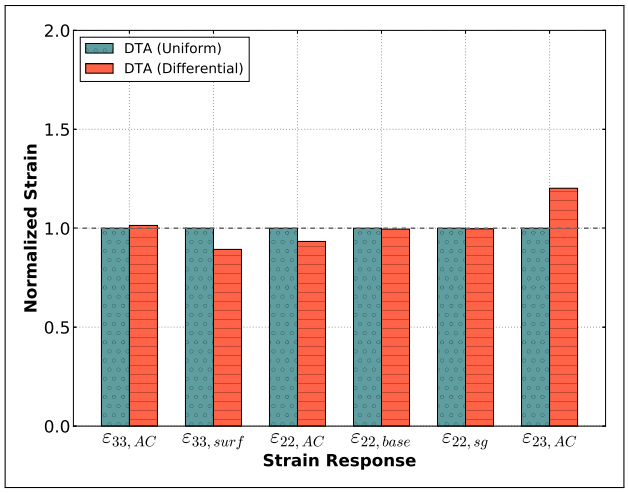

(a) Critical strain responses.

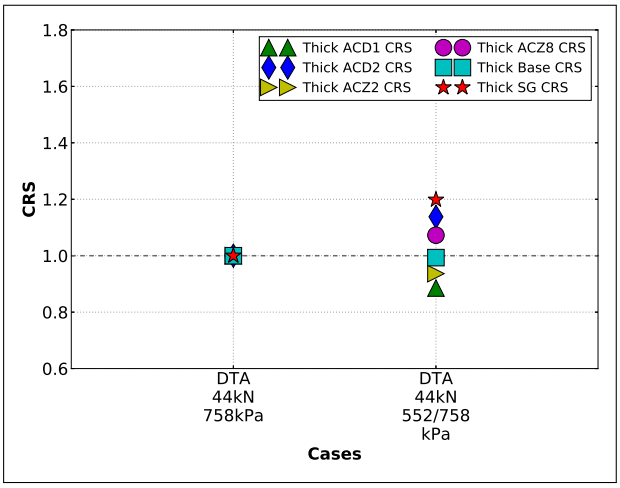

(b) Cumulative stress ratios of individual critical zones within the thick thin pavements.

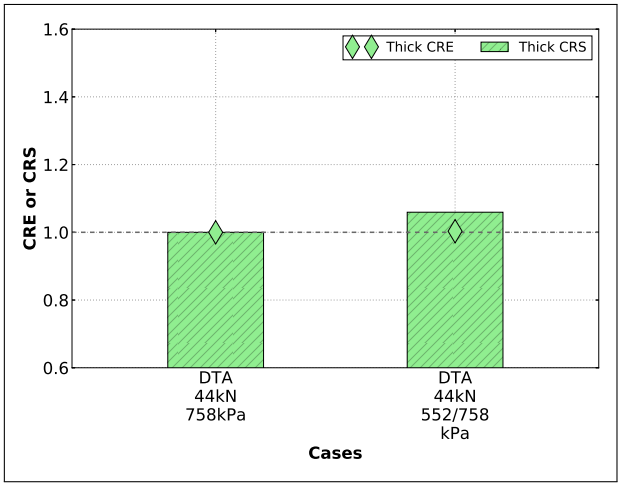

(c) Weighted sum of critical zones within the thick pavement.

Fig. 3.16. Critical strain responses and domain analysis ratios for Case III considering DTA with differential tire-inflation pressures.

3.6 Summary

Domain Analysis is designed to assess the pavement structure in three dimensions and to provide a more comprehensive assessment of the stresses and strains imposed by tires on pavements. Given that a pavement fails due to bulk weakening rather than a damage at one point, in the case of fatigue cracking and rutting, this new approach considers the bulk pavement damage potential induced by 3D and non-uniform contact stresses. The implementation of Domain Analysis is comprised of four major steps: calculation of multi-axial responses using advanced FEM, identification of critical zones in the pavement, comparison of responses with respect to a failure criteria, and computation of a scalar to

represent the load demand on a given pavement structure.

This dissertation provided an opportunity to test the capabilities of Domain Analysis through three loading scenarios. First, after analyzing a thick pavement subjected to experimentally measured contact loads of NG-WBT and DTA, the new method was able to capture the complex and asymmetric pavement response distribution. The steer tire, typically accounted for with a lower load distribution factor relative to trailer axles, resulted in a higher damage potential in comparison to the DTA at near-surface due to higher contact stresses. Second, using numerically-generated contact stresses, it was observed that many of the critical point responses of typical thin and thick pavements were not significantly influenced by the tire-inflation pressure, while Domain Analysis estimated an increase of approximately 17% in the damage potential when tire-inflation pressure was increased from 480 to 830 kPa. Finally, based on loading a thick pavement structure with differentially inflated DTA (from experimental measurements), Domain Analysis captured the greater propensity of the higher inflated tire to potentially lead to higher damage, whereas single-point responses cannot effectively capture this multi-axial difference. A direct implication of similar single-point strains is the inability to properly predict damage; in the MEPDG scheme, the resulting number of repetitions to failure via transfer functions would be indistinguishable. Moreover, near-surface behavior is unaccounted for by the currently established transfer functions.

Domain analysis can serve as a computationally efficient method for analyzing the impact of multi-axial tire-pavement contact stresses on pavement responses. Particularly, it effectively quantified complex details at the near-surface region, which are predominantly governed by contact stress distribution. The applicability of the Domain Analysis method could easily extend to other pavement structures, tire types and configurations, and loading conditions; along with considering other failure criteria.

CHAPTER 4

INFLUENCE OF AIRCRAFT TIRE TURNING MANEUVER ON PAVEMENT RESPONSES

4.1 Introduction

In flexible airfield pavement design, two critical distresses are considered: asphalt fatigue cracking and subgrade rutting [58]. These distresses are linked to strain responses at the bottom of the asphalt concrete (AC) layer and at the top of the subgrade, respectively. Using transfer functions, pavement damage is evolved over the prescribed design life. The output provides the number of loading repetitions to failure before structural capacity is reached; however, accuracy of the prediction is limited by the scope of the data bounding the transfer functions. New tire designs, new pavement technologies, aircraft load and configurations, and other innovative solutions may not be appropriately considered in the current design approach. A recent study on highway flexible pavements using truck tires reported that a change in the tire-inflation pressure produced a minimal change in the critical strains [59]. Hence, without differences in strains, the same level of pavement damage would be reached by two distinctly different loading conditions.

For aircraft tires, high magnitudes of applied loads are transferred to the pavement through tire-pavement contact. At this localized interface, three-dimensional (3D) and nonuniform contact stresses govern the response within the near-surface region. During taxiing, a fully loaded aircraft induces high levels of shear, typically within 50 to 100 mm from the surface. Furthermore, current airfield pavement design schemes inadequately account for potential near-surface damage, including shoving and slippage cracking. Per the Federal Aviation Administration (FAA) Advisory Circular 150/5380-6C, slippage cracks within flexible pavements arise due to high shear stresses imposed by braking or turning maneuvers of aircraft tires. A combination of high shear tire-pavement contact stresses and low shear resistance (or a poor interfacial bond) of pavement materials may lead to slippage and the formation of crescent-moon-shaped cracks with ends pointing away from the traffic direction [60].

In 2002, a high-speed exit on landing runway (4R-22L) at the Newark International

Airport experienced slippage failures due to high trafficking of airplanes, landing, and traversing the runway during summer months [61]. With increased ambient temperature, AC deforms more severely, directly impacting the layer's shear resistance. Song and Garg [62] found that increased aircraft tire-inflation pressure and high temperature conditions further exacerbated potential damage at near-surface. Observations of slippage cracking at the Newark International Airport runway were verified by a recent instrumentation project (on the lead line from runway to high-speed exit) by Cook et al. [63]. The authors reported that areas experiencing high repetitions of braking and turning exhibited interfacial delamination and rapid deterioration. Exceeding the AC shear strength at the near-surface region may pose a major safety concern. To reduce the risk of slippage at near-surface, appropriate pavement and lift designs must be adequate to ensure dissipation of high shear forces [61, 64]. Hence, it is imperative to understand the critical combination of loading and environmental conditions that affect near-surface damage.

4.2 Research Objective

In this research, the near-surface response of airfield pavements due to aircraft tire turning conditions was quantified using advanced numerical modeling. The analysis included comparison of critical strains per FAA flexible pavement design procedure. In addition, the Domain Analysis method was implemented to evaluate the 3D pavement bulk response.

4.3 Analysis Matrix

4.3.1 Tire-Pavement Contact Stress under Turning Conditions

Tire-pavement contact stresses for a single tire of an A-380 aircraft landing gear were represented as 3D and non-uniformly distributed within a predefined contact area [65, 11, 66, 67]. Following the protocol by Hernandez and Al-Qadi [66], aircraft tire-pavement contact stresses under free-rolling conditions are generated. For the contact area, the width and length dimensions are assumed 320 and 560 mm, respectively. A total of five ribs were considered: two 70-mm outer ribs, one 90-mm middle rib, and two intermediate 45-mm ribs.

As the aircraft tire turns, the slip angle defines the difference between the actual direction of rolling tire and direction in which the tire is pointing. Inherently, the maneuver results in

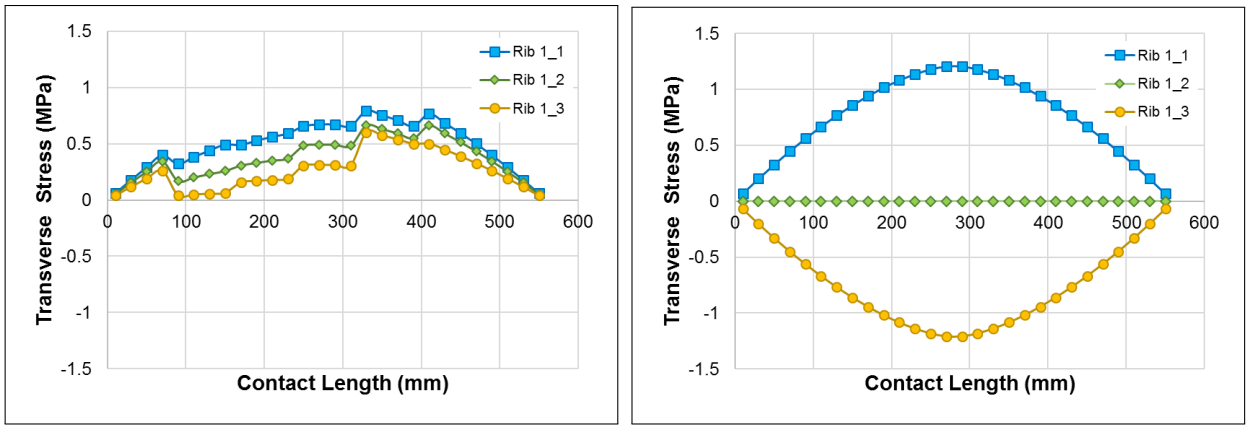

(a) Free-rolling. **(b)** Turning maneuver.

Fig. 4.1. Sample transverse contact stresses under free-rolling and turning maneuver.

a lateral shift of forces toward the inner edge of the turn. Hence, contact stress distributions become asymmetric due to the shift in loading. Utilizing the relationship found between contact stresses under various rolling conditions of a validated truck tire model [12], turning ratios were generated. Figure 4.1 presents the influence of turning on sample transverse contact stresses within the rib nearest to the point of turn.

It was imperative to ensure that equilibrium is maintained during maneuvering; such that the summation of resultant load within the footprint equates to the applied load. Figure 4.1 presents the load distribution within each tire rib as the tire rolling condition is altered from free-rolling (FR) to turning (with slip angles of 2°, 4°, and 6°). Figure 4.2a illustrates the transfer of load from one rib to another, while achieving equilibrium. Not only is the lateral shift in load evident along the vertical direction, but also along the transverse and longitudinal directions. Figures 4.2b and 4.2c reveal a lateral shift of the cumulative shear contact stresses toward the inner edge of turning. It is worth noting that the cumulative transverse contact stresses under free-rolling is zero due to symmetry. However, under the turning maneuver, the contact stresses increase with the slip angle due to the asymmetry.

In this dissertation, 12 loading scenarios considered an applied tire load of 262 kN with varying tire-inflation pressures, velocities, and slip angles. The nomenclature used to identify each load case is as follows:

- Tire-inflation pressure (S): $S1 = 1.45$ MPa, $S2 = 1.69$ MPa;
- Velocity (V): $V1 = 8$ kph, $V2 = 20$ kph; and
- Slip angle (FR): $FR2 = 2°$ and $FR4 = 4°$.

Given that the free-rolling condition is defined by a slip angle of 0°, the FR variable is omitted from the load case designation. For example, considering a tire-inflation of 1.45

MPa and free-rolling speed of 8 kph, the load case name is $S1V1$.

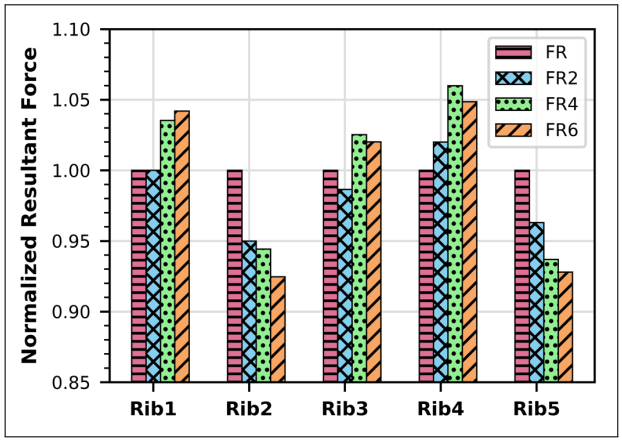

(a) Normalized resultant vertical load.

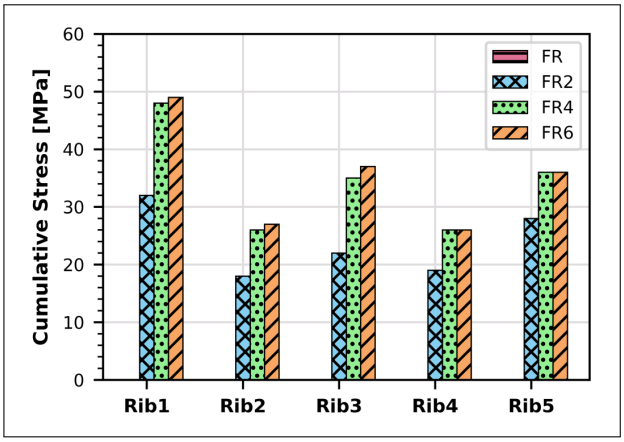

(b) Cumulative transverse contact stresses.

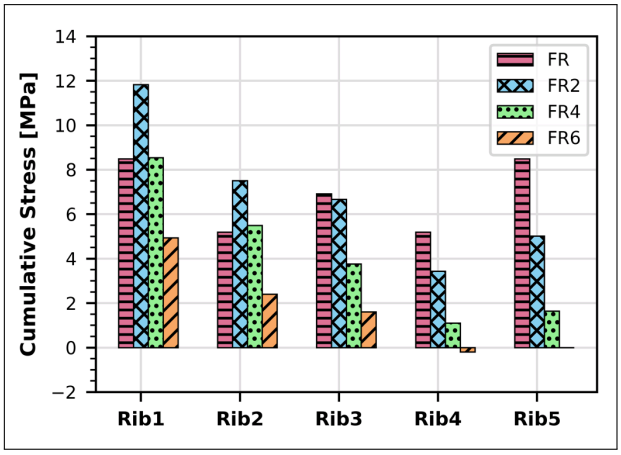

(c) Cumulative longitudinal contact stresses.

Fig. 4.2. Overall influence of turning on aircraft tire-pavement contact loads/stresses.

4.3.2 Airfield Pavement Structures

The generated database of continuously moving A-380 single tire load was simulated over two airfield pavement structures. First, a National Airport Pavement Test Facility (NAPTF) flexible pavement (previously constructed in the High Tire Pressure (HTP) test area) consisted of 125 mm AC (P401), 200 mm crushed stone base (P209), 150 mm Econocrete (P306), and 810 mm uncrushed stone (P154) over subgrade [62]. For consistency, the material designations used in this dissertation follow FAA design guidelines [58]. Notably, the HTP section may not be constructed at airport facilities per FAA Advisory Circular; however, it was built at NAPTF to allow for high temperature testing. Second,

from the recent NAPTF Construction Cycle 7 (CC7), the LFP4-N test section represented a conventional flexible airfield pavement [68], wherein a select number of load cases were simulated onto the LFP4-N pavement structure. The LFP4-N pavement comprised of 200 mm AC and 1025 mm uncrushed stone base over subgrade.

The AC was assumed as a linear viscoelastic material, while the supporting layers below the crushed stone base were characterized as linear elastic. On the contrary, a nonlinear, isotropic, and stress-dependent material model was considered for the crushed stone base layer to account for the influence of high stress levels induced by the A-380 landing gear tire. For the LFP4-N test section, stress-dependent material properties for the subgrade, provided by FAA, were used within the pavement finite element (FE) model. Additionally, the developed FE model considered a continuously moving load, temperature profile within the AC layer, interface properties, and infinite boundary elements to represent far-field behavior [69, 27, 57, 70, 71, 72]. Details of the pavement model for the HTP test section, including material characteristics and mesh sensitivity analysis can be found elsewhere [67]. The same model preparation scheme was implemented for the LFP4-N pavement structure to ensure optimum mesh configuration while balancing computational effort and accuracy.

4.4 Results and Discussion

To determine the influence of the turning maneuver of an A-380 aircraft tire on pavement responses, two analysis approaches were completed. The first approach coincides with the conventional use of critical strains at predetermined locations: tensile strain at the bottom of the AC and vertical strain on top of the subgrade. Per FAA design methodology, these responses control bottom-up fatigue cracking and secondary rutting, respectively. Domain Analysis was also used to account for multiaxial stress and strain states within the pavement model via a single scalar parameter. Recent applications of the Domain Analysis include truck and aircraft tire loading under free-rolling conditions [59, 73].

4.4.1 Point Responses

Congruent to traditional pavement analysis, maximum strains at critical locations were obtained from the pavement model output database, including, tensile strains within the surface and bottom region of the AC layer, shear strains within each pavement layer, and vertical strains within each pavement layer. In particular, the tensile strain at the bottom of the AC ($\varepsilon_{11,ac}$) and vertical strain on top of the subgrade ($\varepsilon_{22,sg}$) were obtained. In addition,

surface strain ($\varepsilon_{33,sf}$), shear strain within the AC ($\varepsilon_{23,ac}$), which affect near-surface cracking; and vertical compressive strain within each layer, which is associated with rutting ($\varepsilon_{22,ac}$, $\varepsilon_{22,P209}$, $\varepsilon_{22,P306}$, $\varepsilon_{22,P154}$), were also analyzed.

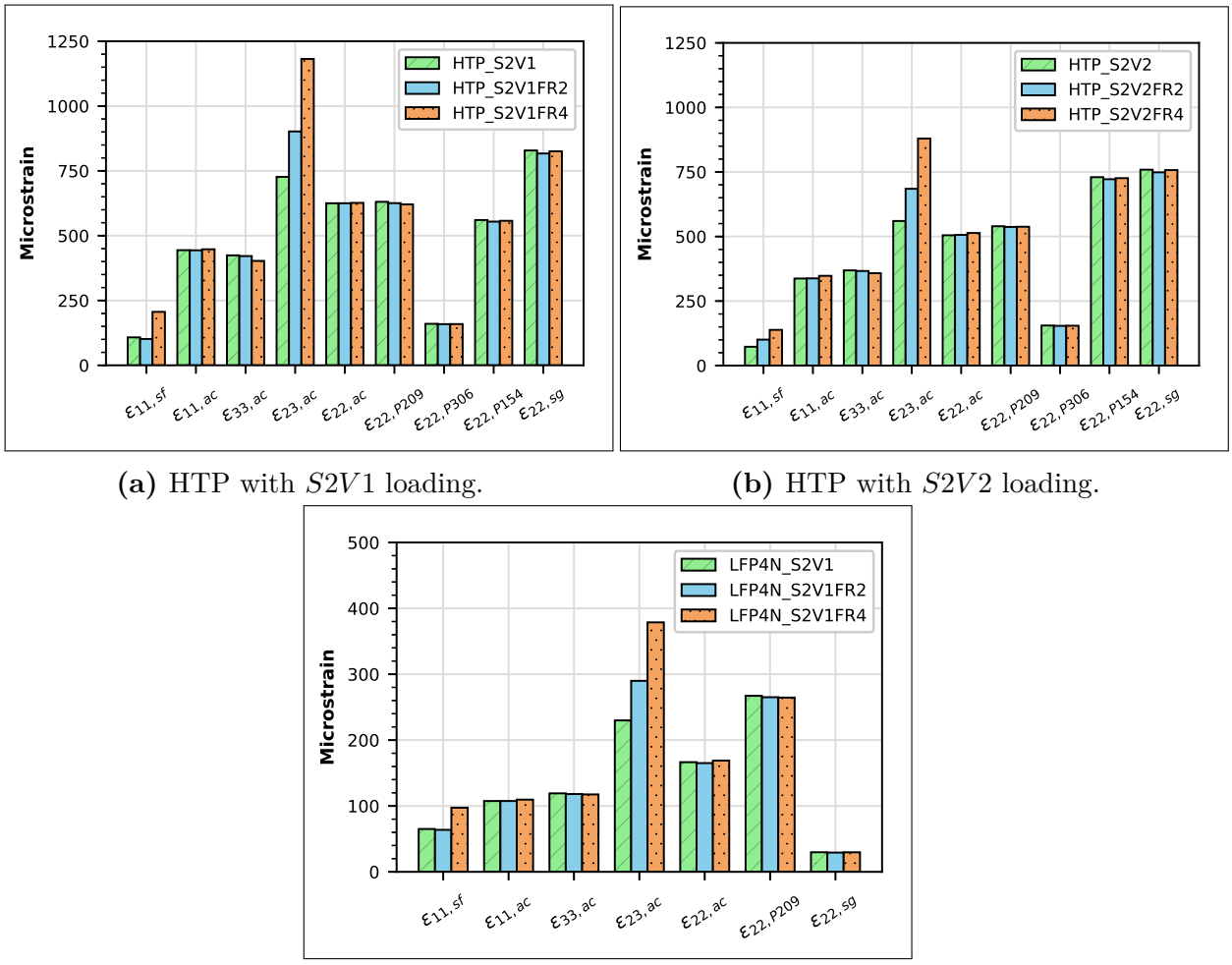

(a) HTP with $S2V1$ loading.

(b) HTP with $S2V2$ loading.

(c) LFP4-N with $S2V1$ loading.

Fig. 4.3. Critical strains at point locations of HTP and LFP4-N pavement simulations.

Figure 4.3 illustrates the effect of an aircraft tire's turning maneuver on critical strains. Note that each bar type represents a combination of pavement structure (HTP or LFP4-N), tire-inflation pressure, speed, and slip angle. For example, $HTP_S1V1FR2$ denotes that the HTP section is loaded with a moving A-380 tire at an inflation pressure of 1.45 MPa, a speed of 8 kph, and a slip angle of 2°. For both HTP and LFP4-N pavement structures, critical strain values were minimally influenced by the turning maneuver as $\varepsilon_{11,ac}$ and $\varepsilon_{22,sg}$ revealed a negligible change; less than a 5% difference from the free-rolling condition (zero slip angle). Given the $\varepsilon_{11,ac}$ and $\varepsilon_{22,sg}$ values, the predicted damage would be similar despite the difference in loading conditions. On the other hand, near-surface strains, i.e. $\varepsilon_{33,sf}$ and

$\varepsilon_{23,ac}$, increased as much as 91%, suggesting the impact of tire maneuvering within near-surface of the AC layer. This finding aligns with the fact that near-surface region is directly influenced by tire-pavement contact stresses. Unfortunately, the current airfield pavement design method does not consider near-surface damage.

4.5 Domain Analysis

In lieu of point strains, Domain Analysis quantifies the full influence of tire-pavement contact stresses within a loaded pavement model by considering multiaxial stresses and strains. Realistically, pavement damage is driven by the combined influence of shear and hydrostatic, whereas point strains describe pavement behavior at specific locations and directions.

The recently developed analysis scheme includes four main steps: i) calculation of multi-axial stress and strain states; ii) discretization of the pavement to identify critical zones; iii) comparison of stress and strain states relative to the failure criteria; and iv) combination of the damage potential from selected critical regions to generate a unitless scalar called cumulative ratio. Extensive details of Domain Analysis can be found in Chapter 3. A summary of the modeling assumptions and limitations is tabulated in Appendix A.

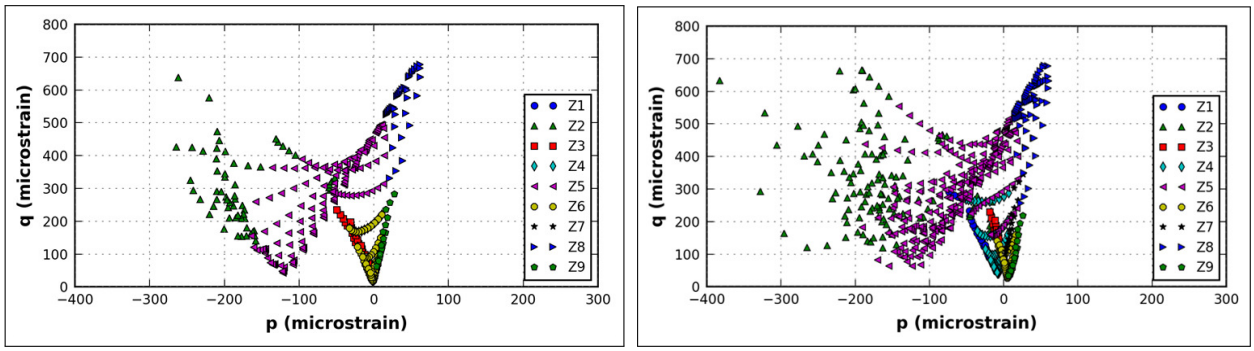

(a) HTP with $S2V1$ loading. **(b)** HTP with $S2V1FR4$ loading.

Fig. 4.4. p-q diagrams of the AC layer comparing free-rolling and turning maneuver.

The highest levels of shear and compression were observed within the near-surface region ($Z2$) of the AC layer due to direct interaction of a rolling aircraft tire with the flexible pavement surface (Figure 4.4). Particularly, the point cloud of $Z2$ defines the combination of shear and compression and is exacerbated as a turning maneuver occurs (Figure 4.4b). Moreover, the impact of turning further propagates into the middle zone ($Z5$) as one could observe a greater spread of p-q coordinates. In this dissertation, Domain Analysis was

focused on the near-surface zone related to near-surface cracking and rutting, and bottom zone ($Z8$) of the AC related to bottom-up cracking. Moreover, the top zone ($Z2$) of each supporting layer was included to determine rutting susceptibility.

4.5.1 Domain Analysis Ratios

For each critical zone, the cumulative ratios, CRS and CRE, within selected critical zones were calculated. Two groups were created to categorize the loading cases per traveling speed. Each group utilized a reference case, which considered low tire-inflation pressure ($S1 = 1.45$ MPa) and free-rolling condition. Inherently, the ratios define the increase or decrease in damage potential relative to the reference case.

4.5.2 HTP Test Section

Considering a high tire-inflation pressure ($S2 = 1.69$ MPa) and low speed ($V1 = 8$ kph) on an inverted pavement, a shift in q values within the AC layer is clearly influenced by the gravity of turning. Figure 4.5 illustrates the change in shear values as the slip angle increases from a free-rolling condition to a critical slip angle of 4°, per aircraft manufacturer recommendations. This indicates that the inner point of turn is expected to have the highest propensity for slippage cracking (in the presented example, this region is within 50 mm distance to the right of the tire edge).

Furthermore, the asymmetric behavior propagates deeper into the AC layer within the middle zone $Z5$. Two new parameters are introduced to capture the influence of aircraft tire load up to 100 mm depth by partitioning $Z2$ and $Z5$ into two regions (Figure 4.5c). The combination of the right halves of the top and middle zones are designated as $ACD1$, whereas the left haves are named as $ACD2$.

Expanding the analysis into the 3D domain, the resulting CRS and CRE values consider the change in the p-q distribution along the traveling direction. Figure 4.6 presents the cumulative ratios within critical zones of the AC layer ($Z2$, $Z8$, $ACD1$, and $ACD2$). The near-surface AC region, $Z2$, experienced an increase in CRE as the aircraft tire turned with a higher slip angle. Moreover, the CRE approximately doubled, in contrast to the $S1V1$ case, as the loading condition considered an increase of tire-inflation pressure by 17% and the most severe turning condition, $S2V1FR4$ (Figure 4.6a). The disparity between $ACD1$ and $ACD2$ ratios also became apparent as the slip angle increased, which alluded to the load shift during a turning maneuver. Although this is also evident within the

top and bottom zones ($Z2$ and $Z8$, respectively), volume averaging within the entire zone diminishes the asymmetric pavement behavior that was clearly captured by $ACD1$ and $ACD2$ ratios.

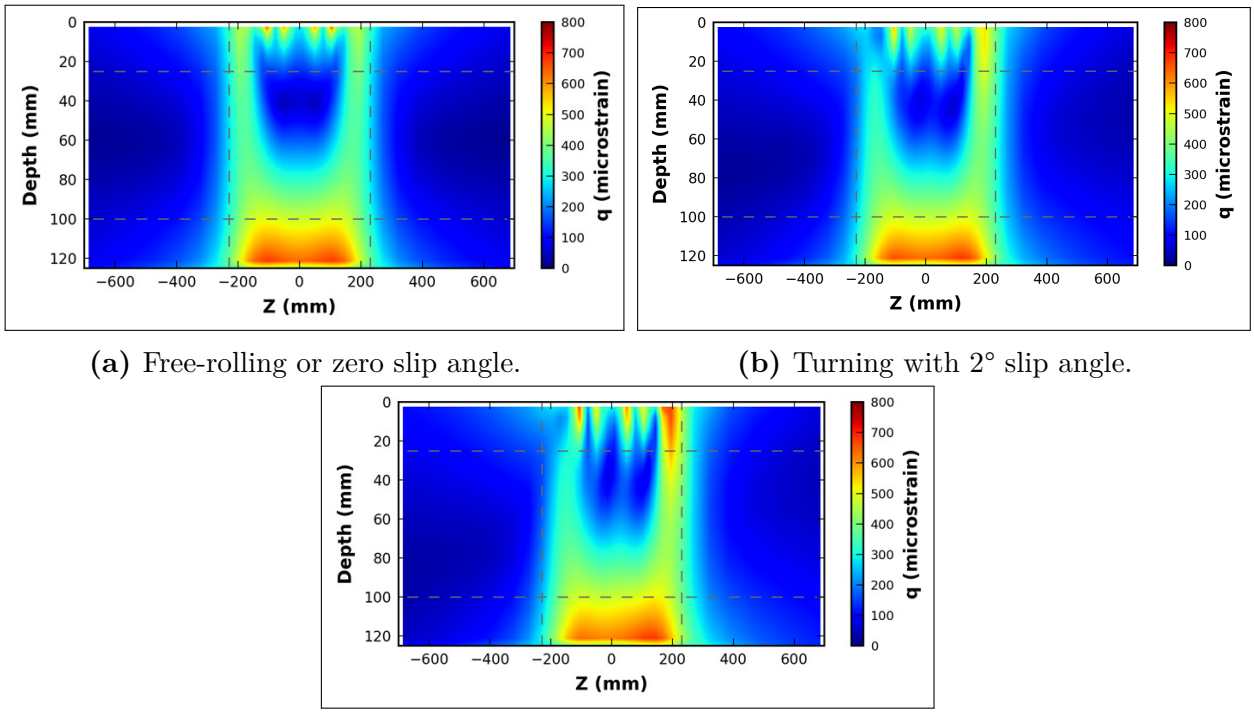

(a) Free-rolling or zero slip angle.

(b) Turning with 2° slip angle.

(c) Turning with 4° slip angle.

Fig. 4.5. q contour along the AC layer depth of the HTP test section considering $S2V1$ with varying turning conditions.

The corresponding CRS values followed similar trends, as illustrated in Figures 4.6c and 4.6d; however, the ratios were noticeably lower than the CRE. The disparity between the stress and strain states was attributed to the nonlinear pavement behavior and the fact that the 125-mm AC layer experienced large deformations at relatively low stress levels. This trend was also observed within the bottom zone $Z8$ and followed a monotonic increase in the CRS values of $Z2$ as the turning maneuver became more severe and the tire-inflation pressure increased.

As the depth of analysis increased, the turning maneuver induced CRE and CRS increments up to 7.5% within the supporting layers below the AC (i.e. crushed stone base, Econocrete, uncrushed stone base, and subgrade). Similar influence of the turning maneuver, tire-inflation pressure, and tire speed within the AC layer was observed for the supporting structure; this was, however, at a lower extent. Hence, this finding confirms the fact that the influence of tire-pavement contact stresses diminishes with increasing

pavement depth.

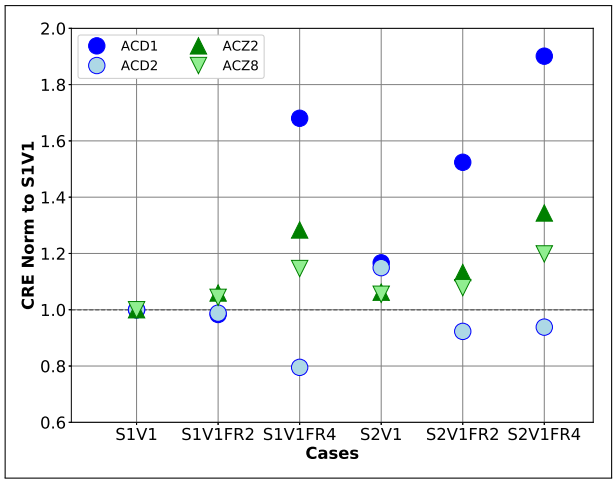

(a) CRE for HTP cases with $V1$.

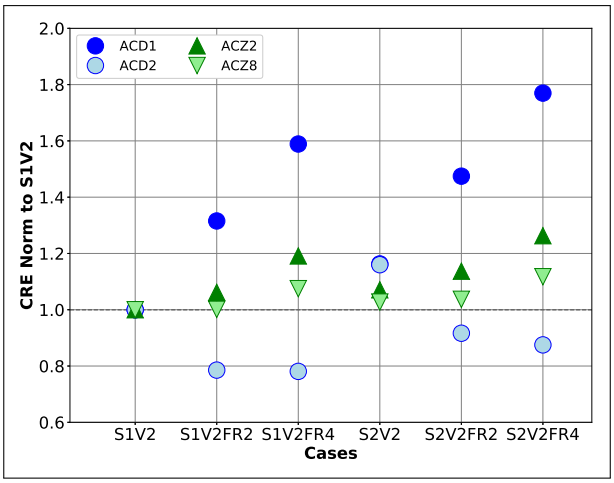

(b) CRE for HTP cases with $V2$.

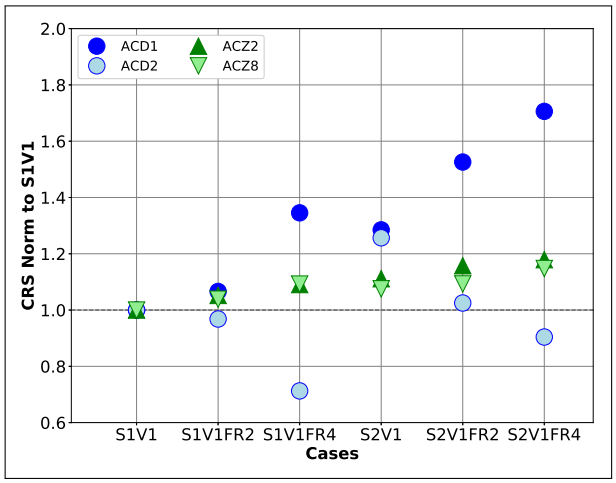

(c) CRS for HTP cases with $V1$.

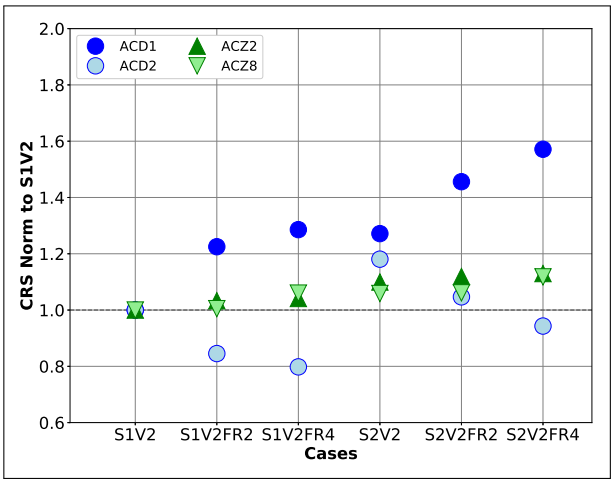

(d) CRS for HTP cases with $V2$.

Fig. 4.6. Domain Analysis ratios for HTP pavement simulations.

4.5.3 CC7 LFP4-N Test Section

A select number of loading cases within the numerical matrix was applied onto a conventional flexible pavement structure, LFP4-N, to understand the implications of tire turning maneuver on a realistic airfield pavement. As anticipated, the near-surface region ($Z2$) of the AC layer was significantly influenced by the turning maneuver due to a clear increase in the CRE and CRS values as the slip angle increased (Figure 4.7). Relative to the reference case $S1V1$, the worst turning condition of 4° slip angle influenced both near-surface regions, $ACD1$ and $ACD2$. Considering the LFP4-N pavement and $S2V1FR4$ loading, the strain

domain $ACD2$ ratio resulted in 1.078, contrast to CRE of 0.938 when the HTP pavement is analyzed. As the critical level of turning was reached for a conventional flexible airfield pavement, the lateral shift in contact stresses not only impacted the near-surface region closest to the turning point but also the opposing region ($ACD2$). This finding may be used in designing AC layers that would adequately resist high levels of shearing stresses induced by heavy aircraft loads.

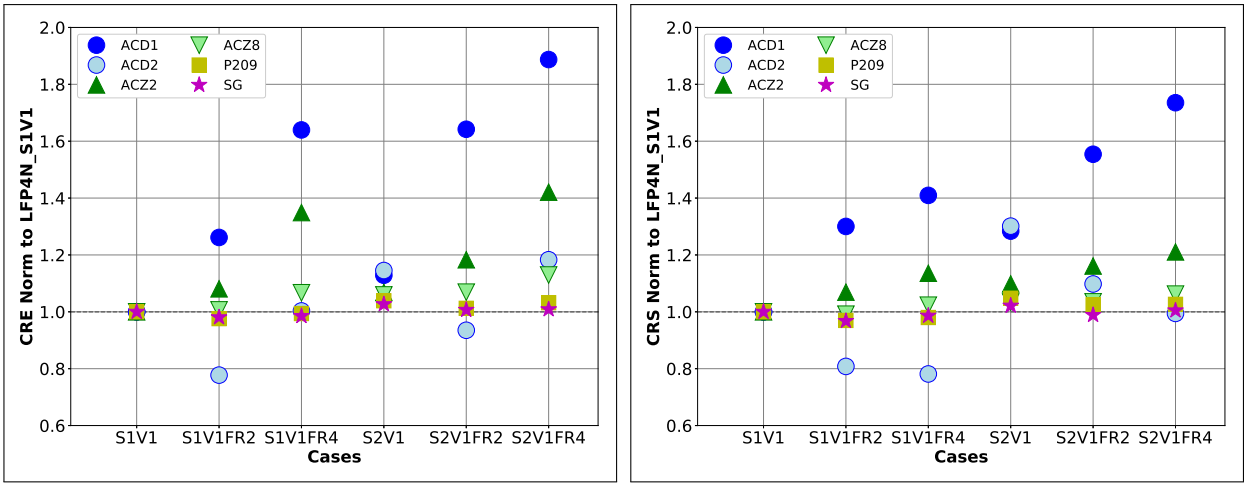

(a) CRE for LFP4-N cases with $V1$. **(b)** CRS for LFP4-N cases with $V1$.

Fig. 4.7. Domain Analysis ratios for the LFP4-N pavement simulations.

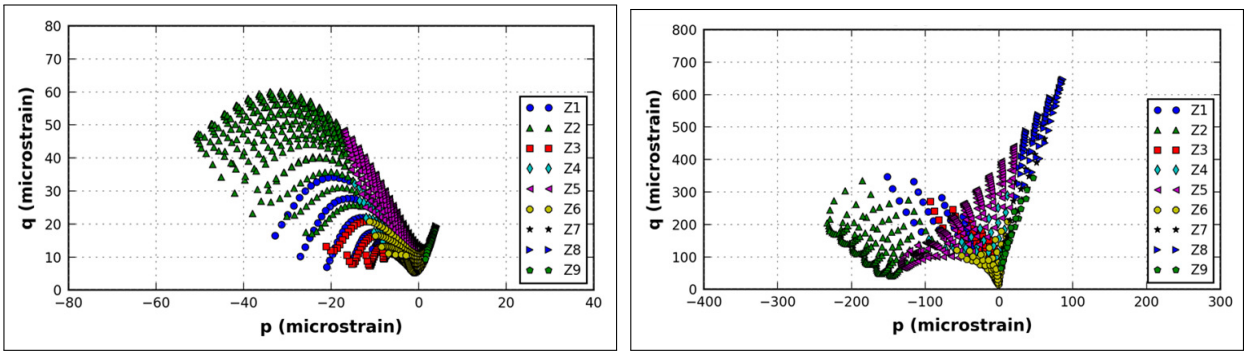

(a) HTP pavement section. **(b)** LFP4-N pavement section.

Fig. 4.8. p-q diagram of the crushed stone base layer.

Although the ratios for the critical zones of the granular base layer and subgrade remained close to unity in Figure 4.7, their multiaxial behavior differed significantly from the HTP pavement structure. Figure 4.8 illustrates the disparity in point cloud behavior of the stress-dependent granular base, directly underneath the AC layer, between the two pavement structures. Figure 4.8a illustrates a higher sensitivity to tension for the HTP section,

whereas Figure 4.7b revealed a more significant combination of shear and compression for the LFP4-N section. Domain Analysis presents an in-depth investigation of pavement behavior using the p-q plots, though the CRS and CRE values showed minimal damage relative to the reference case. Naturally, a granular base layer from the two pavement structures would experience distinctly different paths to damage.

4.6 Summary

Bottom-up cracking within the AC layer and rutting within the subgrade govern airfield pavement design and analysis. For inverted and conventional airfield flexible pavement, surface tensile and shear strains within the near-surface region of the AC layer are highly affected by the turning maneuver of aircraft tires. Given the current design protocol, any potential near-surface damage may neither be quantified nor analyzed.

For instance, cases of slippage cracking, driven by high levels of near-surface shear, impose significant safety issues for an active airport. One of the major drawbacks of relying on single-point strains is that the structural evaluation is narrowed down only to a specific location and direction. Pavement damage generally nucleates within a given region of influence and not solely at a single point. Hence, in lieu of point strains, bulk damage warrants a more extensive analysis to quantify the full influence of tire-pavement contact stresses, which has the highest impact at the near-surface region. Domain Analysis characterizes damage potential by accounting for multiaxial stresses and strains within a 3D subdomain. One of the useful applications of Domain Analysis is characterizing damage potential at the near-surface, precisely where tire-pavement contact stress has the highest influence.

Inherently, the turning maneuver of the A-380 tire did not change the total load applied onto the pavement structure. However, the distribution of the contact stresses was impacted and that a direct implication on pavement responses. The p-q contours and domain ratios captured that an asymmetric stress excitation not only induced asymmetric behavior but also promoted an increase of combined shear and compression at near-surface. In particular, an increased potential for damage within the near-surface region could be due to the turning maneuver of a heavy aircraft tire. Hence, special attention in the design of turning areas is needed to ensure desired pavement performance and safe use of airports.

CHAPTER 5

THERMOMECHANICAL COUPLING OF A HYPER-VISCOELASTIC TRUCK TIRE AND A PAVEMENT LAYER AND ITS IMPACT ON THREE-DIMENSIONAL CONTACT STRESSES

5.1 Introduction

As a loaded tire traverses over a pavement surface, distortions within the tire produces deformation cycles, often associated with local heat generation. Approximately 60% of the total hysteretic loss is due to the direct contact of tire treads with the pavement surface [74]. The two primary mechanisms of a tire's rolling loss are convection between inside and outside surfaces of the tire and conduction between the tire and the pavement surface. Due to the complex tire structure, temperature variations exist throughout. Thus, certain locations tend to dissipate heat more than others.

Three regions are typically considered on a rolling tire during thermal analysis. The first region is designated for most of the contact patch between the tire treads and pavement surface, except the initial treads that experience a change in velocity upon entering the tire-pavement contact patch. This first region accounts for the frictional heat generated due to sliding motion. The second region accounts for the remainder of the tire that is not in contact with the pavement, but experiences convective heat transfer with air. The third and final region includes the area where tire treads initially contact the pavement surface and transfer heat to the road. Earlier studies have determined that the heat transfer coefficient between the tire and the air was greater than that between the tire and the road [75]. Allen et al. suggest that heat loss to the outside surface of a numerical tire model was insubstantial, due to low temperature differences between the element temperature and the external air temperature [76]. Rolling conditions, however, have a significant impact on the heat transfer. A rolling tire tends to be hottest within the inner surface, whereas a skidding tire is hottest at the outer surface. This finding indicates that the frictional energy tends to dissipate within the thin layer closest to the surface. During rolling, the outer tire temperature is near the pavement temperature and increases with skidding [77].

The basic assumption of phenomenological distortion models is that complex stress and strain cycles can be attributed to basic distortion mechanisms. This approach, however,

neglects thermal effects on the local rates of energy dissipation [78]. At the same time, a predominantly thermal model can effectively consider the relation of the hysteretic loss to viscoelastic and tire deflection, but it fails to capture the interaction between the thermal and mechanical states of the tire [79, 80].

Prevorsek et al. [81] related tire-rolling resistance to the total heat loss using theoretical and experimental programs, but the model could not yield information regarding the tire-strain field. Futamura and Goldstein [82] created a deformation index as a measure of the cyclic strain energy sensitivity to changes in material stiffness, with the goal of simplifying the coupled thermomechanical analysis. Rao et al. [83] performed a three-stage, finite-element analysis consisting of a deformation, dissipation, and thermal models to determine the influence of groove-tread patterns, rolling speed, tread profile, inflation pressure, normal load, and ambient temperature on rolling resistance.

Li and his colleagues [84] evaluated two extreme ambient temperature conditions to simulate the winter and summer seasons. Their results revealed that the tire temperature rose linearly with the increase of ambient temperature and that the highest compaction at the tread on the contact zone occurred during the summer. Another study investigated the effect of pavement, ambient, and contained air temperatures on the tire-pavement frictional behavior. Anupam et al. [85] determined that higher temperatures resulted in lower hysteretic friction and that the pavement with a higher macrotexture resulted in a higher energy dissipation, which resulted in a higher hysteretic friction.

Present models that analyze coupled mechanical and thermal simulations generally use the Arbitrary Lagrangian Eulerian framework. Behnke and Kaliske [86] formulated a sequentially coupled solution scheme, wherein the mechanical module assumes a constant temperature, and the thermal module assumes constant deformation. The authors considered a viscoelastic, non-equilibrium response of the rubber compounds and rotation-induced inertia forces of the rolling tire. In addition to investigating the effect of tire temperature and pavement surface texture, Sriangram et. al. [87] developed a framework that considered tire-slip ratio on hysteretic friction.

Although there is a clear trajectory of advancements in tire and pavement modeling, current considerations of the tire-pavement interaction are still lacking. Often, one of the two contributing systems to the interaction is simplified. Given that loading and environmental conditions are the main drivers of pavement responses along pavement structural characteristics, this dissertation provides a means to quantify and evaluate the potential implications of thermomechanical coupling on contact stresses for pavement structures.

5.2 Coupled Thermomechanical Analysis

Heat transfer is comprised of three basic mechanisms – conduction, convection, and radiation. Understanding the overall response at the tire-pavement interface due to thermomechanical coupling requires appropriately accounting for heat transfer modes. Conduction refers to the transmission of internal energy due to molecular collision and diffusion between neighboring particles, given the presence of a temperature gradient. Fourier's law (shown below in Equation 5.1) describes heat conduction, wherein the negative sign accounts for the heat flow from a higher to lower temperature.

$$\mathbf{q} = -k\nabla\theta \tag{5.1}$$

Here $\mathbf{q}$ is the heat flux, k is the thermal conductivity, and $\nabla\theta$ is the temperature gradient.

On the contrary, convection considers the advection and diffusion processes, which usually describes the dominant form of heat transfer in fluids. Compared to conduction, convective heat transfer may be difficult to assess due to its unpredictable nature. As a fluid passes over a solid, the movement can be categorized as a forced or natural convection. Natural convection accounts for warmer air rising through buoyancy, whereas forced convection constitutes a controlled movement of the fluid. Contrasting to the first two modes of heat transfer, radiation describes the energy transfer due to electromagnetic waves. In this dissertation, radiation is not considered because conduction and convection are assumed to govern tire-pavement behavior.

Heat flux through a material is determined by imposing temperature at the boundary of elements or a body. Generally, the exterior temperatures are unknown; however, temperatures surrounding the body are known and can be designated as thermal-boundary conditions. The prescribed heat flux on the surface due to convection is governed by Newton's Law of Cooling, which postulates that the surface flux in convection is directly proportional to the temperature difference between the surface and the streaming fluid.

$$\mathbf{q} = h(\theta - \theta_0) \tag{5.2}$$

Here in Equation 5.2, h, is the heat transfer coefficient (or the constant of proportionality), θ is the surface temperature, and θ_0 is the reference sink temperature.

The governing equations for a coupled thermomechanical analysis are comprised of solving the equations of energy and momentum conservation. The energy balance is defined

by Equation 5.3:

$$\rho C_p \frac{\partial \theta}{\partial t} + \nabla \cdot \mathbf{q} - \dot{Q} = 0 \tag{5.3}$$

where ρ is the density, C_p is the specific heat, and $\dot{Q}$ is the volumetric heating rate. Momentum conservation is prescribed at each time increment using Cauchy's equation as shown in Equation 5.4.

$$\nabla \cdot \sigma + \rho \mathbf{f} = 0 \tag{5.4}$$

Here σ is the Cauchy stress tensor and $\mathbf{f}$ is the body force per unit mass. The displacement vector $\mathbf{u}$, is the solution variable that is related to the stress field via kinematic and constitutive relations.

Considering the interface between the tire and pavement bodies, a mechanical contact is enforced to ensure a non-penetration condition. Moreover, the heat transfer between the two is imposed through gap conductance, wherein the thermal conductivity between the two surfaces activates at zero clearance or a closed gap. As the clearance between the tire and pavement surfaces surpasses a user-specified minimum value, the conductivity value, k, immediately drops to zero; thereby terminating heat conductance.

5.3 Tire-Pavement Model

Capturing the realistic behavior of truck tires due to the coupled influence of loading and temperature conditions requires additional considerations, including viscoelasticity, thermal properties and boundary conditions, and appropriate element and analysis types. Earlier work for the interaction model between the truck tire and pavement considered a steady-state transport analysis of a hyperelastic tire on an analytically rigid surface [88].

5.3.1 Material Characterization

Rubber is a hyper-viscoelastic material, which is subjected to cyclic loading, such as rolling the tire. The viscous components impose a lag on the material recovery. In this scenario, rubber tends to absorb more heat than it can dissipate. The lost energy, or heat stored, in the rubber is defined as the hysteretic loss. If the material is assumed to be elastic, the viscous component is ignored. This would then require a separate, explicit behavior to account for the hysteretic loss. Building on the calibrated hyperelastic tire model, a dynamic mechanical analysis (DMA) was conducted at a private laboratory to determine the viscoelastic characterization of various sections of the tire (see Figure 5.1).

The laboratory results were used to generate the Prony series parameters, $\bar{g}_i$ and $\bar{k}_i$, and the William-Landel-Ferry (WLF) coefficients,$C1$ and $C2$, and appended to the Mooney-Rivlin constants to characterize rubber as a hyper-viscoelastic material (see Table 5.1). Moreover, the steel reinforcement, such as beads, belts, and plies, were assumed to be linear elastic properties.

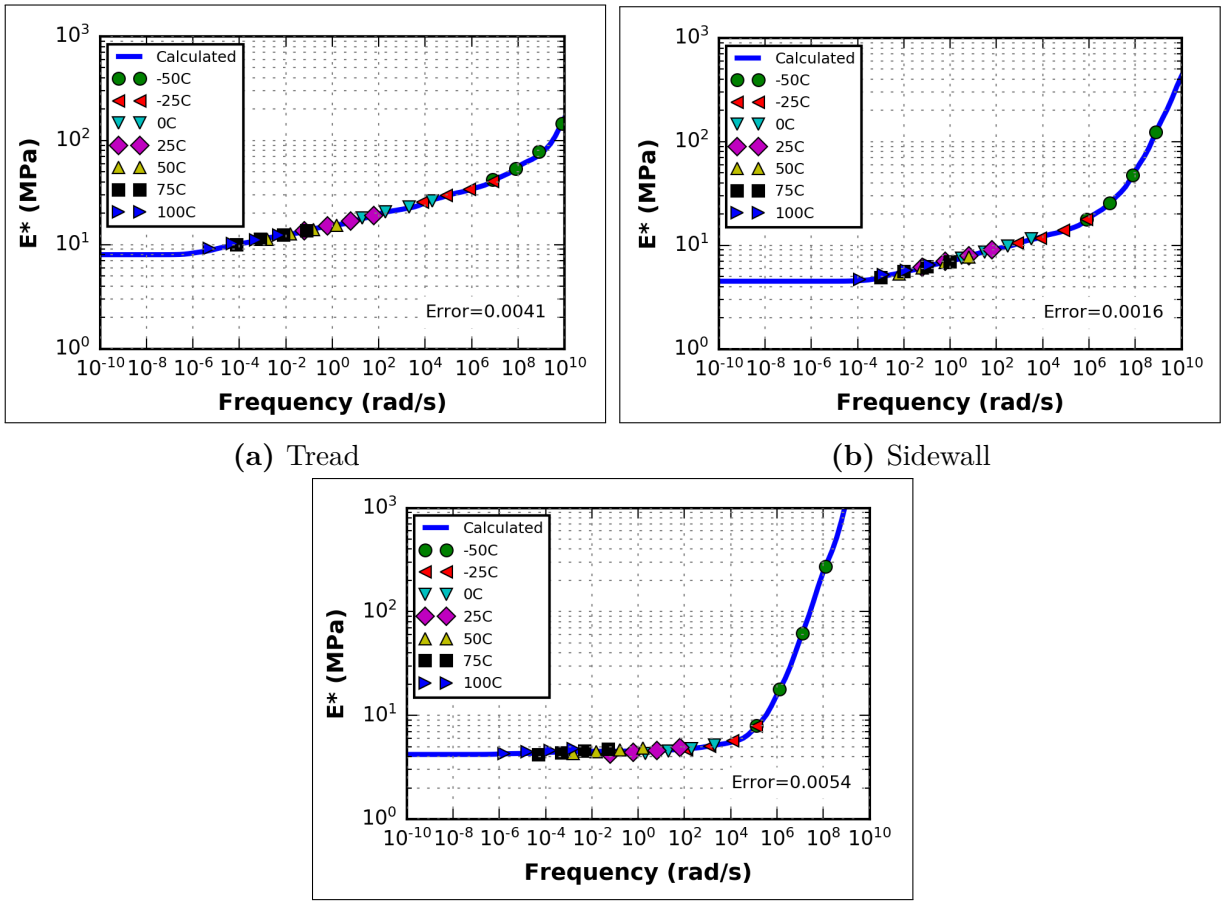

(a) Tread **(b)** Sidewall

(c) Shoulder

Fig. 5.1. Master curves for the tread, sidewall, and shoulder locations.

Furthermore, the thermal conductivity and specific heat for the rubber were assumed as 0.293 W/m·°C and 1600 J/kg·K, respectively [89, 90]. The heat transfer coefficients for the thermal boundary conditions are presented in Table 2. At the tire-pavement contact, a sliding-velocity-dependent friction model is assumed, which implements a decaying friction value as the traveling speed increases.

Table 5.1. Prony Series and WLF Coefficients to Represent Viscoelastic Properties

		$\bar{g}_i$, $\bar{k}_i$		
i	ρ_i	*Tread*	*Sidewall*	*Shoulder*
1	1.00E-10	6.41E-01	7.50E-01	9.81E-01
2	1.00E-09	7.20E-02	1.52E-01	-
3	1.00E-08	7.72E-02	4.70E-02	1.54E-02
4	1.00E-07	4.51E-02	1.55E-02	2.56E-03
5	1.00E-06	2.00E-02	1.00E-02	7.13E-04
6	1.00E-05	1.84E-02	3.10E-03	2.07E-04
7	1.00E-04	2.33E-02	2.83E-03	3.80E-05
8	1.00E-03	6.97E-03	2.70E-03	3.56E-05
9	1.00E-02	1.32E-02	1.79E-03	1.58E-05
10	1.00E-01	1.12E-02	2.15E-03	5.40E-06
11	1.00E+00	4.63E-03	1.30E-03	5.59E-06
12	1.00E+01	8.45E-03	1.42E-03	1.33E-06
13	1.00E+02	4.17E-03	9.96E-04	-
14	1.00E+03	6.05E-03	1.07E-03	5.97E-06
15	1.00E+04	4.56E-03	1.48E-04	1.16E-05
16	1.00E+05	4.73E-03	-	2.04E-06
17	1.00E+06	2.45E-03	-	7.34E-06
WLF Coefficients				
C1		15.7	8.12	28.3
C2		214.0	157.6	416.6

Table 5.2. Heat Transfer Coefficients used for the Thermal Boundary Conditions [89, 90]

Boundary Condition	$h(W/m^2°C)$
Tread/road	12,000
Tread/air	16.18
Sidewall/air	16.18
Body ply/cavity air	5.9
Liner/rim	88,000

5.3.2 Model Generation

The model generation followed a similar scheme as the hyperelastic tire model using an axisymmetric model under a constant tire-inflation pressure and a three-dimensional (3D) model using the *Symmetric Model Generation* capability in Abaqus. The final stage to perform rolling analysis, however, assumed a Lagrangian description rather than the Arbitrary Lagrangian-Eulerian approach that was implemented for the steady-state transport analysis. Given the computational effort required to roll the tire model in contact

with a pavement layer, the resulting contact stress and energy values under the pre-rolling condition were analyzed to evaluate the impact of the analysis type, including static, quasi-static, and coupled temperature-displacement. A brief description of each analysis type is presented as follows.

Static

Because static-stress analysis imposes a static load step, inertia and time-dependent material effects are insignificant. This analysis type is considered a baseline for the implementation of the hyperelastic tire model.

Quasi-Static

The *Visco* module in Abaqus assumes a quasi-static stress analysis, wherein inertia effects are neglected, though it does account for the time-dependent material response. The influence of temperature is captured by prescribing the nodal temperature distribution throughout the entire model, which inherently defines the associated material characterization.

Coupled Temperature Displacement

The *Coupled Temperature-Displacement* (CTD) module enables a fully coupled thermal-stress analysis to simultaneously solve mechanical and thermal solutions while accounting for time-dependent material response. In this current application, using Abaqus/Standard to implement a fully coupled thermal-stress analysis inherently neglects inertia effects and assumes weak coupling between the mechanical and thermal solutions. In other words, the off-diagonal submatrices are much smaller compared to the components of the diagonal submatrices. Moreover, the CTD analysis requires elements with both temperature and displacement degrees of freedom, such as C3D8HT, indicating a thermally coupled eight-noded brick with an hourglass control. In particular, hybrid elements, designated "H" in the element nomenclature, are required when considering hyperelastic materials. The drawback of using hybrid elements is that they are only available in Abaqus/Standard. It is also worth noting that heat generation for the current model is mainly due to friction and has not been activated within the hyper-viscoelastic rubber materials. In the future, to appropriately account for heat generation within the tire and inertial effects, Abaqus/Explicit may have

to be performed. A summary of the modeling assumptions and limitations is tabulated in Appendix A.

5.4 Temperature Impact on Pre-Rolled Condition

Several parametric analyses were completed to assess various analysis types, tire-pavement friction properties, and loading conditions (i.e. applied load P and tire-inflation pressure S combinations). Note that the following variable names are used in the succeeding plots.

- Half-axle load (kN): $P1 = 26.7$, $P2 = 35.6$, $P3 = 44.4$, and
- Tire-inflation pressure (kPa): $S1 = 552$, $S2 = 690$, $S3 = 758$.

5.4.1 Effect of Analysis Type

Baseline scenarios, considering uniform temperature within the tire and pavement bodies, are presented. Figure 5.2 illustrates change in vertical, longitudinal, and transverse contact stresses with respect to change in uniform temperature and analysis type. A decline in the magnitude of the contact stress can be observed, more significantly for the vertical, S_z, and longitudinal contact stresses, S_x, than the transverse contact stress, S_y. The observed increase in S_z and S_x for both *Visco* and CTD analyses resulted in nearly the same and five times greater than the static case, respectively, by simply appending the influence of temperature.

Moreover, as temperature increased, the distribution for the three orthogonal directions increased. This finding aligns with the expected behavior of increased contact area as higher temperature imposed a greater deformation. As the analysis type changed from *Visco* to CTD, S_z and S_y were marginally affected, while S_x experienced an 84% increase as the analysis changed from *Visco* to CTD. Although the results considered a pre-rolled condition, any increase in S_x due to uniform temperature would directly affect the corresponding rolling resistance. It is worth noting that Figure 5.2 is a limited representation of the contact stress distribution. Here, the plots represent the values along the contact length at a specific meridian, i.e. points along the width along the circumferential direction.

The associated internal, creep dissipation, and frictional dissipation energies are presented in Figure 5.3. The total internal energy for the static analysis, denoted as HE in Figure 5.3, resulted in values comparable to the *Visco* analysis. A significant increase up to 15 times, however, was observed as the CTD analysis was implemented. As would be

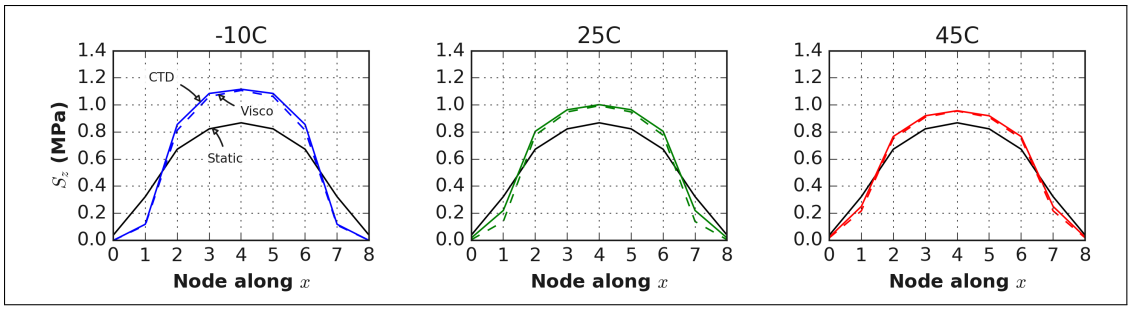

(a) Vertical contact stress

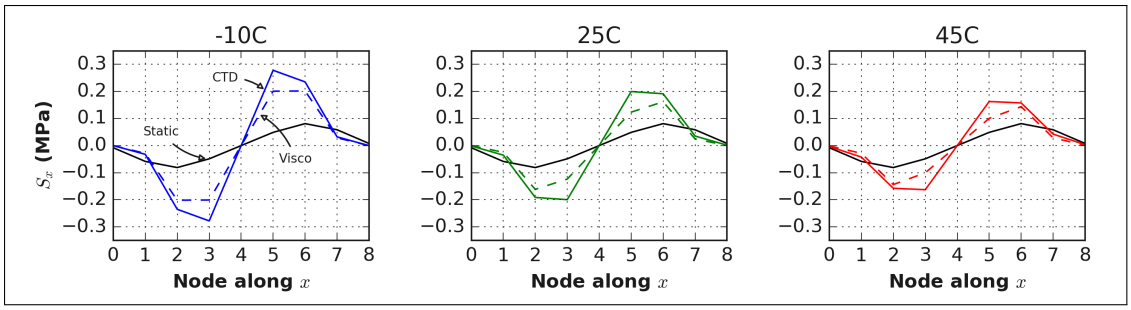

(b) Longitudinal contact stress

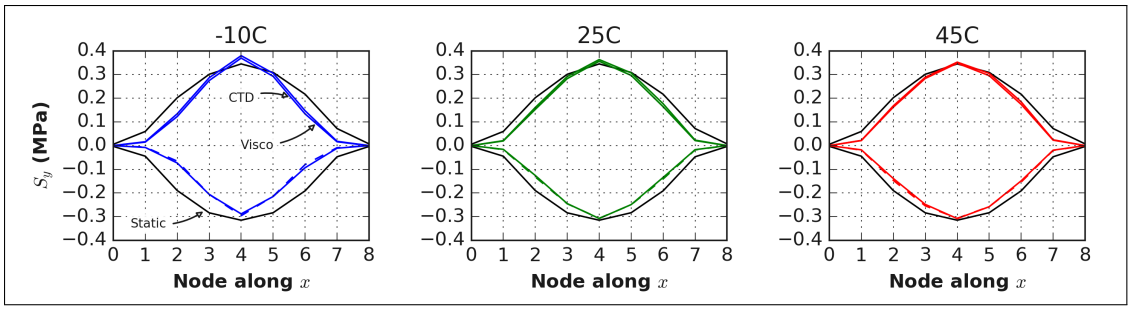

(c) Transverse contact stress

Fig. 5.2. Sample contact stress along the imprint length considering the effect of analysis type and uniform temperature conditions from -10°C to 45°C at pre-rolled condition.

expected, a hyperelastic tire incurred zero creep dissipation energy. On the other hand, as the temperature increased in the CTD cases, the internal energy increased while the creep and frictional dissipation energies decreased. All maintained higher magnitudes than those resulting from static and *Visco* analyses.

5.4.2 Effect of Friction

Several friction characteristics at the tire-pavement interface were considered, ranging from $\mu = 0.0$ to 0.5 for both static and decay friction models, which are designated as U and D in Figure 5.4, respectively. The applied load and tire-inflation pressures were

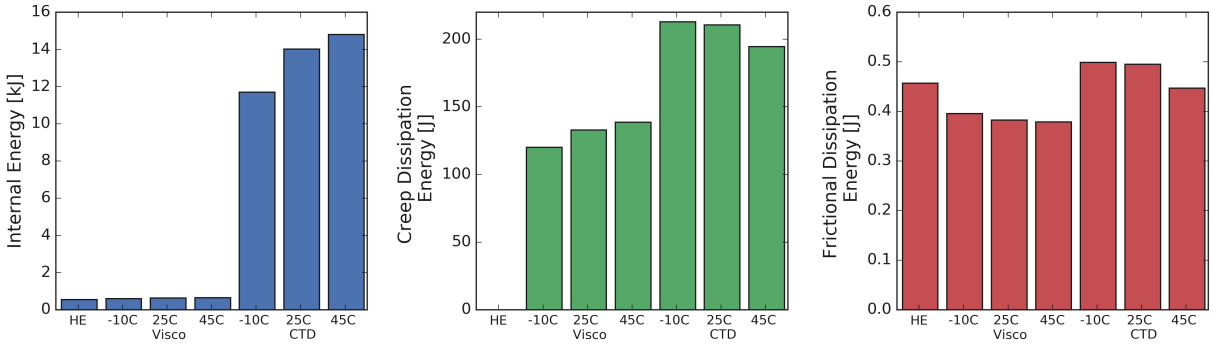

Fig. 5.3. Internal, creep dissipation, and frictional dissipation energies comparing static, *Visco*, and CTD analyses and uniform temperature conditions from -10°C to 45°C at pre-rolled condition.

held constant while the friction level was increased incrementally. That led to an increase in the longitudinal and transverse contact stresses. It was evident that S_x and S_y were significantly influenced compared to S_z, as the resulting curves were nearly coincidental in Figure 5.4a. A difference between static and decay friction scenarios was minimal, given that the presented contact stresses are associated with the pre-rolled condition.

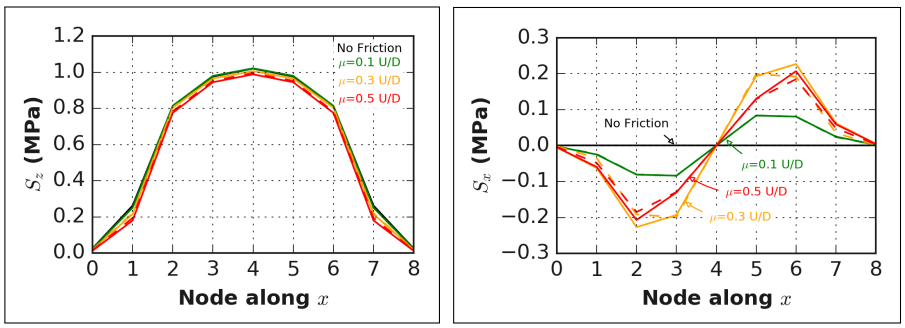

(a) Vertical contact stress **(b)** Longitudinal contact stress

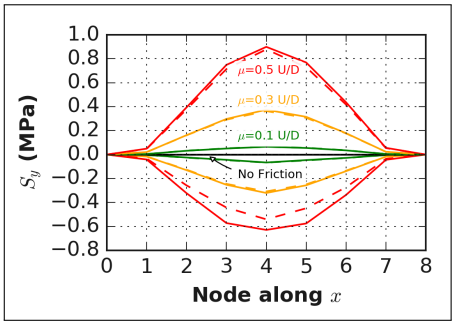

(c) Transverse contact stress

Fig. 5.4. Sample contact stress along the imprint length considering the effect of friction while holding the applied load, tire-inflation pressure, and temperature constant.

5.4.3 Effect of Load

The same numerical matrix for the hyperelastic-tire-model simulations were completed at the pre-rolled condition as a benchmark to quantify the effect of temperature on tire-pavement contact stresses. The applied load varied between $P1 = 26.7$, $P2 = 35.6$, and $P3 = 44.4$ kN, while the tire-inflation pressure was altered between $S1 = 552$, $S2 = 690$, and $S3 = 758$ kPa. This nomenclature is used in the following plots. Additionally, the plots describe the contact stress values at a specific contact length location and along each meridian (i.e. nodes along the tire width).

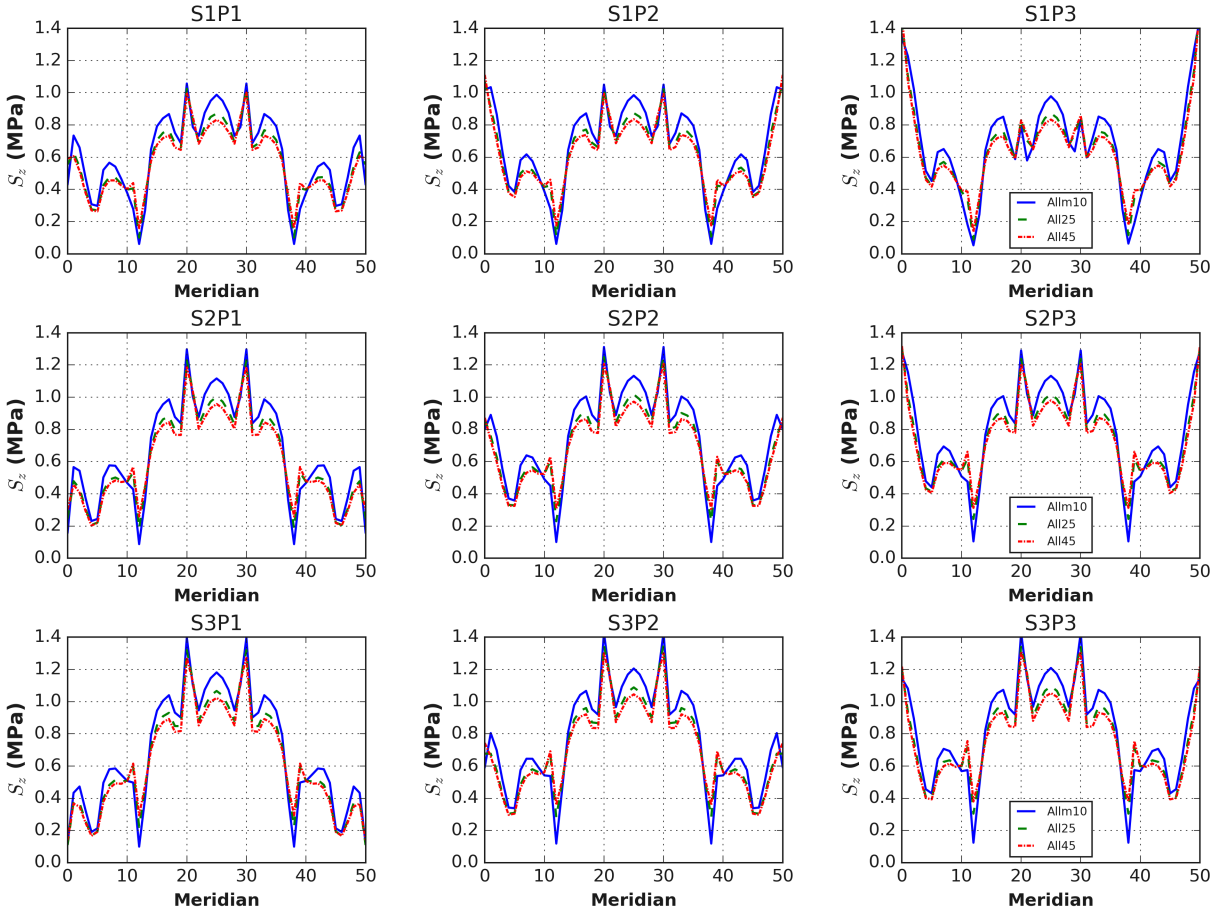

Fig. 5.5. Vertical contact stresses for various inflation pressures, applied loads, and uniform temperatures (-10°C to 45 °C) at pre-rolled condition. Note that the stresses are extracted at mid-contact length and along the contact width.

At uniform temperatures, a similar behavior was observed for varied load and tire-inflation pressure combinations. As the tire-inflation pressure increased, S_z increased, especially at the rib edges (see Figure 5.5). Incorporating a uniform temperature for both the tire and pavement layer, the vertical contact stress increased by up to 20% at the

low-temperature condition. On one hand, the transverse contact stresses were marginally affected by the varied temperature condition as the values were nearly coincidental along each meridian (see Figure 5.6). On the other hand, the effect of temperature on the longitudinal contact stresses was more pronounced with increasing the disparity up to 230% between the temperature conditions as P and S increased (see Figure 5.7).

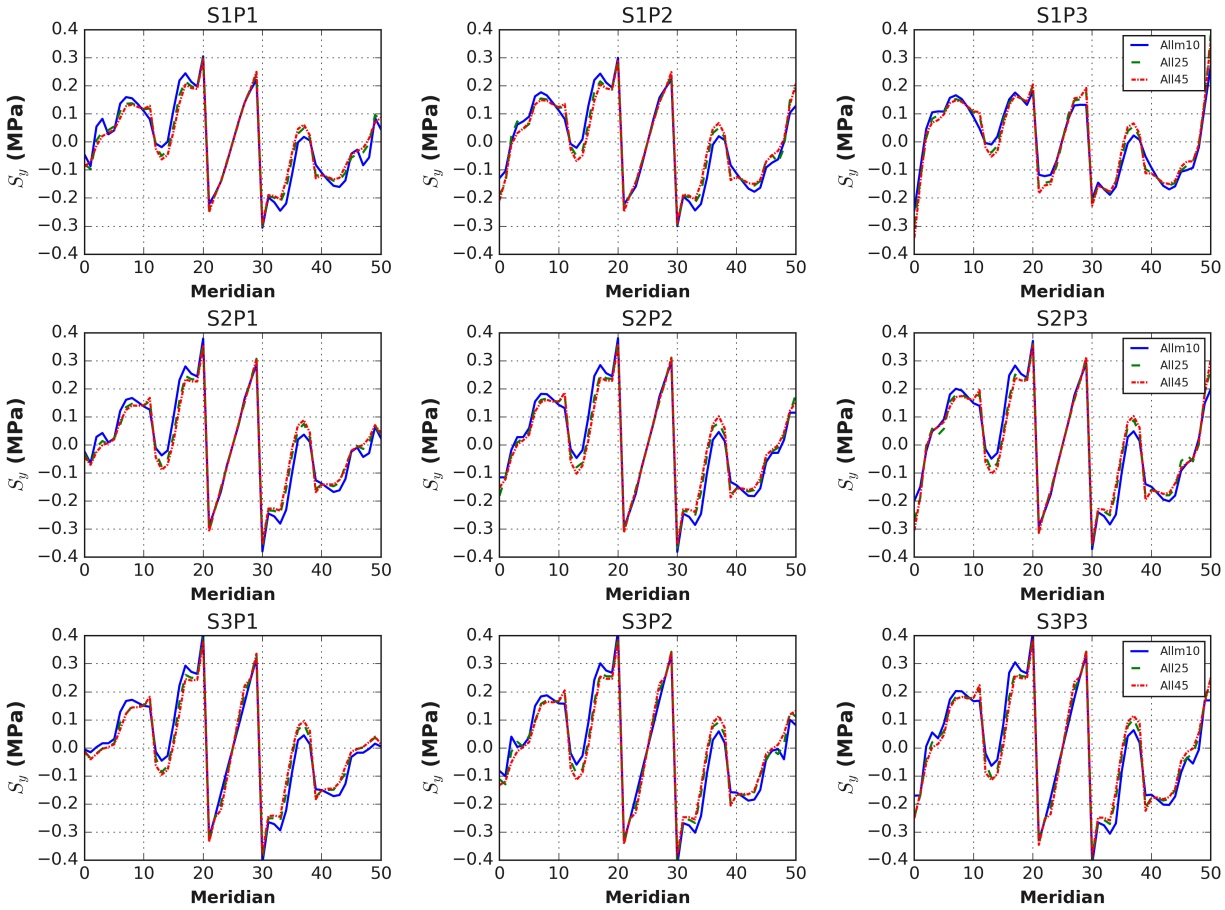

Fig. 5.6. Transverse contact stresses for various inflation pressures, applied loads, and uniform temperatures (-10°C to 45 °C) at pre-rolled condition. Note that the stresses are extracted at mid-contact length and along the contact width.

5.5 Temperature Impact during Rolling

Following the observation of the effect of uniform temperature on a pre-rolled condition, a hyper-viscoelastic tire is rolled under three velocities – $V1 = 8$, $V2 = 65$, and $V3 = 115$ kph – and under varying nonuniform temperature profiles. The nonuniform temperature profiles were generated by varying temperature sink conditions along the inner rim mount,

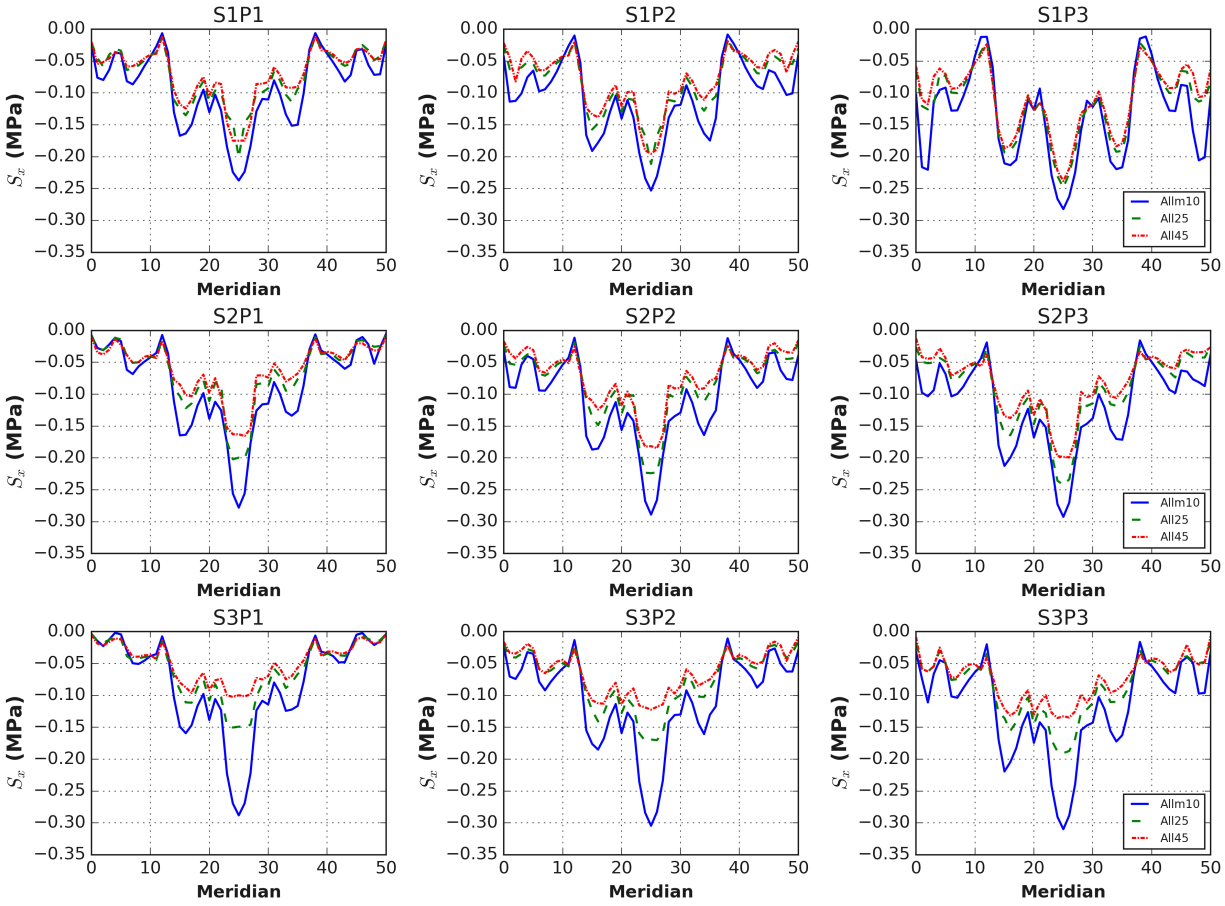

Fig. 5.7. Longitudinal contact stresses for various inflation pressures, applied loads, and uniform temperatures (-10°C to 45 °C) at pre-rolled condition. Note that the stresses are extracted at mid-contact length and along the contact width.

which is representative of the inner tire temperature, as well as the sidewall, pavement layer surface, and tread grooves, which are related to the ambient condition (see Figure 5.8). The pavement layer temperature was assumed uniform, and the analyses were aimed to capture the change in the contact stresses for various steady-state operating conditions of a truck tire.

5.5.1 Uniform Temperature

Four uniform temperature conditions were imposed on the tire-pavement interaction model while considering the same physical properties, loading, and rolling conditions. Figure 5.9 illustrates S_z, S_x, S_y, and the temperature along the contact width, held at the middle node of the contact length. As the uniform temperature changed from 25°C to

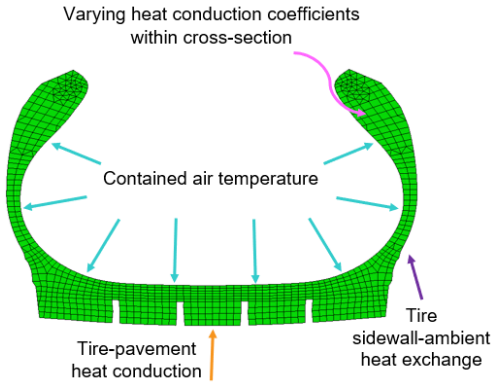

Fig. 5.8. Schematic for thermal boundary conditions along the tire cross-section.

-10°C, an increase of 17.5% was observed at the middle of the imprint width, which corresponded to the maximum contact-stress magnitude. As the temperature increased from 25°C to 45°C, the contact stress value decreased by 7.31% at the same point. In addition, S_z values showed a similar trend as the applied load increased, wherein the edge values became more pronounced. For the tire-rolling condition, the disparity between the contact stresses, induced by the uniform temperature, was more pronounced than those observed in Figure 5.5 (under pre-rolled conditions). S_y minimally changed, which may be attributed to the straight-line rolling condition.

5.5.2 Nonuniform Temperature Profiles

To quantify the stress distribution within the contact imprint, the kernel density was estimated not only to account for clustering of contact stress values, but also to incorporate the features of the neighboring values. Kernel Density Estimate (KDE) is used to estimate the probability distribution by representing the density as a weighted sum of Gaussian distribution at the location of each input point. Inherently, each point implements a Gaussian kernel and the smoothness is further controlled by the assumed kernel bandwidth – a higher value induces a higher level of smoothness, which may potentially lose the fine details of the data distribution.

Various temperature profiles were imposed on the tire-pavement interaction model by assuming a myriad of temperature sink combinations. Tire pressure, load, and speed were assumed constants as $S2 = 690$ kPa, $P1 = 13.35$ kN, and $V2 = 65$ kph, respectively. Figure 5.10 illustrates sample cases for low, intermediate, and high steady-state temperature profiles. Particularly, the temperature KDE plots highlight that varying temperature sinks along the outer surface of the rolling tire in contact with ambient air have a more significant

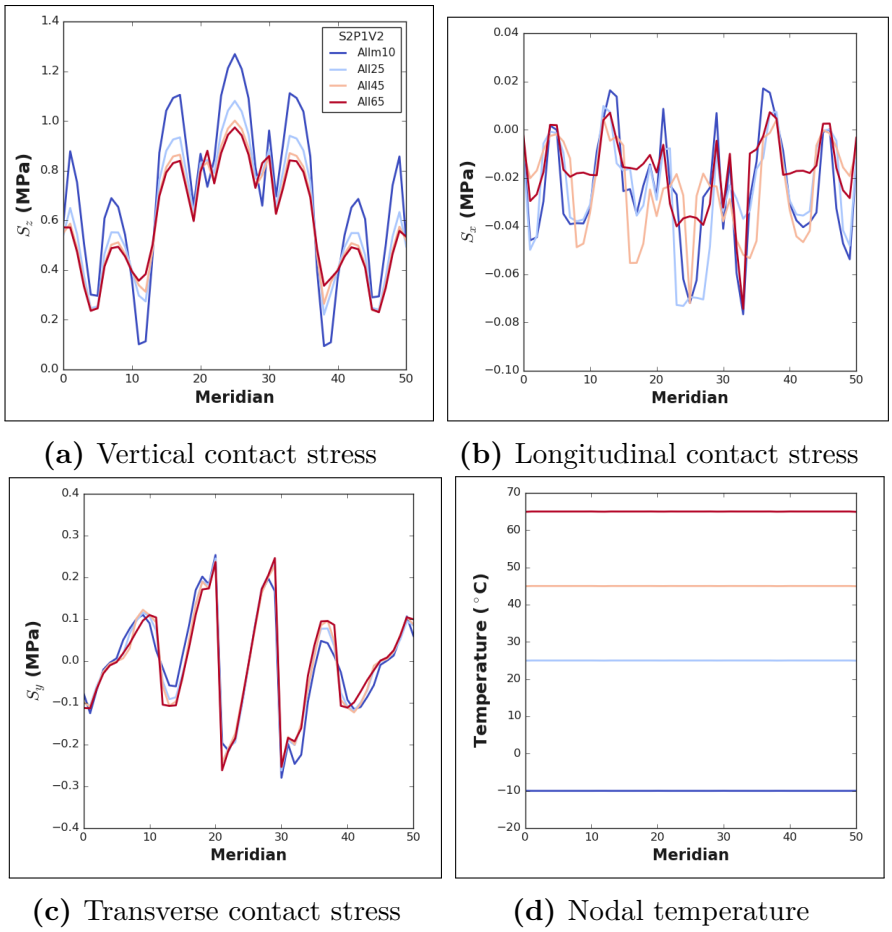

(a) Vertical contact stress **(b)** Longitudinal contact stress

(c) Transverse contact stress **(d)** Nodal temperature

Fig. 5.9. Contact stress and temperature values for various uniform temperature conditions (-10°C to 65°C) while maintaining the tire-inflation pressure, applied load, and rolling speed. Note that the values are extracted at mid-contact length and along the contact width.

influence on the resulting temperature profile than those within the inner tire surface (see Figures 5.10a, 5.10b, and 5.10c).

For low temperature profiles, an increase in the internal air temperature resulted in similar temperature KDE shapes with changes in amplitude and a shift in the temperature range (see Figure 5.10a). The resulting low temperature profile of the rolled tire minimally influenced the distribution of the vertical and transverse contact stresses. It did, however, induce a higher impact on the longitudinal contact stress distribution.

Further increase in temperature magnitudes, as illustrated in Figure 5.10b, resulted in significant differences on the contact-stress distributions along all three orthogonal directions. Note that for Figure 5.10b, the ambient condition was varied while the pavement surface and internal tire temperatures were assumed to be 25 and 35°C, respectively.

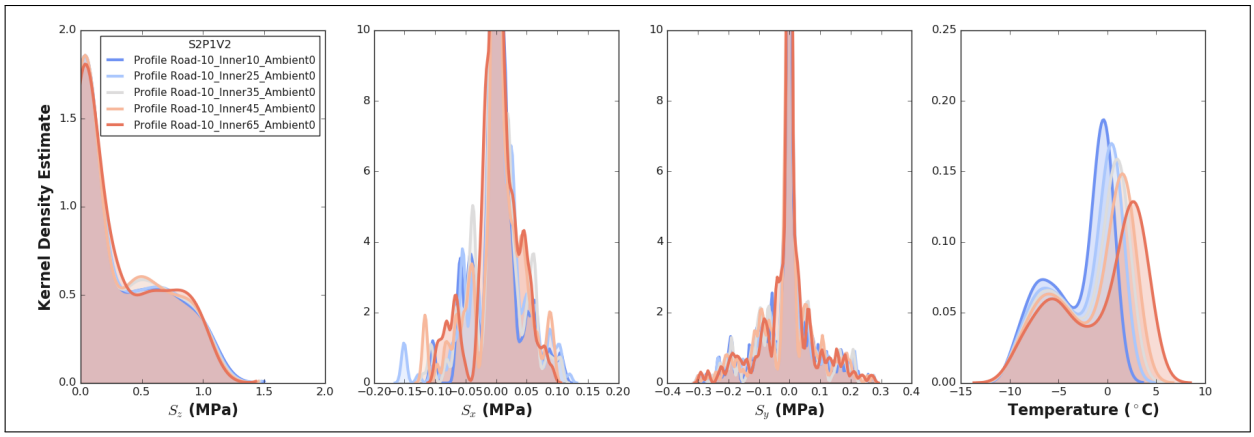

(a) Low temperature profiles

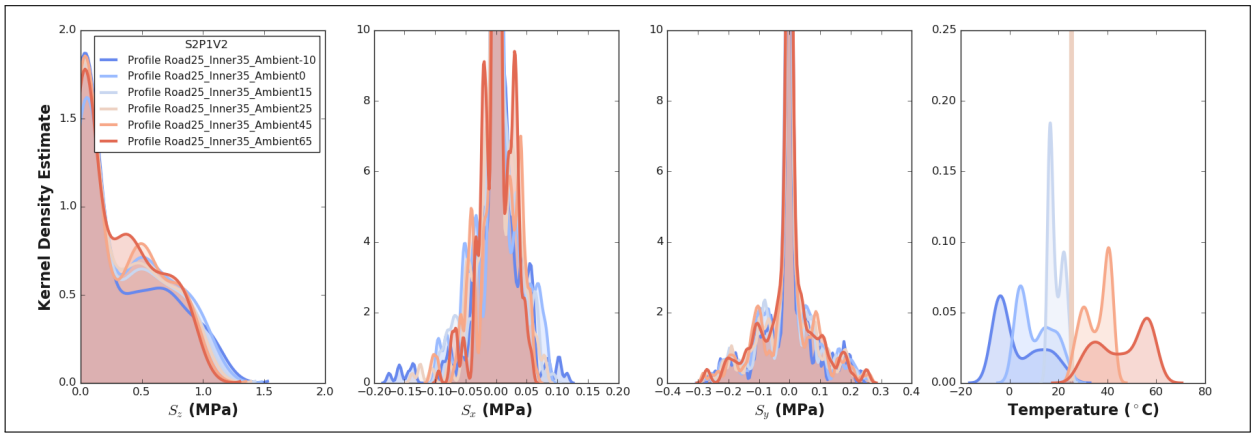

(b) Intermediate temperature profiles

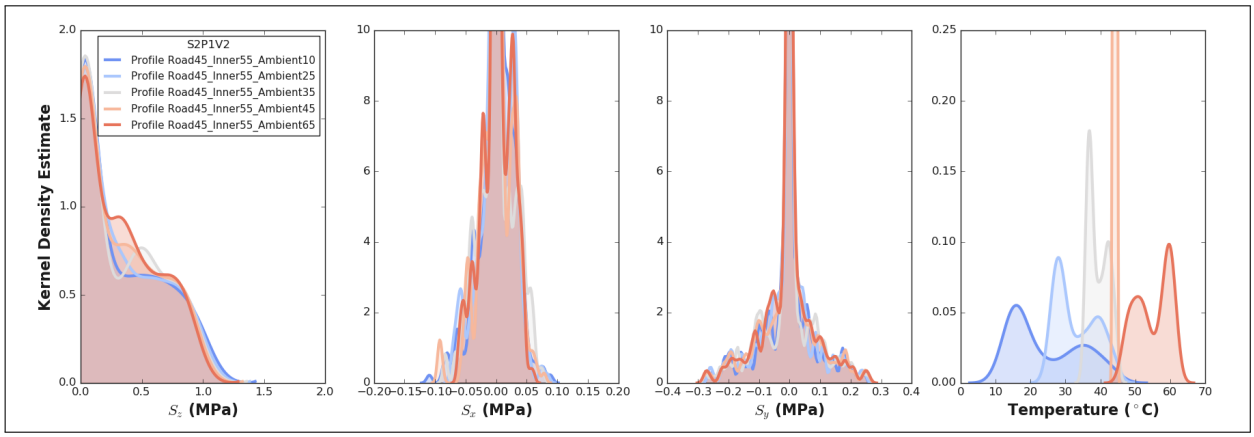

(c) High temperature profiles

Fig. 5.10. Kernel density estimate of contact stresses and temperature distribution due to various non-uniform temperature profiles, while the tire-inflation pressure, applied load, and rolling speed are held constant.

The S_z KDE difference became apparent above 200 kPa. An increase of temperature induced higher KDE values for S_z, between 200 and 1,000 kPa, which indicates that this range of vertical contact stress values are governed by high temperatures and a corresponding increase in the contact area. On the other hand, higher S_z magnitudes became pronounced at low temperatures. This finding aligns with the expected decreased contact area. Thus, a higher stress concentration was observed and the redistribution of S_z became apparent given the flattening of the KDE curve at lower S_z values. In addition, the lower temperature profile resulted in an increased range of S_x, while the change for S_y is lower despite the significant difference in steady-state temperature profiles. The observed minimal changes in S_y may not hold true under turning maneuvers.

Finally, high temperature profiles (as illustrated in Figure 5.10c) resulted in similar findings from the scenarios that considered intermediate temperature profiles (see Figure 5.10b). The KDE curve ranges, however, became narrower and tended towards lower values as if the S_z curves were compressed towards S_z=0. In contrast to the S_x values from the intermediate temperature cases, those presented in Figure 5.10c resulted in a narrower S_x range and more coincidental KDE curves.

5.6 Summary and Conclusions

Tire-pavement contact stresses are governed by two deformable bodies, the corresponding geometry and material characteristics, and by the loading and environmental conditions. A thermomechanical coupling between a hyper-viscoelastic tire and a representative pavement layer was conducted to assess the resulting temperature profiles and their inherent impact on the mechanical behavior of the truck tire model. A myriad of steady-state temperature profiles was imposed to determine the significance of considering temperature as a variable in contact stress prediction.

Benchmark cases revealed a significant increase, up to 40%, in vertical contact stress values and a change in distribution range when uniform temperature distribution is considered. Moreover, the longitudinal contact stresses were impacted more than the transverse contact stresses; nonetheless, the behavior may change under a turning maneuver. By appending the temperature into the truck-tire model, change in magnitude and distribution of the contact stresses was observed. This directly impacts pavement responses, predominantly within the near-surface region, where contact stresses have the highest influence.

Reality, however, dictates that the temperature profiles of a tire rolling on a pavement are nonuniformly distributed along the tire cross-section. Based on Kernel Density plots,

high temperature tended to govern the range of lower vertical contact stress values, less than 1.0 MPa, while low temperature defined the resulting distribution of vertical contact stress magnitudes over 1.0 MPa. Transverse contact stresses were impacted less by the thermomechanical coupling, while the longitudinal contact stress distribution varied more significantly and more predominantly at the leading/front part of the contact. A higher disparity on the contact stress distribution was observed as ambient conditions were altered relative to the change of internal air temperature. This finding revealed that ambient conditions had a greater influence on the resulting tire-pavement contact stresses than the internal air temperature.

The thermomechanical model between the truck tire and pavement layer demonstrated the importance of incorporating temperature profiles due to ambient, internal air, and pavement surface conditions. Analogous to winter, the low temperature profiles induced a smaller contact area that led to stress localization or higher stress magnitudes with a lower spread. On the other hand, high temperature conditions observed during the summer imposed higher tire deformations that led to a wider contact area. Hence, lower contact stress magnitudes were observed with a wider distribution. In either condition, the longitudinal contact stresses varied more notably than the transverse contact stresses, which impacts rolling resistance and near-surface behavior of pavements. Rolling conditions, such as braking, accelerating, and cornering would affect both transverse and longitudinal contact stresses, and transverse contact stresses under a turning maneuver.

CHAPTER 6

CONTACT STRESS AND ROLLING LOSS ESTIMATION VIA THERMOMECHANICAL INTERACTION MODELING OF A TRUCK TIRE ON A PAVEMENT LAYER

6.1 Introduction

In classical mechanics, rolling resistance is defined as the energy loss per distance traveled by a vehicle due to nonelastic deformations of the tires and wheel suspension system losses [91]. This is related to the rotation about the wheel axle and the rolling motion of traveling forward. Upon the invention of pneumatic tires in 1888, rolling resistance became an immediate concern. The first published experiment on this subject was reported in *The Mechanics' Magazine* [92]. While the same concern is still valid today, more attention is now given to reducing fuel consumption.

In the past, tire manufacturers successfully designed and produced tires to minimize energy losses. For instance, the energy consumption of radial tires has been reduced by approximately half, in contrast to bias-ply tires [93]. Additional tire design improvements have been focused on the tread design, which directly excites the tire-pavement interaction. A positive outcome of reducing tread deformation is better rolling resistance. To achieve this, manufacturers reduced the tire aspect ratio, which stiffens the tire by allowing less flexibility. Other tire design factors that affects rolling resistance include tire mass, rubber formulation, inflation pressure, applied load [94], and tire vibrations [95].

The two main mechanisms of rolling loss are: (i) convection into the surrounding air both inside and outside the tire; and, (ii) conduction into the wheel and pavement surface. Rubber's viscoelastic heat dissipation, due to hysteretic losses, generally accounts for over 90% of the tire rolling losses for the pneumatic tire's rolling resistance. The remaining losses, on the other hand, are influenced by operating conditions, weather conditions, road curvature, slippage and adhesion between the tire and road, road contaminants, and the aerodynamic drag and friction between the tire and the rim, and the tire and the pavement surface [95].

Accounting for transient dynamic rolling analysis allows for a more realistic simulation. However, considering a three-dimensional and full-patterned tire model not only requires a

significant computational effort but it also produces strain time histories with high levels of oscillation time histories with high levels of oscillation [96]. Due to the complex structure of a tire, a variation of temperature throughout the tire exists wherein certain locations tend to dissipate more than others.

To better understand rolling resistance, many experimental measurement devices have been invented and many theoretical frameworks have been developed. Williams and Dudek [97] generated relations between the footprint load-deflection hysteresis and rolling resistance drag form, quantifying the contribution of the tread and sidewall deformation to hysteresis. Luchini et al. [98] created a finite element model based on directional incremental hysteresis to predict rolling resistance. Vantsevich and Stuart [99] utilized probabilistic characteristics of a vehicle and road to model the interaction along with rolling resistance using a quarter-car model. Qui et. al. [100] developed a full two-dimensional semi-analytical model for viscoelastic cylinders rolling on a rigid surface to address high-speed contact problems for layered viscoelastic rollers and standing-wave phenomena. Moreover, Sandberg [101] developed a macromodel of rolling resistance to show the importance of tire temperature.

Chupin et al. [102] tackled the rolling resistance problem by computing the structure-induced rolling resistance for a vehicle using mechanistic responses of a layered viscoelastic medium with a moving load. The authors concluded that the extra fuel consumption from the viscoelastic behavior of asphalt concrete pavements is relatively small, under the reported assumed conditions. More recently, Hernandez et al. [103] established an equilibrium-based rolling resistance estimation that accounts for the effect of tire inflation pressure, traveling speed, applied load, and tire temperature on a wide-base tire. Kim et al. proposed stochastic pavement models combined with a mechanics-based vehicle model to estimate the dissipated energy from the vehicle suspension of a quarter-car [104] and half-car models [105]. Kang et al. [106] developed a tractor-trailer model not only to capture complex dynamic motion but also calculate excess fuel consumption of trucks equipped with new-generation wide base tire and dual tire assembly. A recent study by Liu and Al-Qadi established a three-dimensional truck model to predict excess fuel consumption with varying pavement roughness [107].

In Chapter 5, it was observed that uniform and non-uniform temperature profiles could induce an evident change in the contact stress distribution [108]. A change of up to 40% in vertical contact stresses was observed due to varying uniform temperatures. In this dissertation, the analysis matrix considered varying the load and temperature conditions. The implications of the combined thermomechanical behavior of the rolling tire on contact stress, heat flow, and rolling loss are presented in the following sections.

6.2 Thermomechanical Model Overview

One of the tires of the dual tire assembly (DTA), conventionally used in heavy semi-truck fleets, was simulated using the finite element method via Abaqus. The partitioning of the tire mesh along the cross-section is illustrated in Figure 6.1. The description of the model generation and testing to establish the truck tire thermomechanical model have been described in detail elsewhere [12, 108]. A brief overview of the model is provided as follows.

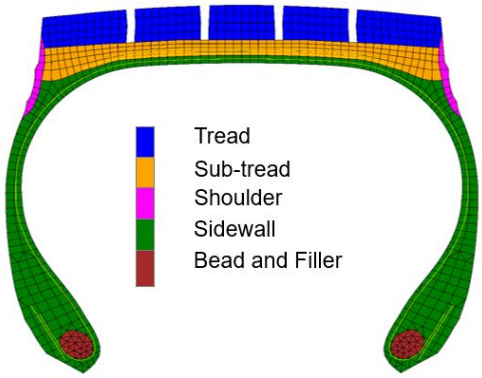

Fig. 6.1. Truck tire cross-section.

First, the axisymmetric model was established based on accurate measurements of the tire cross-section. Using the *Symmetric Model Generation* module in Abaqus, the axisymmetric model was rotated circumferentially to create the three-dimensional (3D) tire model. The load steps at this stage comprised of inflation, initial tire-pavement contact using a low value of displacement, and load application. Given that only one of the DTA was simulated, the applied load is only a quarter of the anticipated trailer axle load.

The sections within Figure 6.1 also defined the boundaries of material property assignments. The tread, sub-tread, sidewall, and shoulder assumed hyper-viscoelastic properties, whereas the steel reinforcements (i.e., two plies and three belts) and bead-and-filler region were characterized as linear elastic. The bead-and-filler region included steel beads and polymer filler; however, the area was homogenized due to numerical computation issues related to adjacent areas that had a high disparity in material behavior (i.e., high versus low moduli). Moreover, the friction property assumed between the tire-pavement interface considered a decay friction model that varied on the slip speed [66]. The next step in the simulation was to roll the tire on an elastic pavement layer that included temperature sink conditions to promote heat transfer within the tire, between the tire and pavement surfaces, and along the inner and external surfaces of the tire.

To capture a fully coupled thermal-stress analysis, the simulation implemented the Lagrangian description. Notably, the current model setup neglects inertia effects using

Abaqus/Standard; the implicit analysis provides a means to utilize elements with fully coupled temperature and displacement degrees of freedom (e.g., C3D8HT for a thermally coupled eight-node brick with hourglass control). Moreover, the "H" parameter in the element nomenclature has been recommended for hyperelastic materials, which is a feature available only in Abaqus/Standard. The parametric analysis considered the tire-inflation pressure, applied load, velocity, and range of temperature sink in the numerical simulations, as listed below.

- Tire-inflation pressure, S (kPa): 690,
- Applied tire load, $P(kN)$: 13.5,
- Velocity, $V(mm/s^2)$: $V1 = 2222.2$, $V2 = 18055.6$, and $V3 = 31944.4$, and
- Range of temperature sinks ($°C$): -10 to 65.

6.3 Distribution Analysis

Rolling loss is defined here as the conversion of mechanical energy into heat as a tire moves for a unit distance on a pavement. Given the complex nature of a rolling tire, the gravity of compounding the selected parameters and full coupling of the thermal and mechanical stress analysis warranted quantifying the distributions of the energy dissipation, heat flow, and contact stresses.

To describe the probability distribution of the output data, the Kernel Density Estimate (KDE) was used; a method utilized in machine learning. KDE is defined as the weighted sum of the Gaussian distribution surrounding the point of analysis. If one were to discretize the KDE curves into a given increment or bin size, the percentage of points belonging to the corresponding increment could be estimated. Not only are the range and density along each input point described, but this also accounts for the influence of the neighboring points. In contrast to a histogram, KDE removes the dependence of the analysis on the bin size.

6.3.1 Dissipation within Tire Sections

The KDE plots, presented in Figure 6.2, capture the full distribution of creep dissipation energy density ($CDED$) within each hyper-viscoelastic region of the tire over a wide range of temperatures assumed for the ambient condition from -10 to 65°C. This parameter

relates to the hysteretic dissipation of the tire. Considering that only ambient temperature conditions were altered, the tread and shoulder resulted in the highest difference in the *CDED* range and spread, compared to the subtread and sidewall.

Comparing Figures 6.2a and 6.2d, the shoulder region resulted in the highest variation, despite having the smallest spatial coverage within the tire structure (recall from Figure 6.1). For tire designers, this tends to be a critical region due to high levels of localized stresses that can affect tire durability. As the ambient temperature increased for the shoulder region, *CDED* values decreased significantly and became localized within a narrower range. The tread, on the other hand, resulted to varying trends between the cases along the *CDED* value range. A similar trend of shift and truncation of *CDED* values (i.e., toward zero) was observed as the ambient temperature increased.

A similar trend of reduced spread of *CDED* values for the tread was observed (Figure 6.3a) for the pavement and inner tire surfaces while varying the ambient temperature from low to high levels; however, the overlap between the KDE curves is greater than those presented in Figure 6.2a. As the pavement surface and ambient temperature conditions were maintained at low levels with varying inner tire surface temperatures, a slight shift and range variation of the creep energy dissipation densities were observed. That said, this was not as pronounced as those induced by changing the ambient temperature (Figure 6.3b). Hence, for the three sets of temperature profiles, the ambient temperature condition had a greater influence on creep dissipation of the rolling tire than on the road and inner tire surfaces. This finding aligns with the fact that the ambient conditions induced a higher disparity on the contact stress distribution relative to the change of internal air temperature [108].

6.3.2 Relation of Heat Flux with Tire-Pavement Contact Stresses

The corresponding heat flux values for Figure 6.2 are illustrated in Figure 6.4. These values impose the final state of the tire tread temperature, as influenced by the ambient, road surface, and internal air boundary conditions, for one revolution. On one hand, the values along the longitudinal direction experienced the highest disparity and spread as the temperature sink conditions were varied. A shift in the longitudinal heat flux values could be observed, following the curves from right to left (i.e., blue being the coolest while red indicates the hottest). The shift and change in sign followed the expected heat transfer, which flowed from high to low temperatures.

On the other hand, the transverse heat flux remained symmetrically distributed along

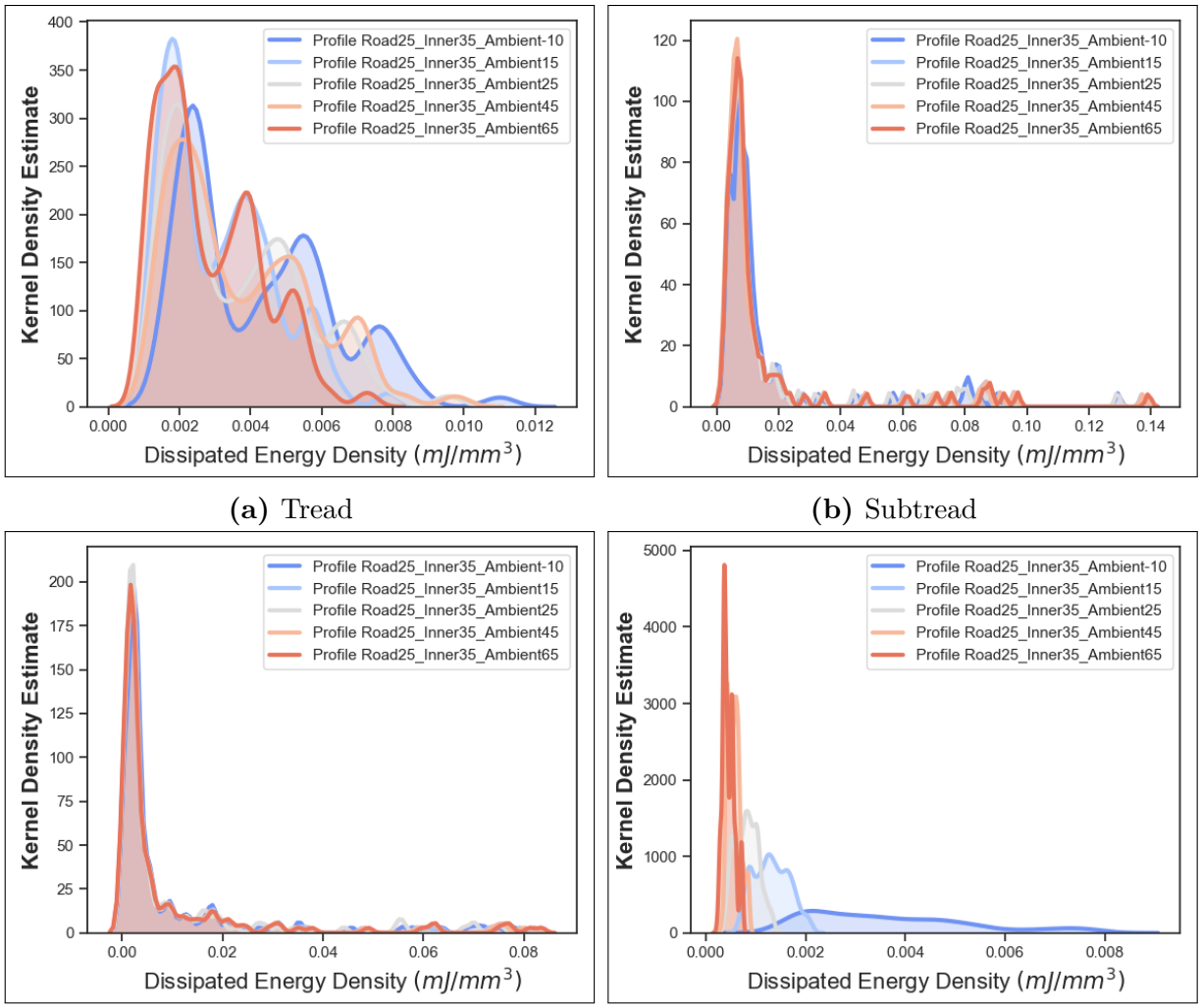

(a) Tread **(b)** Subtread

(c) Sidewall **(d)** Shoulder

Fig. 6.2. Kernel density estimates of creep dissipation for varying temperature profiles: road surface and inner tire temperatures were set to 25°C and 35°C, respectively, while ambient temperature conditions were varied between -10°C to 65°C.

the x-axis. As the ambient temperature increased, the "spike" or localization reduced significantly. A "plateau" near the origin could be observed for the highest temperature sink along the outer wall of the tire (which was assumed to be exposed to air temperature). As the temperature increased, one may observe undulations along the "plateau" that could be related to the presence of grooves and convection along the rib spacing with the ambient condition. The resulting values along the vertical direction changed, modestly, compared to the other two directions.

It is evident that the resulting heat flux vector fields became evidently concentrated within the tire-pavement contact region. As illustrated in Figure 6.5, the highest magnitude

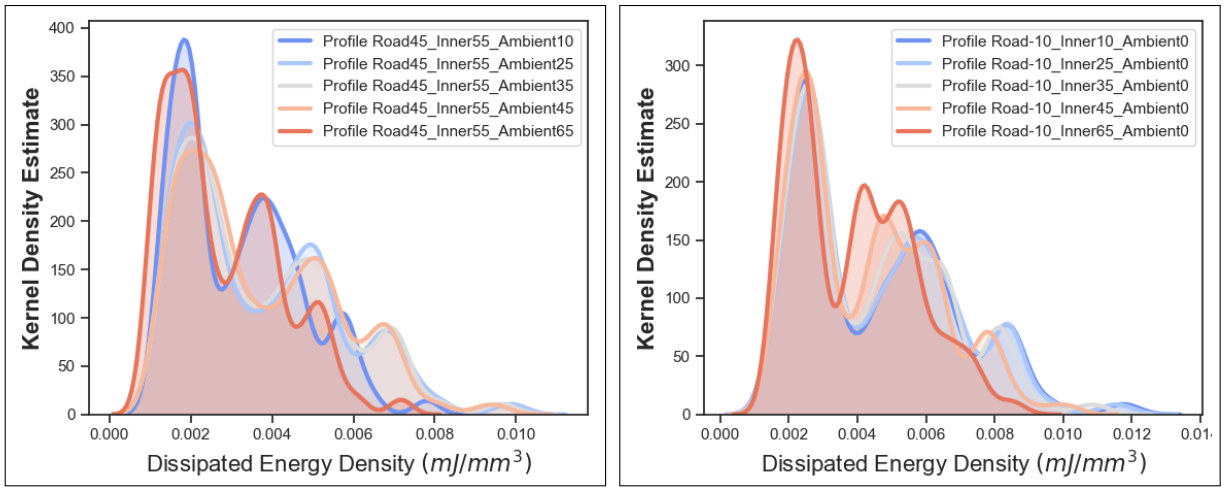

(a) High temp profile **(b)** Low temp profile

Fig. 6.3. Kernel density estimates of creep dissipation for (a) high and (b) low temperature variations. The plot on the left assumed the road surface and inner tire temperatures as 45°C and 55°C, respectively, while ambient temperature conditions were varied between 10°C to 65°C. On the other hand, the plot on the right assumed road surface and ambient temperatures as -10°C and 0°C, respectively, while inner tire temperatures were varied between 10°C to 65°C.

and change in direction occurred toward the middle of the contact imprint. The resultant vectors in Figures 6.5a and 6.5c are in accordance with the KDE distribution curves observed in Figure 6.4. As the imposed temperature differential was reduced within the tire, the heat flux vectors tended to a lower variation in magnitude (Figure 6.5b)). As the tire exited contact, a lag in temperature to reach the ambient temperature sink was observed that eventually diminished as tire revolved.

Extending the cases to other non-uniform temperature profiles, Figure 6.6 illustrates the resulting creep energy dissipation and heat flux (Figure 6.6a) and the corresponding contact stress and temperature distributions (Figure 6.6b). As the inner tire temperature varied while low temperatures were maintained for the road surface and ambient conditions, heat flux distribution shifted and scaled up/down while maintaining its general shape. This trend was also followed by the resulting state of the temperature distribution—i.e., the temperature distribution shifted to the right and narrowed with increased KDE peak values. On the contrary, the $CDED$ spread for the same cases changed minimally when only the inner tire temperature was altered. Therefore, the hysteretic loss difference between the given scenarios in Figure 6.6 was low and inherently led to a low change in the contact stress distribution; hence, the observed overlap.

Appending the common operating temperature for truck tires, 35°C, with the assumed

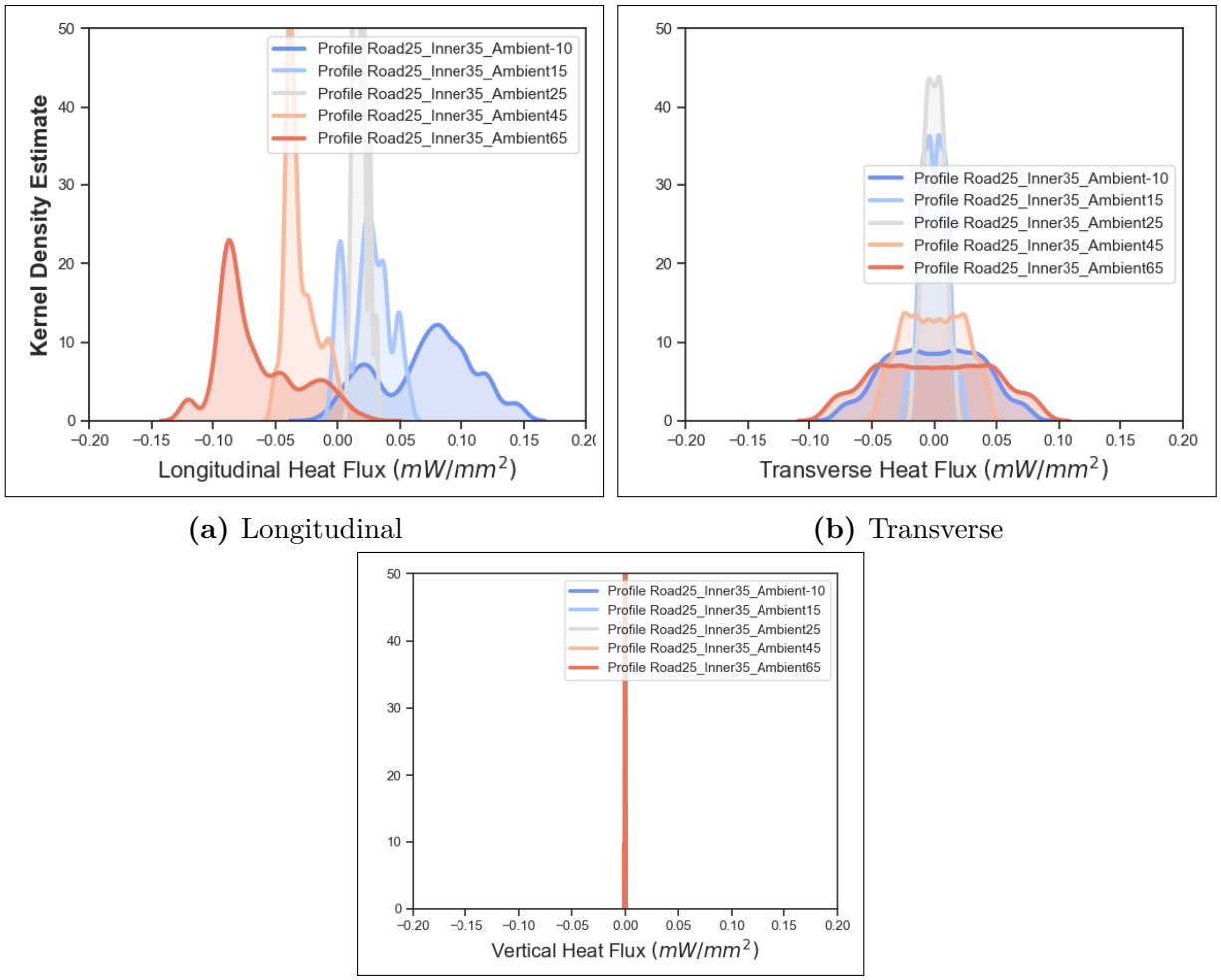

(a) Longitudinal **(b)** Transverse

(c) Vertical

Fig. 6.4. Heat flux within the tread section along the (a) longitudinal, (b) transverse, and (c) vertical directions. Note that the road surface and inner tire temperatures were set to 25°C and 35°C, respectively, while ambient temperature conditions were varied between -10°C to 65°C.

25°C for the road surface condition, Figure 6.7 showcases the simulation results as the ambient temperature varies between -10 to 65°C. In contrast to Figure 6.6, significant differences in the heat flux values revealed prominent changes in the final temperature state. Moreover, a clear disparity in the creep dissipation energy density induced a higher level of variation on the contact stress distribution. Therefore, verifying that ambient temperature induces the highest influence contrast to the road and inner tire surfaces, within the thermal boundaries.

It is worth noting that free rolling was assumed in the tire simulations. The observed trends may change when braking, accelerating, or cornering conditions are imposed. Ad-

ditionally, the current simulation setup does not impose an increase in the tire-inflation pressure, despite the potential of the tire "heating up" during rolling. As a future research direction, a user subroutine may be established that utilizes state variables to redefine the tire-inflation pressure.

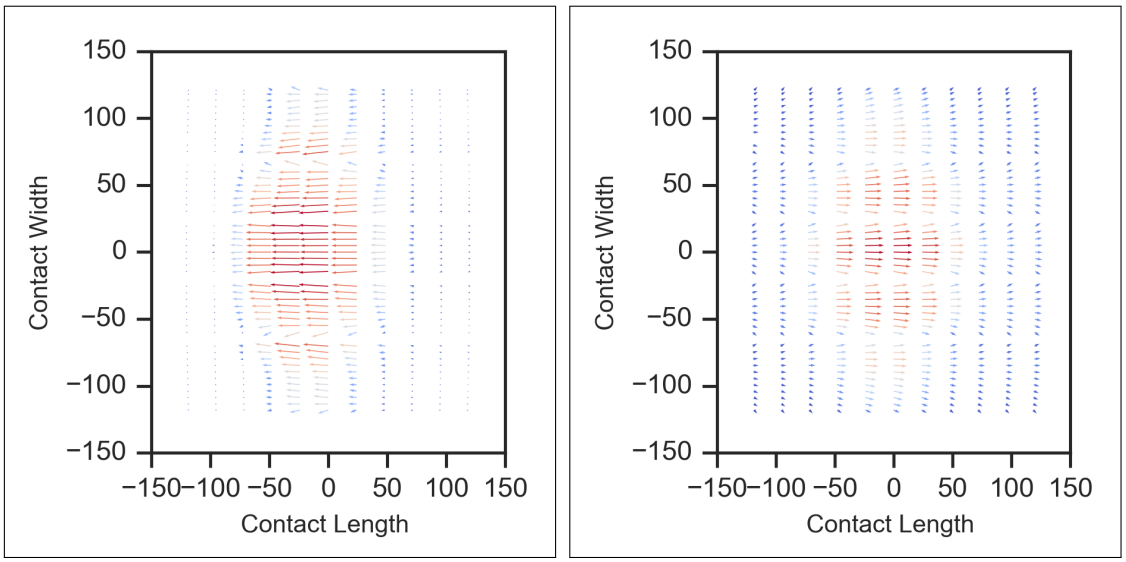

(a) Low ambient temperature **(b)** Room ambient temperature

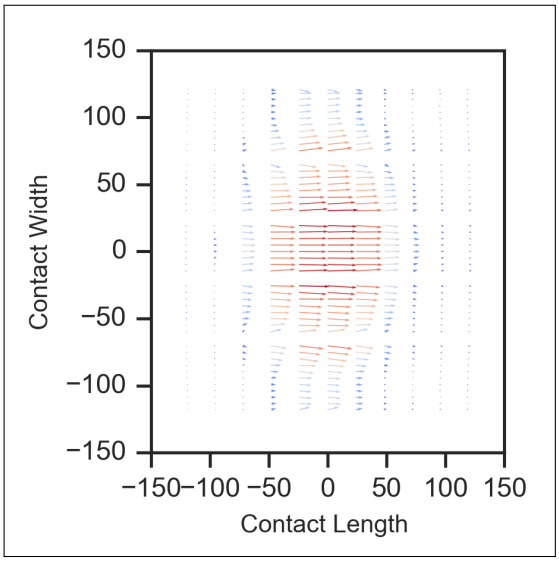

(c) High ambient temperature

Fig. 6.5. Heat flux vectors along the longitudinal and transverse directions, considering change in ambient condition.

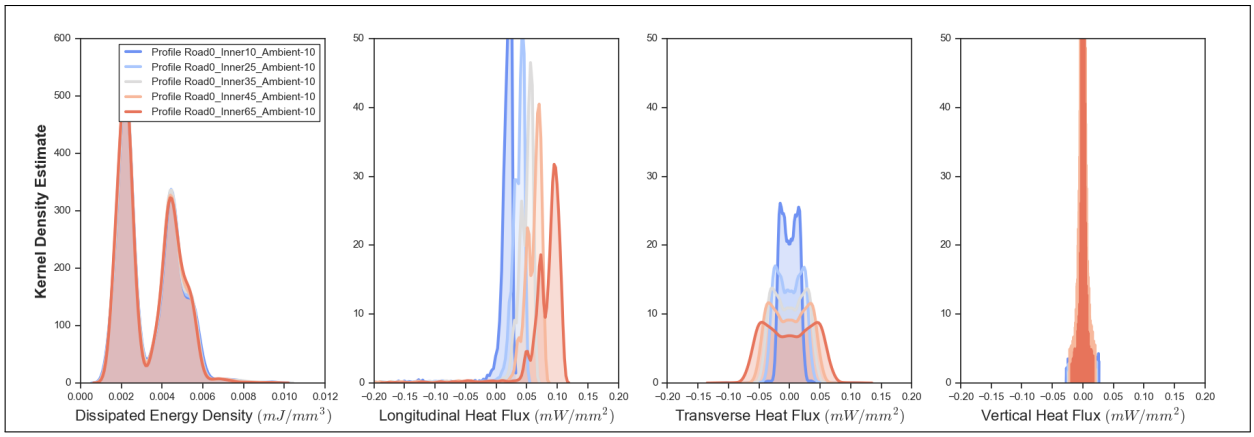

(a) Creep dissipation and heat flux distributions

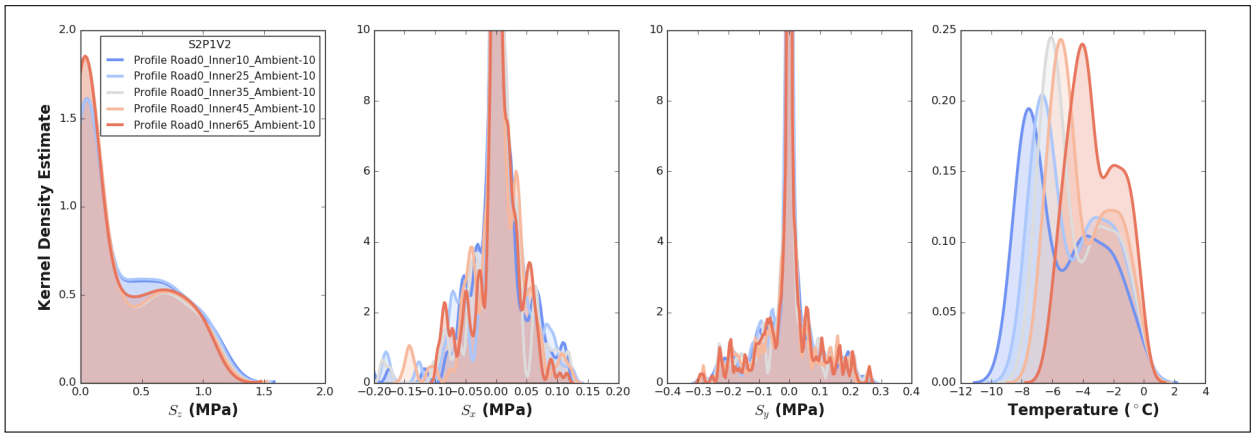

(b) Contact stress and temperature distributions

Fig. 6.6. Kernel density estimates of creep dissipation, heat flux, and contact stresses due to varying inner tire surface temperatures from 10°C to 65°C, while maintaining the road surface and ambient temperatures at 0°C and -10°C, respectively.

6.3.3 Nonlinear Regression Analysis to Predict Thermomechanical Contact Stresses

Nonlinear regression analysis was applied to characterize the tire-pavement contact stress database and to establish a prediction scheme that considered mechanical and thermal conditions, including their inherent interaction. Previous work by Hernandez et al. [88] guided the basis of the functional form of the vertical contact stress equation; however, it was only applicable for the wide-base tire. The first step in establishing the relation for the DTA required the use of the hyperelastic tire model output (Chapter 2). The influence of the mechanical loading via tire-inflation pressure, applied load, and speed was well-captured by the set of terms in brackets (Equation 6.1). To append the thermal interaction, the first

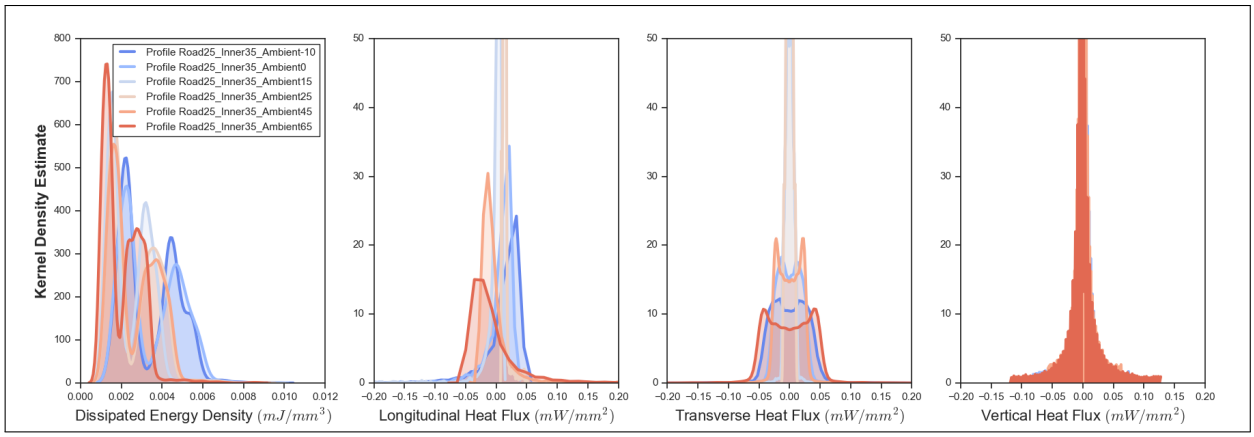

(a) Creep dissipation and heat flux distributions

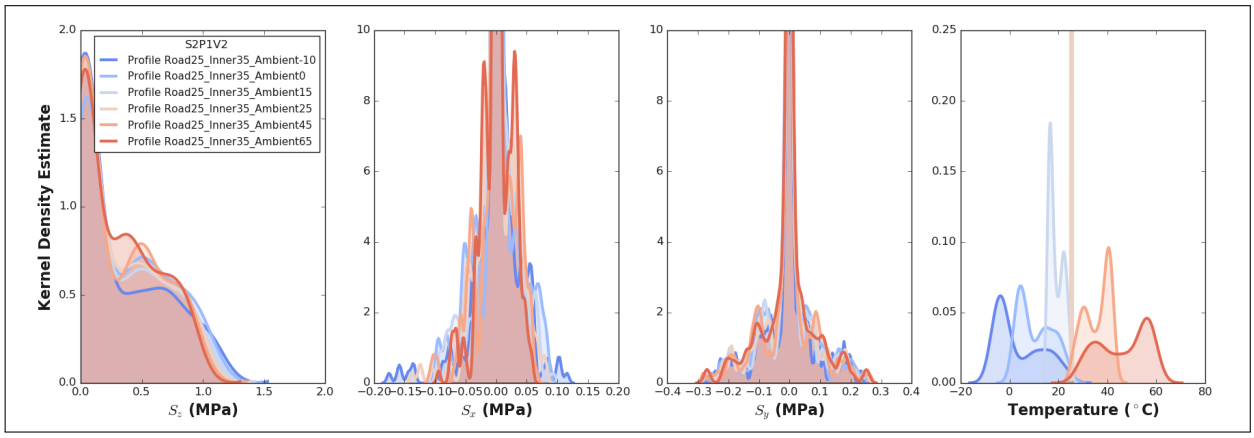

(b) Contact stress and temperature distributions

Fig. 6.7. Kernel density estimates of creep dissipation, heat flux, and contact stresses for varying ambient temperatures from -10°C to 65°C, while maintaining the road and inner tire surface temperatures at 25°C and 35°C, respectively.

term was added to incorporate the temperature sink boundaries.

$$\sigma_Z(\xi) = \left(\frac{{T_{in}}^{\beta}}{{T_{road}}^{\gamma}}\right)\left[\alpha\left(\frac{P}{2ab}\right)\left(1-\xi^{2n}\right)\left(1-\delta\xi\right)\left(\frac{S}{V}\right)^{m}\right] \tag{6.1}$$

Here σ_Z is the vertical contact stress in MPa, ξ is the normalized contact length coordinate from -1 to 1, P is the applied load in N, a is half the contact length in mm, b is the contact width in mm, S is the inflation pressure in MPa, V is the speed in mm/s, and T_{in} and T_{road} are the temperature sinks for the inner tire and road surfaces, respectively, and α, β, δ, γ, n, and m, are the nonlinear regression fitting coefficients.

Considering the same tire-inflation pressure of 690 kPa and applied load of 13.5 kN for one tire, non-uniform temperature profiles were varied. Following the Pareto Principle,

80-20 partitioning was implemented to define the training and testing data sets, respectively. As illustrated in Figure 6.8a, majority of comparison points remained within specific boundaries; 83.9 percent where within ±10%, 98.3 percent are within ±20%, and 99.8 percent are within ±30% from the equality line. Results using the testing data revealed similar trends (Figure 6.8b). Hence, vertical contact stress distributions may be established using the coefficients presented in Table 6.1. The three fitting coefficient values per rib of the dual tire assembly were utilized in predicting the thermomechanical vertical contact stresses. A simplified approach may be used by using an average value for each rib.

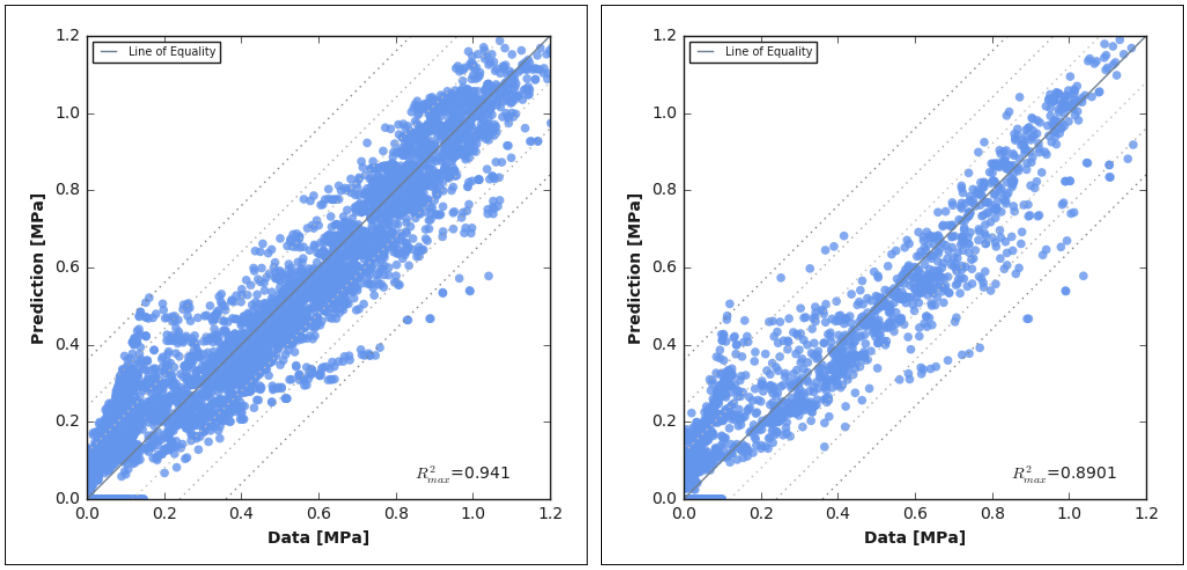

(a) Training set **(b)** Testing set

Fig. 6.8. Comparison of FE model output and nonlinear regression prediction for the (a) training and (b) testing data sets of the vertical contact stresses considering varying temperature profiles.

Equations 6.2 and 6.3 were used to estimate the longitudinal and transverse contact stresses, respectively.

$$\sigma_X(\xi) = ({\sigma_{z,max}}^a)\left({T_{in}}^b\right)({T_{road}}^c)\left(1+\frac{1}{d}\right)(1-|2\xi-1|^e)(1-f(2\xi-1)) \tag{6.2}$$

$$\sigma_Y(\xi) = ({\sigma_{z,max}}^a)\left({T_{in}}^b\right)({T_{road}}^c)(1+d)(1-|2\xi-1|^e)(1-f(2\xi-1)) \tag{6.3}$$

where σ_X and σ_Y are the longitudinal and transverse contact stresses in MPa, respectively, ξ is the normalized contact length coordinate from 0 to 1, T_{in} and T_{road} are the temperature sinks for the inner tire and road surfaces, respectively, and a, b, c, d, e, and f are the nonlinear regression fitting coefficients.

Table 6.1. Nonlinear Regression Coefficients to Predict Thermomechanical Vertical Contact Stresses

Rib Number	n	alpha	delta	m	beta	gamma
Rib 1	0.249	1.107	0.475	-0.172	-0.243	0.197
	0.251	1.119	0.379	-0.091	-0.176	0.196
	0.304	1.005	0.388	0.336	0.409	-0.002
Rib 2	0.391	1.157	0.579	0.477	0.574	-0.183
	0.672	1.111	0.301	-0.124	-0.257	-0.057
	0.642	0.992	0.263	-0.001	0.011	0.011
Rib 3	0.825	1.118	0.308	0.000	0.083	0.018
	1.045	1.116	0.211	-0.169	-0.267	-0.065
	0.771	1.082	0.218	0.037	0.140	0.009
Rib 4	0.644	1.118	0.244	-0.078	-0.027	0.007
	0.623	1.139	0.193	-0.181	-0.247	-0.058
	0.372	1.055	0.347	0.590	0.733	-0.333
Rib 5	0.293	1.178	0.374	0.184	0.433	0.046
	0.232	1.046	0.229	-0.252	-0.131	0.249
	0.232	1.076	0.230	-0.303	-0.166	0.244

As a tire freely rolls, the treads experience compression at the contact entrance and tension during exiting; hence, two distinct peaks may occur along the traveling direction. Equation 6.2 was established corresponding to the longitudinal contact stress under compression and tension. Tables 6.2 and 6.3 present the coefficients for the first and second skewed functions, respectively. Similarly, this approach was applied to the transverse contact stresses prediction using Equation 6.3 to generate the corresponding coefficients (Table 6.4).

Comparison of the contact stress data and predicted values for both training and testing sets are illustrated in Figures 6.9 and 6.10 for the longitudinal and transverse contact stresses, respectively. It is evident that the data did not converge as closely as the vertical contact stress values. Inherent spurious behavior of horizontal contact stresses resulted in a greater spread compared to those in the vertical direction. This requires further fine-tuning; however, this represents the first step to generate three-dimensional contact stresses considering the thermomechanical interaction between the truck tire and pavement.

Table 6.2. Nonlinear Regression Coefficients to Predict Thermomechanical Longitudinal Contact Stresses for the First Skew

Rib Number	a	b	c	d	e	f
Rib 1	1.622	-1.101	1.519	-52.949	-0.360	-0.661
	2.745	2.431	-2.180	-45.573	-0.357	-0.225
	2.676	0.229	0.210	-49.649	-0.358	-0.737
Rib 2	2.113	0.484	-0.166	-1.367	-0.341	-0.333
	3.016	1.326	-0.189	-2.649	-0.339	-0.871
	5.414	0.018	-0.263	-2.008	-0.339	-0.269
Rib 3	4.573	0.372	-0.820	-0.271	-0.337	0.024
	2.920	-0.176	0.333	-0.219	-0.329	-0.547
	4.971	0.434	-1.170	-0.901	-0.336	0.000
Rib 4	5.738	-0.038	-0.011	-2.084	-0.339	-0.551
	3.370	0.755	-0.267	-2.390	-0.339	-0.812
	2.943	1.263	-0.838	-1.940	-0.343	-0.333
Rib 5	2.180	0.714	0.194	-52.757	-0.357	-0.673
	1.075	1.359	-3.144	-27.788	-0.357	-0.252
	1.555	-1.012	0.949	-52.224	-0.358	-0.691

Table 6.3. Nonlinear Regression Coefficients to Predict Thermomechanical Longitudinal Contact Stresses for the Second Skew

Rib Number	a	b	c	d	e	f
Rib 1	0.520	-0.327	0.474	0.759	1.915	1.859E+03
	-0.441	-0.984	0.538	1.458	1.860	1.727E+05
	1.470	-0.190	0.146	0.443	1.762	2.901E+04
Rib 2	0.642	0.033	-0.714	1.480	1.515	1.097E+05
	3.480	0.893	-1.360	1.463	0.609	4.434E+05
	7.366	0.040	-0.585	1.092	0.921	3.537E+05
Rib 3	3.698	1.354	-0.678	0.808	0.418	9.967E+04
	4.559	2.062	-2.709	1.608	0.423	2.116E+05
	4.682	0.813	-1.191	1.033	0.791	2.796E+05
Rib 4	6.458	-0.267	-0.108	0.888	0.951	2.564E+05
	4.392	1.168	-0.542	0.776	1.065	4.897E+05
	0.997	0.190	-0.750	1.817	1.741	3.724E+05
Rib 5	3.036	-0.535	0.150	0.916	1.859	3.708E+04
	-0.264	-1.497	1.613	0.640	2.506	9.584E+04
	-0.199	-0.613	0.964	1.142	2.021	9.445E+04

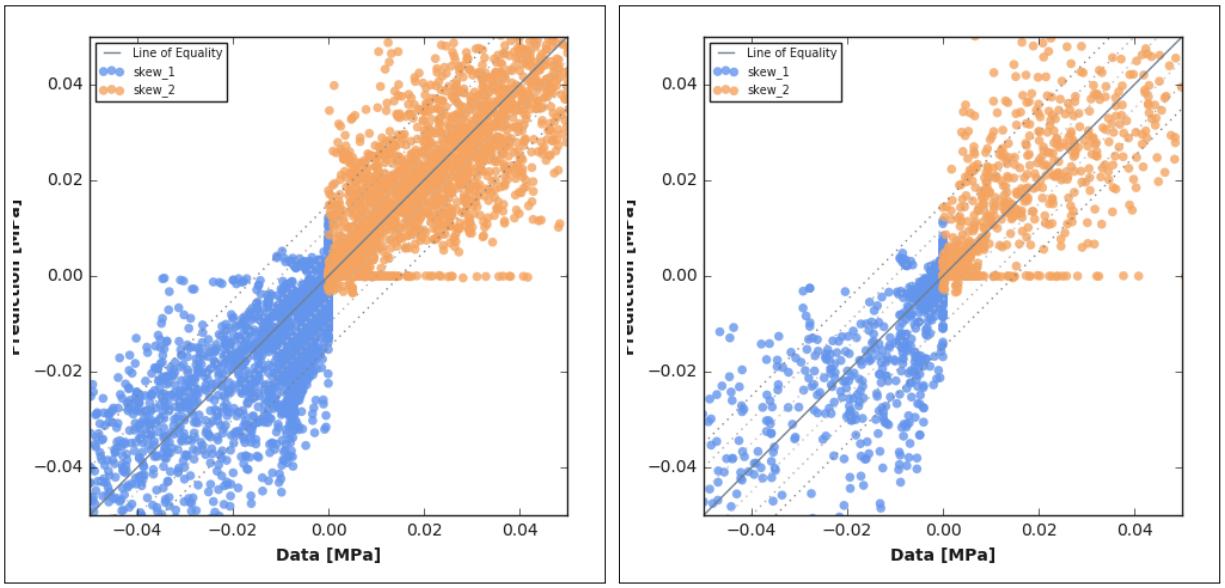

(a) Training set **(b)** Testing set

Fig. 6.9. Comparison of FE model output and nonlinear regression prediction for the (a) training and (b) testing data sets of the longitudinal contact stresses considering varying temperature profiles.

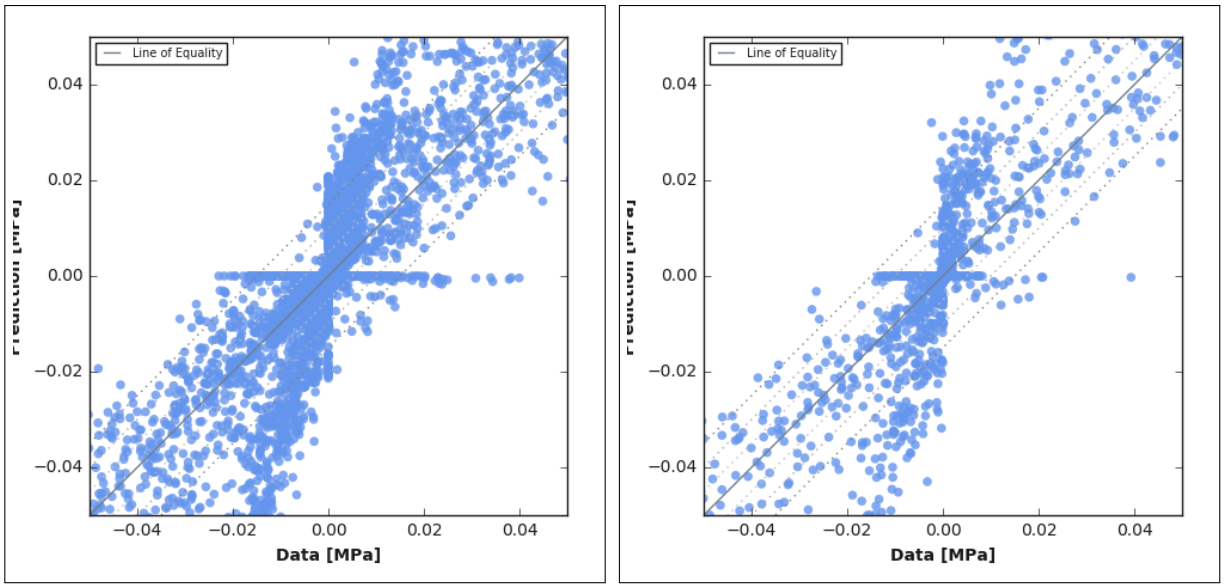

(a) Training set **(b)** Testing set

Fig. 6.10. Comparison of FE model output and nonlinear regression prediction for the (a) training and (b) testing data sets of the transverse contact stresses considering varying temperature profiles.

Table 6.4. Nonlinear Regression Coefficients to Predict Thermomechanical Transverse Contact Stresses

Rib Number	a	b	c	d	e	f
Rib 1	0.383	0.013	-0.311	0.435	0.946	0.094
	-1.288	0.565	-0.290	0.434	1.559	-0.453
	0.926	-0.072	0.000	0.413	0.212	4.941
Rib 2	1.972	-0.343	0.239	0.453	0.891	4.847
	-0.927	0.422	-0.296	0.880	0.379	-0.948
	0.167	0.079	-0.042	0.905	0.131	-0.796
Rib 3	0.511	-0.055	0.058	1.195	0.341	-0.706
	0.768	0.037	0.036	18.607	0.501	-0.960
	0.127	-0.067	0.024	0.999	0.175	-0.517
Rib 4	0.625	-0.004	0.027	1.024	0.219	-0.739
	8.673	1.330	-0.003	1.659	0.342	-0.982
	1.344	-0.334	-0.002	0.323	0.550	916.2
Rib 5	0.958	-0.036	-0.056	0.451	0.359	2.842
	0.282	2.626	-1.550	0.383	0.278	-0.849
	-0.473	0.209	-0.432	0.320	0.436	-0.576

6.4 Rolling Loss due to Temperature Profiles

Using the energy balance approach by Pillai and Fielding-Russell [109], the following expression was adopted to express the tire rolling resistance, F_r, with respect to the tire hysteresis ratio, H.

$$F_r = \frac{H F_z d_z w}{A} \tag{6.4}$$

Here F_z is the tire load in N, d_z is the tire deflection in mm, w footprint width in mm, and A is the footprint area in mm^2.

The whole tire hysteresis ratio defines the ratio of the energy lost to the total energy input into the tire as it undergoes the loading-unloading cycle. As indicated by Pillai [110], the following relation assumes that the energy loss for the rolling tire is due to hysteretic loss. Hernandez et al. [103] report that rolling resistance increased with an increase in load, while it decreased as tire-inflation pressure and temperature increased.

In this dissertation, the tire-inflation pressure and the applied load were held constant at 690 kPa and 13.5 kN, respectively, as the previous hyperelastic model completed the parametric analysis that varied the mechanical load [12]. The numerical matrix for the thermomechanical model has focused mainly on the impact of coupling and varying temperature conditions while maintaining the mechanical load. The relative rolling resistance estimates are presented in Figure 6.11.

The resulting F_r were normalized relative to the first bar of each plot. For simplicity, each bar label is assigned with the nomenclature "TPn" that corresponds to a temperature profile, indexed with n. As an example, Figure 6.11a illustrates the four uniform temperature profiles (TP1 to TP4) that was previously mentioned (-10, 25, 45, and 65 °C, respectively). The temperature profiles are arranged from the lowest temperature (blue) to highest temperature (red).

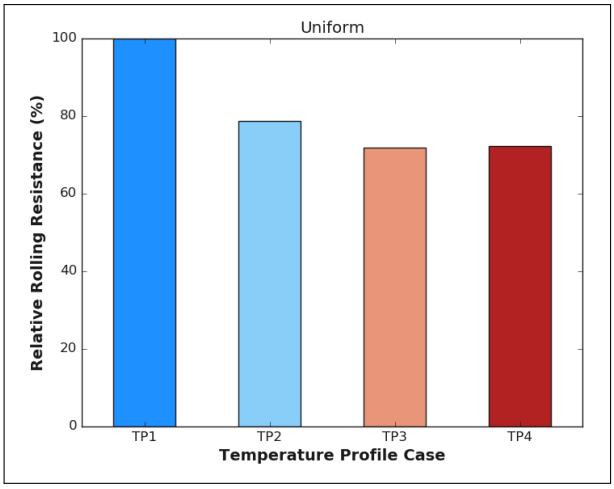

(a) Uniform temp

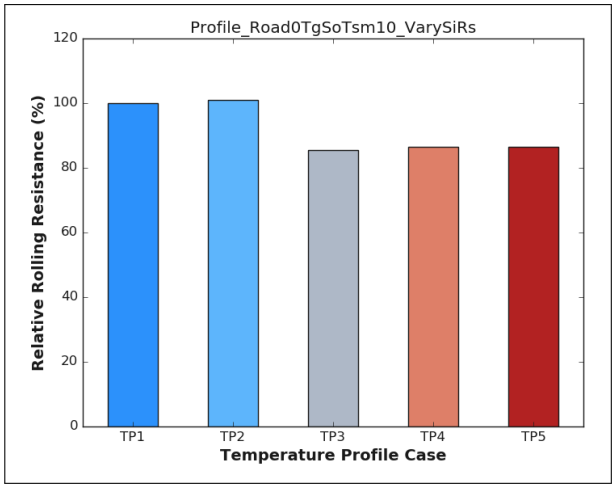

(b) Varied ambient temp with road and inner surfaces at 0 and -10°C, respectively

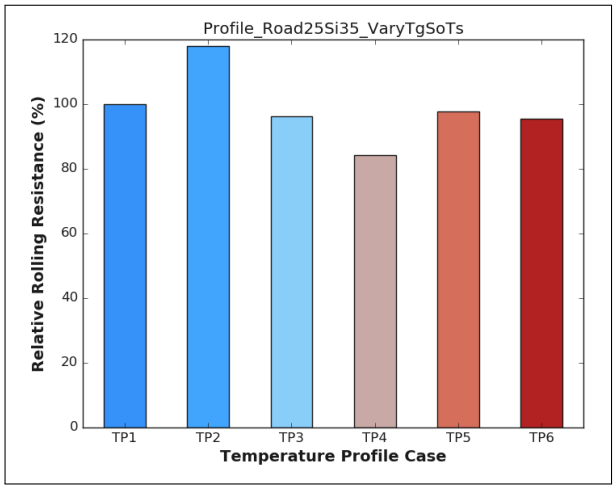

(c) Varied ambient temp with road and inner surfaces at 25 and 35°C, respectively

Fig. 6.11. Relative rolling resistance for a rolling tire under uniform and non-uniform temperatures.

Figure 6.11a illustrates a decline in rolling resistance up to 30% as the uniform temperature increased from -10 to 65°C. On the other hand, two sets of non-uniform temperature

profiles in Figures 6.11b and 6.11c (the same cases presented in Figures 6.6 and 6.7, respectively) changed up to 15%. In contrast to the uniform temperature profile, the rolling resistance variation between non-uniform temperature cases was lower. It is worth noting that the estimated whole-tire hysteresis ratio did not vary significantly despite the change in temperature profile. This could be attributed to the fact that the global hysteretic loss had a lower variation than the local hysteric loss observed within the tread section, which experienced the highest change in creep dissipation.

6.5 Summary and Conclusions

The thermomechanical coupling of a hyper-viscoelastic tire with a deformable pavement layer provided a means to quantify the impact and extent of temperature influence on the hysteretic loss of a rolling tire. The tread and shoulder regions experienced the highest difference in creep dissipation energy densities, in contrast to those of the subtread and sidewall. One could observe that a higher spread in creep dissipation energy density resulted from a lower temperature profile contrast to higher temperature profiles. While the shoulder occupied a smaller partition along the tire cross section, the resulting KDE curves within the shoulder showcased the highest disparity as the tire was subjected to varying non-uniform temperature conditions.

The heat flux distribution along the longitudinal direction of the tread section resulted in predominantly negative values under high temperatures, while those under low temperature tended to be positive values. This finding was indicative of the direction of heat transfer and revealed a higher variation and non-symmetric distribution relative to ones in the transverse and vertical directions. Moreover, the heat flux vector fields illustrated the change in direction from the low to high ambient temperature and predominantly with high magnitudes within the middle of the contact imprint. As the tire exited the contact, the tire model experienced a lag or that the remainder of the heat exchange slowly tended to ambient temperature conditions as the tire continued rolling.

Differences in the resulting contact stresses and rolling energy loss was observed between imposing uniform and non-uniform temperature profiles. Both the range and magnitudes of stresses throughout the tire-pavement contact imprint changed drastically as varying temperature profiles were implemented. Ranking the influence of thermal boundary conditions, the ambient temperature induces the highest impact on the dissipation energy and change in contact stress distribution, followed by the road and inner tire surface conditions. Moreover, the global hysteretic loss within the tire as a myriad of temperature profiles were

imposed did not change significantly; however, the creep dissipation observed within the contact imprint revealed a higher disparity.

A scheme to predict the three-dimensional contact stress distribution was established that incorporated the thermomechanical interaction between a rolling hyper-viscoelastic truck tire and a deformable pavement layer. The fully coupled thermal-stress model addressed two distinct yet intertwined perspectives: 1) establishing a thermomechanical database and prediction tool to generate contact stresses as inputs for pavement structural design, and 2) quantifying the associated rolling loss at the tire-pavement interaction that relates to tire design configurations and environmental impacts.

CHAPTER 7

FINDINGS, CONCLUSIONS, AND RECOMMENDATIONS FOR FUTURE RESEARCH

Asphalt concrete (AC) and rubber tires behave analogously, given their interdependence on temperature and loading conditions. Both are deformable in nature and the interaction between the two implicate their corresponding performance over time. As numerous heavy truck fleets traverse over flexible pavement networks, the tire-pavement interaction governs pavement responses and the eventual pavement damage.

A thermomechanical interaction model between a tire and pavement layer was developed to determine the impact of combined loading and temperature conditions on tire-pavement contact stresses and rolling loss. In the first step, a hyperelastic truck tire model was simulated over an analytically rigid surface considering free-rolling, braking, accelerating, and cornering conditions. Experimental measurements of 3D dual-tire assembly contact stresses were utilized to validate and calibrate the model. Utilizing the 3D and non-uniform contact stresses as inputs for a loaded pavement simulation, a new post-processing scheme, Domain Analysis, was established to fully quantify the impact of the contact stress distribution on multiaxial pavement response. This approach overcomes the limitation of conventional methods that rely on single-point strains, which misrepresent AC bulk behavior.

Findings from the hyperelastic truck tire model were further extended to understand aircraft landing gear tire loading over airfield pavements under the turning maneuver. Similar to the asymmetric loading when dual tire loads are imbalanced, the turning condition during taxiing exacerbates the level of near-surface responses — implying greater damage potential. The propensity of near-surface behavior may be related to slippage, which is a distress observed in airfield pavements.

Further development of the baseline hyperelastic tire model resulted in the thermomechanical model between a hyper-viscoelastic tire and deformable pavement layer. Prior to imposing a free-rolling condition, effect of uniform and resulting non-uniform temperature profiles were studied, along with the comparison of different analysis methods, friction properties, applied loads, and tire inflation pressures. Under static condition, an evident change in the contact stress and energy outputs were observed.

The final step was applying a steady state rolling condition under Lagrangian configuration on a representative pavement layer. As the pavement structural model scale and discretization already required significant computational effort, the thermomechanical model employed a deformable pavement layer to ensure feasible run time. The rolling hyperviscoelastic tire over a deformable pavement layer implemented low, intermediate, and high temperature profiles (-10, 25, 45, and 65°C) to encompass various environmental conditions. Finally, a model that incorporated the effect of thermomechanical coupling on tire-pavement contact stresses and rolling resistance is introduced. A prediction scheme to generate thermomechanical contact stresses is presented, which offers an alternative to define load inputs for a pavement structural analysis without the requirement of the tire-pavement finite element model.

7.1 Findings

Main findings of this dissertation are summarized in the following categories.

7.1.1 Hyperelastic Tire Model on a Rigid Surface

- The applied load and tire-inflation pressure significantly altered the contact stress magnitude and distribution, respectively. The maximum stress value increased, as the tire-inflation increased; whereas an increase in the applied load modified the contact length but maintained the maximum contact stress value.
- The applied load induced greater change in contact stress distribution than the tire inflation pressure and rolling velocity. The edge ribs effects became pronounced with the increase in applied load.
- Vertical and transverse contact stresses did not change significantly for tractive cases. However, the longitudinal contact stresses were impacted; they could reach the interface friction limit at the front and rear ends of the tire for the accelerating and braking scenarios, respectively.
- Cornering, on the other hand, altered the vertical and transverse contact stresses more evidently than the ones in the longitudinal direction. A shift of the contact stresses towards the inner part of the turn was identified.

7.1.2 Domain Analysis of Bulk Pavement Response

- The new Domain Analysis method captured the complex and asymmetric pavement response distribution of measured contact stresses. The steer tire, typically accounted with a lower load distribution factor relative to trailer axles, resulted in a greater damage potential at near-surface contrast to the dual tire assembly because of the earlier higher contact stresses.

- While the critical strains within the typical thin and thick pavements were marginally influenced by the change in tire-inflation pressure, Domain Analysis estimated a 17% increase in potential damage due to tire-inflation change.

- Domain Analysis can capture the impact of differential tire-inflation pressure in the dual tire assembly, which is the most common operating condition for heavy semi-trucks equipped with DTA. The results indicated an increase in potential damage under the tire with the higher inflation pressure. On the contrary, single-point responses did not capture this multiaxial difference.

- For turning maneuvers of an aircraft landing gear tire, the total applied tire load did not change; however, the distribution of the contact stresses altered the closest inner point of turn with higher magnitudes. A combined state of shear and compression at significantly high levels were observed at near-surface. Hence, special attention in the airfield pavement design, particularly turning areas, requires modifications to ensure long-lasting pavement performance and safe use of airports.

7.1.3 Thermomechanical Interaction Model

- Incorporating uniform temperature into the hyper-viscoelastic tire model increased the vertical contact stress values by 40% and changed the distribution range. A higher change in the longitudinal contact stresses than the transverse contact stresses was observed; that said, the behavior may change under a turning, braking, or accelerating maneuver.

- Using kernel density estimation plots, high temperatures impacted vertical contact stress values less than 1.0 MPa, while low temperatures defined the resulting distribution of vertical contact stress magnitudes over 1.0 MPa.

- The thermomechanical model simulated the influence of ambient, internal air, and pavement surface temperatures. Analogous to winter conditions, low temperature

profiles resulted in a smaller contact area that leads to localized stresses. On the other hand, at high temperatures like those during the summer, greater tire deformation leads to an increase in contact area and reduced contact stress magnitudes.

- The thermomechanical coupling impact on longitudinal contact stress distribution varied, especially at the leading edge of the contact imprint, while it remained low for transverse contact stresses. This behavior may change under different rolling conditions.
- The tread and shoulder regions of the tire are highly impacted by creep dissipation energy densities, contrast to those of the subtread and sidewall.
- The longitudinal direction of heat transfer is higher and has non-symmetric distribution relative to ones in the transverse and vertical directions.
- The global hysteretic loss within the tire when subjected to a myriad of temperature profiles did not change drastically; however, an evident change in the creep dissipation energy densities within the tire-pavement contact was observed.

7.2 Conclusions

The following conclusions can be made:

- The accurate prediction of tire-pavement contact stresses requires careful consideration of the geometry, material properties, and pavement surface characterization. As the tire model can be considered to be dissipative, temperature influence and coupling with the mechanical load further influences the resulting contact stresses.
- In lieu of point responses, the Domain Analysis is introduced that captures the full extent of the tire load distribution that critically defines the near-surface behavior. Also, the applicability of the Domain Analysis method could easily extend to other pavement structures, tire types and configurations, and loading conditions, along with considering other failure criteria.
- The tire rolling condition, e.g. turning or cornering, induced a different damage potential behavior and extent than in the free rolling condition. Hence, pavement sections that may experience a high magnitude and frequency of non-free-rolling conditions require modified design parameters to control potential shear and slippage distresses.

- Temperature profiles have a significant effect on the contact stresses and rolling energy loss. Tire-pavement contact stresses during the winter differ from those during the summer, further exacerbating flexible pavement responses that are also impacted both by loading and temperature.

- Pavement deformability and temperature surface conditions influence the resulting behavior at the tire-pavement interaction. A model is introduced that captured the coupled thermal-stress behavior of two deformable bodies and a prediction scheme is presented to generate tire-pavement contact stress distributions without the need of finite element simulations.

7.3 Recommendations for Future Research

This dissertation work focused on the tire-pavement interaction that explored new areas and revealed future avenues of research:

- The thermomechanical contact stress prediction, considering temperature profile variations, requires further fine-tuning including the use of advanced data science methods.

- As rolling conditions, such as braking, accelerating, and cornering, influence the contact stress distribution, the thermomechanical tire-pavement interaction model should be modified to incorporate such effects. Future work should also implement deep learning methods to extend the current tire-pavement contact stress database, while strategically planning the finite element simulation matrix (i.e. minimize the number of simulations while maintaining good accuracy in predicting contact stresses).

- Due to the complexity of the coupling, the temperature profiles were excited by assigning temperature sink conditions. A more robust definition that represents realistic and local conditions should be introduced and provided to transportation agencies for modifying the applied loads.

- Domain Analysis is a baseline procedure that identifies the importance of characterizing the bulk behavior of pavements; however, the penalty scheme for defining potential damage offers a clear opportunity for improvement. Additionally, damage evolution needs to be appended.

- Some studies have suggested that a parallel rheological framework might be more appropriate than hyper-viscoelastic properties to characterize tires. An in-depth investigation may be needed to define the most appropriate approach moving forward.
- The full coupling of the tire and pavement layer implemented implicit analysis; however, a more advanced scheme to account for heat generation within the tire should be explored via explicit analysis.
- Pavement roughness increases the tire dynamic loading, which may also affect the thermomechanical interaction model. An exploratory study is needed, including characterization of the tire-pavement interface inhomogeneous friction condition, along with pressure- and temperature-dependency.

REFERENCES

[1] D. Cooke, "Engines for change: From cell phones to sodas, how new truck standards can improve the way america ships goods," Union of Concerned Scientists USA, MA, Tech. Rep., March 2015.

[2] M. Mammetti, D. Gallegos, A. Freixas, and J. Muñoz, "The influence of rolling resistance on fuel consumption in heavy-duty vehicles," *SAE International*, 1981.

[3] D. Whicker, A. L. Browne, D. J. Segalman, and L. E. Wickliff, "A thermomechanical approach to tire power loss modeling," *Tire Science and Technology*, vol. 9, no. 1–4, pp. 3–18, 1981.

[4] M. G. Pottinger, "Apparatus for measuring tire tread force and motion," Jan. 22 1991, uS Patent 4,986,118.

[5] M. Pottinger and J. McIntyre III, "Effect of suspension alignment and modest cornering on the footprint behavior of performance tires and heavy duty radial tires," *Tire Science and Technology*, vol. 27, no. 3, pp. 128–160, 1999.

[6] M. De Beer, J. Groenendijk, and C. Fischer, "Three dimensional contact stresses under the lintrack wide base single tyres, measured with the vehicle-road surface pressure transducer array (vrspta) system in south africa," Council for Scientific and Industrial Research, Tech. Rep., 1996.

[7] M. De Beer, C. Fisher, and L. Kannemeyer, "Towards the application of stress-in-motion (sim) results in pavement design and infrastructure protection," in *Loads, Roads and the Information Highway*, 2004.

[8] S. Koehne and A. Rieger, "Measurement of the slip of tread blocks in the contact patch," *Tire Science and Technology*, vol. 32, no. 2, pp. 69–80, 2004.

[9] S. Koehne, B. Matute, and R. Mundl, "Evaluation of tire tread and body interactions in the contact patch," *Tire Science and Technology*, vol. 31, no. 3, pp. 159–172, 2003.

[10] J. A. Hernandez, I. Al-Qadi, and M. De Beer, "Impact of tire loading and tire pressure on measured 3d contact stresses," in *Airfield and Highway Pavement 2013: Sustainable and Efficient Pavements*. ASCE, 2013, pp. 551–560.

[11] J. Hernandez, A. Gamez, I. Al-Qadi, and M. De Beer, "Analytical approach for predicting three-dimensional tire-pavement contact load," *Transportation Research Record: Journal of the Transportation Research Board*, vol. 2456, pp. 75–84, 2014.

[12] J. A. Hernandez, A. Gamez, M. Shakiba, and I. L. Al-Qadi, "Numerical prediction of three-dimensional tire-pavement contact stresses," Illinois Center for Transportation, Tech. Rep., 2017.

[13] H. Wang, I. L. Al-Qadi, and I. Stanciulescu, "Effect of surface friction on tire–pavement contact stresses during vehicle maneuvering," *Journal of Engineering Mechanics*, 2014.

[14] J. Oden and J. Martins, "Models and computational methods for dynamic friction phenomena," *Computer Methods in Applied Mechanics and Engineering*, vol. 52, no. 1, pp. 527 – 634, 1985. [Online]. Available: http://www.sciencedirect.com/science/article/pii/004578258590009X

[15] J. Y. Wong, *Theory of ground vehicles*. John Wiley & Sons, 2008.

[16] J. Pauwelussen, *Essentials of vehicle dynamics*. Butterworth-Heinemann, 2014.

[17] AASHTO, "Mechanistic-empirical pavement design guide-a manual of practice," AASHTO, Tech. Rep., 2008.

[18] E. C. D. ARA, Inc., "Guide for mechanistic-empirical design of new and rehabilitated pavement structures," National Cooperative Highway Research Program, Tech. Rep., 2004.

[19] O. E. Gungor, I. L. Al-Qadi, A. Gamez, and J. A. Hernandez, "Development of adjustment factors for mepdg pavement responses utilizing finite-element analysis," *Journal of Transportation Engineering, Part A: Systems*, vol. 143, no. 7, p. 04017022, 2017.

[20] L. A. Myers, R. Roque, and B. E. Ruth, "Mechanisms of surface-initiated longitudinal wheel path cracks in high-type bituminous pavements," *Journal of the Association of Asphalt Paving technologists*, vol. 67, 1998.

[21] C. Drakos, R. Roque, and B. Birgisson, "Effects of measured tire contact stresses on near-surface rutting," *Transportation Research Record: Journal of the Transportation Research Board*, no. 1764, pp. 59–69, 2001.

[22] H. Wang and I. Al-Qadi, "Combined effect of moving wheel loading and three-dimensional contact stresses on perpetual pavement responses," *Transportation Research Record: Journal of the Transportation Research Board*, vol. 2095, pp. 53–61, 2009.

[23] P. J. Yoo and I. L. Al-Qadi, "The truth and myth of fatigue cracking potential in hot-mix asphalt: Numerical analysis and validation," *Asphalt Paving Technology-Proceedings*, vol. 77, p. 549, 2008.

[24] I. L. Al-Qadi and P. J. Yoo, "Effect of surface tangential contact stresses on flexible pavement response (with discussion)," *Journal of the Association of Asphalt Paving Technologists*, vol. 76, 2007.

[25] M. A. Elseifi, I. L. Al-Qadi, and P. J. Yoo, "Viscoelastic modeling and field validation of flexible pavements," *Journal of engineering mechanics*, vol. 132, no. 2, pp. 172–178, 2006.

[26] H. Wang and I. L. Al-Qadi, "Impact quantification of wide-base tire loading on secondary road flexible pavements," *Journal of Transportation Engineering*, vol. 137, no. 9, pp. 630–639, 2010.

[27] P. Yoo, I. L. Al-Qadi, M. Elseifi, and I. Janajreh, "Flexible pavement responses to different loading amplitudes considering layer interface condition and lateral shear forces," *The International Journal of Pavement Engineering*, vol. 7, no. 1, pp. 73–86, 2006.

[28] P. Yoo and I. Al-Qadi, "Effect of transient dynamic loading on flexible pavements," *Transportation Research Record: Journal of the Transportation Research Board*, no. 1990, pp. 129–140, 2007.

[29] I. Al-Qadi, H. Wang, and E. Tutumluer, "Dynamic analysis of thin asphalt pavements by using cross-anisotropic stress-dependent properties for granular layer," *Transportation Research Record: Journal of the Transportation Research Board*, no. 2154, pp. 156–163, 2010.

[30] M. Kim, E. Tutumluer, and J. Kwon, "Nonlinear pavement foundation modeling for three-dimensional finite-element analysis of flexible pavements," *International Journal of Geomechanics*, 2009.

[31] T. Freeman and S. Carpenter, "Characterizing permanent deformation in asphalt concrete placed over portland cement concrete pavements," *Transportation Research Record*, vol. 1070, 1986.

[32] M. Ameri-Gaznon and D. N. Little, "Permanent deformation potential in asphalt concrete overlay over portland cement concrete pavements," Texas Transportation Institute, Tech. Rep. FHWA/TX-88/452-3F, 1988.

[33] M. Ameri-Gaznon, J. W. Button, D. Perdomo, D. Little, and D. Zollinger, "Avoiding early failure of intersection pavements," Texas Transportation Institute, Tech. Rep. 1172-1F, 1989.

[34] J. Button and D. Perdomo, "Identifying and correcting rut-susceptible asphalt mixtures," Report . Federal Highway Administration and Texas Department of Transportation, Tech. Rep. FHWA-TX-91/1121-2F, 1991.

[35] H. Wang and I. Al-Qadi, "Near-surface pavement failure under multiaxial stress state in thick asphalt pavement," *Transportation Research Record: Journal of the Transportation Research Board*, vol. 2154, pp. 91–99, 2010.

[36] H.-J. Lee, J. S. Daniel, and Y. R. Kim, "Continuum damage mechanics-based fatigue model of asphalt concrete," *Journal of Materials in Civil Engineering*, vol. 12, no. 2, pp. 105–112, 2000.

[37] J. S. Daniel and Y. R. Kim, "Development of a simplified fatigue test and analysis procedure using a viscoelastic, continuum damage model (with discussion)," *Journal of the Association of Asphalt Paving Technologists*, vol. 71, 2002.

[38] N. Gibson, C. Schwartz, R. Schapery, and M. Witczak, "Viscoelastic, viscoplastic, and damage modeling of asphalt concrete in unconfined compression," *Transportation Research Record: Journal of the Transportation Research Board*, no. 1860, pp. 3–15, 2003.

[39] R. Kim, G. Chehab, R. Schapery, M. Witczak, and R. Bonaquist, "Characterization of asphalt concrete in uniaxial tension using a viscoelastoplastic continuum damage model," *Journal of the Association of Asphalt Paving Technologists*, pp. 315–355, 2003.

[40] D.-W. Park, "Characterization of permanent deformation in asphalt concrete using a laboratory prediction method and an elastic-viscoplastic model," Ph.D. dissertation, Texas A & M University, College Station, Texas, 2004.

[41] Q. Dai, M. H. Sadd, and Z. You, "A micromechanical finite element model for linear and damage-coupled viscoelastic behaviour of asphalt mixture," *International journal for numerical and analytical methods in geomechanics*, vol. 30, no. 11, pp. 1135–1158, 2006.

[42] Y.-R. Kim, D. D. H. Allen, and D. N. Little, "Computational constitutive model for predicting nonlinear viscoelastic damage and fracture failure of asphalt concrete mixtures," *International Journal of Geomechanics*, vol. 7, no. 2, pp. 102–110, 2007.

[43] M. Perl, J. Uzan, and A. Sides, "Visco-elasto-plastic constitutive law for a bituminous mixture under repeated loading," *Transportation Research Record*, vol. 911, pp. 20–26, 1983.

[44] Y. Lu and P. J. Wright, "Numerical approach of visco-elastoplastic analysis for asphalt mixtures," *Computers & structures*, vol. 69, no. 2, pp. 139–147, 1998.

[45] A. Collop, A. Scarpas, C. Kasbergen, and A. de Bondt, "Development and finite element implementation of stress-dependent elastoviscoplastic constitutive model with damage for asphalt," *Transportation Research Record: Journal of the Transportation Research Board*, no. 1832, pp. 96–104, 2003.

[46] J. M. Krishnan and K. Rajagopal, "Triaxial testing and stress relaxation of asphalt concrete," *Mechanics of Materials*, vol. 36, no. 9, pp. 849–864, 2004.

[47] L. Tashman, E. Masad, D. N. Little, and R. Lytton, "Damage evolution in triaxial compression tests of hma at high temperatures (with discussion)," *Journal of the Association of Asphalt Paving Technologists*, vol. 73, 2004.

[48] Y. Kim, B. Underwood, S. Mun, and M. Guddati, "Perpetual pavement evaluation using the viscoelastic continuum damage finite element program," in *Proceedings of the 2006 International Conference on Perpetual Pavement, Columbus, Ohio*, 2006.

[49] B. Underwood, Y. R. Kim, S. Savadatti, S. Thirunavukkarasu, and M. Guddati, "Response and fatigue performance modeling of alf pavements using 3-d finite element analysis and a simplified viscoelastic continuum damage model," in *Asphalt Paving Technology 2009, AAPT*, 2009.

[50] R. K. A. Al-Rub, T. You, E. A. Masad, and D. N. Little, "Mesomechanical modeling of the thermo-viscoelastic, thermo-viscoplastic, and thermo-viscodamage response of asphalt concrete," *International Journal of Advances in Engineering Sciences and Applied Mathematics*, vol. 3, no. 1-4, pp. 14–33, 2011.

[51] M. K. Darabi, R. K. A. Al-Rub, E. A. Masad, C.-W. Huang, and D. N. Little, "A modified viscoplastic model to predict the permanent deformation of asphaltic materials under cyclic-compression loading at high temperatures," *International Journal of Plasticity*, vol. 35, pp. 100–134, 2012.

[52] M. K. Darabi, R. K. A. Al-Rub, E. A. Masad, and D. N. Little, "Thermodynamic-based model for coupling temperature-dependent viscoelastic, viscoplastic, and viscodamage constitutive behavior of asphalt mixtures," *International Journal for Numerical and Analytical Methods in Geomechanics*, vol. 36, no. 7, pp. 817–854, 2012.

[53] Y. Zhang, M. Bernhardt, G. Biscontin, R. Luo, and R. L. Lytton, "A generalized drucker–prager viscoplastic yield surface model for asphalt concrete," *Materials and Structures*, vol. 48, no. 11, pp. 3585–3601, 2015.

[54] J. A. Hernandez, A. Gamez, and I. L. Al-Qadi, "Effect of wide-base tires on nationwide flexible pavement systems: Numerical modeling," *Transportation Research Record: Journal of the Transportation Research Board*, 2016, accepted for Publication.

[55] S. Helwany, *Applied Soil Mechanics with ABAQUS Applications*. John Wiley & Sons, Inc., 2007.

[56] S. Gokhale, D. Anderson, D. W. Christensen, and R. Bonaquist, "Simplified protocol for triaxial testing of hot-mix asphalt concrete," in *Asphalt Paving Technology 2009, AAPT*, 2005.

[57] I. Al-Qadi, H. Wang, P. Yoo, and S. Dessouky, "Dynamic analysis and in situ validation of perpetual pavement response to vehicular loading," *Transportation Research Record: Journal of the Transportation Research Board*, vol. 2087, pp. 29–39, 2008.

[58] *Advisory Circular 150/5320-6F/Airport Pavement Design and Evaluation*, US Department of Transportation, Federal Aviation Administration, 2016.

[59] A. Gamez, J. A. Hernandez, H. Ozer, and I. L. Al-Qadi, "Development of domain analysis for determining potential pavement damage," *Journal of Transportation Engineering, Part B: Pavements*, vol. 144, no. 3, p. 04018030, 2018.

[60] *Advisory Circular 150/5380-6C/Guidelines and Procedures for Maintenance of Airport Pavements*, US Department of Transportation, Federal Aviation Administration, 2014.

[61] C. J. Bognacki, A. Frisvold, and T. Bennert, "Investigation of asphalt pavement slippage failures on runway 4r-22l, newark international airport," in *2007 Worldwide Airport Technology Transfer ConferenceFederal Aviation AdministrationAmerican Association of Airport Executives*, 2007.

[62] I. Song and N. Garg, "High tire pressure and temperature effects on hot mix asphalt concrete permanent deformation using customized asphalt pavement analyzer," in *Proc., 2010 FAA Worldwide Technology Transfer Conf*, 2010.

[63] K. Cook, N. Garg, A. Singh, and M. Flynn, "Detection of delamination in the hma layer of runway pavement structure using asphalt strain gauges," *Journal of Transportation Engineering*, vol. 142, no. 11, p. 04016047, 2016.

[64] X. Hu and L. F. Walubita, "Effects of layer interfacial bonding conditions on the mechanistic responses in asphalt pavements," *Journal of Transportation Engineering*, vol. 137, no. 1, pp. 28–36, 2010.

[65] K. Guo and D. Lu, "Unitire: Unified tire model for vehicle dynamic simulation," *Vehicle System Dynamics*, vol. 45, no. S1, pp. 79–99, 2007.

[66] J. A. Hernandez and I. L. Al-Qadi, "Airfield pavement response caused by heavy aircraft takeoff: Advanced modeling for consideration of wheel interaction," *Transportation Research Record: Journal of the Transportation Research Board*, vol. 2471, pp. 40–47, 2015.

[67] J. A. Hernandez, A. Gamez, and I. L. Al-Qadi, "Domain analysis for airfield pavement: Moving forward from point responses," in *Tenth International Conference on the Bearing Capacity of Roads, Railways and Airfields*, 2017.

[68] R. Aponte and C. Budesa, "National airport pavement test facility construction cycle 7 history report," U.S. Department of Transportation, Federal Aviation Administration, Tech. Rep., May 2016.

[69] K. D. Hjelmstad, Z. Qiuhai, and J. Kim, "Elastic Pavement Analysis Using Infinite Elements," *Transportation Research Record: Journal of the Transportation Research Board*, vol. 1568, pp. 72–76, 1997.

[70] H. Wang, I. L. Al-Qadi, S. Portas, and M. Coni, "Three-dimensional finite element modeling of instrumented airport runway pavement responses," *Transportation Research Record: Journal of the Transportation Research Board*, vol. 2367, pp. 76–83, 2013.

[71] J. A. Hernandez, A. Gamez, and I. L. Al-Qadi, "Effect of wide-base tires on nationwide flexible pavement systems: Numerical modeling," *Transportation Research Record: Journal of the Transportation Research Board*, vol. 2590, pp. 104–112, 2016.

[72] I. L. Al-Qadi, J. A. Hernandez, A. Gamez, M. Ziyadi, O. E. Gungor, and S. Kang, "Impact of wide-base tires on pavements: A national study," *Transportation Research Record*, p. 0361198118757969, 2018.

[73] A. Gamez, J. A. Hernandez, and I. L. Al-Qadi, "Development of domain analysis to predict multi-axial flexible airfield pavement responses due to gear and environmental loadings," *Transportation Research Record*, p. 0361198118758025, 2018.

[74] T. Ebbott, R. L. Hohman, J. P. Jeusette, and V. Kerchman, "Tire temperature and rolling resistance prediction with finite element analysis," *Tire Science and Technology*, vol. 27, pp. 2–21, 1999.

[75] S. Yeow, M. El-Sherbiny, and T. Newcomb, "Thermal analysis of a tyre during rolling or sliding," *Wear*, vol. 48, pp. 157–171, 1978.

[76] J. Mc Allen, A. M. Cuitiño, and V. Sernas, "Numerical investigation of the deformation characteristics and heat generation in pneumatic aircraft tires: Part ii. thermal modeling," *Finite Elements in Analysis and Design*, vol. 23, pp. 265–290, 1990.

[77] R. R. Hegmon and J. J. Henry, "Thermal analysis of a skidding tire," *Wear*, vol. 24, pp. 361–380, 1973.

[78] D. Prevorsek, Y. Kwon, R. Sharma, and C. Beringer, "Analysis of tire deformation in operation from the data of temperature rise," 1980.

[79] N. M. Trivisonno, "Non-steady-state thermal analysis of a rolling aircraft tire," sae paper 720871, society of automotive engineers," 1972.

[80] N. M. Trivisonno, "Applications of tire thermography to rolling resistance," in *Proceedings of the Conference on Tire Rolling Losses and Fuel Economy – an T and D Planning Workship*, October 1977, pp. 103–109.

[81] D. Prevorsek, Y. Kwon, R. Sharma, and C. Beringer, "The tire rolling resistance – via viscoelastic analysis of components," in *Proceedings of the Conference on Tire Rolling Losses and Fuel Economy – an T and D Planning Workship*, October 1977, pp. 75–86.

[82] S. Futamura and G. A., "A simple method of handling thermomechanical coupling for temperature computation in a rolling tire," *Tire Science and Technology*, vol. 32, pp. 56–68, 2004.

[83] K. V. Narasimha Rao, R. K. Kumar, and P. C. Bohara, "A sensitivity analysis of design attributes and operating conditions on tyre operating temperatures and rolling resistance using finite element analysis," *Proceedings of the Institution of Mechanical Engineers, Part D: Journal of Automobile Engineering*, vol. 220, no. 5, pp. 501–517, 2006. [Online]. Available: http://pid.sagepub.com/content/220/5/501.abstract

[84] Y. Li, W. Y. Liu, and S. Frimpong, "Effect of ambient temperature on stress, deformation and temperature of dump truck tire," *Engineering Failure Analysis*, vol. 23, pp. 55–62, 2012.

[85] K. Anupam, S. Srirangam, A. Scarpas, and C. Kasbergen, "Influence of temperature on tire-pavement friction," *Transportation Research Record: Journal of the Transportation Research Board*, vol. 2369, pp. 114–124, 2013.

[86] R. Behnke and M. Kaliske, "Thermo-mechanically coupled investigation of steady state rolling tires by numerical simulation and experiment," *International Journal of Non-Linear Mechanics*, vol. 68, pp. 101 – 131, 2015, mechanics of Rubber - in Memory of Alan Gent. [Online]. Available: http://www.sciencedirect.com/science/article/pii/S0020746214001371

[87] S. Srirangam, K. Anupam, A. Scarpas, and C. Kasbergen, "Development of a thermomechanical tyre–pavement interaction model," *International Journal of Pavement Engineering*, vol. 16, no. 8, pp. 721–729, 2015. [Online]. Available: http://dx.doi.org/10.1080/10298436.2014.946927

[88] J. A. Hernandez and I. L. Al-Qadi, "Hyperelastic modeling of wide-base tire and prediction of its contact stresses," *Journal of Engineering Mechanics*, vol. 142, no. 2, p. 04015084, 2015.

[89] T. Tang, D. Johnson, R. E. Smith, and S. D. Felicelli, "Numerical evaluation of the temperature field of steady-state rolling tires," *Applied Mathematical Modelling*, vol. 38, no. 5-6, pp. 1622–1637, 2014.

[90] F. Farroni, A. Sakhnevych, and F. Timpone, "Physical modelling of tire wear for the analysis of the influence of thermal and frictional effects on vehicle performance," *Proceedings of the Institution of Mechanical Engineers, Part L: Journal of Materials: Design and Applications*, vol. 231, no. 1-2, pp. 151–161, 2017.

[91] L. Andersen, J. Larsen, E. Fraser, B. Schmidt, and J. Dyre, "Rolling resistance measurement and model development," *Journal of Transportation Engineering*, vol. 141, no. 2, p. 04014075, 2015. [Online]. Available: http://dx.doi.org/10.1061/(ASCE)TE.1943-5436.0000673

[92] E. Tompkins, *History of Pneumatic Tyre*. Lavenham, Suffolk, UK: Eastland Press, 1981.

[93] D. J. Schuring, "Effect of tire rolling loss on vehicle fuel consumption," *Tire Science and Technology*, vol. 22, pp. 148–161, 1994.

[94] D. J. Schuring, "The influence of rolling resistance on fuel consumption in heavy-duty vehicles," *SAE International*, 2013.

[95] D. J. Schuring, "The rolling loss of pneumatic tires," *Rubber Chemistry and Technology*, vol. 53, no. 3, pp. 600–727, 1980. [Online]. Available: http://dx.doi.org/10.5254/1.3535054

[96] J. Cho, H. Lee, W. Jeong, K. Jeong, and K. Kim, "Numerical estimation of rolling resistance and temperature distribution of 3-d periodic patterned tire," *International Journal of Solids and Structures*, vol. 50, no. 1, pp. 86 – 96, 2013. [Online]. Available: http://www.sciencedirect.com/science/article/pii/S002076831200385X

[97] F. Williams and T. Dudek, "Load-deflection hysteresis and its relationship to tire rolling resistance," in *Rubber division symposia*, ser. Rubber Division, vol. 1. Akron, OH: American Chemical Society, October 1983, pp. 105–139.

[98] J. R. Luchini, J. M. Peters, and R. H. Arthur, "Tire rolling loss computation with the finite element method," *Tire Science and Technology*, vol. 22, no. 4, pp. 206–222, 1994. [Online]. Available: http://dx.doi.org/10.2346/1.2139542

[99] V. Vantsevich and C. Stuart, "Probabilistic interactions of vehicles with surroundings: Modeling for dynamic control," in *ASME 2007 International Mechanical Engineering Congress and Exposition*, ser. Mechanical Systems and Control, Parts A, B, and C, vol. 9. Seattle, WA: American Society of Mechanical Engineers, November 2007, pp. 105–139.

[100] X. Qiu, "Full two-dimensional model for rolling resistance. ii: Viscoelastic cylinders on rigid ground," *Journal of Engineering Mechanics*, vol. 135, no. 1, pp. 20–30, 2009. [Online]. Available: http://dx.doi.org/10.1061/(ASCE)0733-9399(2009)135:1(20)

[101] T. Sandberg, "Heavy truck modeling for fuel consumption simu- lations and measurements," Ph.D. dissertation, Linkőping University, S-581 83 Linkőping, Sweden, 2001.

[102] O. Chupin, J.-M. Piau, and A. Chabot, "Evaluation of the structure-induced rolling resistance (srr) for pavements including viscoelastic material layers," *Materials and Structures*, vol. 46, no. 4, pp. 683–696, 2012. [Online]. Available: http://dx.doi.org/10.1617/s11527-012-9925-z

[103] J. A. Hernandez, I. L. Al-Qadi, and H. Ozer, "Baseline rolling resistance for tires' on-road fuel efficiency using finite element modeling," *International Journal of Pavement Engineering*, vol. 18, no. 5, pp. 424–432, 2017. [Online]. Available: https://doi.org/10.1080/10298436.2015.1095298

[104] R. E. Kim, S. Kang, B. F. Spencer, I. L. Al-Qadi, and H. Ozer, "New stochastic approach of vehicle energy dissipation on nondeformable rough pavements," *Journal of Engineering Mechanics*, vol. 143, no. 4, p. 04016118, 2017.

[105] R. E. Kim, S. Kang, B. F. Spencer, H. Ozer, and I. L. Al-Qadi, "Stochastic analysis of energy dissipation of a half-car model on nondeformable rough pavement," *Journal of Transportation Engineering, Part B: Pavements*, vol. 143, no. 4, p. 04017016, 2017.

[106] S. Kang, H. Ozer, I. L. Al-Qadi, and B. F. Spencer, "Stochastic analysis of rolling resistance energy dissipation for a tractor-trailer model," *Transportation Research Record*, vol. 2673, no. 11, pp. 593–603, 2019.

[107] X. Liu and I. L. Al-Qadi, "A mechanistic approach to predict excess fuel consumption of a 3d truck on rough pavements," *Transportation Research Record*, 2020, (in press).

[108] A. Jayme and I. L. Al-Qadi, "Thermomechanical coupling of a hyper-viscoelastic truck tire and a pavement layer and its impact on three-dimensional contact stresses," *Transportation Research Record: Journal of the Transportation Research Board*, in review.

[109] P. Pillai and G. Fielding-Russell, "Tire rolling resistance from whole-tire hysteresis ratio," *Rubber chemistry and technology*, vol. 65, no. 2, pp. 444–452, 1992.

[110] P. Pillai, "Total tire energy loss comparison by the whole tire hysteresis and the rolling resistance methods," *Tire Science and Technology*, vol. 23, no. 4, pp. 256–265, 1995.

APPENDIX A

MODELING ASSUMPTIONS AND LIMITATIONS

Table A.1. Summary of Modeling Assumptions and Limitations

Chapter	Assumptions	Limitations
CH 2 *Hyperelastic Tire Rolling on a Rigid Surface*	· Hyperelastic characterization for rubber using Mooney-Rivlin relation · Velocity-dependent friction, applied uniformly between the tire tread and analytically rigid pavement surface · Arbitrary Lagrangian-Eulerian formulation to simulate various rolling conditions	· Tire material characterization can only account for mechanical loading, without temperature dependency · Pavement surface definition does not include the influence of pavement roughness, texture, and deformability, applied normal stress, and temperature
CH 3 *Development of Domain Analysis to Evaluate Pavement Bulk Behavior*	· Tire loading was applied using three-dimensional contact stress distribution · Zoning along the cross-section is user-dependent; vertical limit assumed in range of 50 to 100 mm, while the horizontal limit assumed to be 50 mm extended from the left and right of the contact width · Modified Drucker-Prager was selected as the baseline failure criteria for the penalty/weight factor · Pre-selected critical zones related to typical regions of pavement distress	· Failure criteria may not accurately represent asphalt material behavior · Domain analysis ratio links realistic tire loading condition to pavement bulk response; however, the method will require future improvement in order to integrate the results into conventional pavement design and analysis · Description of pavement bulk response was constrained to the cumulative stress/strain state without evolution over time · Final scalar ratio requires a reference case for the relative comparison
CH 4 *Influence of Aircraft Tire Turning Maneuver on Pavement Responses*	· Free-rolling aircraft tire contact stresses by Hernandez and Al-Qadi [66] were transformed to consider various levels of turning using factors, which were established using results from Chapter 2 · Airfield pavements assumed linear viscoelastic asphalt concrete layers and stress-dependent granular and subgrade layers · Inputs for the failure criterion were altered but assumed the same Modified Drucker-Prager definition	· Limited availability of aircraft tire-pavement contact stresses constrained the analyses to one type of commercial aircraft

Table A.2. Summary of Modeling Assumptions and Limitations Cont.

Chapter	Assumptions	Limitations
CH 5 *Thermomechanical Coupling of a Hyper-Viscoelastic Truck Tire and A Pavement Layer and Its Impact on Three-Dimensional Contact Stresses*	· Rubber is characterized as hyper-viscoelastic material and implemented C3D8RHT elements (brick element with reduced integration and hybrid with temperature) · Friction between the tire and pavement surfaces in contact is dependent only on velocity, without properly accounting for dependency on normal stress or temperature · Temperature sink boundaries were user-defined to represent the steady-state condition of a rolling truck tire · Pavement was assumed as an elastic layer with a corresponding surface temperature sink	· Heat generation for the thermomechanical model is mainly due to frictional heat generation; future improvement may include heat generation due to viscous dissipation within the rubber sections Inflation pressure was maintained; future improvement may include a user subroutine to change the inflation pressure as the tire "heats" up · Friction was specified and maintained as the traveling speed was constant during the simulation; however, in reality the friction value changes due to surface texture and temperature conditions

APPENDIX B

ROLLING HYPERELASTIC TIRE: *FREE-ROLLING*

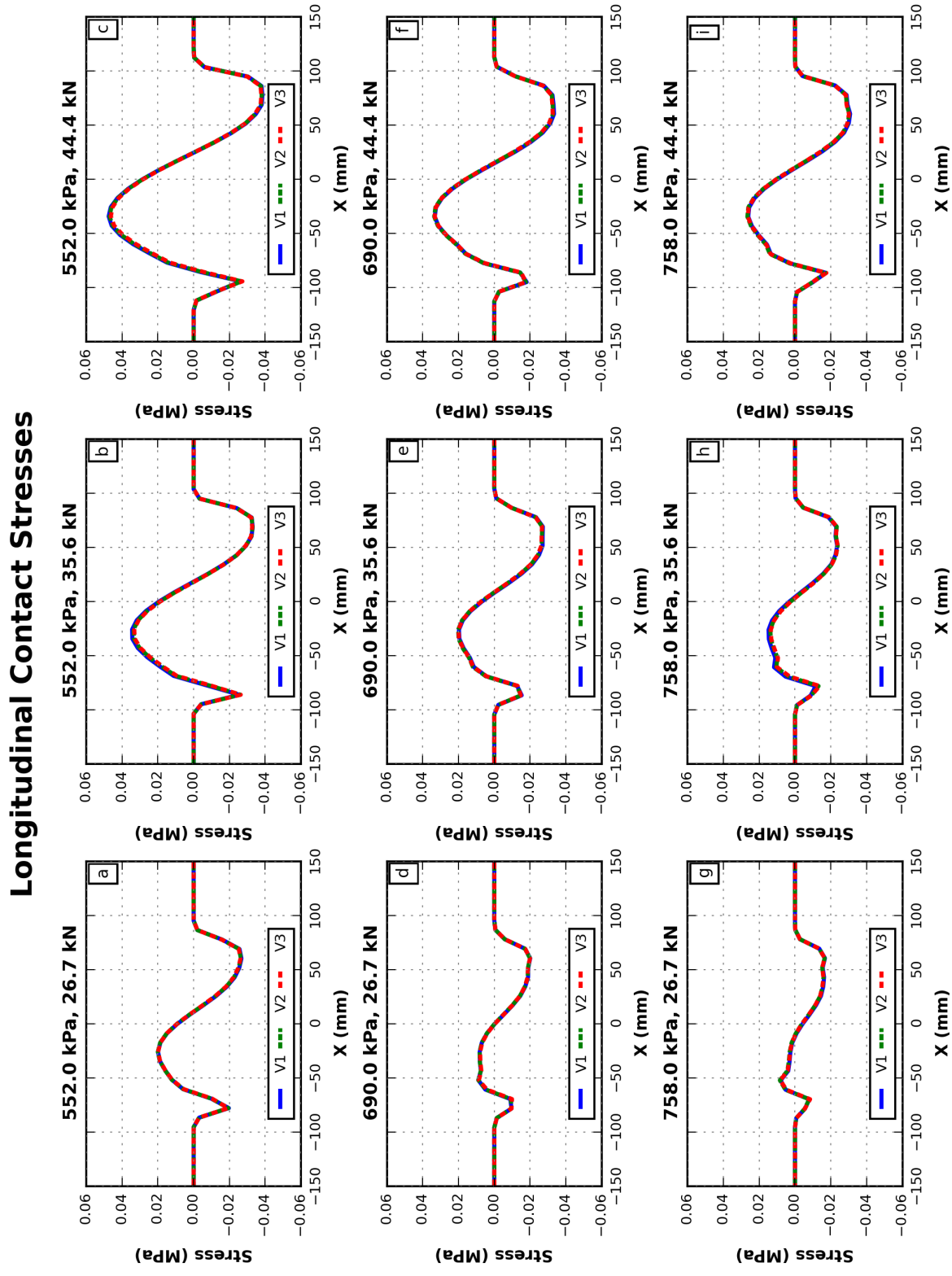

Fig. B.1. Longitudinal contact stresses under free-rolling and varying speeds.

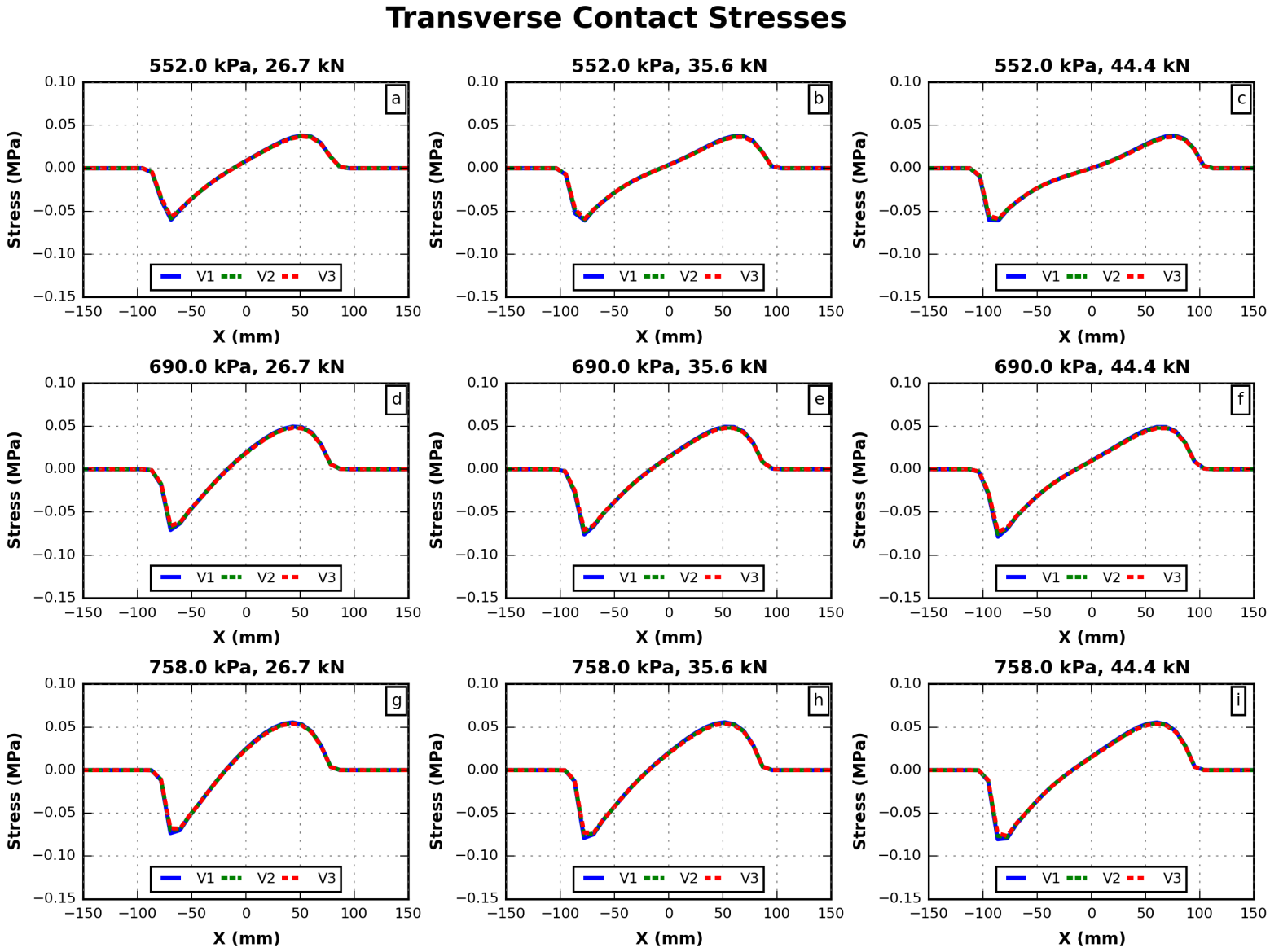

Fig. B.2. Transverse contact stresses under free-rolling and varying speeds.

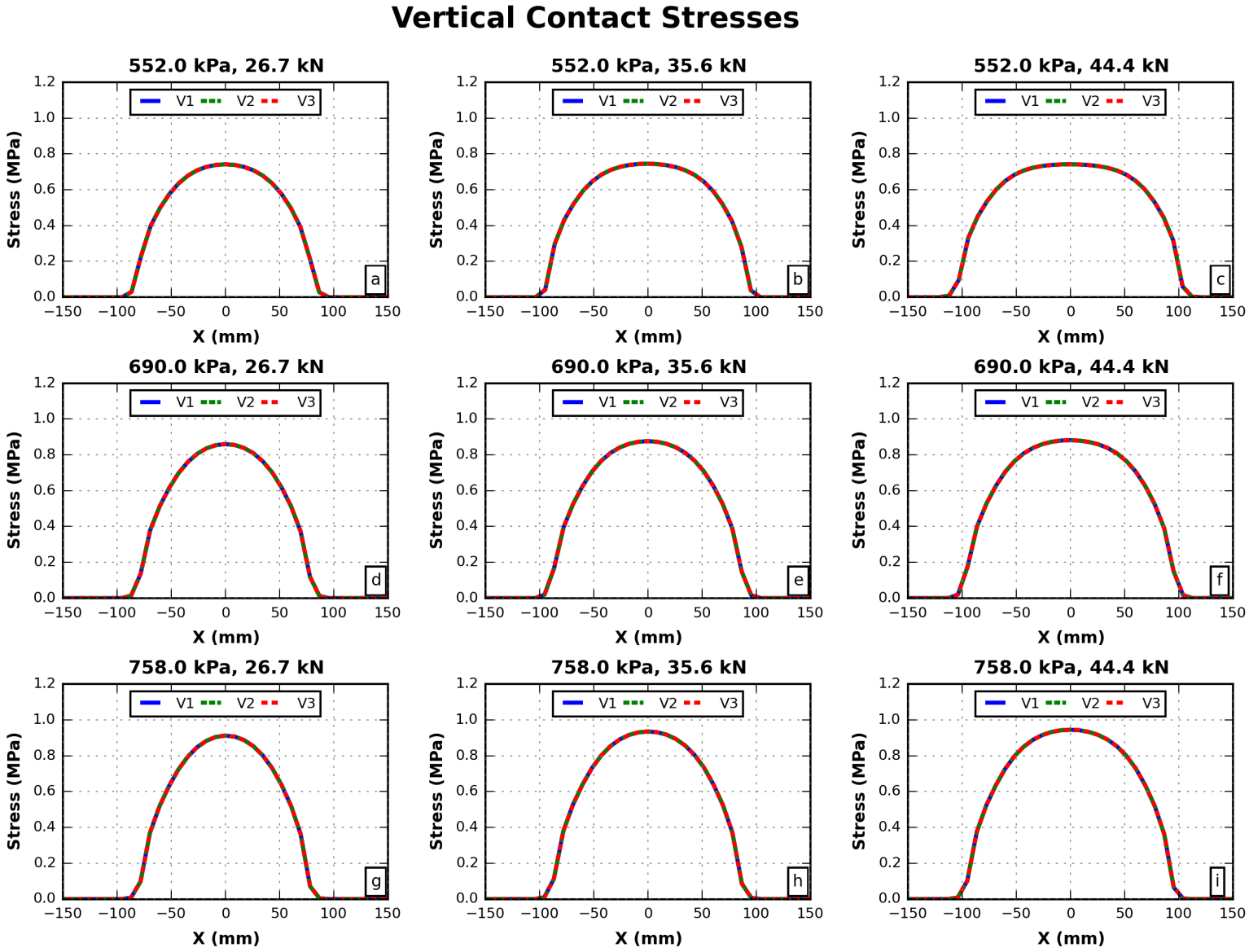

Fig. B.3. Vertical contact stresses under free-rolling and varying speeds.

APPENDIX C

ROLLING HYPERELASTIC TIRE: *ACCELERATING*

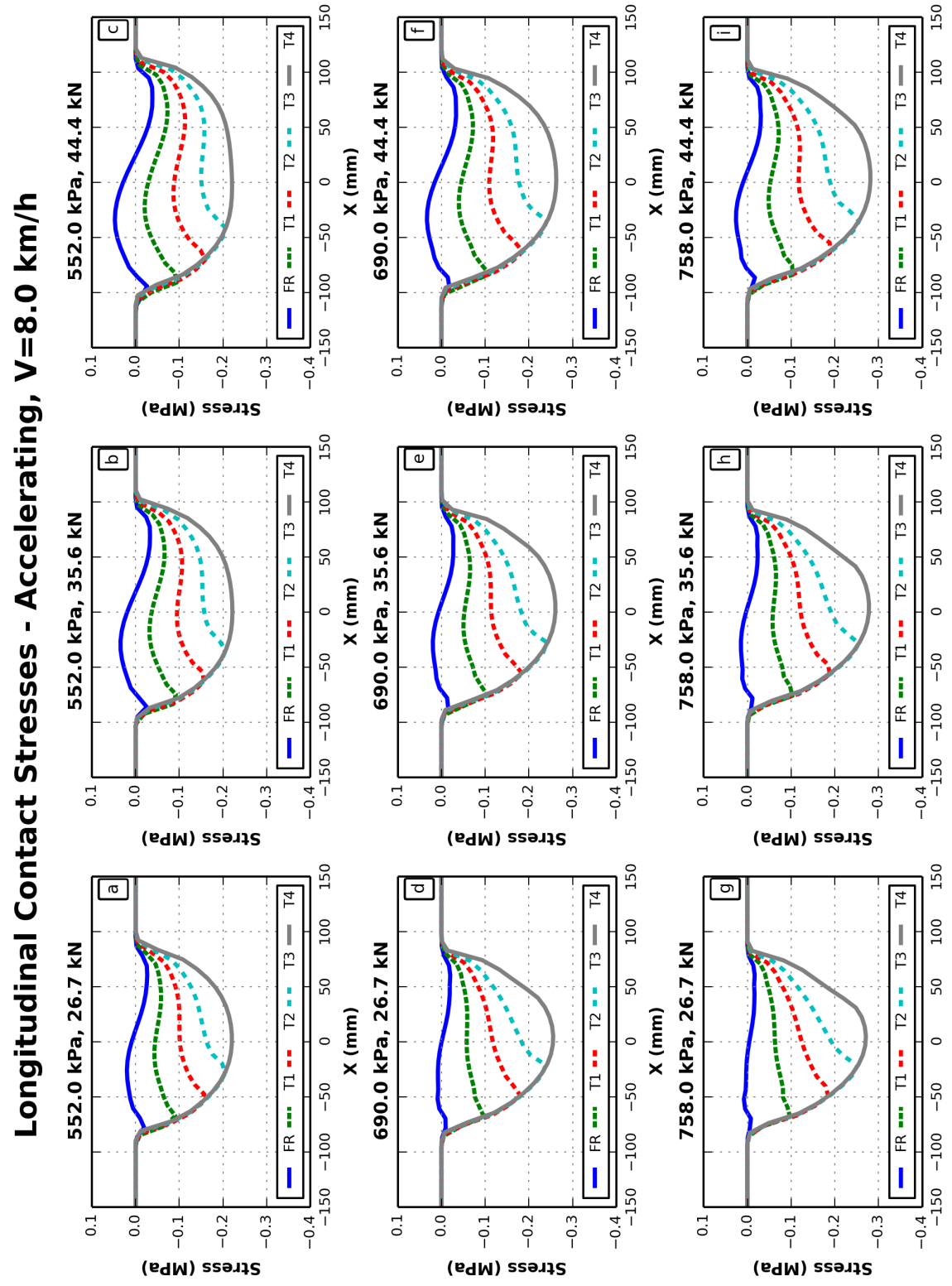

Fig. C.1. Longitudinal contact stresses under braking condition and V=8 km/h.

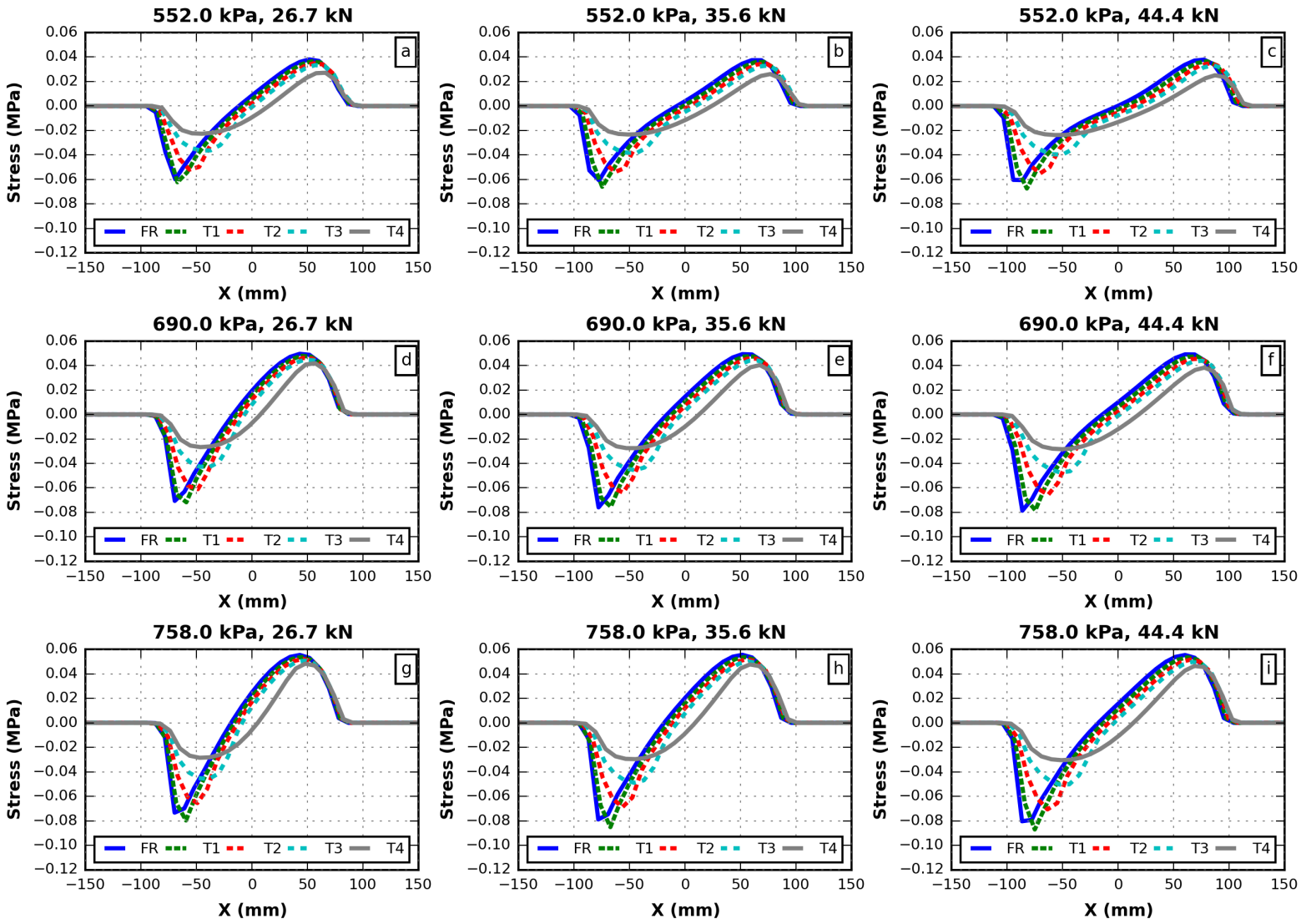

Fig. C.2. Transverse contact stresses under braking condition and V=8 km/h.

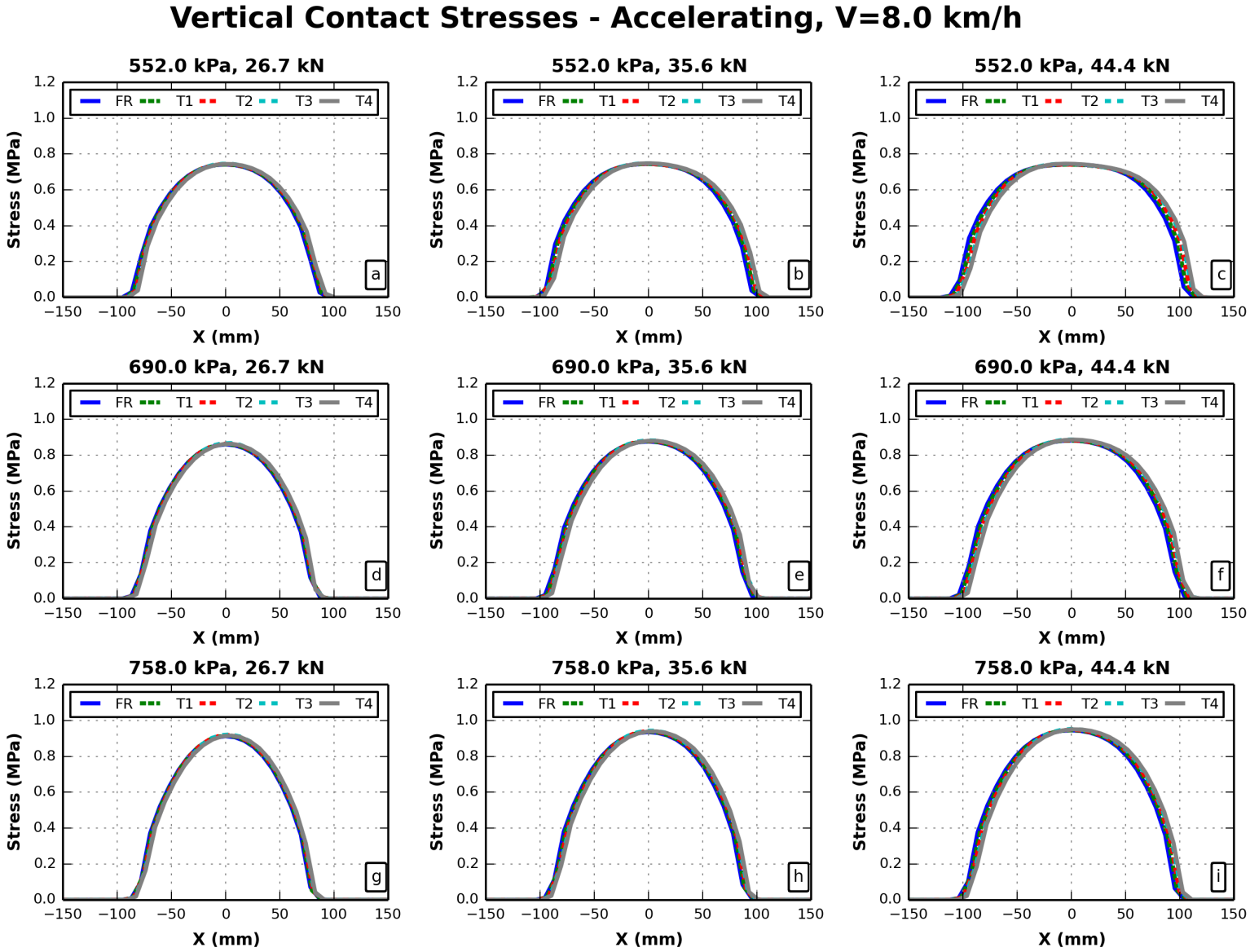

Fig. C.3. Vertical contact stresses under braking condition and V=8 km/h.

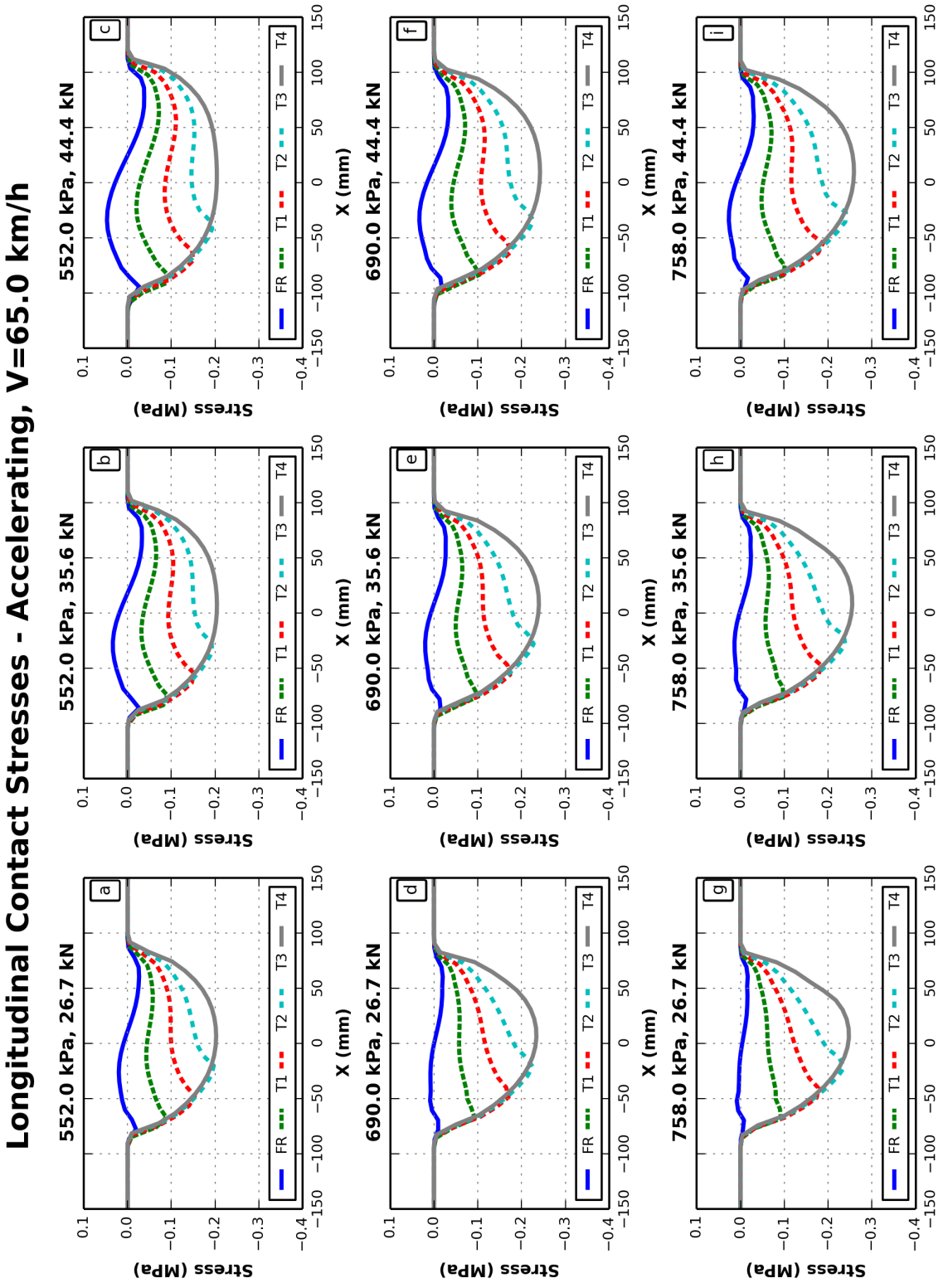

Fig. C.4. Longitudinal contact stresses under braking condition and V=65 km/h.

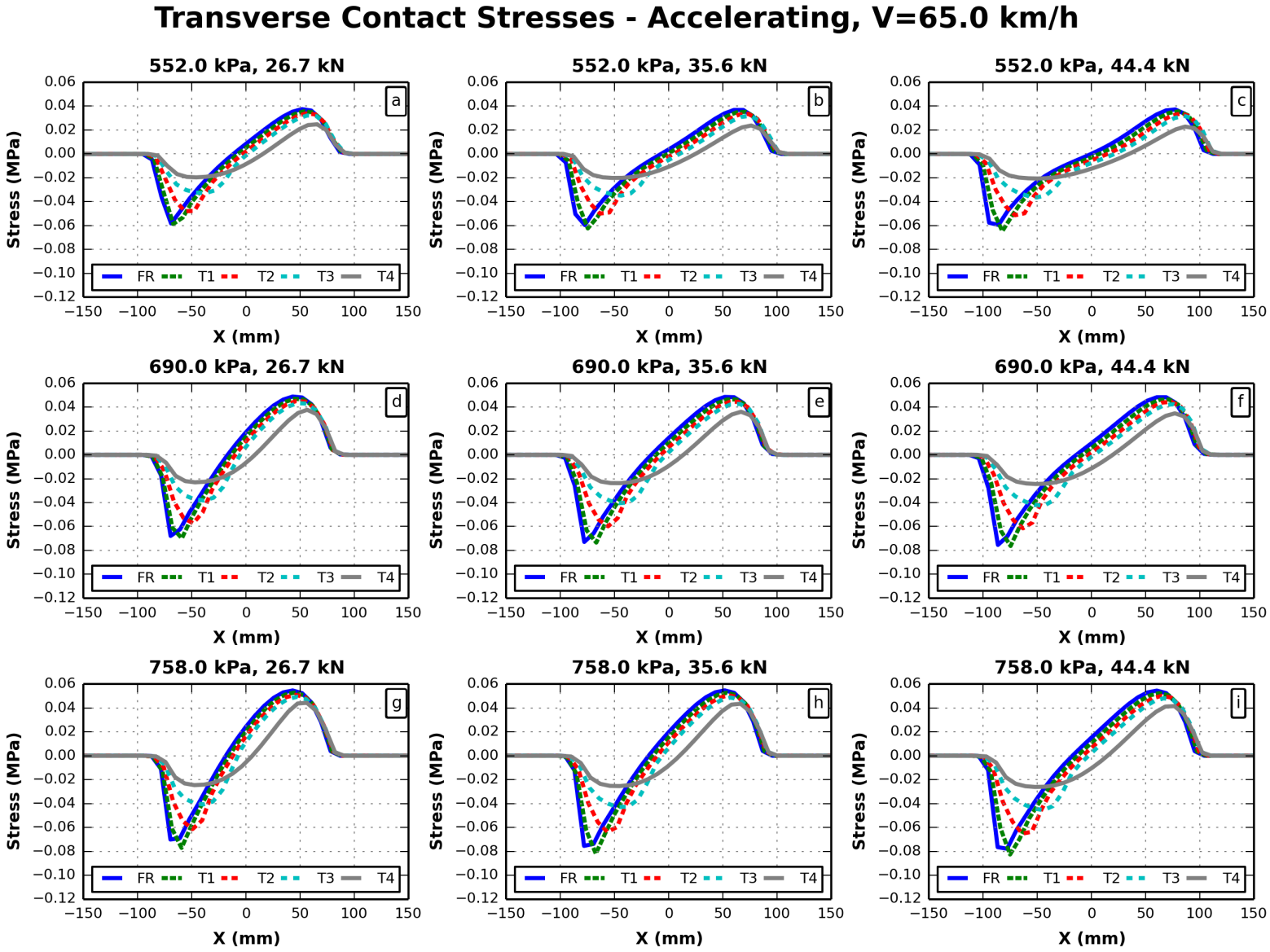

Fig. C.5. Transverse contact stresses under braking condition and V=65 km/h.

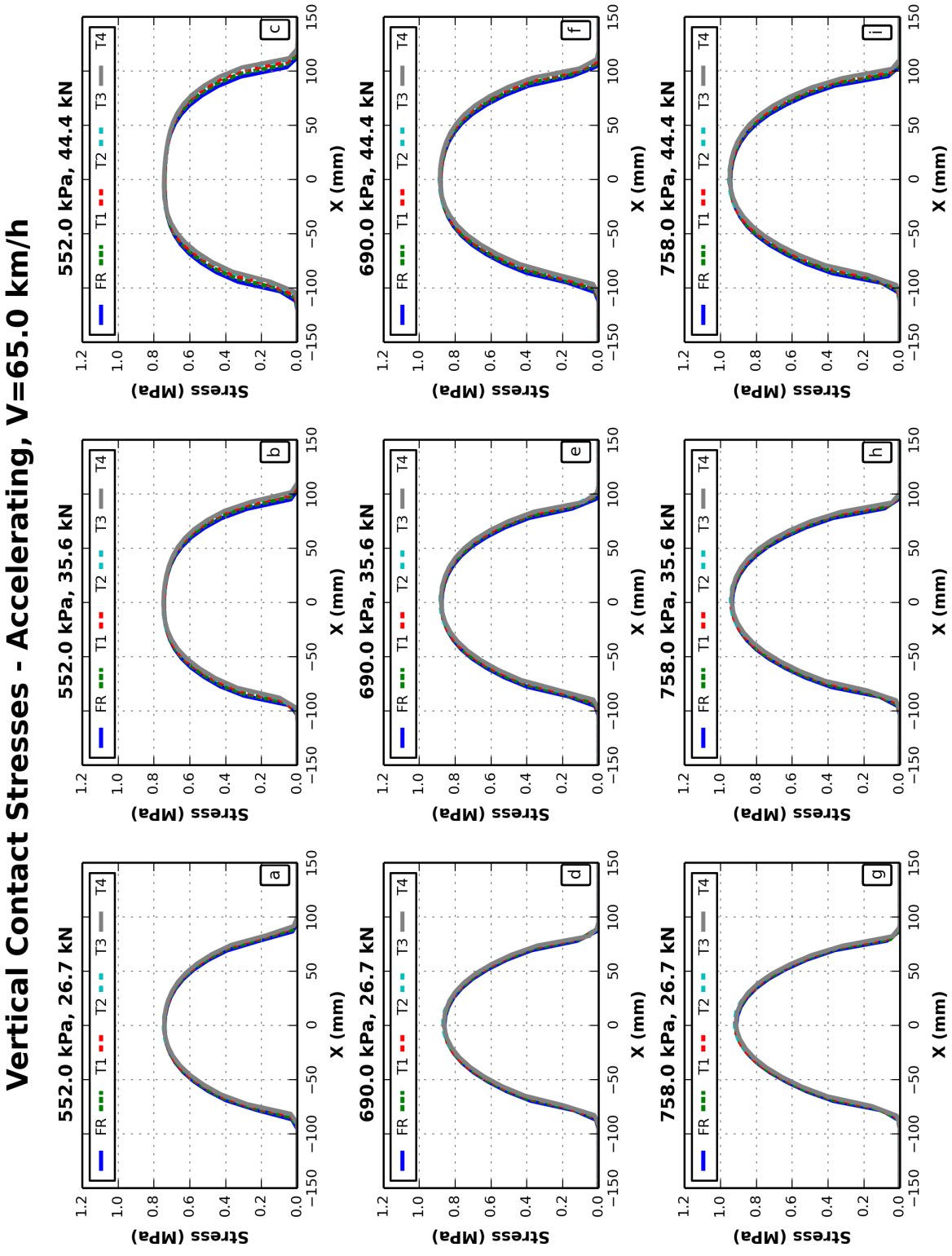

Fig. C.6. Vertical contact stresses under braking condition and V=65 km/h.

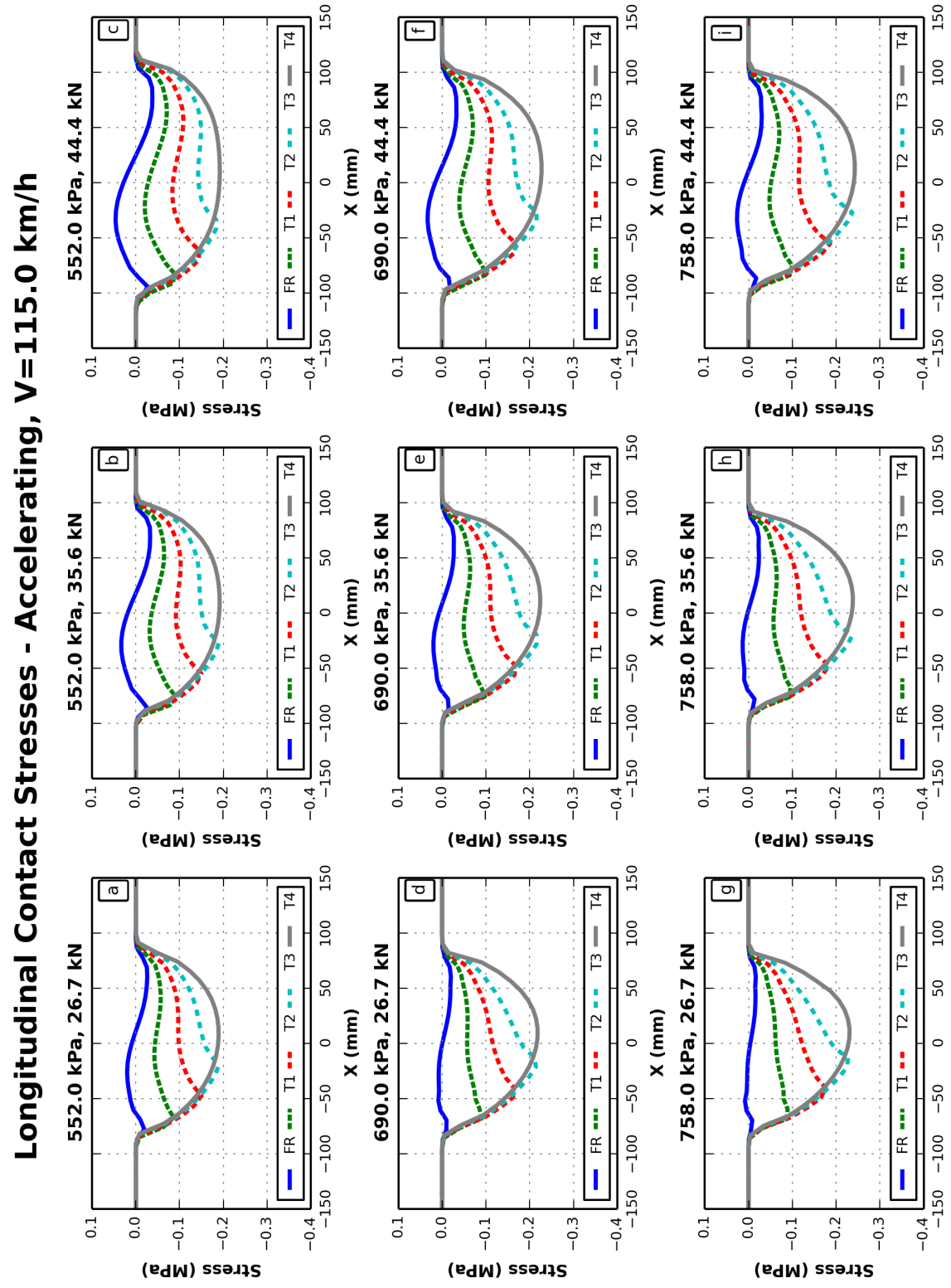

Fig. C.7. Longitudinal contact stresses under braking condition and V=115 km/h.

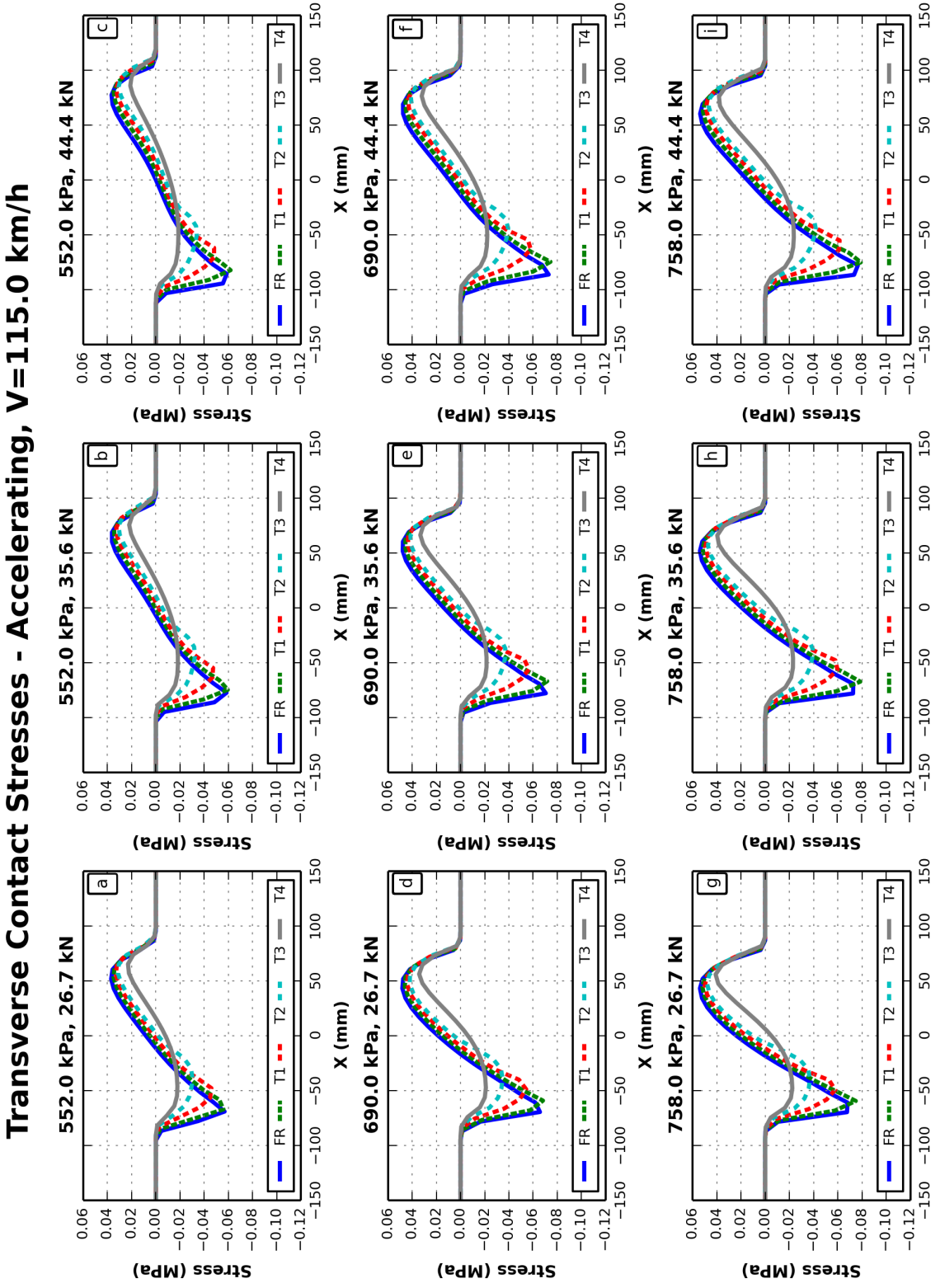

Fig. C.8. Transverse contact stresses under braking condition and V=115 km/h.

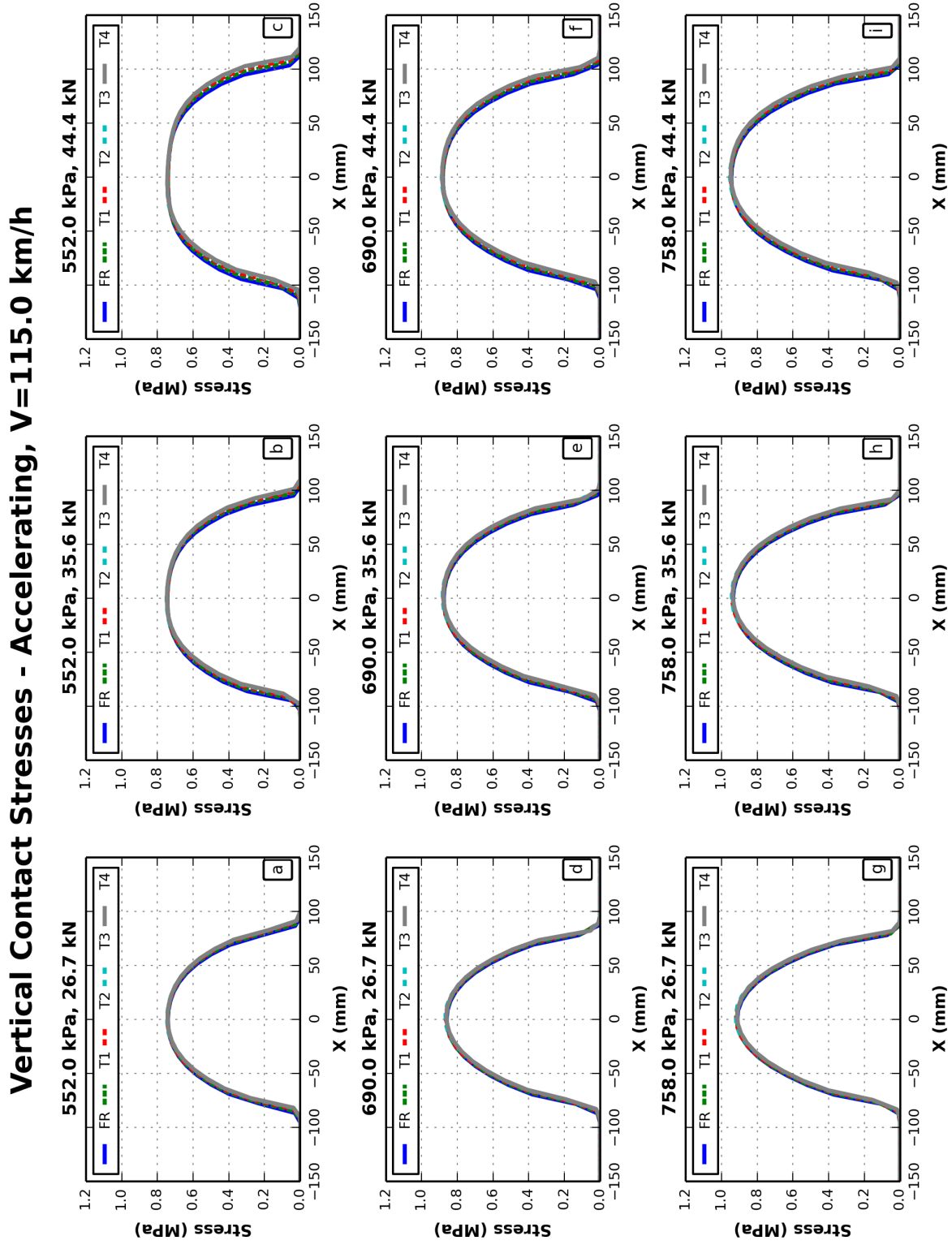

Fig. C.9. Vertical contact stresses under braking condition and V=115 km/h.

APPENDIX D

ROLLING HYPERELASTIC TIRE: *BRAKING*

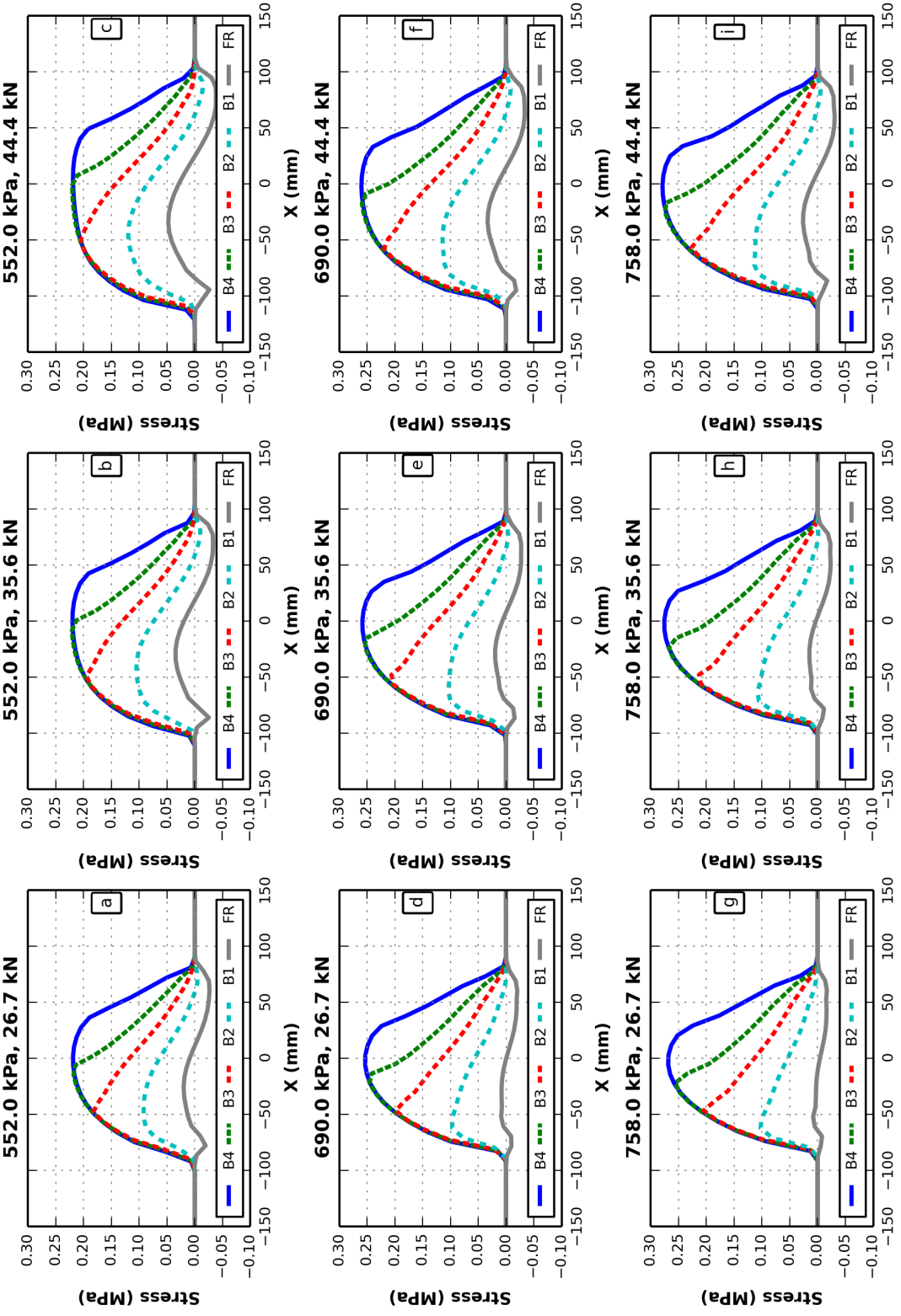

Fig. D.1. Longitudinal contact stresses under braking condition and V=8 km/h.

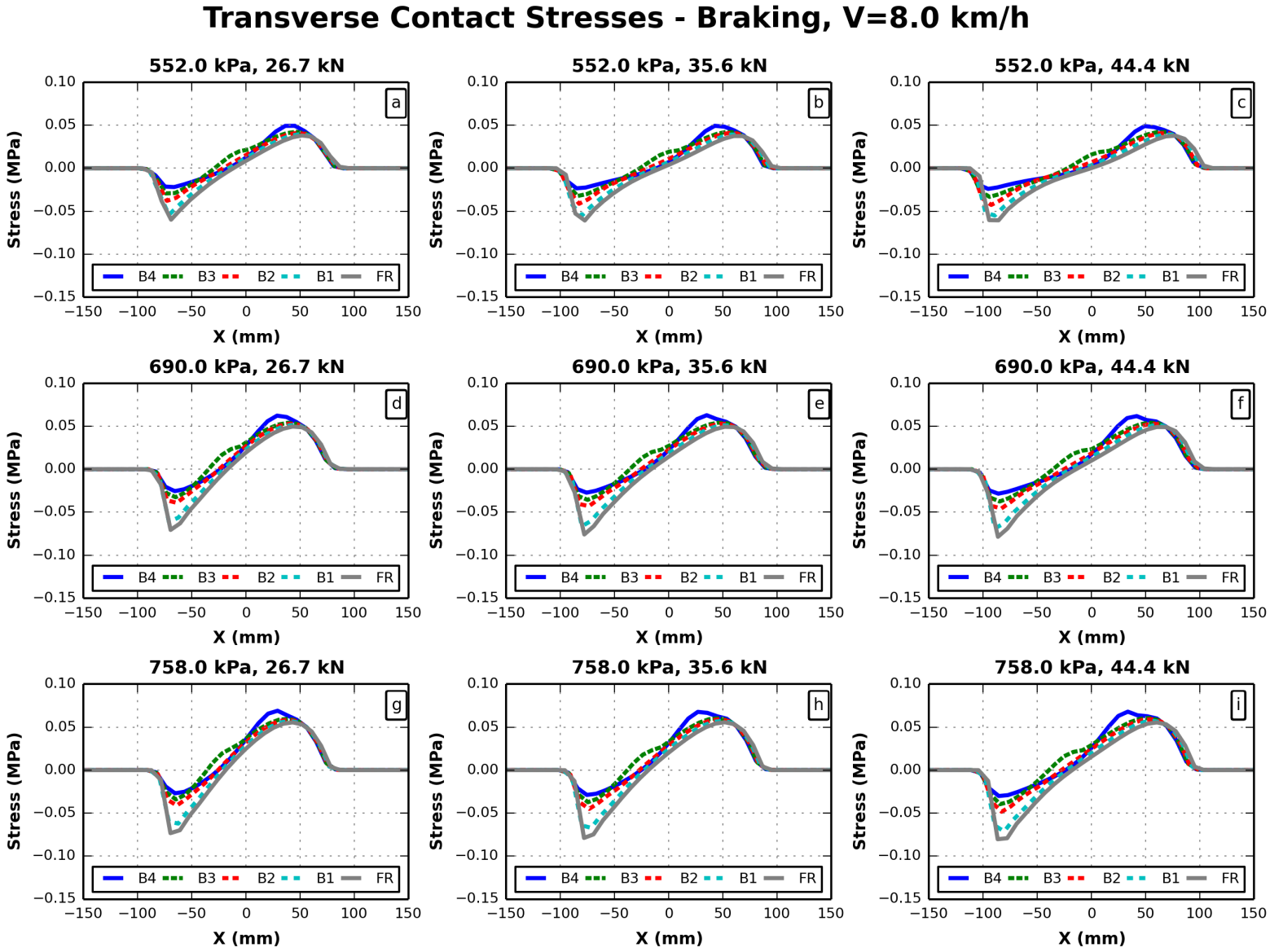

Fig. D.2. Transverse contact stresses under braking condition and V=8 km/h.

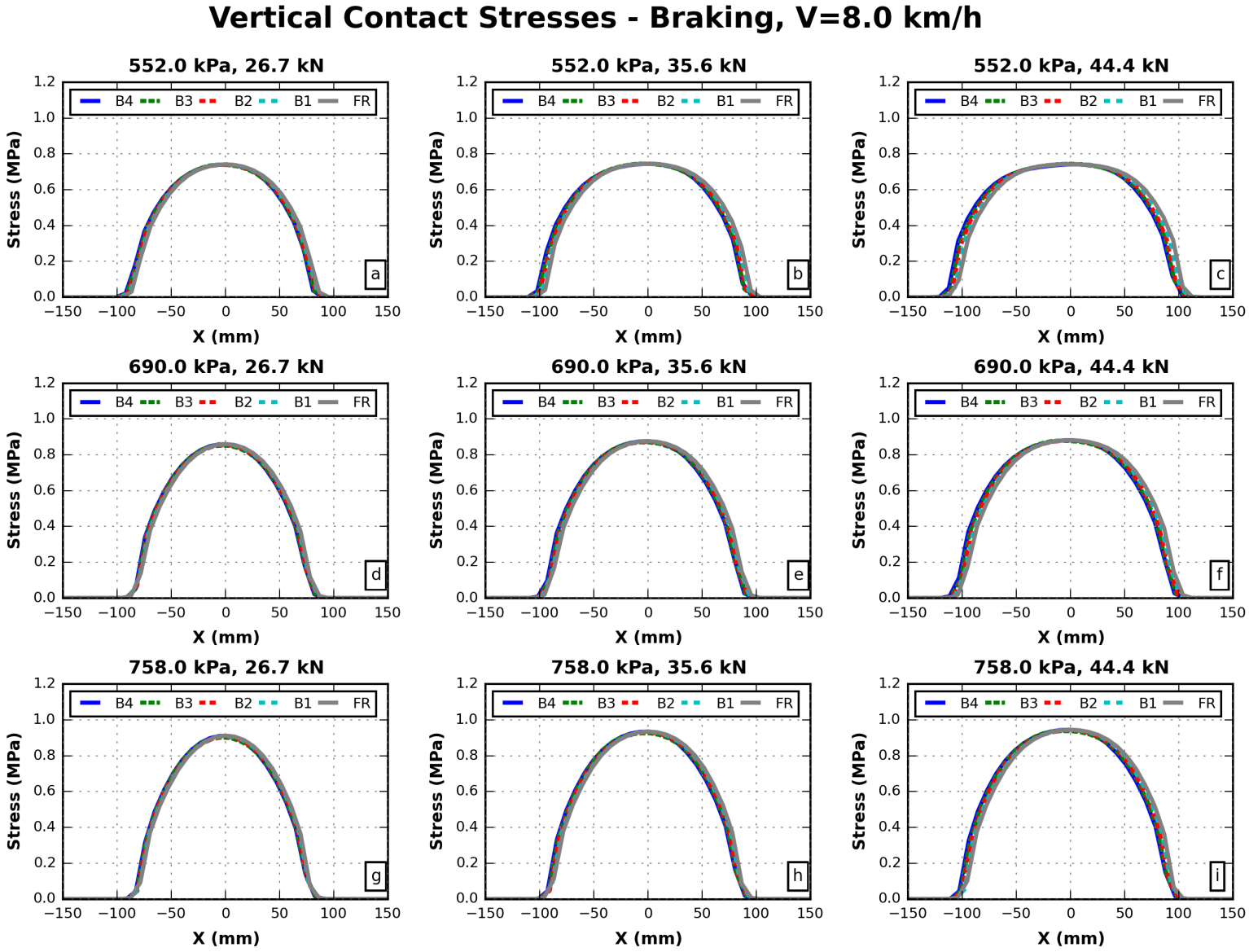

Fig. D.3. Vertical contact stresses under braking condition and V=8 km/h.

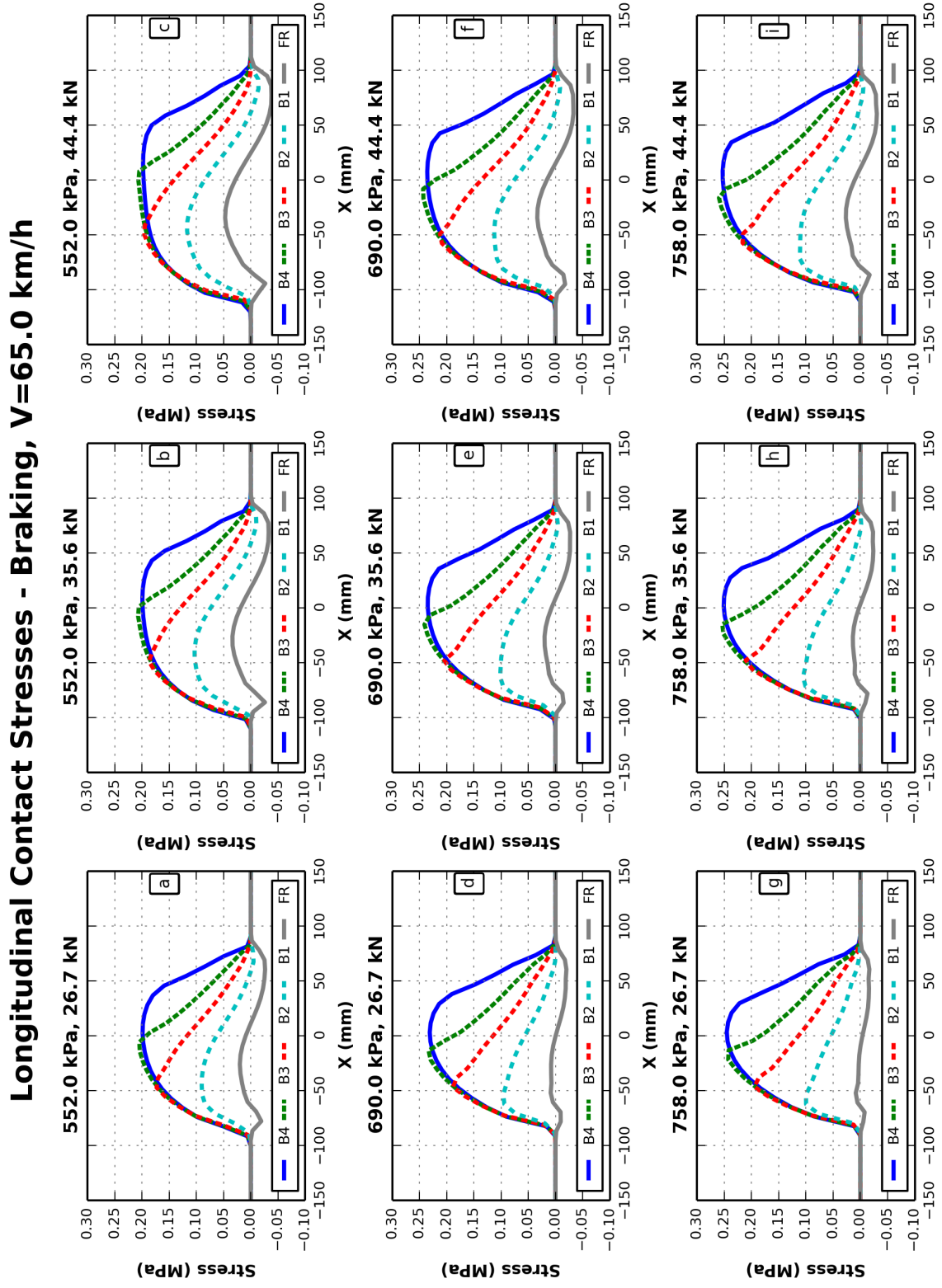

Fig. D.4. Longitudinal contact stresses under braking condition and V=65 km/h.

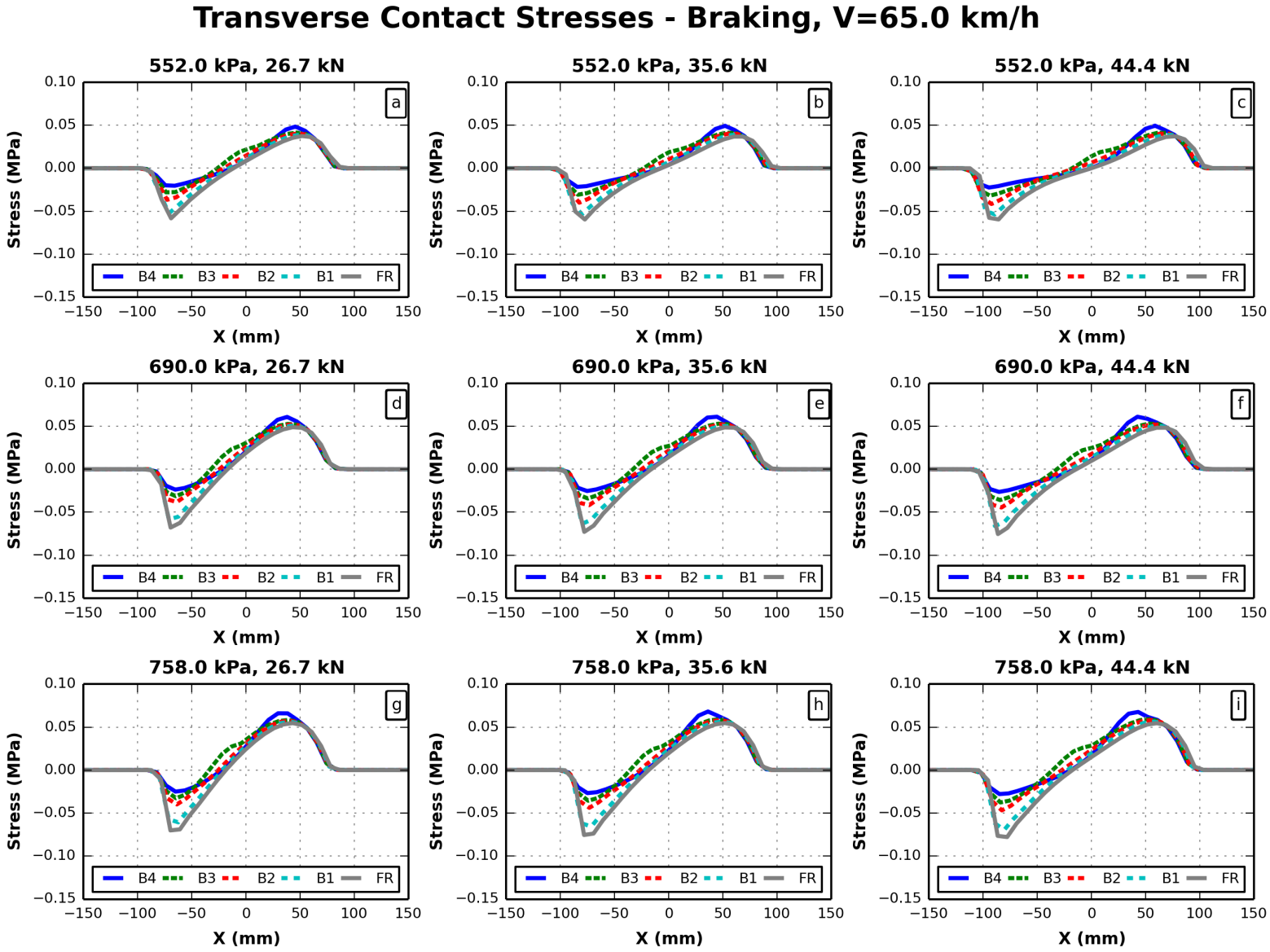

Fig. D.5. Transverse contact stresses under braking condition and V=65 km/h.

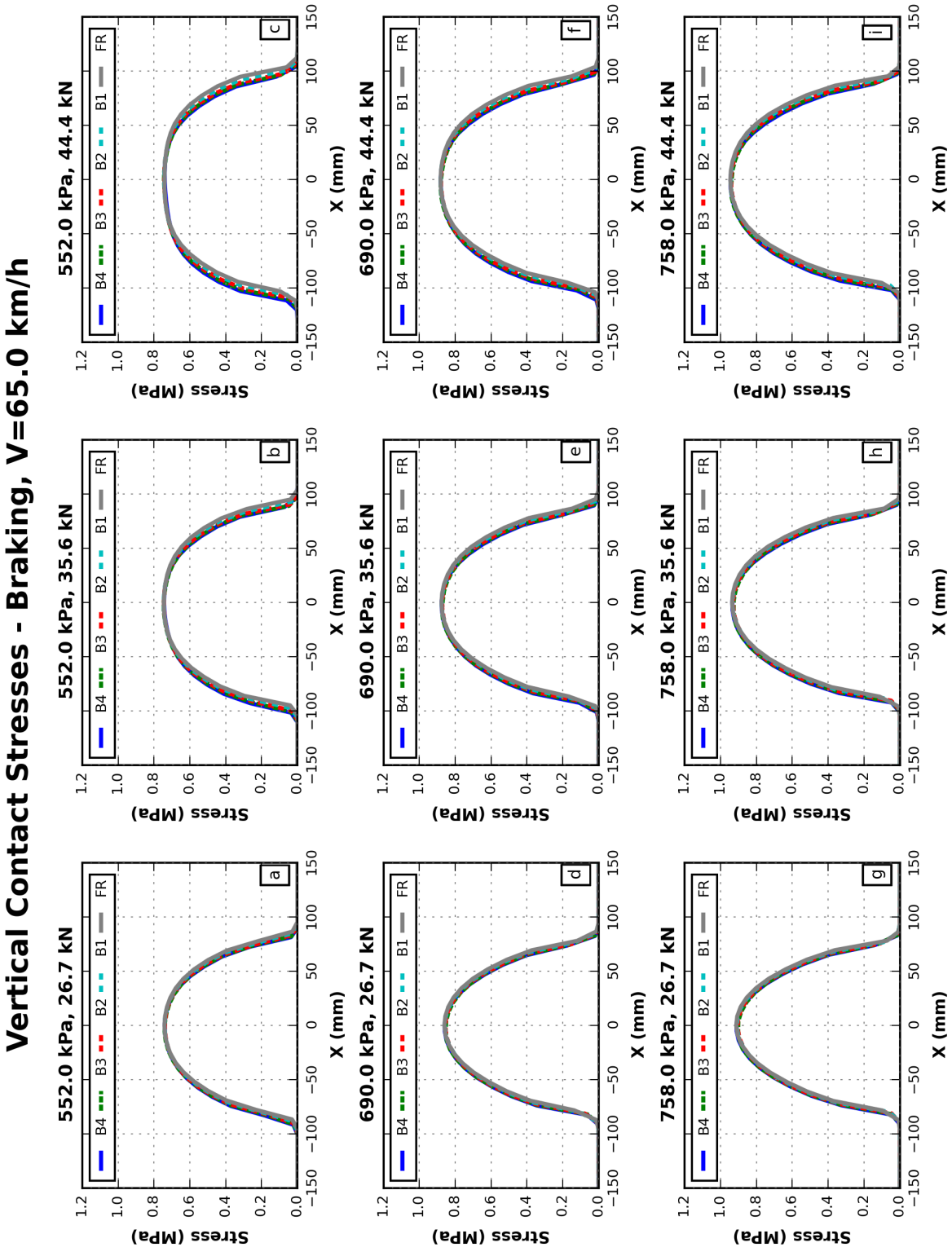

Fig. D.6. Vertical contact stresses under braking condition and V=65 km/h.

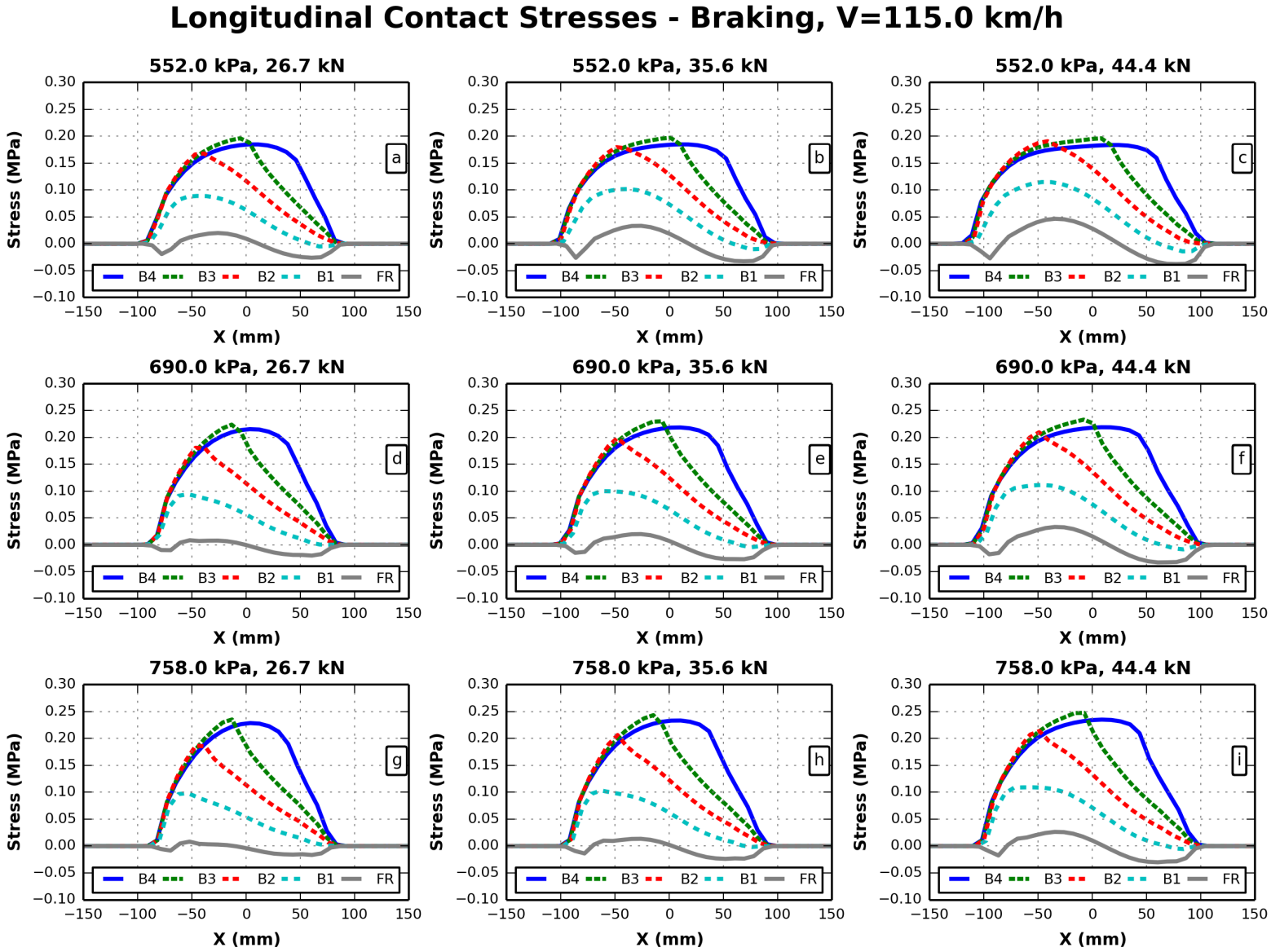

Fig. D.7. Longitudinal contact stresses under braking condition and V=115 km/h.

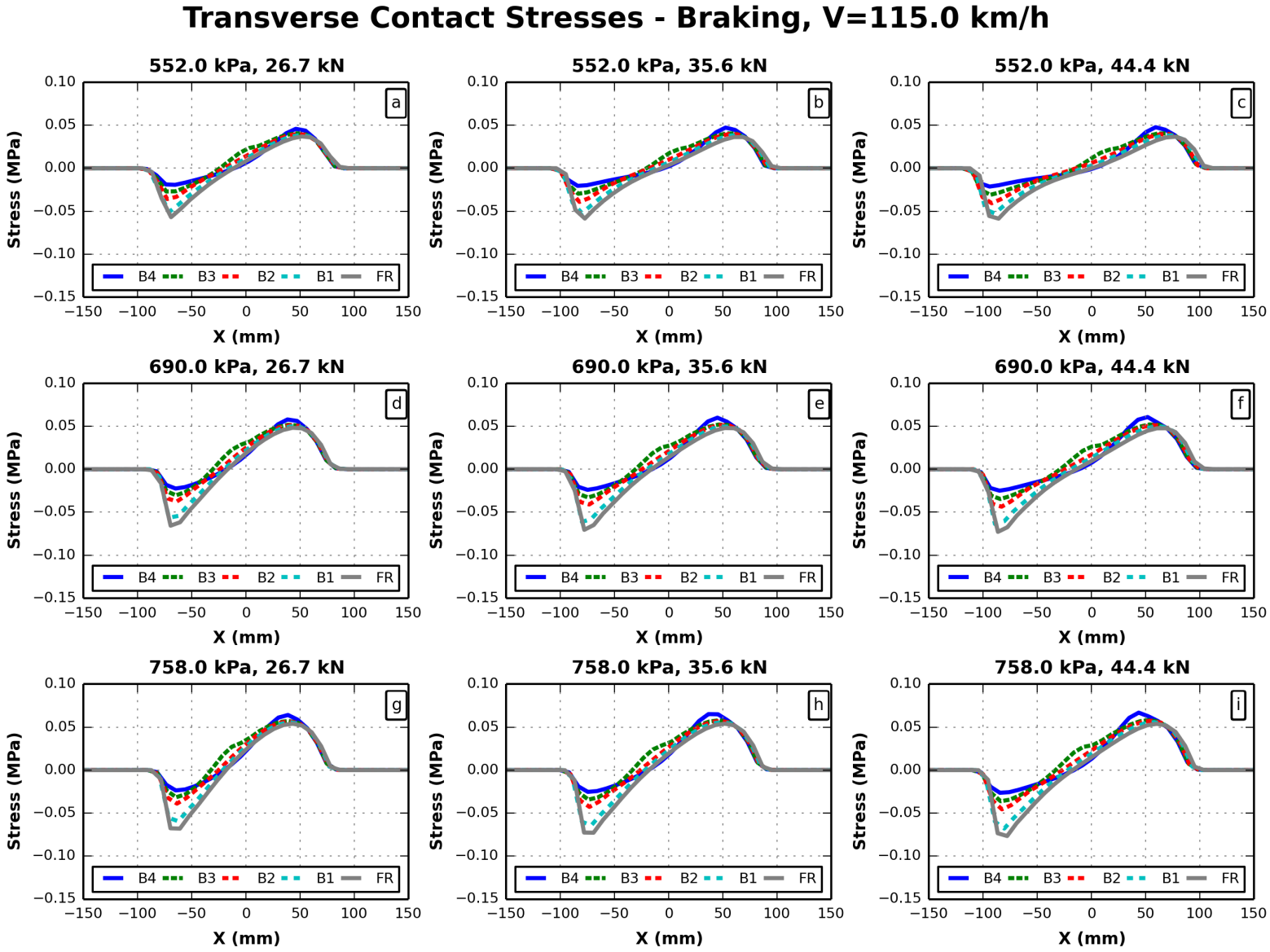

Fig. D.8. Transverse contact stresses under braking condition and V=115 km/h.

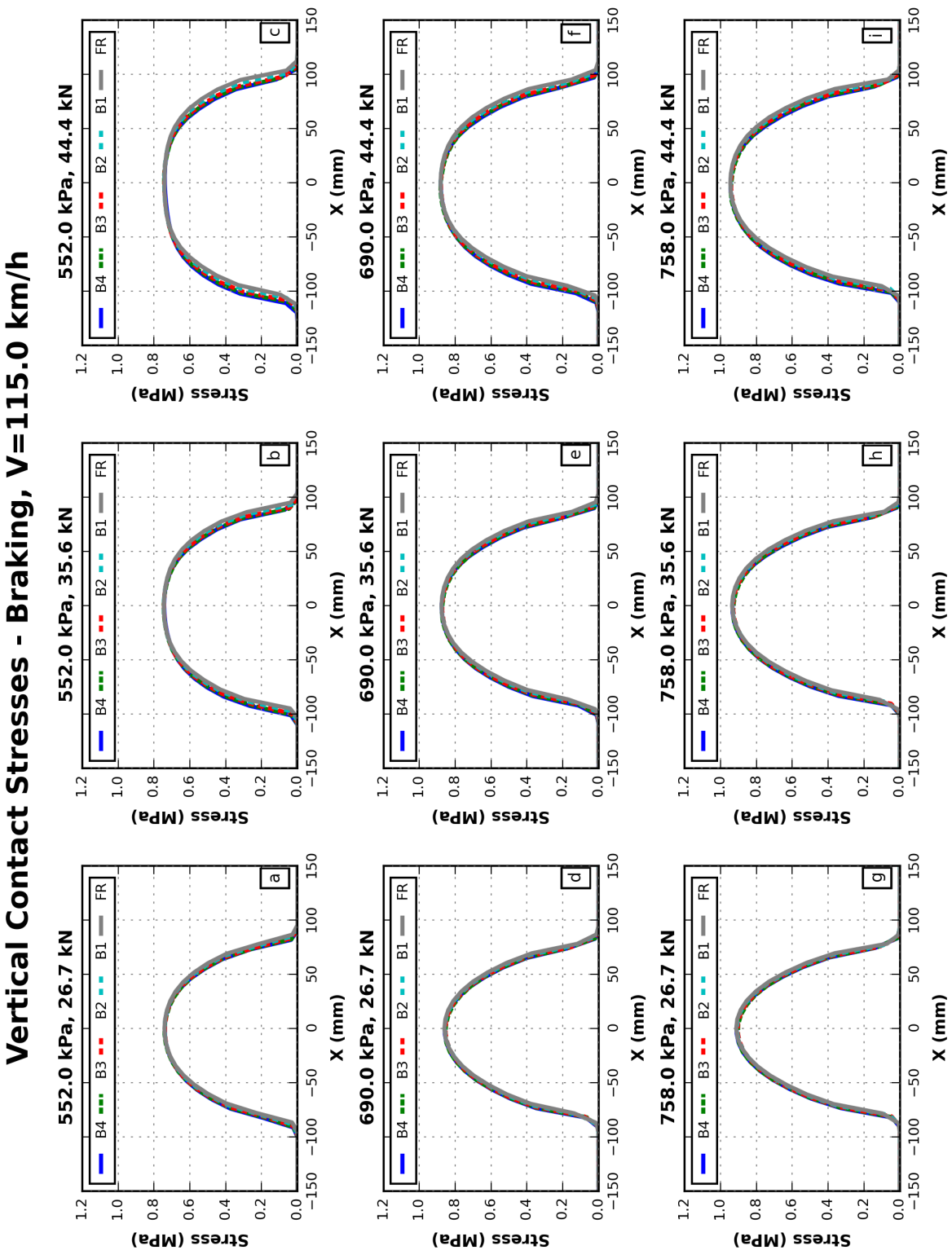

Fig. D.9. Vertical contact stresses under braking condition and V=115 km/h.

APPENDIX E

ROLLING HYPERELASTIC TIRE: *CORNERING*

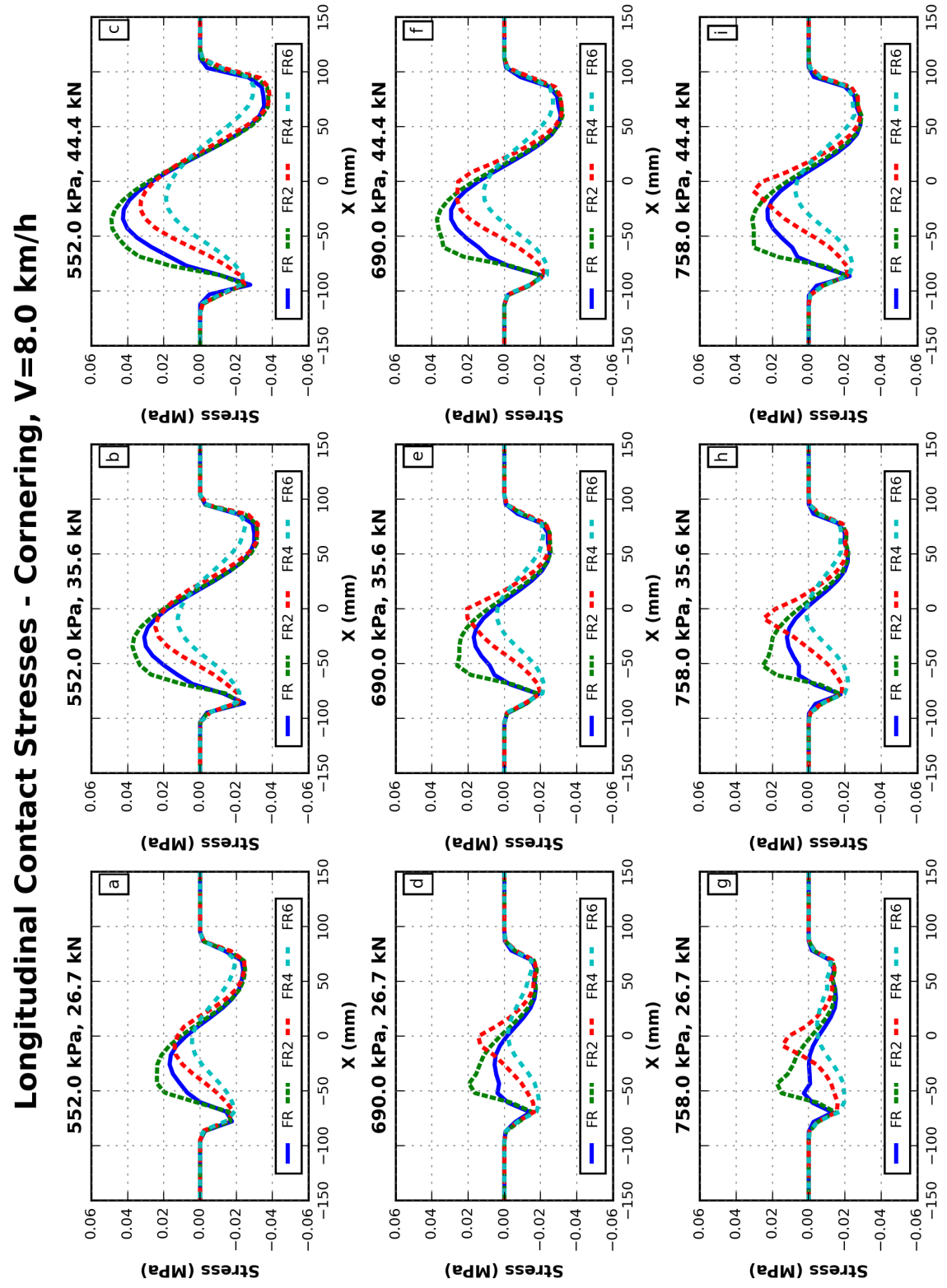

Fig. E.1. Longitudinal contact stresses under braking condition and V=8 km/h.

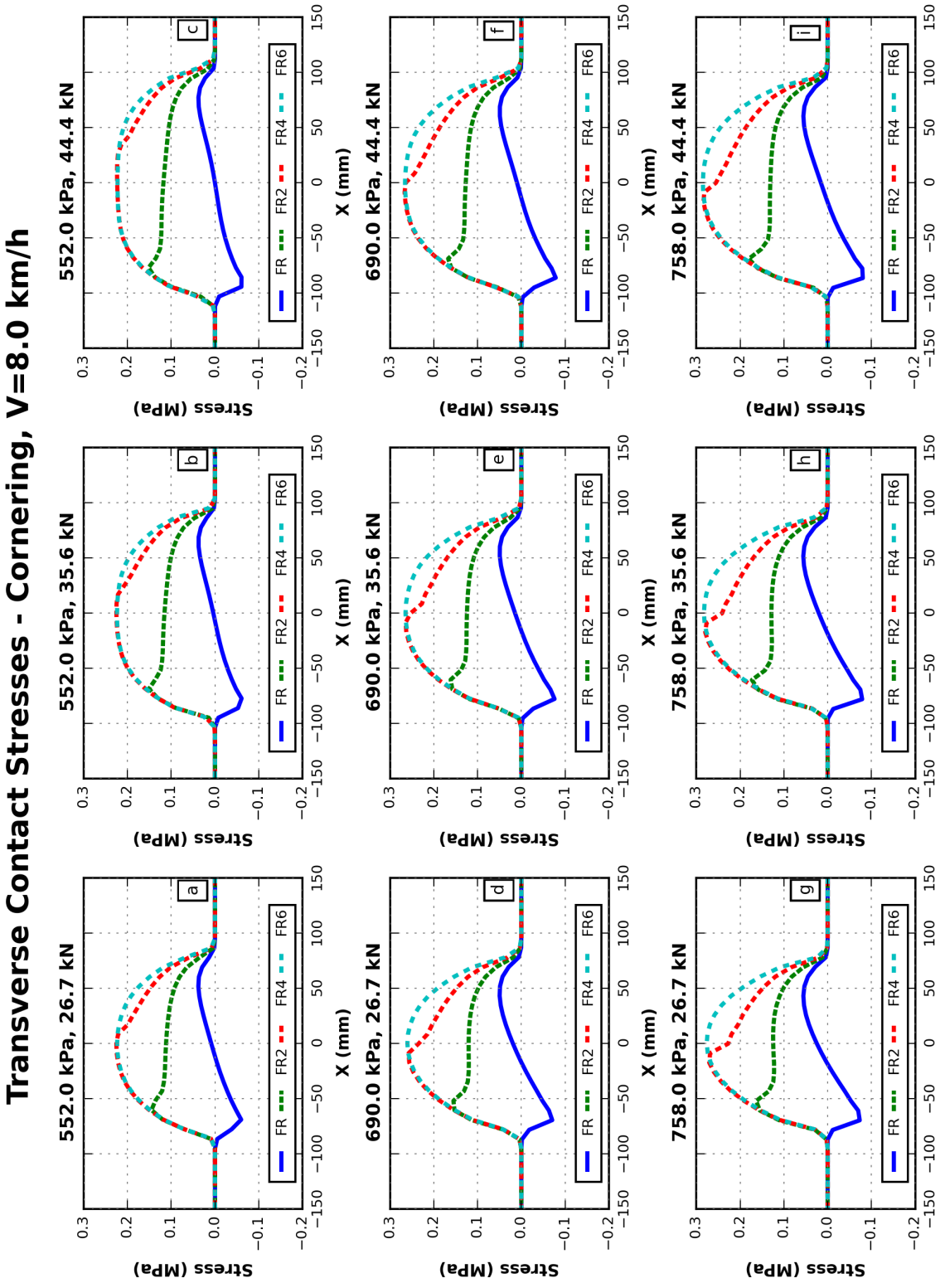

Fig. E.2. Transverse contact stresses under braking condition and V=8 km/h.

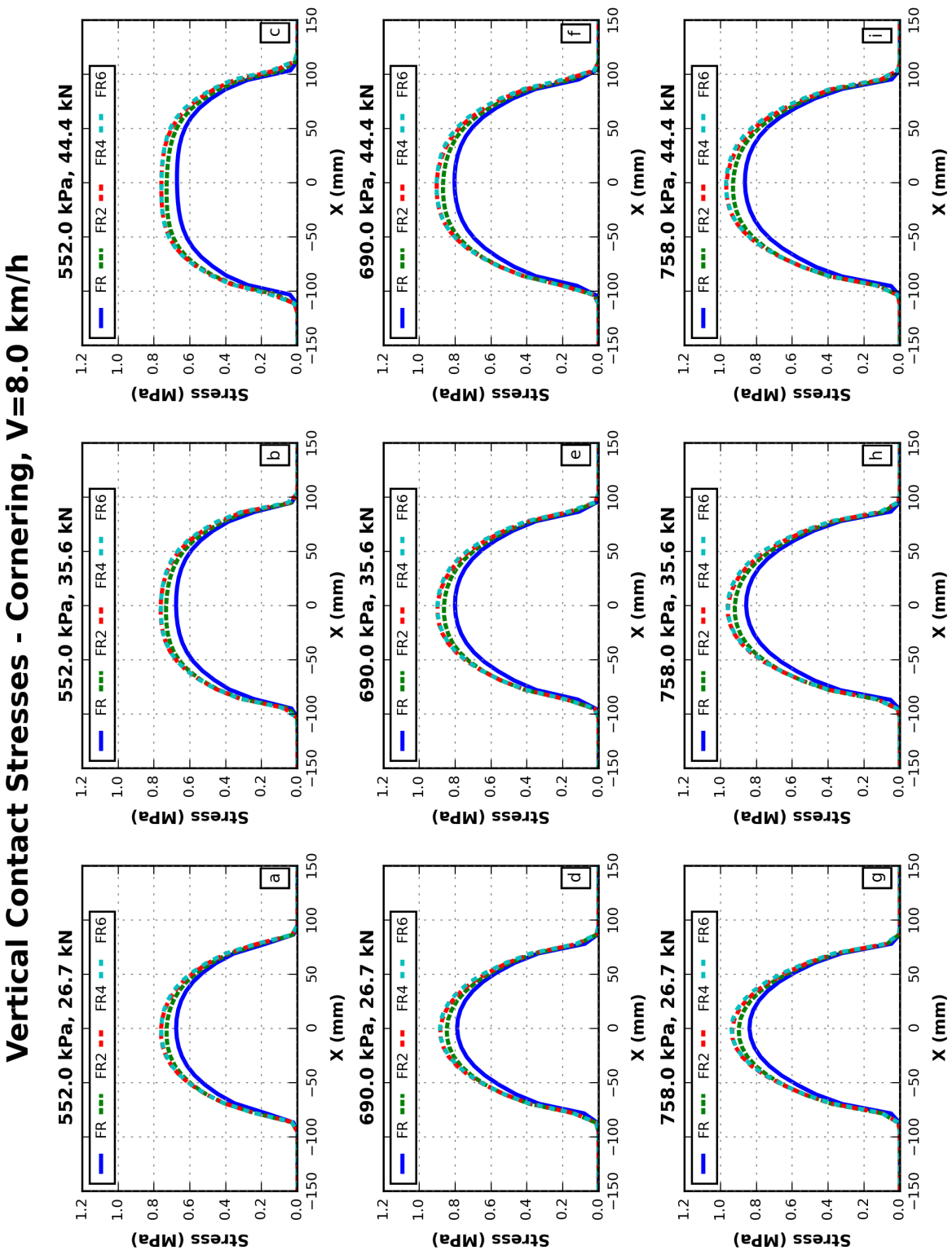

Fig. E.3. Vertical contact stresses under braking condition and V=8 km/h.

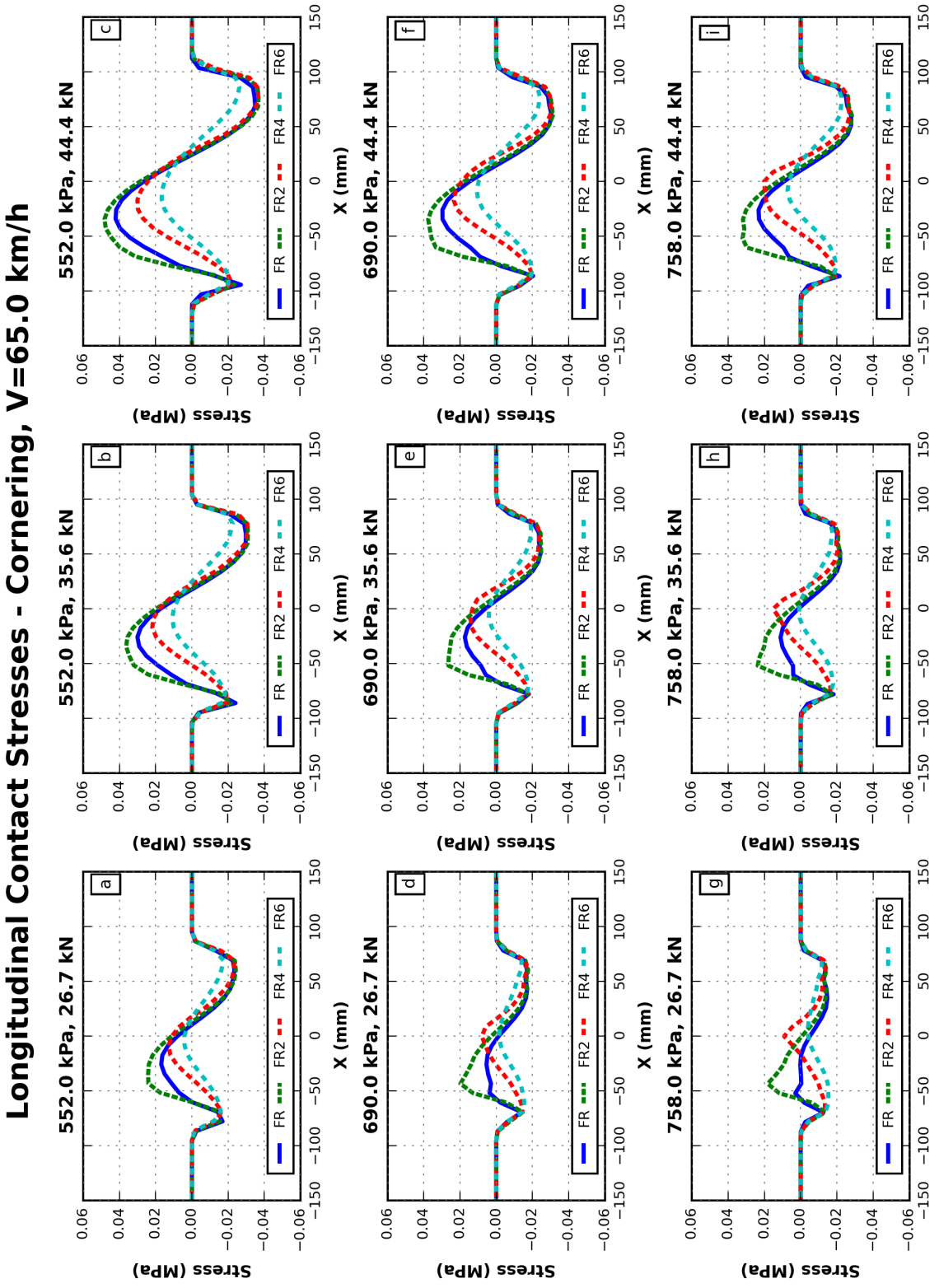

Fig. E.4. Longitudinal contact stresses under braking condition and V=65 km/h.

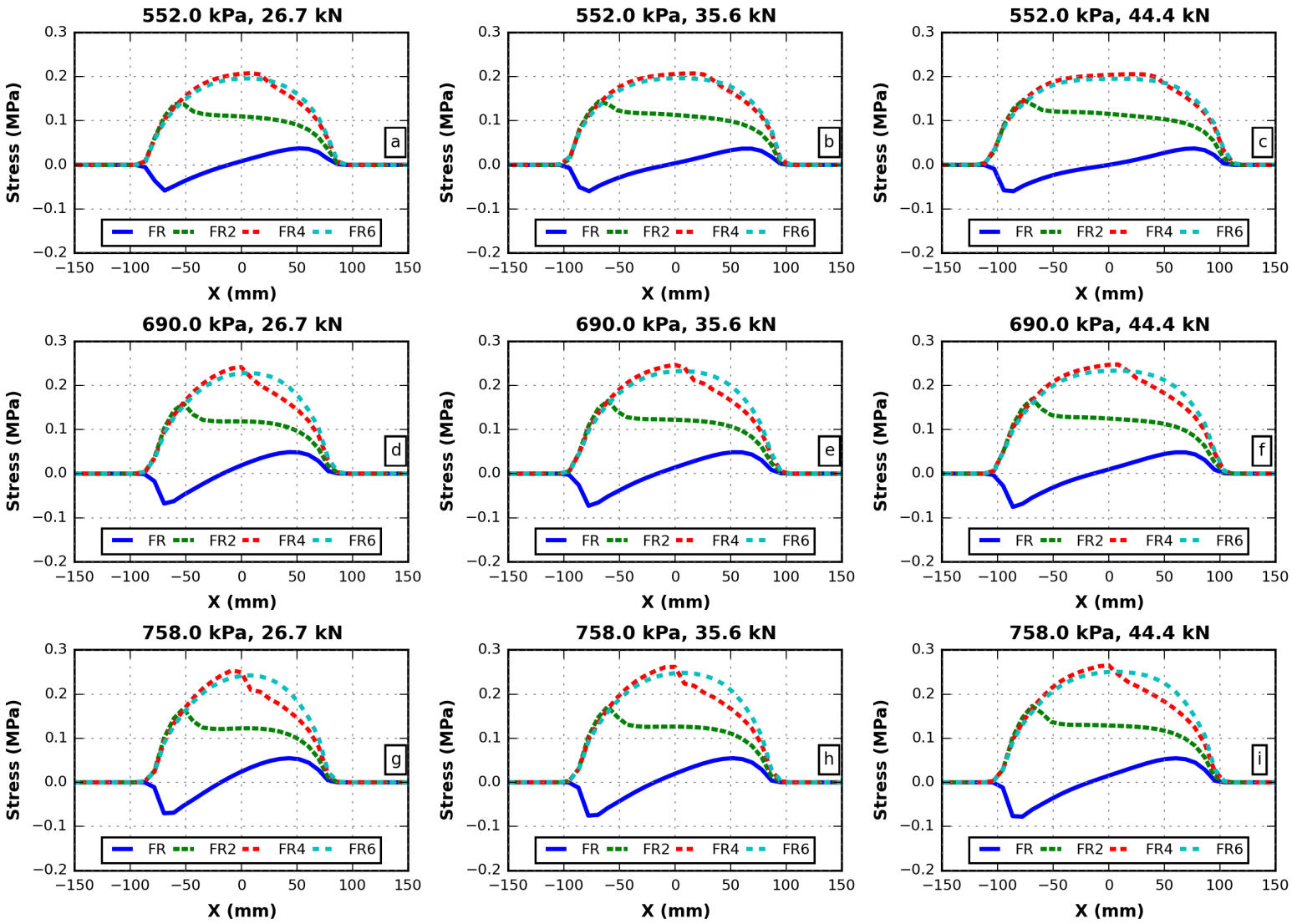

Fig. E.5. Transverse contact stresses under braking condition and V=65 km/h.

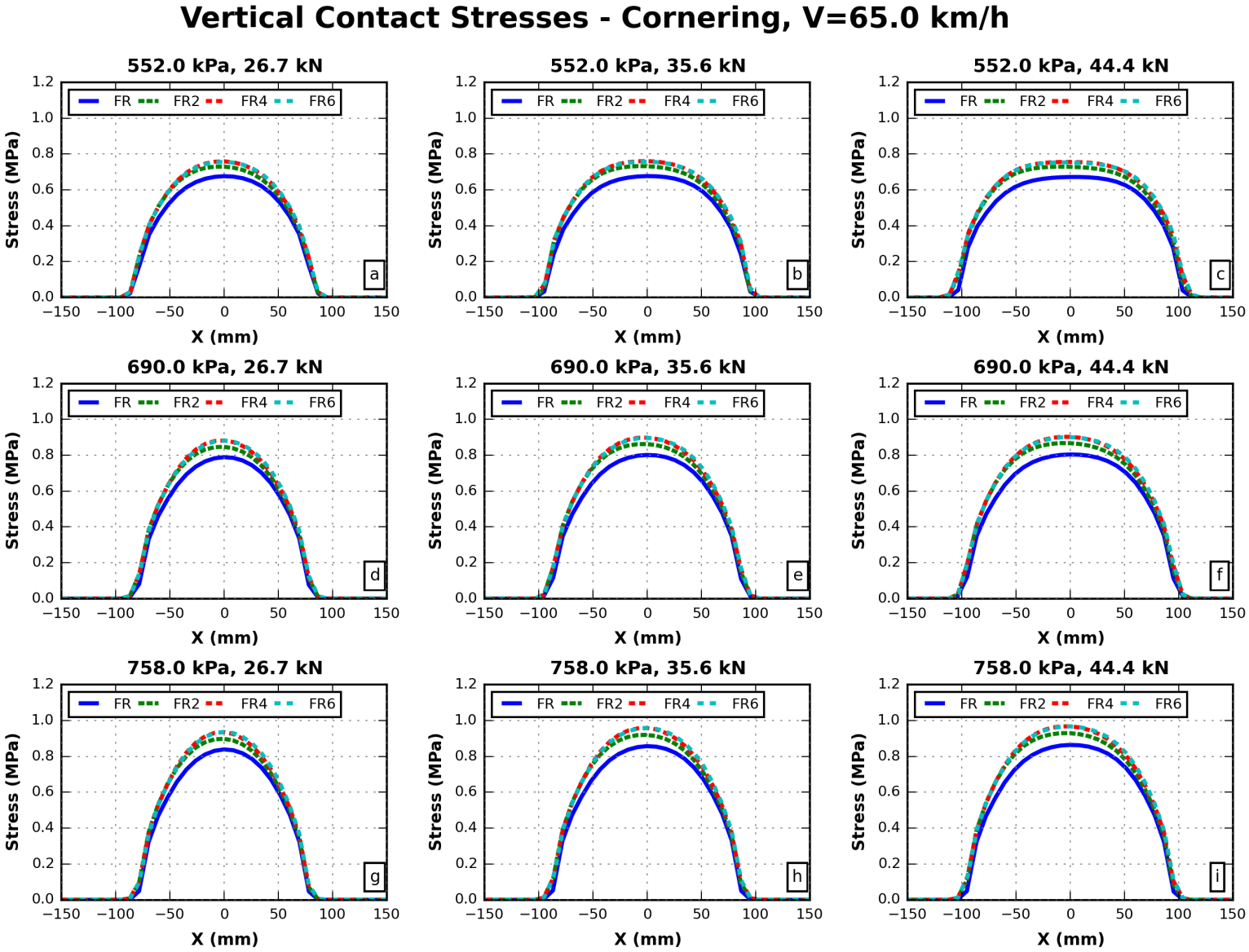

Fig. E.6. Vertical contact stresses under braking condition and V=65 km/h.

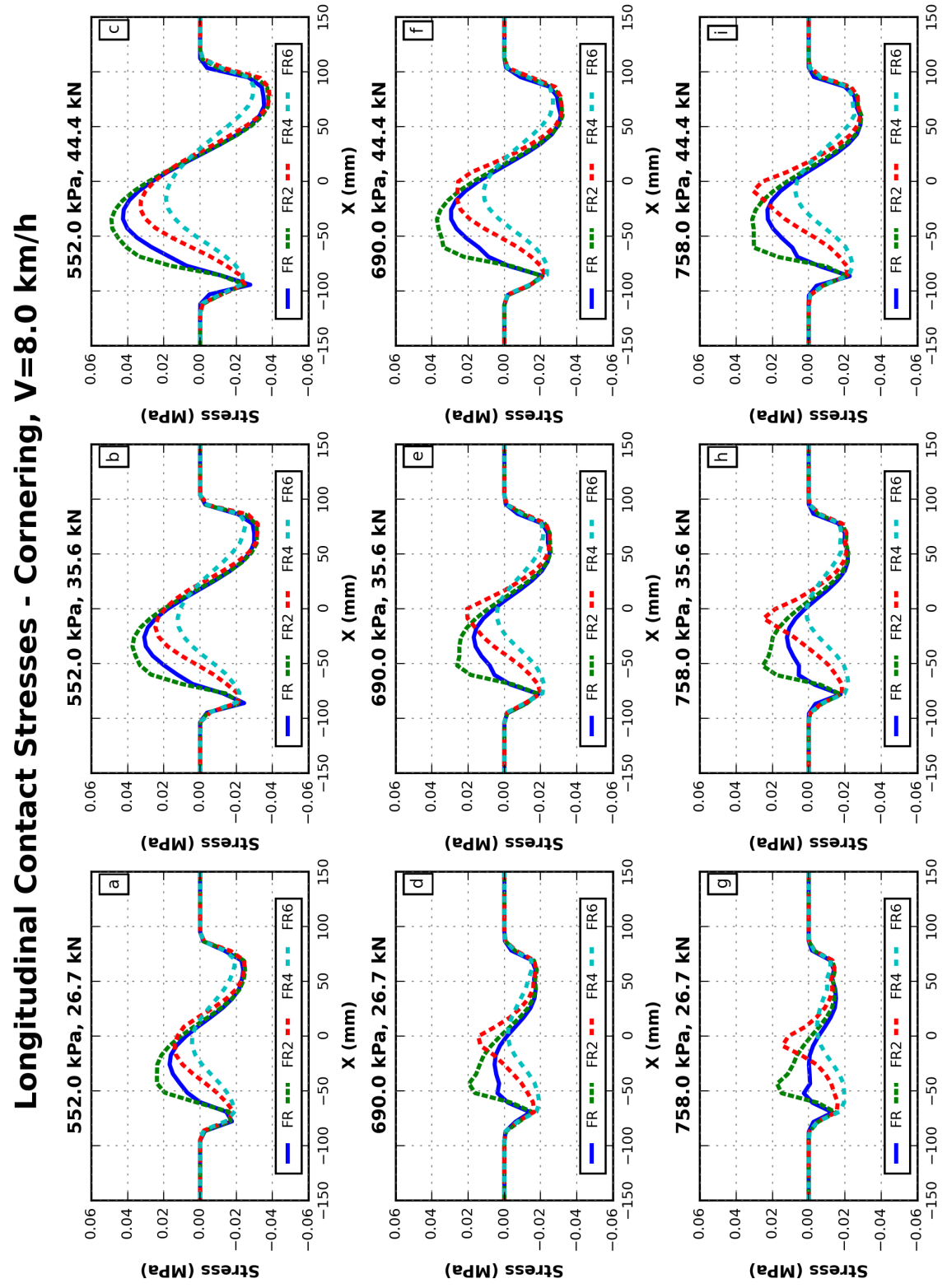

Fig. E.7. Longitudinal contact stresses under braking condition and V=115 km/h.

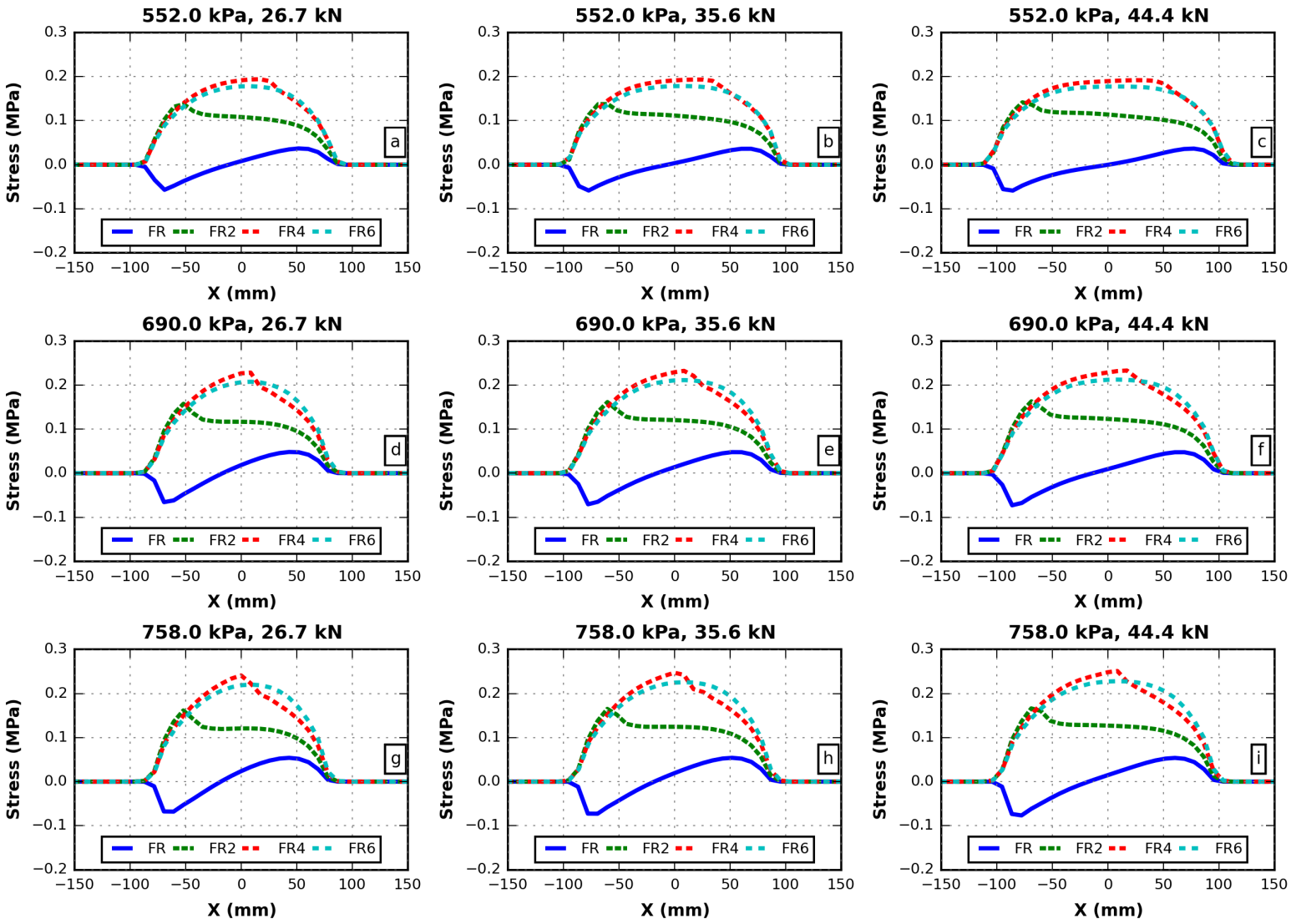

Fig. E.8. Transverse contact stresses under braking condition and V=115 km/h.

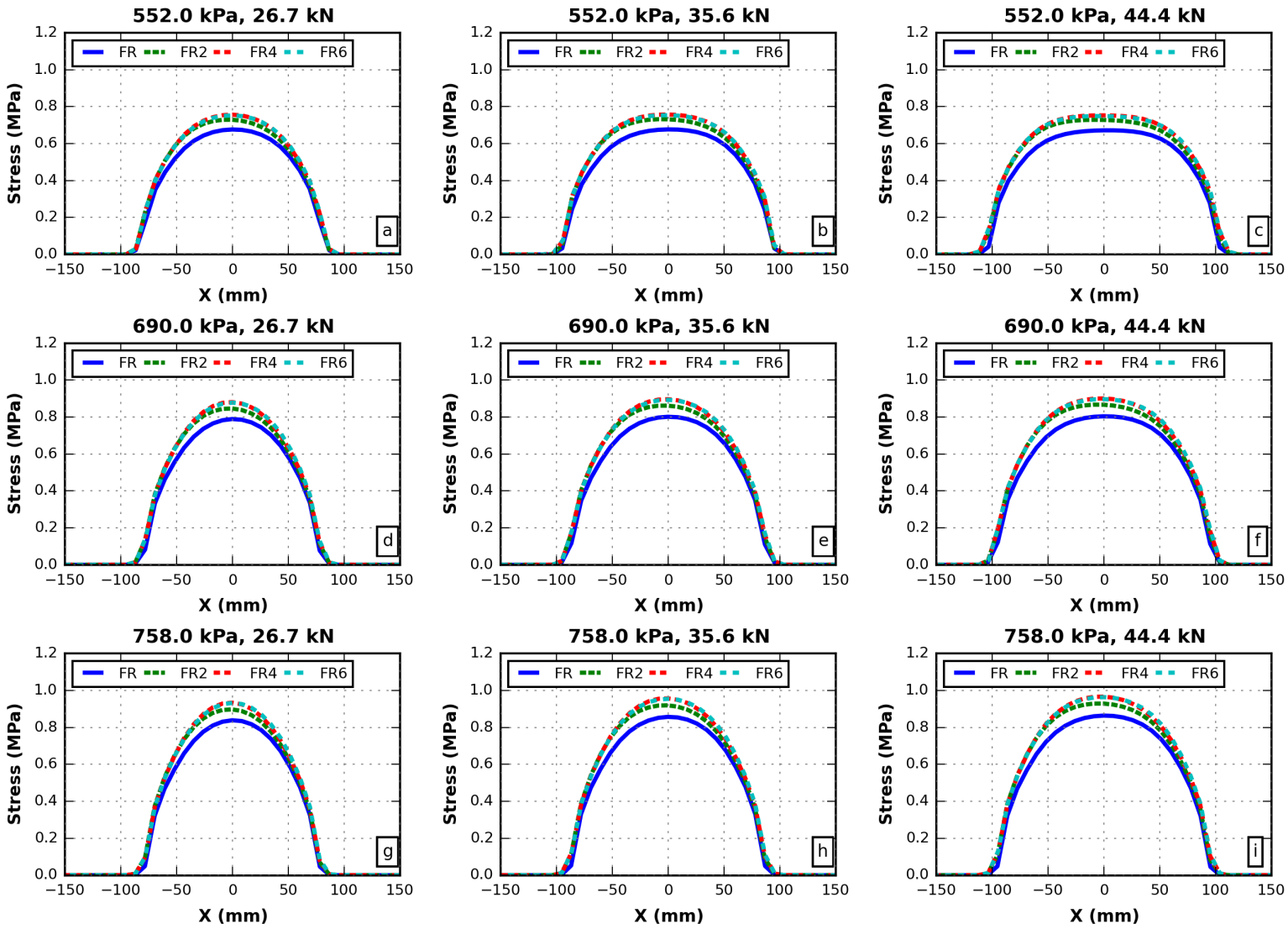

Fig. E.9. Vertical contact stresses under braking condition and V=115 km/h.